THE UNIVERSITY OF CHICAGO

VISUALIZING REACTIONS AT SURFACES: EXPLORING REACTIVE SURFACE DYNAMICS UTILIZING A NOVEL COMBINATION OF SUPERSONIC MOLECULAR BEAMS AND SCANNING TUNNELING MICROSCOPY

A DISSERTATION SUBMITTED TO

THE FACULTY OF THE DIVISION OF THE PHYSICAL SCIENCES

IN CANDIDACY FOR THE DEGREE OF

DOCTOR OF PHILOSOPHY

DEPARTMENT OF CHEMISTRY

BY

TIMOTHY PAUL GRABNIC

CHICAGO, ILLINOIS

MARCH 2021

Copyright © 2020 by Timothy Grabnic

All Rights Reserved

“I failed my way to success”

Thomas Edison

Table of Contents

List of Figures vii

List of Tables x

Acknowledgements xi

Abstract 1

1 Introduction 2

2 Experimental Methods 6

2.1 Scanning Tunneling Microscopy (STM) 6

2.2 Supersonic Molecular Beams 9

2.3 Auger Electron Spectroscopy (AES) 11

2.4 Low-Energy Electron Diffraction (LEED) 12

2.5 Instrument Design 13

2.5.1 Supersonic Molecular Beam 14

2.5.2 Load Lock 16

2.5.3 Preparation Chamber 16

2.5.4 Scanning Probe Microscope Chamber 18

2.6 Sample Orientation and Movement Throughout the UHV Chamber 21

2.7 Molecular Beam Characterization 22

2.7.1 Time-of-Flight Analysis 23

2.7.2 Beam Flux Calculation 23

2.7.3 Characterization of Vibrational Excitation from Nozzle Heating 24

2.7.4 Beam Alignment 26

2.8 Sample Cleaning and Preparation 27

2.9 Image Processing and Data Extraction 29

2.9.1 Processing 30

2.9.2 Data Extraction 31

3 Atomically-Resolved Oxidative Erosion and Ablation of Basal Plane HOPG Graphite Using Supersonic Beams of O_2 with Scanning Tunneling Microscopy Visualization 32

3.1 Introduction 34

3.2 Experimental 36

3.3 Results and Discussion 38

3.4 Conclusions 50

4 Room Temperature Oxidation of GaAs(110) Using High Translational Kinetic Energy Molecular Beams of O_2 Visualized by STM 52

4.1 Introduction 54

4.2 Experimental 57

4.3 Results and Discussion 59

4.4 Conclusions 68

5 STM Visualization of N_2 Dissociative Chemisorption on Ru(0001) at High Impinging Kinetic Energies 70

5.1 Introduction 71

5.2 Experimental 73

5.3 Results and Discussion 76

5.4 Conclusions 85

A Appendices 86

A1 Atomically-Resolved Oxidative Erosion and Ablation of Basal Plane HOPG Graphite Using Supersonic Beams of O_2 with Scanning Tunneling Microscopy (Chapter 3) 87

A2 Room Temperature Oxidation of GaAs(110) Using High Translational Kinetic Energy Molecular Beams of O_2 Visualized by STM (Chapter 4) 160

A3 STM Visualization of N_2 Dissociative Chemisorption on Ru(0001) at High Impinging Kinetic Energies (Chapter 5) 171

A4 Copyright Attribution 178

References 179

List of Figures

2.1	Ultra-high vacuum chamber	6
2.2	Theoretical description of STM	8
2.3	Schematic of a molecular beam apparatus	10
2.4	Pictorial representation of Auger electron spectroscopy	12
2.5	Schematic of UHV instrument with aperture and sample stage distances	15
2.6	Images of flag style sample plates and heating mounts	17
2.7	RHK PanScan STM schematic	19
2.8	Diagram and images of the custom STM assembly	20
2.9	Schematic of sample plate and crystal orientation in UHV chamber	22
3.1	STM images of an unsputtered and sputtered HOPG surface	38
3.2	Effect of sputtering on nucleation phase	39
3.3	Formation of hexagonal etch pits on an HOPG surface	40
3.4	Formation of circular etch pits on an HOPG surface	41
3.5	Reactivity plots of 0.4 eV O_2 on HOPG at different temperatures	43
3.6	Nucleation time dependence on O_2 kinetic energy	45
3.7	STM images of anisotropic etch features formed by 0.7 eV O_2	46
3.8	Symmetric etch pits formed on SPI-2 grade HOPG	48
3.9	STM images of reactive multilayer etch pits	49
3.10	Etch pit formation resulting from O_2 impinging at 45°	50
4.1	Representative STM images of the GaAs(110) surface	60
4.2	GaAs(110) reactivity dependence on O_2 kinetic energy	61
4.3	STM image of representative GaAs(110) oxide island	62
4.4	Visualization of dramatic vertical growth of GaAs(110) oxide island	63
4.5	STM visualization of terrace elevation	63
4.6	Same-spot STM imaging of oxide formation on the GaAs(110) surface	64
4.7	Representative STM images of homogenous oxidation	66
4.8	Homogeneous oxidation reactivity plot	67
4.9	Heterogeneous and homogeneous comparative reactivity	68
5.1	Representative STM image of monolayer and bilayer graphene on the Ru(0001) surface	76
5.2	Characterization of clean and ordered Ru(0001) surface	77
5.3	Representative STM image of adsorbed nitrogen atoms	77
5.4	Negligible diffusion of nitrogen adsorbates	78
5.5	Representative STM images of the Ru(0001) surface before and after exposure to 1.1 eV N_2	79
5.6	Sticking probability of 1.1 eV N_2 on a room temperature Ru(0001) surface as a function of exposure	80
5.7	Representative STM images of low coverage 1.1 eV N_2 normal exposures	81

5.8 Nitrogen pair distances for 1.1 eV N_2 impinging A) normal to the surface and B) 45° with respect to surface normal 81
5.9 Azimuthal incident direction of N_2 beam during angled exposures 82
5.10 Schematic of N_2 dissociation events imaged in real time 83
5.11 N_2 binding at step edges 84
A1.1 First set of 36 images used in Figure 3.2 87
A1.2 Second set of 36 images used in Figure 3.2 89
A1.3 Third set of 36 images used in Figure 3.2 91
A1.4 Fourth set of 36 images used in Figure 3.2 93
A1.5 Fifth set of 36 images used in Figure 3.2 95
A1.6 Last set of 11 images used in Figure 3.2 97
A1.7 First set of 36 images used in the top graph of Figure 3.5 and the first row of Table 3.1. 98
A1.8 Last set of 22 images used in the top graph of Figure 3.5 and the first row of Table 3.1 100
A1.9 First set of 36 images used in the middle graph of Figure 3.5, Figure 3.6, and the second row of Table 3.1 101
A1.10 Second set of 36 images used in the middle graph of Figure 3.5, Figure 3.6, and the second row of Table 3.1 103
A1.11 Third set of 36 images used in the middle graph of Figure 3.5, Figure 3.6, and the second row of Table 3.1 105
A1.12 Fourth set of 36 images used in the middle graph of Figure 3.5, Figure 3.6, and the second row of Table 3.1 107
A1.13 Last set of 35 images used in the middle graph of Figure 3.5, Figure 3.6, and the second row of Table 3.1 109
A1.14 First set of 36 images used in the bottom graph of Figure 3.5 and the third row of Table 3.1 111
A1.15 Last set of 22 images used in the bottom graph of Figure 3.5 and the third row of Table 3.1 113
A1.16 First set of 36 images used in the fourth row of Table 3.1 114
A1.17 Second set of 36 images used in the fourth row of Table 3.1 116
A1.18 Third set of 36 images used in the fourth row of Table 3.1 118
A1.19 Fourth set of 36 images used in the fourth row of Table 3.1 120
A1.20 Fifth set of 36 images used in the fourth row of Table 3.1 122
A1.21 Last set of 27 images used in the fourth row of Table 3.1 124
A1.22 First set of 36 images used in the fifth row of Table 3.1 125
A1.23 Last set of 35 images used in the fifth row of Table 3.1 127
A1.24 First set of 36 images used in Figure 3.6 and the sixth row of Table 3.1 129
A1.25 Second set of 36 images used in Figure 3.6 and the sixth row of Table 3.1 131
A1.26 Third set of 36 images used in Figure 3.6 and the sixth row of Table 3.1 133

A1.27 Fourth set of 36 images used in Figure 3.6 and the sixth row of Table 3.1 135
A1.28 Fifth set of 36 images used in Figure 3.6 and the sixth row of Table 3.1 137
A1.29 Sixth set of 36 images used in Figure 3.6 and the sixth row of Table 3.1 139
A1.30 Seventh set of 36 images used in Figure 3.6 and the sixth row of Table 3.1 141
A1.31 Eighth set of 36 images used in Figure 3.6 and the sixth row of Table 3.1 143
A1.32 Last set of 23 images used in Figure 3.6 and the sixth row of Table 3.1 145
A1.33 First set of 34 images used in the seventh row of Table 3.1 146
A1.34 Second set of 36 images used in the seventh row of Table 3.1 148
A1.35 Last set of 19 images used in the seventh row of Table 3.1 150
A1.36 First set of 36 images used in the eighth row of Table 3.1 151
A1.37 Second set of 36 images used in the eighth row of Table 3.1 153
A1.38 Third set of 36 images used in the eighth row of Table 3.1 155
A1.39 Fourth set of 36 images used in the eighth row of Table 3.1 157
A1.40 Last set of 15 images used in the eighth row of Table 3.1 159
A2.1 First set of 36 images used in Figure 4.2 and the heterogeneous reactivity series in Figure 4.9 160
A2.2 Second set of 36 images used in Figure 4.2 and the heterogeneous reactivity series in Figure 4.9 162
A2.3 Third set of 36 images used in Figure 4.2 and the heterogeneous reactivity series in Figure 4.9 164
A2.4 Last set of 5 images used in Figure 4.2 and the heterogeneous reactivity series in Figure 4.9 166
A2.5 First set of 36 images used in Figure 4.8 and the homogeneous reactivity series in Figure 4.9 167
A2.6 Last set of 28 images used in Figure 4.8 and the homogeneous reactivity series in Figure 4.9 169
A3.1 First set of 2 images used in Figure 5.4 and first set of 34 images used for Figure 5.6 171
A3.2 Second set of 36 images used in Figure 5.6 173
A3.3 Last set of 2 images used in Figure 5.6, first set of 34 images used Figure 5.8 175
A3.4 Last set of 11 images used in Figure 5.8 177

Note: All images, photographs, and figures (except where noted) belong to the author.

List of Tables

2.1	Tabulated UHV chamber distances and aperture sizes	16
2.2	Set values for STM imaging	20
2.3	Vibrationally excited N_2 population at different nozzle temperatures	25
3.1	O_2 reaction probabilities	44

Acknowledgements

Thank you to my advisor Steve Sibener, for giving me the opportunity to succeed in graduate school. Thank you for being a caring mentor and making me a better scientist, as well as for teaching me the art of the conversation and where to get delicious pastrami in Chicago.

Thank you to the incredible teachers and professors along the way who have supported and inspired me: Mrs. Jimenez, Doc Munson, Betsy Sumerfield, Elizabeth Guldan, Mark Ams, Ryan Van Horn, and Doros Petasis, among many others.

Thank you to the incredible people that I have had the pleasure to work with and be around in GCIS: Maria, Brenda, John, Tanya, Melinda, Vera, Beatriz, and Jack. Thank you for your support, your help, and your kindness; my experience at UC has truly been made better because of you all.

Thank you to my committee members, Andrei Tokmakoff and David Mazziotti, for taking an interest in my science and for being excellent members of the department.

Thank you to the entire Sibener group: Bryan, Grant, Kevin, Jon, Jeff, Darren, Jacob, Rachael, Becca, Ross, Sarah B., Michelle, Julia, Ali, Caleb, Sarah W., Stephen, and Josh. You made the past years a lot more enjoyable and productive than I could have imagined.

Thank you to Kevin Gibson, for the generosity of your knowledge and continual help.

Thank you to Josh for being a pleasure to mentor during my last year here.

Thank you to Jacob for your endless knowledge and always being there to help.

Thank you to Rachael–queen of all things STM–for your help, support, and “unprofessionalism”.

Thank you to Michelle for always being so helpful in lab and for your put-together sassiness.

Thank you to Sarah W. for always helping me to evaluate my job performance, and for all of your support and for being such a great friend. Never change.

Thank you to my baseball and neighborhood families for your lifetime of love and support.

Thank you to Darren, Tony, Kade, Dan M., and Coach Brad, for being such beautiful people, friends, and showing me the important things in life.

Thank you to Laura, one of my oldest friends in graduate school. You are a wonderful person and caring friend; I do not think I would have made it through this program without your support.

Thank you to the beautiful people I have met and friends I have gained in Chicago: Chris, Zosia, Rahul, Kyle, Misha, Mayank, the whole ND crew, among many others.

Thank you to my S East View Park roommates: Hannah, Lawson (and Greta), and Chris. I feel like I can never have roommates again because of how amazing you have all been.

Thank you to my extended Chicago family: Doug, Alexis, Jeff, and Lindsey. There is not enough space here to adequately express how thankful I am for you all to be in my life.

Thank you to my college friends: Brian, Pat, Paul, and Dan Marcus. You have all given me some of the best memories of my life, and I look forward to many more to come.

Thank you to Sean, Mark, Rob, and Nick for being the best brothers a guy could ask for. Thank you–and Katie and Lindsey–for your encouragement and for teaching me the uncertainty principle.

Thank you to my family for a lifetime of support, great food, and loving company.

Thank you to Maggie for being encouraging, supportive, and a better partner than I thought was possible. You inspire me to a better person, and I am so incredibly thankful that you are in my life.

Thank you to Jessie for being the most amazing and thoughtful big sister. I could not be more honored to be an uncle to Owen and a brother-in-law to Dan (and the entire Ezzi family). You epitomize hard work; thank you for being someone I can always look up to.

Mom and dad: everything I have accomplished in life is because of the opportunities you have given me, and because of the love and support with which you raised me. Thank you for teaching me the importance of hard work and respect. This is for you.

Abstract

The work presented in this thesis explores multiple different systems with one overarching theme: a powerful new approach to understanding reactive surface dynamics. Reactions at surfaces–or more broadly speaking, interfacial chemistry–are ubiquitous in the world. From the development of materials that protect spacecrafts upon atmospheric reentry, to semiconductor fabrication for electronic devices, to heterogeneous catalysts used for industrial processes, understanding and controlling interfacial reactivity is crucial to science and technology. At a fundamental level, these three applications critically depend on the gas-surface interactions of O_2 with graphite, O_2 with gallium arsenide (GaAs), and N_2 with ruthenium, respectively. Utilizing a unique and custom built ultra-high vacuum (UHV) chamber that combines a supersonic molecular beam with a scanning tunneling microscopy (STM), the reactive evolution of each of these three interfaces after exposure to energy- and angle-selected gas molecules is visualized to obtain an understanding of the chemistry and physics that govern their behavior.

In the case of O_2 reacting with a well-characterized form of graphite–highly oriented pyrolytic graphite (HOPG)–the impinging O_2 energy and angle, as well as the HOPG surface temperature, affect the subsequent reaction between oxygen and carbon in ways that are both kinetically and morphologically distinct. Similarly, the oxidation of GaAs(110) with O_2 proceeds by two kinetically and morphologically distinct mechanisms: the nucleation and subsequent growth of spatially heterogeneous oxide islands and spatially homogeneous random oxidation leading to layer-by-layer growth. Lastly, increasing the kinetic and vibrational energy of impinging N_2 on a Ru(0001) surface activates dissociative adsorption on otherwise nonreactive terrace sites, and the resulting spacing and orientation of the nitrogen atom pairs provide critical information about the energy transfer and potential nonadiabatic nature of the dissociation event.

Chapter 1: Introduction

Interfaces are ubiquitous in our everyday world, and exceptionally interesting chemistry happens at these interfaces. The boundary between two phases, such as solids and liquids, gases and liquids, or most importantly to this thesis, the gas-solid interface, represents a two-dimensional surface that acts uniquely from the bulk of either of the two phases. From food production (industrial ammonia synthesis) to automotive transportation (catalytic converter), the unique properties of gas-surface interfaces have a profound impact on science and society.

The contents of this thesis utilize a novel approach to explore fundamental interfacial dynamics of gas-surface systems, in which scanning tunneling microscopy (STM) is used in conjunction with a supersonic molecular beam (SMBs) in an ultra-high vacuum (UHV) environment. Many aspects of the instrument contribute to the novelty and utility of this system as a means to uniquely probe chemistry at surfaces, which is the overarching theme of this thesis.

UHV conditions ($<10^{-9}$ Torr) are paramount to study fundamental reactions on plane surfaces; in atmospheric air, a chaotic mixture of nitrogen, oxygen, and other gases are bombarding any part of the surface at a variety of energies and angles approximately a billion times a second. A clean environment therefore must be achieved before isolating and characterizing individual reactions on surfaces. UHV chambers achieve this necessary condition by using vacuum pumps to reduce the pressure inside the chamber to $<10^{-9}$ Torr, where reactive gases will form a monolayer film on the surface only after >1000 seconds. It is under these conditions that all of the experiments in this thesis were performed, ensuring that any observed morphological evolution of the surface is a result of the specific gas-surface interaction being studied.

In addition to a clean environment, the surface being studied must be free of impurities, ordered, and well-characterized to fully understand the complex interactions between it and the

reactant gas. The different semiconductor, semimetal, and metal surfaces used in the presented experiments were meticulously prepared; the details of each preparation procedure, in addition to the characterization of each system, will be described in **Chapter 2**. These preparations reduce the complexity of the system and enable the study of isolated interactions and reactions as opposed to observing the result of a complicated ensemble. While this does remove factors that may be present in real-world environments, isolating individual events on planar surfaces is critical to understanding and controlling the outcomes of more convoluted systems. As Nobel Laureate (1932) and one of the progenitors of modern surface science Irving Langmuir stated,[1] *"In order to simplify our theoretical consideration of reactions at surfaces, let us confine our attention to reactions on plane surfaces. If the principles in this case are well understood, it should then be possible to extend the theory to the case of porous bodies."* Said more generally, studies done on well-characterized planar surfaces provide the fundamental basis to understand systems of much higher complexity.

Enabled by a clean environment and surface, the combination of molecular beam and STM techniques represent a new and powerful method to study gas-surface interfacial reactivity. The molecular beam provides a collimated beam of reactant gas with a narrow energy and angle distribution as it hits the surface; the translational kinetic energy and impinging angle of the reactant gas can be tuned through various methods to probe many different reactive parameter spaces. STM visualization provides atomic-scale topographical and electronic information as it scans the surface of the reacted sample. The STM in my instrumental setup is in line with the molecular beam, so that the surface can be exposed to the collimated, monoenergetic reactant gas while in the microscope. Furthermore, the STM has a unique orientation that allows the surface to be visualized *during* exposures to the molecular beam. As will be discussed in depth in **Chapter**

2, this one-of-a-kind UHV setup provides previously unattainable information about the spatio-temporal evolution of reacting interfaces.

One reacting interface of great technological interest is the O_2/graphite system, due to the use of graphite and carbon-based composites in high-altitude aircraft and spacecraft reentry applications, among others. In **Chapter 3**, the reactivity of highly oriented pyrolytic graphite (HOPG) in UHV conditions was investigated as a function of surface temperature as well as impinging O_2 energy and angle. Results demonstrate that the surface is most reactive at ~1375 K, and that the reactivity of impinging O_2 increases with increasing translational kinetic energy (0.4-1.2 eV) normal to the surface. Additionally, the morphological evolution of the reacting interface at higher kinetic energies of O_2 is distinct from that of lower kinetic energy oxidation processes. Oxidation and subsequent erosion of the HOPG surface is therefore both kinetically and morphologically distinct. The individual contributions of impinging O_2 kinetic energy and angle as well as surface temperature on the reactivity of HOPG are presented in this chapter, providing insight into the spatio-temporal correlations that govern the reactive evolution of this system.

Chapter 4 details the distinct morphological evolution of a room temperature GaAs(110) surface in response to impinging O_2 at varying kinetic energies. Results demonstrate that oxidation of the GaAs(110) surface proceeds *via* two morphologically and kinetically distinct pathways: spatially heterogeneous growth of oxide islands and spatially homogenous oxidation of randomly distributed chemisorbed oxygen atoms leading to layer-by-layer growth. The spatially heterogeneous mechanism is activated at O_2 impinging kinetic energies ≥0.7 eV and is kinetically favored over the homogenous oxidation method at increasingly high (≥1.0 eV) kinetic energies. Defects and imperfections on the surface are shown to play a large role in the system's reactivity and evolution in response to the oxidative processes. The investigations in this chapter reveal a

novel method of oxidizing the GaAs(110) surface without the need for destructive methods or increased surface temperature, which represent a potential pathway for the creation of ultrathin oxide films on this technologically important semiconductor surface.

The Born-Oppenheimer approximation, first proposed in 1927,[2] assumes that the motion of a system's nuclei and electrons can be treated separately, whereby the total wavefunction of the system is $\boldsymbol{\Psi}_{total} = \psi_{nuclear}\psi_{electronic}$. This breakthrough revolutionized molecular quantum mechanics (for reference, it was been cited ~7000 times in peer-reviewed publications) by enabling scientists to more accurately describe the quantum states of molecular systems. While an extremely powerful tool even today, this paradigm-shifting approximation does not work for all systems of study. An interesting example of this is shown in **Chapter 5**, where the activated dissociative adsorption of N_2 on Ru(0001) is investigated. Ruthenium is an important next-generation catalyst for industrial NH_3 production; as a result, N_2 dissociation on ruthenium has been extensively studied. Despite this large literature base, questions still remain about the mechanism and surface dynamics that govern the odd sticking behavior of N_2 on Ru(0001). The preliminary results of **Chapter 5** represent the first direct STM visualization of high-energy N_2 dissociation on Ru(0001) terrace sites. By measuring the distance and angle between previously paired adsorbed nitrogen atoms as well as probing their site specificity, detailed information about the surface dynamics is obtained. In conjunction with theoretical insight, these results will help elucidate the channels of energy dissipation that govern N_2 dissociation on Ru(0001), providing critical experimental insight into the importance of nonadiabatic processes to this reactive event.

Chapter 2: Experimental Methods

All of the experiments described in this thesis were performed utilizing a novel UHV instrument combining a supersonic molecular beam and scanning probe microscope (SPM) with both STM and atomic force microscope (AFM) capabilities. The UHV instrument, along with a labeled schematic, is shown in **Figure 2.1**. Sample characterization techniques in the preparation chamber include low-energy electron diffraction (LEED) to determine surface structure and Auger electron spectroscopy (AES) to determine elemental surface composition. The contents of this chapter include a theoretical description of the experimental methods utilized in the instrument, the experimental setup and design of each implemented technique, and the preparation/characterization procedures used for each of the studied systems.

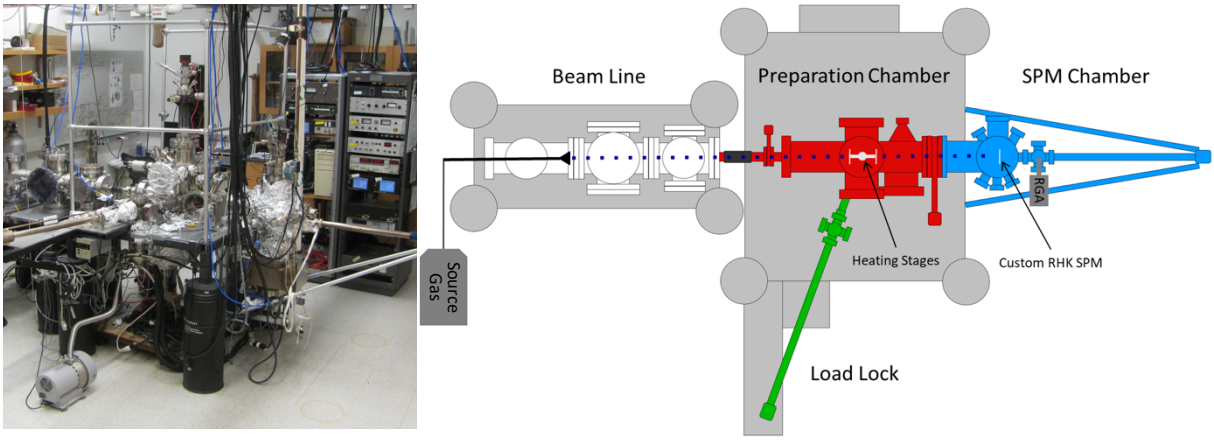


Figure 2.1: **Ultra-high vacuum chamber**. An image of the novel UHV experimental apparatus (left) with a schematic of the chamber (right); the instrument combines a supersonic molecular beam with an in-line, *in situ* scanning probe microscope.

2.1: Scanning Tunneling Microscopy (STM)

First developed by Gerd Binnig and Heinrich Rohrer in 1982,[3,4] the STM gave scientists the ability to visualize conductive surfaces with atomic resolution, leading to innumerable scientific discoveries and the 1986 Nobel Prize in Physics.[5] Scanning tunneling microscopy

utilizes the quantum mechanical concept of tunneling: a particle with energy, E, can pass through a potential barrier, V, even without sufficient energy to surmount the potential barrier classically ($E < V$). This phenomenon occurs in an STM by bringing a sharp conductive tip near a conductive surface (on the order of 1 nm) and applying a voltage bias between the sample and the tip. Classically, electron transfer between the tip and sample is forbidden; the electrons instead tunnel through the barrier to establish a tunneling current (on the order of 1 nA) that is then measured by the instrument.

The tunneling current, I_t, can be derived using the WKB (or JWKB for Jeffreys, Wentzel, Kramer, Brillouin) approximation, which is a technique used to calculate approximate solutions to one-dimensional (or spherically symmetric) time-independent differential equations.[6] In this case, the solved equation is the time-independent Schrödinger equation, and assuming that the potential barrier varies slowly with respect to the de Broglie wavelength, the following tunneling current can be derived:

$$I_t = \int_0^{eV} \rho_s(E)\rho_T(E - eV) exp\left[-\left(\frac{2z\sqrt{2m}}{\hbar}\right)\left(\sqrt{\frac{\phi_s+\phi_T}{2} + \frac{eV}{2} - E}\right)\right] dE, \qquad \textbf{(E2-1)}$$

where ρ_s and ρ_T are the density of states of the sample and tip, respectively, e is the charge of an electron, V is the applied bias voltage, z is the height of the tip above the surface, m is the mass of an electron, and ϕ_s and ϕ_T are the work functions of the sample and tip, respectively. The tunneling current in an STM is therefore dependent on the density of states of both the sample and the tip (ρ_s and ρ_T), the applied bias voltage (V), and the distance (z) between the tip and the sample. As the pioneering work of Tersoff and Hamann demonstrates,[7] by invoking the (validated) assumption that the tip has a spherical wavefunction, I_t becomes directly proportional to ρ_s and V and exponentially dependent on z. The exponential dependence of the tunneling current on the tip-sample distance provides STM measurements with 1 Å lateral resolution and 0.1 Å vertical

resolution, which enables visualization of atomic-scale features on conductive and semiconductive surfaces.

Equation **E2-1** highlights the unique capabilities and strengths of scanning tunneling microscopy that make it an incredibly powerful technique for surface analysis. First, the exponential dependence of z on I_t enables modern STM instruments to have spatial resolution on the order of 10 pm vertically and 100 pm laterally. The dependence on the applied bias voltage enables different energy states as well as both occupied- and unoccupied-states to be investigated. **Figure 2.2** schematically depicts both unoccupied- and occupied-state imaging; when a positive bias is applied to the sample, the Fermi level of the sample effectively lowers, causing electrons to tunnel from the tip into unoccupied-states of the sample. When a negative bias is applied to the sample, the Fermi level of the sample effectively raises, causing electrons to tunnel from occupied-states of the sample to the tip. It is important to emphasize that the tunneling current depends upon both the sample-tip distance (z) as well as the density of states of the sample (ρ_s). These two

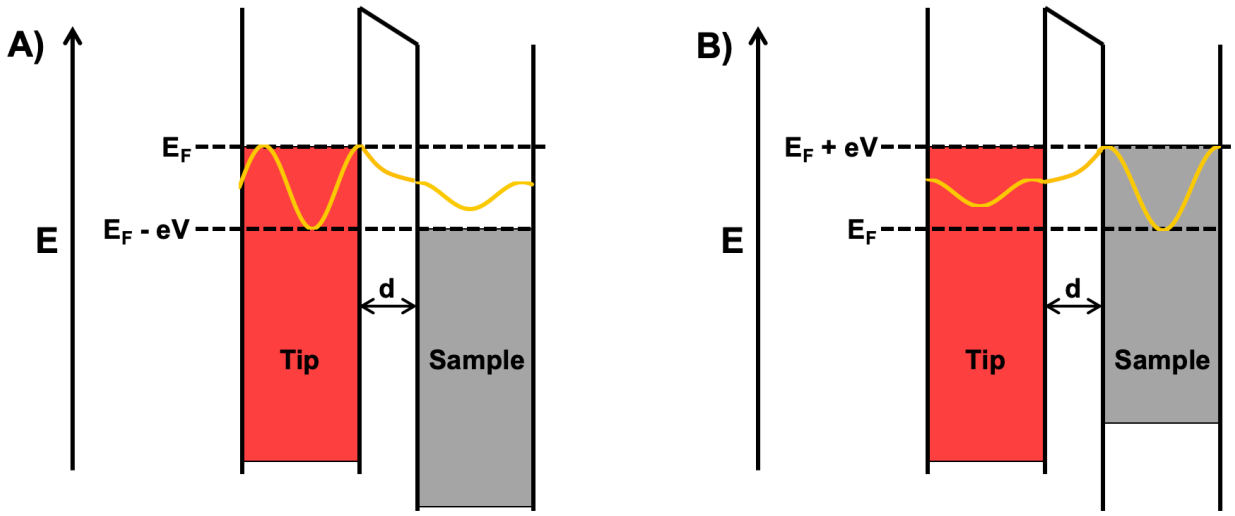


Figure 2.2: **STM Theoretical description**. A schematic illustrating the concept of unoccupied- (**A**) and occupied-state (**B**) imaging, where *d* describes the distance between the tip and sample through the vacuum and E_F is the Fermi level. **A)** Electrons tunnel from the tip to the sample due to a positive potential bias applied to the sample; **B)** Electrons tunnel from the sample to the tip due to a negative potential bias applied to the sample.

factors cannot be disentangled from one another; the tunneling current therefore represents a convolution of the surface's electronic and topographical profile.

To obtain images of the surface, the STM tip follows a raster pattern that consists of a forward and backward scan, followed by an incremental step down in a perpendicular direction to the next line. This is continued until a complete, square image is visualized. The STM tip can be operated in both constant-height or constant-current modes, although constant-current mode is most widely used and was used exclusively for all images presented in this thesis. In constant-current mode, the tip height above the surface is modulated by a PID (proportional-integral-gain) loop to maintain a constant tunneling current; when the tunneling current drops below the set current, the tip moves closer to the surface, and vice versa when the tunneling current exceeds the set current. The tip movement is controlled by a piezoelectric material, which is a material that reversibly generates an electric charge in response to mechanical stress (direct piezoelectric effect), or changes in length in response to an applied voltage (inverse piezoelectric effect). Consequently, a voltage is applied to the piezoelectric material attached to the tip to correct the tunneling current when it does not match the set current. The STM then maps the corrective voltages, converts the voltages to distances based on the calibrated piezoelectricity of the material, and generates an image that represents a convolution of the density of states and topographical profile of the surface with atomic resolution.

2.2: Supersonic Molecular Beams

Supersonic molecular beams are generated when a source of high-pressure gas is expanded through a small nozzle into a space of much lower pressure. In the limit where the mean free path of the gas particles, λ, is much smaller than the width of the nozzle, d ($\lambda \ll d$), the nozzle converts

most of the translational and internal energy of the high pressure gas into directed mass motion.[8–12] Assuming the expansion of an ideal gas without viscous or heat-exchange effects, the phenomenon is an isentropic expansion described by equation **E2-2**, where the specific enthalpy (enthalpy per unit mass) of the high-pressure gas system, h_0, is converted into directed velocity, v, and residual enthalpy based on the internal temperature of the expanding gas, h.[13,14]

$$h_0 = \frac{1}{2}v^2 + h \qquad \textbf{(E2-2)}$$

Figure 2.3 illustrates a schematic of a typical molecular beam apparatus. The source of high-pressure gas (p_0) expands through the nozzle into the low-pressure chamber (1st chamber, p_1); the gas molecules with velocities in the direction of the beam expansion are selected by a conical, knife-edged skimmer, which selects only the lowest temperature gas molecules (minimal internal collisions and vibrations) to travel into a differentially pumped secondary (2nd chamber, p_2) and drastically reduces residual gas scattering. The result is a roughly collimated beam of gas molecule with a characteristic Mach number, M, described in equation **E2-3** for an ideal gas:

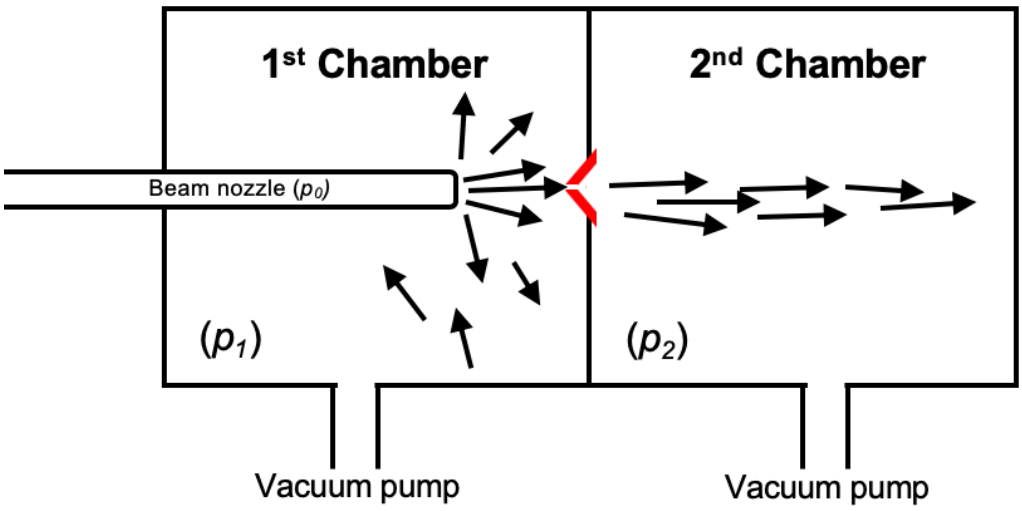


Figure 2.3: Schematic of a molecular beam apparatus. A diagram illustrating a representative molecular beam apparatus; the skimmer is in red for emphasis, and the length and direction of the arrows represents characteristic velocities of gas molecules from the beam nozzle. The skimmer selects gas molecules with similar velocities to form the molecular beam.

$$M = \frac{u}{c} = u\sqrt{\frac{m}{\gamma kT}} \quad \textbf{(E2-3)}$$

where u is the flow velocity, c is the speed of sound in the beam, m is the mass of the gas molecules, γ is the heat capacity ratio, k is the Boltzmann constant, and T is the temperature of the beam. Due to the expansion of the gas into the low-pressure chamber, the flow velocity increases and the speed of sound in the beam, which is proportional to the square root of T for an ideal gas, simultaneously decreases; at the point where the flow velocity exceeds the speed of sound in the beam, the molecular beam becomes supersonic ($M > 1$). In comparison to the velocities of gas molecules in a Maxwell-Boltzmann distribution, the distribution of translational kinetic energies in a supersonic beam narrows and shifts towards higher energies due to the decrease in temperature of the gas molecules during the isentropic expansion to supersonic velocities. More narrow energy distributions correspond to higher Mach numbers and "better" molecular beams.

2.3: Auger Electron Spectroscopy (AES)

Auger electron spectroscopy is a surface sensitive spectroscopy technique that provides the chemical composition of a sample.[15] AES makes use of the Auger effect, which is a chain of electronic events resulting in the ejection of Auger electrons with kinetic energies that are unique to each element. Discovered independently by Lise Meitner[16] and Pierre Auger[17] in the 1920's, the Auger effect is a three-step electronic process, depicted schematically in **Figure 2.4**: First, a high-energy electron from a collimated electron beam removes a core electron from an atom. Second, a secondary electron relaxes down to fill the hole left by the core electron. Third, the transition energy from the relaxation event is imparted on a third, outer core electron that is then ejected with a characteristic kinetic energy. The kinetic energy of the Auger electron, E_{KE}, is approximately:

$$E_{KE} = E_{core} - E_{relax} - E_{Auger} \quad \textbf{(E2-4)}$$

where E_{core}, E_{relax}, and E_{Auger} are the binding energies (positive values measured from the vacuum level) of the core, secondary, and outer (Auger) electrons. The kinetic energies of the Auger electrons are element-specific due to the unique binding energies of each electron in the three-electron process. Additionally, the ejected Auger electrons typically have kinetic energies ranging from 50 eV to 3 keV corresponding to an escape depth on the order of a few nanometers, indicating that only electrons from surface or near-surface atoms are being measured.[18] Consequently, AES is a powerful tool to acquire surface-sensitive information about the elemental composition of a sample.

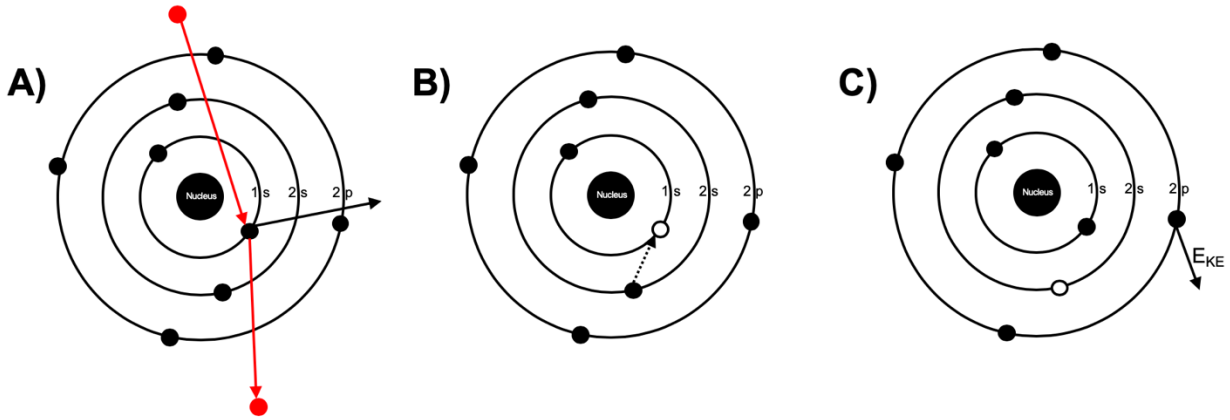


Figure 2.4: Pictorial representation of Auger electron spectroscopy. A generalized view of Auger electron spectroscopy: **A)** A high-energy incident electron (red) removes an inner electron from the atom. **B)** An outer electron relaxes to the hole left from the ejected inner electron. **C)** The energy released from the relaxation event in **B)** is imparted on the "Auger" electron which is then ejected from the atom; this electron has a characteristic kinetic energy that is measured and is unique to each element.

2.4: Low-Energy Electron Diffraction (LEED)

Low-energy electron diffraction is a technique that utilizes the wavelike nature of electrons to determine the surface symmetry and structure of single-crystalline materials.[18] In a typical LEED setup, a sample is bombarded with a collimated beam of low-energy (20-200 eV) electrons.

The electrons are diffracted off of the surface and into a detector system that contains multiple grids and phosphor (or other positron-sensitive) screen. The grids screen out inelastically scattered electrons that would otherwise obscure the diffraction pattern, and the phosphor screen visualizes the LEED pattern. The low-energy electrons in LEED have an escape depth of ~0.1 nm, which means that only the first layer or two of the surface is sampled. LEED is therefore a surface-sensitive technique used to accurately determine the surface symmetry and structure prior to experimentation.

2.5: Instrument Design

The novel UHV instrument used for all of the experiments in this thesis (see **Figure 2.1**) is comprised of four separate components: a triply-differentially pumped supersonic molecular beam, load lock, preparation chamber, and SPM chamber containing a custom scanning probe microscope with the surface plane normal (when the incident angle of the beam is set at 0º) to the beam. The supersonic molecular beam and SPM chambers are housed on air leg isolation tables that provide vibrational isolation from one another and the surrounding environment. The overall setup of the instrument and geometric arrangement of the SPM relative to the beam allows individual nanoscopic areas of a surface to be revisited during exposures to the molecular beam. The STM/AFM tip can either be retracted (in the Z direction) or moved in X or Y directions during exposures to reduce shadowing and provide the molecular beam with a line of sight to the surface; control tests are always completed to ensure that the reactive and morphological evolution of the surface is only due to the energy- and angle-selected from the molecular beam and not a result of ambient background gas. Surface exposure from the molecular beam can be achieved at impinging angles of 0-50º due to the ability of the SPM assembly to independently rotate. Stable sample

temperatures from room temperature to 80 K in the SPM assembly can be achieved for imaging and molecular beam exposures by static liquid nitrogen cryocooling. Sample stages (angled normal and 45º to the incident beam) with resistive heating capabilities and with spatial coordinates to position in-line of the molecular beam were used for sample preparation as well as exposures (such as in **Chapter 3**) that required high temperatures during exposures.

2.5.1: Supersonic Molecular Beam

The supersonic molecular beam consists of three differentially pumped chambers (stages). The first and second chambers are each evacuated by an Oerlikon Leybold 600 L s^{-1} magnetically suspended turbomolecular pumps; both of these turbomolecular pumps are backed by the same Edwards nXDS15i 4.75 L s^{-1} dry scroll pump. When the molecular beam is on, the pressurized gas exits the beam and expands into the first chamber through a 30 μm stainless-steel nozzle that is located 8 mm from a skimmer that separates the first and second stages. The entirety of the nozzle is wrapped in resistively-heated wire (1 Nc I 10, Thermocoax) and secured with a sheet of tantalum and copper ties to ensure even, consistent heating. The temperature of the nozzle is monitored by a Type-K thermocouple spot-welded approximately 0.5-1 mm from the aperture. The skimmer is a Beam Dynamics Model #2 skimmer that has a 0.5 mm orifice, 1.0” length, and 25 degree included angle. A metal flag is located inside the second chamber that can be selectively moved in and out of the beam path. The second and third chambers are separated by a 1 mm collimating aperture, and the third stage is evacuated by a 100 L s^{-1} ion pump. The third stage is attached to the preparation chamber with a ConFlat gate valve and custom metal bellows; a final 1 mm collimating aperture separates the third stage of the beamline and the preparation chamber. A schematic and tabulated summary of this data is provided in **Figure 2.5** and **Table 2.1**.

The 1 mm collimating aperture determines the final size of the beam spot on the surface during exposures: the circular beam spot has a diameter of 2 mm and 4 mm when the sample is being exposed in the preparation chamber (when the sample needs to be heated during exposures) and SPM stage, respectively. These beam spots correspond to a distance of 1.3 m between the beam nozzle and sample in the preparation chamber and 1.6 m between the beam nozzle and sample in the SPM stage. When no gas is flowing into the beam chambers, the first, second, and third chambers have respective base pressures of better than 6×10^{-8} Torr, 1×10^{-7} Torr, and 1×10^{-8} Torr. The pressures in the first, second, and third chambers when the molecular beam is operating are on the order of 10^{-3} Torr, 10^{-6} Torr, and 10^{-8} Torr, respectively. The pressure in the first and second chambers are monitored by a glass tubulated and a nude Bayard-Albert ionization gauge (both calibrated to N_2), respectively. Control studies have demonstrated that no noise is introduced

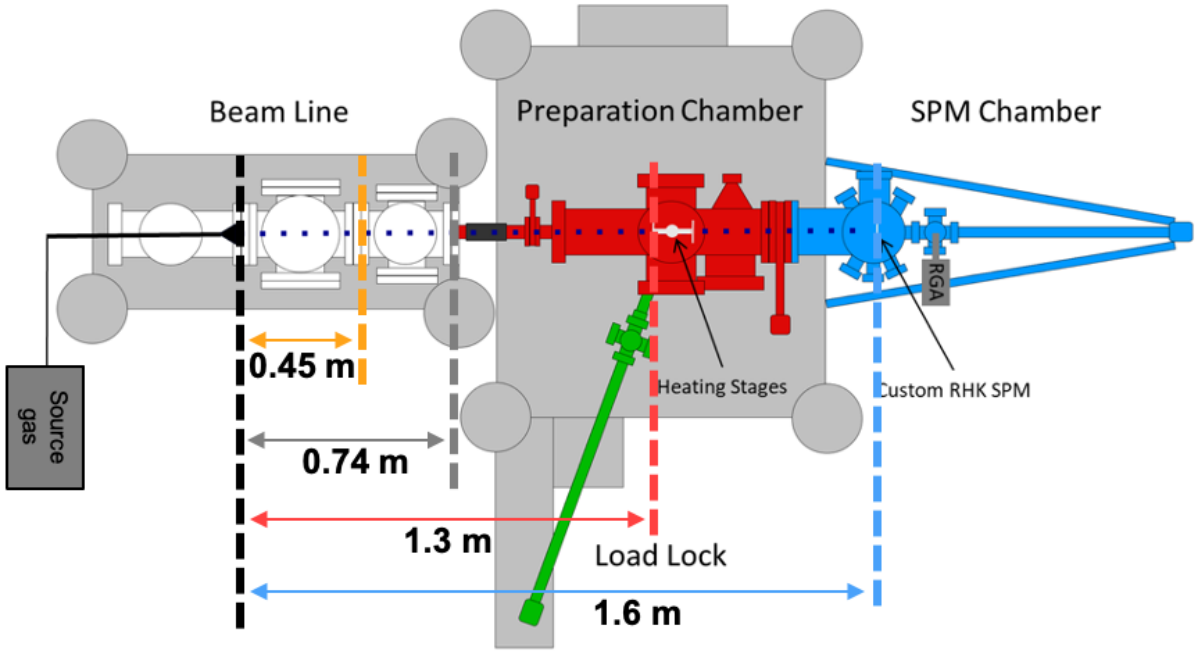


Figure 2.5: Schematic of UHV instrument with aperture and sample stage distances. A schematic of the UHV chamber (**Figure 2.1**) with included distances of the beam nozzle to the apertures and sample stages; this information is tabulated in **Table 2.1**.

	Skimmer (black)	2nd–3rd stage aperture (orange)	3rd–Prep stage aperture (gray)	Prep sample stage (red)	SPM sample stage (blue)
Distance from beam nozzle (m)	0.008	0.45	0.74	1.3	1.6
Aperture diameter (mm)	0.5	1	1	-	-
Beam spot diameter (mm)	-	-	-	2	4

Table 2.1: Tabulated UHV chamber distances and aperture sizes. A table listing the distances of the various apertures and sample stages from the beam nozzle. The diameter of the apertures as well as the diameter of the beam spot at the different sample stages is also provided.

to the STM scans with the molecular beam operating, which enables STM imaging to be performed concurrently with molecular beam exposures.

2.5.2: Load Lock

The load lock is a small chamber that allows samples to be introduced and removed from the UHV system into atmosphere by a transfer arm that enables movement of samples to the preparation chamber; a gate valve separates the two chambers. The load lock is pumped out by a Balzers TMU65 55 L s^{-1} turbomolecular drag pump that is backed by a Varian SH-110 1.8 L s^{-1} scroll pump resulting in a base pressure better than 1×10^{-9} Torr when completely baked out. The pressure is monitored from atmosphere to 10 mTorr with a TC gauge and from 5×10^{-4} Torr to UHV with a nude Bayard-Albert ionization gauge (calibrated to N_2).

2.5.3: Preparation Chamber

The preparation chamber is evacuated by a Perkin Elmer 220 L s^{-1} DI ion pump equipped with a titanium sublimation pump (TSP) that results in a base pressure better than 8×10^{-11} Torr as monitored by a nude Bayard-Albert ionization gauge (calibrated to N_2). Inside the preparation chamber is a manipulator capable of translation in all three spatial directions and 360º of rotation.

The manipulator has a resistive heating sample mount manufactured by RHK and a custom sample mount with electron beam (e-beam) heating capabilities that accommodate flag style sample plates (see **Figure 2.6**) with length × width × height dimensions of 15×18×1 mm. Samples can be placed on the sample mounts by a transfer arm housed in the preparation chamber and subsequently be positioned in front of viewports, the molecular beam, or preparation/characterization instruments due to the translational and rotational movement of the manipulator.

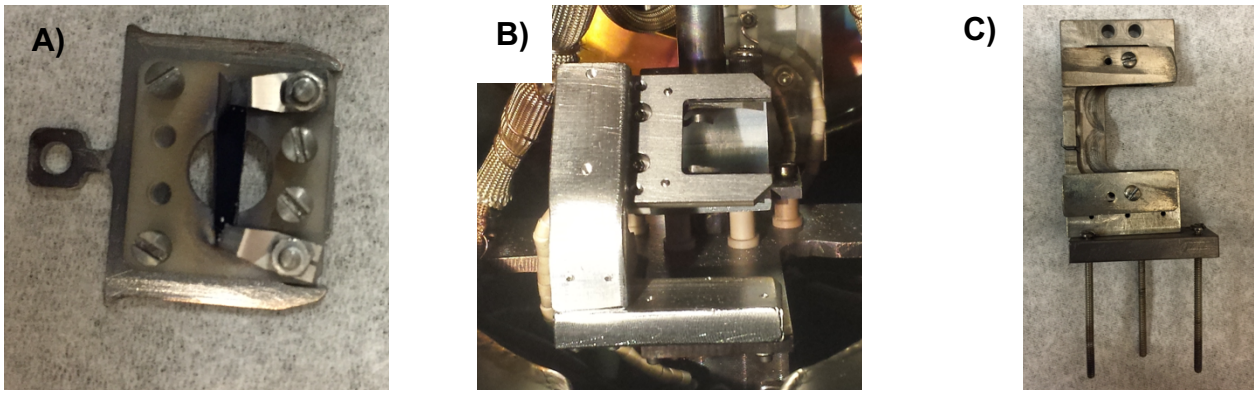


Figure 2.6: Images of flag style sample plates and heating mounts. **A)** A representative flag style sample plate used for all experiments; a ceramic mount to electrically isolate the sample when resistively heating and was removed for e-beam heating, **B)** A standard mount and sample holder for resistive heating of the sample, and **C)** a custom-designed molybdenum sample mount for e-beam heating of the sample.

A PHI 04-150 ion gun (0.5-5 keV) capable of sputtering samples is housed in the preparation chamber. Sputtering, a phenomenon in which gas atoms (or molecules) are ionized and accelerated towards a target material, is a common cleaning technique for UHV surface studies as the momentum exchange between the ionized gas and surface can eject unwanted adsorbates from the sample of interest. A leak valve is attached to the preparation chamber to introduce clean gas molecules of interest for sputtering or background exposures; Ar^+ ions are commonly used for sputtering in this UHV system.

The preparation chamber contains an Omicron NGL 10 SPECTALEED with both LEED and AES capabilities. The electron gun for both LEED and AES functions contains a LaB_6 filament

for its electron source and can produce electron beams with energies as high as 3.5 keV. When performing Auger electron spectroscopy, the rear-view LEED optics are used as a retarding field energy analyzer that select for electrons with specific kinetic energies; the selected electrons are then detected on the LEED and AES spectrum are obtained.

2.5.4: Scanning Probe Microscope Chamber

The SPM chamber is evacuated by a Gamma Vacuum 200 L s^{-1} DC ion pump equipped with a titanium sublimation pump, resulting in a base pressure better than 5×10^{-11} Torr as monitored by a nude Bayard-Albert ionization gauge (calibrated to N_2). This chamber houses a custom-designed RHK PanScan LT scanning probe microscope based on an original design by Shuheng Pan.[19] The SPM has both STM and AFM capabilities but only the STM functionality was used for all experiments in this dissertation due to the superior resolution of the STM as compared to the AFM when imaging atomic features; RHK qPlus sensors are used for all AFM imaging. The entire SPM system is controlled electronically by a low-noise RHK R9 SPM Control System. Movement of the STM tip is controlled by a four-quadrant piezoelectric tube, a diagram of which is given in **Figure 2.7**. Voltages are applied across the tube in order to move it precisely in the X, Y, and Z directions. STM imaging can be performed at sample temperatures from room temperature to 63 K. A small reservoir that is thermally connected to the STM stage and tip can be filled with liquid nitrogen to statically cryocool the STM assembly; the temperature is monitored using a cryostat thermocouple attached to the SPM assembly. The design of the STM assembly maintains the tip and sample at the same temperature to ensure stability during imaging and very low drift (XY drift as low as ~0.2 Å hr^{-1}, Z drift as low as ~0.2 Å day^{-1}).

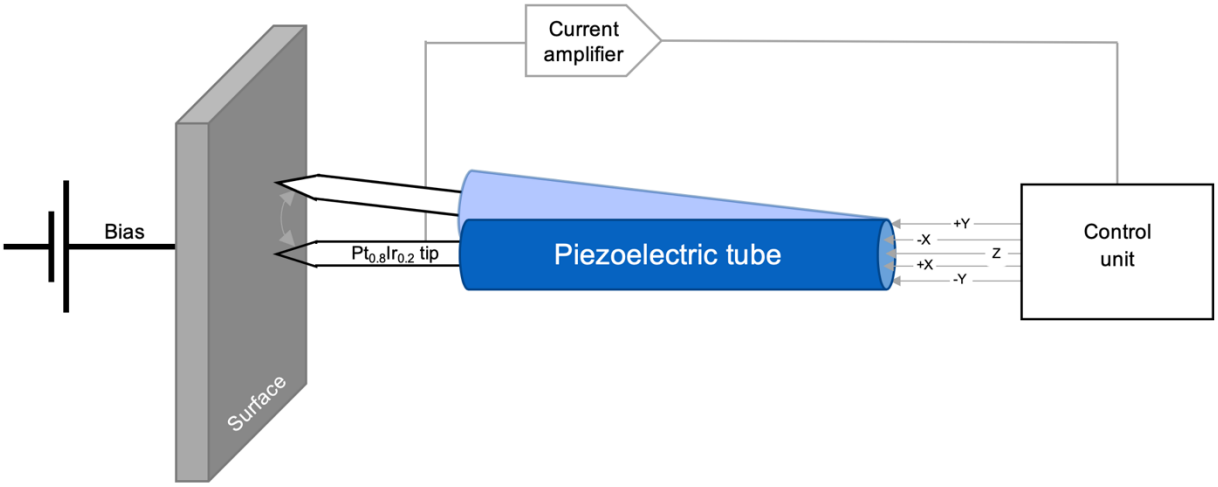


Figure 2.7: RHK PanScan STM schematic. **A)** A diagram of the piezoelectric tube and feedback controls of the custom RHK PanScan STM. The piezoelectric tube is precisely deflected in the x, y, and z directions from voltages applied by the control unit. The point-of-view is from the impinging molecular beam, demonstrating the vertical surface plane allowing a line-of-sight to the surface.

Images of the STM assembly as well as a schematic representation are shown in **Figure 2.8**. The custom designed STM stage is such that the surface plane is vertical, as opposed to being horizontal as in most designs, which allows the surface to be imaged while being exposed to the molecular beam. The entire STM assembly is mounted on springs that provide vibrational isolation in addition to the air legs that support the entire SPM chamber. The STM stage has 50º of rotation, where at 0º the surface is normal to the incoming molecular beam. The design of this STM assembly uniquely enables atomically-resolved visualization of surfaces, *in-situ* and in real time, as these surfaces are exposed to angle- and energy-selected gas molecules. This instrument is the first of its kind and represents a powerful new method of probing fundamental surface dynamics and the correlations that govern reactions at surfaces.

Once a sample on a flag style sample plate and a STM tip is inserted into the respective sample and tip stages, the STM tip manually approaches to within ~1 mm of the surface using a

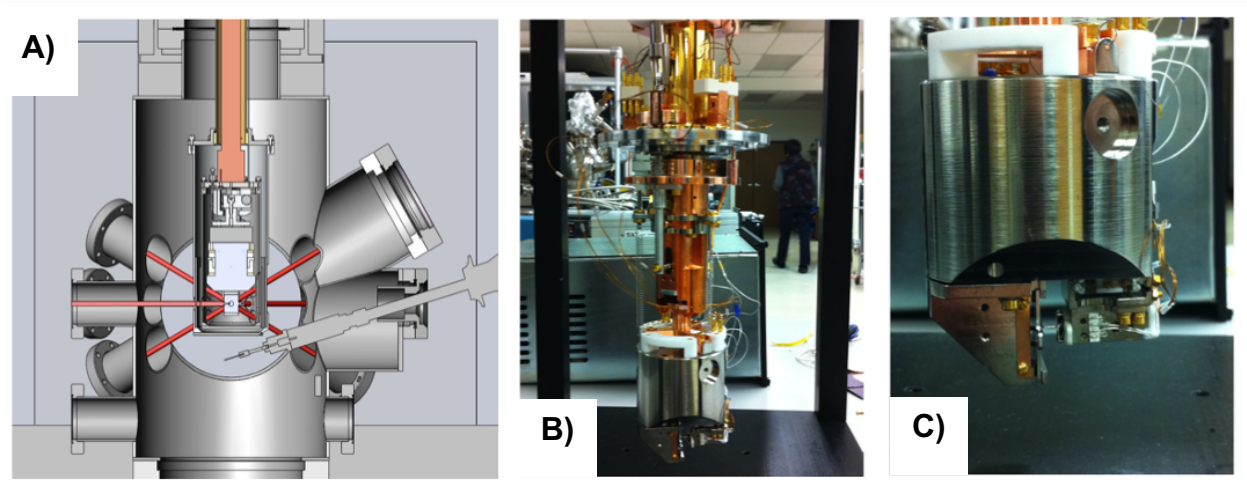


Figure 2.8: Diagram and images of the custom STM assembly. **A)** A schematic of the STM assembly. **B)** An image of the entire STM assembly outside of the UHV chamber. **C)** A magnified view of the sample holder with an inserted sample plate and STM tip, highlighting the vertical orientation of the surface plane.

piezo motor controller (RHK PMC 100) with the visual aid of a camera. At this tip-surface distance, the RHK R9 SPM Control System software then automatically steps the tip towards the surface until the set tunneling current is achieved, which correlates to tip-surface distances on the order of 1 nm. Once the set tunneling current is achieved, images ranging in size from 1 nm^2 to 64 μm^2 can be obtained using the RHK R9 software in constant-current mode. Typical values and ranges of the set points used during imaging are included in **Table 2.2**; the integral gain is set to higher values of ~3-4 km A^{-1} s^{-1} during the automatic tip approach to the surface to bring the tip to imaging ranges much faster.

Bias Voltages (V)	**Set Current (nA)**	**Prop. Gain** (am/A)	**Int. Gain** $(m/A \cdot s)$	**X, Y Comp. (%)**	**Scan Speed** $(\mu m/s)$
0.05-3.0	0.3-1.2	10	10-1000	0-14.0	0.01-1.5

Table 2.2: Set values for STM imaging. A table listing the range of set values used during STM imaging; values vary depending on the surface of interest, tip changes, and surface roughness, among others. "Prop. Gain", "Int. Gain", and "X, Y Comp." stand for proportional gain, integral gain, and x, y compensation, respectively.

2.6: Sample Orientation and Movement Throughout the UHV Chamber

Due to the multiple mechanisms of sample preparation, characterization, and exposure, a discussion of the sample plate and crystal orientation in different parts of the UHV chamber is provided for clarity. **Figure 2.9** schematically depicts the sample plate (gray) and crystal (black) orientation in the (**A**) preparation chamber and the (**B**) SPM stage from a reference frame normal to the surface plane. The crystal is shown with a fixed orientation on the sample plate with a red asterisk to guide the viewer. **Figure 2.9C** shows the incident angle, θ, of the molecular beam with respect to surface normal during an exposure in the SPM chamber.

Figure 2.9A illustrates the viewpoint of an incident electron (LEED and AES), energetic Ar^+ (sputtering), and molecular (high temperature exposures) beam when the sample is situated in a mount in the preparation chamber; this frame of reference is normal to the surface plane of the crystal. **Figure 2.9B** illustrates the viewpoint of the incident molecular beam (normal to the surface plane) when the sample plate is in the SPM chamber; a magnified view of the sample with a schematic of an STM image is given to demonstrate the orientation of the real-space STM image with respect to the crystal and sample plate. The red asterisk is a reference to demonstrate that the top of all STM images presented in this thesis corresponds to the right side of the area of the crystal being scanned, in real space, when the crystal is being viewed in the SPM chamber normal to the surface plane, as in (**B**). It is important to note the 180° rotation of the sample plate between **Figure 2.9**(**A**) and (**B**), as characterization of the crystal can occur in different orientations. For example, this is critical for relating a reciprocal space LEED pattern obtained with the crystal orientation in (**A**) to the real space lattice directions in a STM image taken with the crystal in orientation (**B**).

Figure 2.9C is provided to clearly illustrate the azimuthal angle of the incident beam with respect to surface normal (dashed gray line) during angled exposure experiments performed in the

SPM chamber. The dark red arrow represents the direction of the molecular beam and the red asterisk is located on the right side of the gray line, which provides information about the orientation of the crystal with respect to real space STM images; the handle of the sample plate can also be used as a reference for absolute crystal orientation. **Figure 2.9C** becomes critical when understanding how the incident angle of the molecular beam affects the reactive evolution of a given surface.

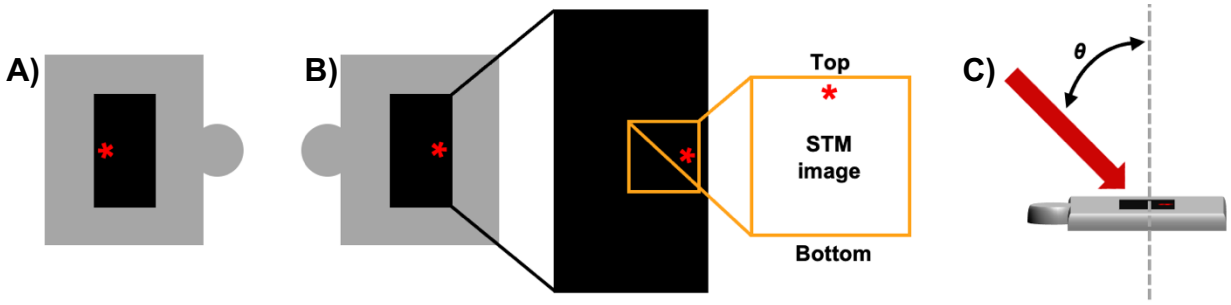


Figure 2.9: Schematic of sample plate and crystal orientation in UHV chamber. A schematic of the sample plate (gray) and crystal (black) in the **A**) preparation chamber sample mount and **B**) SPM stage from a reference frame normal to the surface plane (*i.e.* the reference frame of the incident beam of interest); a red asterisk on the crystal is used as a reference to show the different orientations of the crystal. The magnified view of the crystal and STM image schematic in **B**) is used to demonstrate how real space STM images relate to the crystal orientation. **C)** A schematic of the sample plate in the SPM chamber during angled exposures; this view is provided to demonstrate the azimuthal direction of the incident beam with respect to surface normal (dashed gray line).

2.7: Molecular Beam Characterization

In order to present any supersonic molecular beam data with confidence and accuracy, the energy distribution and flux of the molecular beam must be measured. In addition, the beam must be aligned to reproducibly hit the target sample. Time-of-flight analysis and King and Wells measurements were performed for each experiment to determine the energy distribution and flux, respectively, of the molecular beam used in each of the experiments. Descriptions of vibrational excitation due to nozzle heating and beam alignment techniques are also included.

2.7.1: Time-of-Flight Analysis

All time-of-flight (TOF) measurements were performed in a novel UHV chamber described elsewhere,[20] using experimental conditions that replicate those found in each chapter of this thesis. In a standard TOF measurement,[10] a rotating disc (mechanical chopper) with one or more slits breaks a molecular beam into small packets. The molecular beam packets then pass through an ionization detector that selects the gas molecules according to their velocities; the time-dependent output signal of the detector is amplified and transformed into velocity and/or kinetic energy distributions. A complete description of the methodology and instrumentation used for all time-of-flight measurements in this thesis is provided in Rebecca Thompson's published dissertation.[21]

2.7.2: Beam Flux Calculation

Understanding the beam flux is critical to calculating the absolute and relative reactivities of a system at a given beam energy. The flux of the molecular beam must therefore be calculated for each beam energy to determine the number of gas-surface collisions that occur per unit time. To do this, the pressure rise in the SPM chamber as monitored by the nude Bayard-Albert ionization gauge must first be calibrated to the gas species of interest using a residual gas analyzer (RGA). The chamber, at a steady base pressure, is then exposed to the molecular beam of interest and the chamber is once again allowed to equilibrate at a steady pressure. Under these conditions, the flow rate of the molecular beam into the chamber, Q, is equivalent to the flow of gas out of the chamber by the ion pump. The gas flow rate can be defined as:[22]

$$Q = \frac{d(PV)}{dt} \qquad \textbf{(E2-5)}$$

The known pumping speed of the pump, S, is equivalent the volumetric flow rate $\left(\frac{dV}{dt}\right)$ of the beam into the chamber at constant pressures, ΔP, which is the increase in pressure experienced by the UHV chamber when opened to the beam. Furthermore, assuming ideal gas behavior, the gas flow rate, Q, can be described in terms of the rate of particles, N, entering the chamber, the temperature of the chamber, T, and the Boltzmann constant, k_B.

$$Q = \Delta P \frac{dV}{dt} = \Delta P \cdot S = \frac{dN}{dt} k_B T \quad \textbf{(E2-6)}$$

The flux of the molecular beam, Φ, is equivalent to the rate of change of particles, N, per unit area, A, *i.e.* $\Phi = \frac{dN}{dt}\left(\frac{1}{A}\right)$; A describes the spot size of the beam upon impact on the surface or plane of measurement. Rearranging equation **E2-6**, the flux of the molecular beam is described by the following relationship:

$$\Phi = \frac{\Delta P \cdot S}{k_B T \cdot A} \quad \textbf{(E2-7)}$$

This relationship was used to quantitatively approximate the flux of all molecular beams used in this thesis and utilizes only experimentally determined and commercially known values. An example O_2 beam flux calculation for a room temperature 5% O_2/95% He beam at 20 psi is given below:

$$\Phi_{O_2} = \frac{\Delta P_{O_2} \cdot S}{k_B T \cdot A} = \frac{(2.4 \cdot 10^{-8} Pa) \cdot \left(200 \frac{L}{s} \cdot \frac{1 m^3}{1000\ L}\right)}{(4.11 \cdot 10^{-21} J) \cdot 0.113 cm^2} = 1.0 \cdot 10^{13}\ \frac{O_2\ molecules}{cm^2}$$

2.7.3: Characterization of Vibrational Excitation from Nozzle Heating

Heating of the molecular beam nozzle, in addition to enhancing the translational kinetic energy, also imparts vibrational energy into the expanding gas molecules. By approximating

quantum mechanical molecular vibration as a simple harmonic oscillator, the energy state solutions to the Schrödinger equation become:

$$E_n = h\nu\left(n + \frac{1}{2}\right) = \hbar\left(n + \frac{1}{2}\right)\sqrt{\frac{k}{u}} \quad \textbf{(E2-8)}$$

where n is the vibrational quantum number–often denoted as v but changed in this formalism to avoid confusion with v as the symbol for frequency–with values $n = 0, 1, 2$ ..., k is the molecule's force constant, and u is the reduced mass.

In order to determine the percentage of molecules in the molecular beam that occupy vibrationally excited states at different nozzle temperatures, a Boltzmann factor can be calculated to determine the ratio of probabilities between a given excited vibrational state and the ground vibrational state:

$$\frac{p_i}{p_j} = e^{\left(\frac{\varepsilon_j - \varepsilon_i}{kT}\right)} \quad \textbf{(E2-9)}$$

where p_i and p_j are the probabilities of finding a molecule in the ε_i and ε_j vibrational states, respectively, at a given temperature, T. An example of these calculations is shown in **Table 2.3** for a 3% N_2/97% He mixture expanding through a heated nozzle, as is used in **Chapter 5**; percentages of the N_2 flux that occupy the first ($v = 1$) and second ($v = 2$) vibrationally excited states at varying nozzle temperatures are given. Experimentally determined[23] values of 0.29 and 0.58 eV for the energy difference between $v = 1$ and the ground state ($v = 0$) as well as $v = 2$ and the ground state, respectively, were used to determine the population of vibrationally excited

Nozzle Temperature	700 K	800 K	900 K	1000 K	1100 K	1200 K
$v = 1$	0.8%	1.5%	2.3%	3.4%	4.7%	6.0%
$v = 2$	<0.1%	<0.1%	<0.1%	0.1%	0.2%	0.4%

Table 2.3: Vibrationally excited N_2 population at different nozzle temperatures. Values for the percentage of the N_2 flux at varying nozzle temperatures that occupy the first ($v = 1$) and second ($v = 2$) vibrationally excited states calculated using a Boltzmann factor. A 3% N_2/97% He beam was used in **Chapter 5** at varying nozzle temperatures that would exhibit this type of vibrational excitation.

N_2 in the beam. Note that the experimentally determined values match the energy differences between N_2 vibrationally excited states when calculated using the simple harmonic approximation, using a force constant for N_2 of $k = 2295\ \frac{N}{m}$; these energies correspond to vibrational frequencies of 3.5×10^{13}, 1.0×10^{14}, and 1.8×10^{14} Hz for the $\nu = 0$, $\nu = 1$, and $\nu = 2$ vibrational states, respectively.[23]

2.7.4: Beam Alignment

To maximize the flux and performance of the molecular beam, it must be aligned to flow through the apertures in the beam stages and onto the target surfaces. Complete alignment of the beam through the UHV chamber first requires removal of the apertures between the second and third stages and third stage and preparation chamber, in addition to the RGA located in the SPM chamber; this provides a complete line of sight through the entire UHV system. A telescope looking through the line of sight of the beam line then focuses on the skimmer and SPM stage, individually, which can be adjusted using tilt controls and knobs to center the skimmer and stage. The apertures, (starting with the one between the third stage and preparation chamber) RGA, and beam nozzle are then reinstalled, and the air legs are adjusted until the apertures are centered in the telescope.

Once the course manual adjustments are made, the entire instrument is pumped down to UHV. A beam is then generated, and the flux in the SPM chamber can be measured by either the change in pressure as read by the ionization gauge or RGA. Rotary knobs attached to the flange securing the beam to the chamber can then be used to translate the beam in the X and Y directions to maximize the alignment of the beam nozzle and skimmer. Once a maximum flux is measured in the SPM chamber, the beam is determined to be aligned. The process of adjusting the beam

alignment in UHV must be completed every time the temperature of the beam nozzle is altered due to thermal expansion and contraction of the metal.

2.8: Sample Cleaning and Preparation

All surfaces to be studied are first cleaned in atmosphere to remove any excess oils/water with a methanol and/or isopropanol rinse/sonication. The flag style sample plates that hold the sample of study, as well as any screws and clips that will be introduced into the UHV system, are also sonicated in methanol prior to entering the UHV system. The sample is then placed in the transfer arm in the vented load lock and then pumped down to near UHV pressures ($<1\times10^{-7}$ Torr). The sample can be moved into the preparation chamber once a pressure is achieved in the load lock that will not affect its UHV environment.

Heating (annealing) samples is often an integral part of cleaning and working with surfaces in UHV; samples can be annealed in the preparation chamber either using resistive or e-beam heaters. Annealing can desorb impurities and adsorbates from the surface, order the surface, or even give the surface enough energy to overcome kinetic obstacles and return a reconstructed surface. To resistively heat a sample, current is run through an electrically isolated sample that is then subsequently heated due to the friction between the moving electrons and atomic ions of the sample. The heating power is proportional to the resistance of the conductor multiplied by the square of the current (*i.e.* $P = I^2R$) as described by Joule's first law (Joule–Lenz law). The current through the sample is supplied by an external Electro Industries Model 4025 power supply and the temperature is monitored by a Mikron infrared pyrometer with an emissivity, ε, set to match that of the sample. The manipulator in the preparation chamber has multiple electrical feedthroughs that allow an electrical connection from atmosphere to the UHV system; insulated copper wiring

connects the feedthroughs to electrical connections on the mounts so that electric power can be supplied from the power supply through the sample. Resistive heating is a very clean form of heating and was used in **Chapter 3** to heat the HOPG surfaces during exposures and in **Chapter 4** to anneal the GaAs(110) surfaces during its cleaning cycles.

To heat a sample with an electron beam, a filament is heated resistively until electrons are ejected into the vacuum that are then accelerated into a sample; the energy from the highly energetic electrons is then converted into thermal energy that then heats the sample. The amount of thermal power, P, being imparted on the sample can be approximated by Ohm's law ($P = IV$), where I is the current of high energy electrons impacting the sample and V is the bias voltage between the filament and sample. The e-beam heating assembly in the preparation chamber uses a 0.25 mm diameter 99% W/1 % Th filament wrapped in a tight helix (~1.5 mm in diameter) as its electron source. The filament is placed ~3 mm away from the back of the sample plate and is powered by the external Electro Industries Model 4025 power supply. A molybdenum sample mount holds the sample plate in place and is electrically isolated from the grounded filament and chamber. A bias wire attached to the entire sample mount (and plate) is connected to an external Sorensen Model XG 600-1.4 power supply (through an electrical feedthrough into the UHV system) that positively biases the sample plate with respect to the filament/ground. Sample biases from 300-600 V are used to accelerate electrons into the back of the sample plate; the sample plate then conductively heats the sample, and the temperature is monitored by a Mikron infrared pyrometer. E-beam heating, as opposed to resistive heating, was used to anneal the Ru(0001) surface in **Chapter 5** as the resistance of the Ru(0001) sample was too low to achieve the necessary temperatures of >1500 K through resistive heating.

The PHI 04-150 ion gun housed in the preparation chamber is used to sputter samples for sputter/annealing cycles that clean the surface of impurities and return the appropriate surface structure. A gas line, which can be evacuated by an Edwards nXDS15i 4.75 L s^{-1} dry scroll pump prior to being pressurized, connects a cylinder of argon gas (99.9997% purity) to the preparation chamber through a leak valve. Sputtering of samples is achieved by backfilling the preparation chamber with argon gas to a desired pressure (anywhere from 5×10^{-5} Torr to 1×10^{-7} Torr); the ion pumps are off during this time and the preparation chamber is backed by the Balzers TMU65 55 L s^{-1} turbomolecular drag pump in the load lock.

In **Chapter 3**, sputtering with 4 keV Ar^+ ions was used to create monolayer atomic vacancies on the HOPG surface spanning approximately 1-10 carbon atoms. **Chapter 4** utilized cycles of sputtering with 0.5 keV Ar^+ ions to remove Ga_2O_3 and As_2O_3 species from the GaAs(110) surface followed by subsequent annealing at 700 K ± 30 K to recover the clean, ordered row structure as determined by STM imaging. In **Chapter 5**, hundreds of cycles of 0.5 keV Ar^+ ion sputtering and subsequent e-beam annealing to ~1500 K were required to free the Ru(0001) surface of adsorbate impurities and return a flat, clean, and ordered hexagonal lattice structure as determined by LEED, AES, and STM imaging.

2.9: Image Processing and Data Extraction

To produce high-quality images and extract physically relevant information from the STM images obtained in this thesis, the raw files (sm4) produced by the R9 software are processed and then appropriately analyzed. The following section describes the general processing for all of the STM images presented in this thesis, as well as general procedures for how data was acquired from these sets of images.

2.9.1: Processing

The open-source SPM software, Gwyddion,[24] was used for all STM image analyses presented in this thesis. The level of processing used for each image depended on the quality of the topography image of the raw files. If the raw topography image was sharp, clear, and void of noise, little processing was necessary to produce a quality image file. In these instances, the cleanest topography image (forward and back) is chosen and the built-in "Align Rows" and "Level" operations were used to flatten the image and provide a zero-point topographical plane for accurate and clear quantitative measurements. In addition, the image could be cropped and the color scale could be manipulated to highlight specific features of interest.

Additional processing operations can be utilized to highlight very detailed features, remove noise, or improve the overall quality of STM images. In addition to the built-in "Remove Scars" operation in Gwyddion, forward and back scans of the same area can be combined in reciprocal space to remove residual noise, scarring, or overshoots caused by large, sudden changes in topography which require time for the PID feedback to recover. Combining the forward and back scans of images only worked for images ≤200×200 nm^2, as the drift between the forward and back scans becomes too great above this size to effectively combine the two data sets. To accomplish this, the images are cropped for appropriate overlap, and the "Arithmetic" function is used to ensure that the images are essentially the same. The data from both the forward and back images are then converted into reciprocal space and separated into real and imaginary parts using the "2D Fast Fourier Transform (FFT)" tool. Both pairs of real and imaginary (forward and back scans for each) FFT data sets are then combined again using the "Arithmetic" function using the following expression developed by Dr. Ross Edel to reduce the amount of noise in the image:[25]

$$\left[1 - \left(\frac{|d_1 - d_2|}{max[(|d_1| + |d_2|), 10^{-20}]}\right)\right] \cdot \left(\frac{d_1 + d_2}{2}\right) \quad \textbf{(E2-10)}$$

In this expression, d_1 and d_2 represent the data points from each FFT image; points of opposite signs are omitted entirely. The max expression is used to avoid dividing by zero.

2.9.2: Data Extraction

Gwyddion provides a comprehensive set of tools to extract precise quantitative information from the STM image data sets. The "Extract Profiles" function is capable of making precise topographical measurements in all three spatial directions; this functionality enabled calculation of the heights of step edges, adsorbates, and other protrusions as well as calculating the distance between adsorbates. Reproducible statistical data was often obtained utilizing the "mask" functionality, which allows certain features to be selected if they are above/below a certain height threshold. Measurements can then be made, such as finding the total area of etch pits as described in **Chapter 3**, of the masked/unmasked areas of the STM image. In some cases, other image processing programs such as ImageJ[26] were used in addition to Gwyddion for these purposes. To count features on an individual image, small masks (or grains) were manually placed over each feature; the x and y coordinates of each grain are recorded whenever this is done. The precise location on the xy plane of each feature could then be mapped for each image, from which information such as total number of features and nearest-neighbor distances could be calculated.

Chapter 3: Atomically-Resolved Oxidative Erosion and Ablation of Basal Plane HOPG Graphite Using Supersonic Beams of O_2 with Scanning Tunneling Microscopy Visualization

Summary

The detailed mechanism and kinetics for the oxidative erosion and ablation of highly oriented pyrolytic graphite (HOPG) with molecular oxygen has been examined by monitoring the spatio-temporal evolution of the reacting interface. This has been accomplished using a new, unique gas-surface scattering instrument that combines a supersonic molecular beam with a scanning tunneling microscope (STM) in ultrahigh vacuum. Using this new instrument, we are able to tightly control the energy, angle, and flux of impinging oxygen along with the surface temperature and examine the reacted surface spanning atomic, nano, and mesoscopic length scales. We observe that different oxidation conditions produce morphologically distinct etching features: anisotropic channels, circular pits, and hexagonal pits faceted along crystallographic directions. These outcomes depend upon independent effects of oxygen energy, incident angle, and surface temperature. Reaction probability increased with beam energy and demonstrated non-Arrhenius behavior with respect to surface temperature, peaking at around 1375 K. At the incident collision energies used, it was found that beam impingement angle had only minor effects on the reaction probability and etch pit morphology. Comparison of the relative reactivity of higher grade versus lower grade HOPG indicates that the formation of etched channels largely depends on the presence of grain boundaries. We have also observed the transition to multilayer etching. The influence of structural inhomogeneities such as defects and grain boundaries can now be assessed by real-time visualization of reacting interfaces. For example, the insertion of intentionally created point defects

via ion sputtering leads to marked enhancement in interfacial reactivity. The approach used herein has allowed us to correlate time-evolving surface morphology with atomic-level interfacial kinetics and dynamics, providing new insight into the reactivity of materials in aggressive, energetic environments.

3.1: Introduction

Graphite oxidation is widely studied due to its relevance to technological applications such as high-performance aircraft and propulsion systems and due to its important role as a model system for fundamental studies of materials degradation. The oxidation process with molecular oxygen removes carbon from the surface as the products CO and CO_2, with CO being the dominant reaction product at all surface temperatures[27–30] and impinging oxygen energies.[31–33] Oxygen molecules dissociatively adsorb and diffuse across the surface[34] as adsorbed O before reacting with and removing carbon atoms from the surface. The prismatic plane of HOPG is oxidized much more rapidly than the basal plane, leading to the domination of lateral etching of graphite layers starting from vacancy defects and step edges.[35–39]

In this chapter we present a new approach to studying the dynamics and kinetics of interfacial erosion chemistry where we monitor reactivity not by monitoring CO or CO_2 product formation but rather by visualization of the reacting interface using the combination of supersonic beam scattering coupled with ultra-high vacuum scanning tunneling microscopy (STM). This novel approach allows us to directly link the time-evolving morphology of the reacting interface with the observed reaction kinetics, in essence, giving access to the spatio-temporal correlations that govern time-evolving interfacial reactivity. In this instance, visualization encompasses several length-scales including atomic, nano, and mesoscopic distances. The ability to conduct such information-rich experiments was demonstrated for the site-specific energetic oxidation of Si(111)-(7×7).[40]

Such spatio-temporal measurements of surface morphological change and surface chemical change directly reveal the key roles that minority structures such as grain boundaries and defects play in determining the time evolution of the interface. This statement, in a broader sense,

is especially relevant for intrinsically heterogeneous materials such as functional composites. In this study we intentionally introduce localized defects using ion sputtering, creating single or multi-atom vacancies visible to STM as positive contrast hillocks. These vacancies expose prismatic edge carbons and provide nucleation points for oxidation.[41,42] After a certain induction period, or nucleation phase, the removal of edge carbons results in a visible, negative contrast pit. By providing artificial nucleation points *via* sputtering, the density of etch features is substantially and controllably increased.

Previous research has used STM to examine graphite samples etched in furnaces under a high flux of heated molecular oxygen.[35–38,43–48] Circular, monolayer-deep pits were found to arise from these conditions, nucleating exclusively at natural and artificial defects at low temperatures (<1150 K) but nucleating even on the locally perfect (undefected) basal plane at higher temperatures (>1150 K).[38] In some cases elongated, anisotropic channels were observed on furnace-oxidized graphite, but formed a small minority of features with circular pits dominating.[38,42,49] Pit diameters were found to increase linearly with oxygen exposure, with the lateral etch rate increasing with temperature. The linear growth of pit diameters comports with an overall carbon reaction rate limited by the available density of reactive edge carbons.

At very high temperatures (>1275 K) the overall rate of carbon removal from the surface exhibits apparent non-Arrhenius temperature dependence as a result of the interaction of a number of competing reaction rates. Supersonic beam experiments have determined that reactivity peaks at 1400 – 1500 K, likely due to the increased desorption of adsorbed O atoms at higher temperatures.[31,50–52] An excess of adsorbed O enhances both the formation of new surface vacancies and the etching of existing defects by reducing the barrier to reaction and stabilizing the resulting dangling carbon bonds.[53–55]

More recently, the dependence of etching morphology on surface temperature has been demonstrated, with faceted pits aligned with lattice directions formed below a certain critical temperature, transitioning to circular pits as the temperature was increased.[56] This faceting can be attributed to the preferential reaction of armchair-type edge carbons, leaving only hexagonal pits with zig-zag edges aligned with the < 1 1 -2 0 > lattice directions.[57] Although both zig-zag and armchair sites have two neighboring carbon atoms, zig-zag sites have two fully-coordinated nearest neighbors while armchair sites only have one. The higher stability of zig-zag edges thus slightly favors the removal of armchair sites from the surface ($\Delta E_a \approx 0.52$ eV).[56] Above the transition temperature, the reactivity of the two types of edge carbons becomes essentially equivalent and circular pits result.

3.2 Experimental

These experiments were conducted using a new combined supersonic beam/STM/AFM surface scattering/imaging instrument, **Figure 2.1**.[40] It can be viewed as consisting of three sections: The triply-differentially pumped beam line, a materials preparation and characterization chamber, and a new variable-temperature SPM that differs from our other SPMs in many critical ways including sample orientation, stability, and thermal equilibration between the tip and sample; it is based on the ultra-stable design of Shuheng Pan, and has been designed in conjunction with RHK. Most importantly, it has been constructed to allow the surface plane to be vertical, permitting its use in simultaneous or sequential molecular beam plus scanning probe imaging experiments.

Supersonic beams of molecular oxygen were generated by expanding a 5% O_2/95% He gas mixture through a 30 μm diameter molybdenum pinhole at 20 psi and 70 psi for nozzle

temperatures of 300 K and 600 K, respectively. The nozzle was heated by resistively heated wire, and the temperature was monitored by a thermocouple. A translational kinetic energy of 0.37 eV with an energy distribution width of $\Delta E/E = 0.28$ was found for the beam with a 300 K nozzle using time-of-flight measurements; the translational kinetic energy of the 600 K beam was extrapolated to be ~0.7 eV. A flux on the order of 10^{13} O_2 molecules cm^{-2} s^{-1} was determined for both beam conditions. Samples were positioned 1.3 m from the nozzle, with a 2 mm diameter beam spot at the crystal.

HOPG samples were placed in a UHV chamber (base pressure of 1×10^{-10} Torr) in sample mounts that aligned the surface normal either parallel to the beam or at a 45° angle. The sample was maintained at the appropriate temperature (1275-1475 K) during exposure to the supersonic beam of O_2. After exposure, the cooled sample was transferred under vacuum to the STM chamber for imaging.

For these experiments, highly oriented pyrolytic graphite (HOPG, SPI-2 and SPI-3) samples were cut into approximately 2 mm × 1 cm strips with a sharp blade and cleaved with adhesive tape. Samples were outgassed in a UHV chamber (base pressure of 1×10^{-10} Torr) up to experimental temperatures (1275-1475 K) prior to exposure. The surface temperature was monitored by a Mikron infrared pyrometer and heated by applying current directly through the sample. Several areas on the surface were checked for cleanliness by STM prior to oxygen exposure. Etched $Pt_{0.8}Ir_{0.2}$ tips were used for imaging. When required, a Phi sputter ion gun was used to create atomic vacancies in the HOPG basal plane by bombarding the sample with 4 keV Ar^+ ions. The 4 keV Ar^+ ions used to prepare our samples induce local point defects most likely consisting of 1-10 removed atoms per created vacancy, this based on prior STM studies.[58] At this

scale, the precise atomic-level morphology of the vacancy is obscured by the electronic enhancement resulting from unsaturated dangling bonds.

3.3: Results and Discussion

As the undefected HOPG surface is minimally reactive, defects were introduced by sputtering. **Figure 3.1** shows an unsputtered and unreacted basal plane of HOPG as well as a surface that was sputtered to induce surface vacancies. The average surface density of reactive defects after sputtering was $7\times10^{9} \pm 1\times10^{9}$ cm^{-2}. Sputter defects serve as nucleation points, leading to a higher density of etch features. In addition, the defects shorten the nucleation phase, defined as the period of time (exposure) that transpires before visible etch pits are formed. In the case of a sputtered surface, a certain number of atoms must be removed from around the initial vacancy before it is imaged by STM as a depression rather than a hillock. A longer nucleation phase is

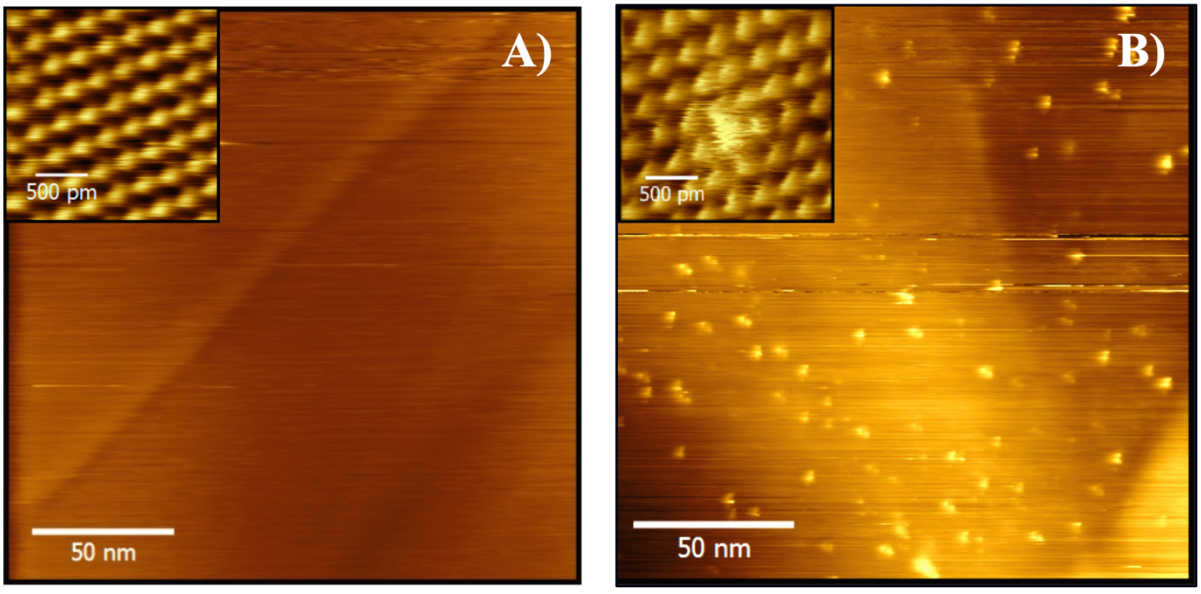


Figure 3.1: STM images of an unsputtered and sputtered HOPG surface. **A)** A typical STM image of the clean basal plane of HOPG with an inset of the clean lattice. **B)** STM image of a typical sputtered HOPG sample (4 keV Ar^{+}) with an inset of a single vacancy formed from collision of an Ar^{+} ion with the HOPG surface. Images taken at 100 mV and 0.6 nA.

observed on a clean basal surface in comparison to an artificially defected surface as a result of the amount of exposure necessary for a very low probability event, the abstraction of a fully coordinated basal carbon atom, to occur before this transition from hillocks to pits can commence. As seen in **Figure 3.2**, the nucleation phase of a sputtered sample is reduced by half as compared to an unsputtered sample. While nucleation was observed predominantly at sputter defects at a surface temperature of 1275 K, at higher surface temperatures pit formation was observed on the undefected portions of the surface that remained after all initial nucleation points had been consumed. This vertical etching has a higher energetic barrier than lateral etching (E_a=2.00 eV compared to E_a=1.48 eV for the latter)[36] because it requires the removal of a carbon atom from an undefected basal plane. Therefore, it only emerges at higher surface temperatures and occurs much more slowly.

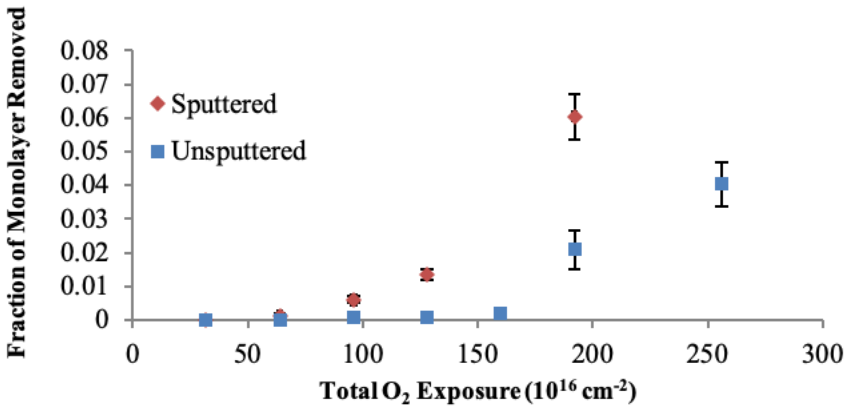


Figure 3.2: Effect of sputtering on nucleation phase. The effect of sputter-induced vacancies on the nucleation phase of a 1375 K HOPG surface exposed to an effusive distribution of background O_2 at 1×10^{-6} Torr.

Along with changes in the overall kinetics of carbon removal from the surface, the surface temperature also affects the morphology of etch pits. Below surface temperatures of ~1325 K, etch pits formed on the surface by exposure to 0.4 eV oxygen were hexagonal. Computational and experimental studies have demonstrated that lower surface temperature etching forms hexagonal

pits on the surface due to small energetic differences between removing a zig-zag and an armchair carbon atom.[56] Consequently, armchair sites will etch at a higher rate than zig-zag sites, leading to the formation of hexagonal pits with zig-zag edges, as seen in **Figure 3.3a**. **Figure 3.3b** demonstrates the difference between zig-zag and armchair sites on the HOPG honeycomb lattice, while **Figure 3.3c** is a schematic representing the sequential removal of zig-zag and armchair carbon atoms during the growth of a hexagonal pit. Note that the STM only images every other basal carbon atom in the full honeycomb lattice (namely, out of the α and β atoms contained in each unit cell only the β atom is detected), as seen in **3.3c** and the inset of **3.3a**.[59]

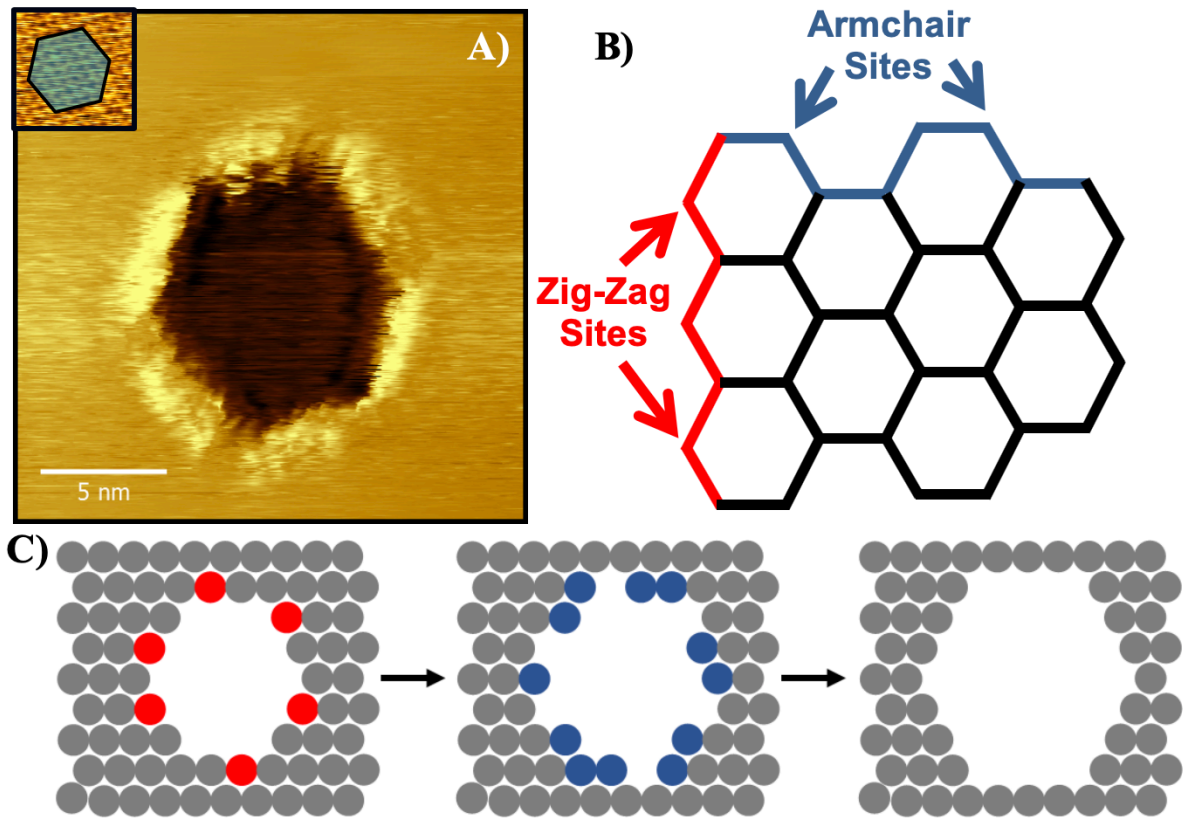


Figure 3.3: Formation of hexagonal etch pits on an HOPG surface. A) STM image of a representative etch pit formed on a sputtered HOPG sample after exposure to 0.4 eV O_2 at a surface temperature of 1275 K, with inset showing lattice aligned with pit edges. Set point: 1.1 V, 0.6 nA. B) Skeleton diagram of the HOPG basal plane demonstrating the difference between zig-zag (red) and armchair (blue) sites. C) Schematic representation of the formation of hexagonal pits through preferential etching of armchair (blue) over zig-zag (red) carbon atoms. The diagram represents the lattice as imaged by STM, as seen in the inset of (A).

At a higher surface temperature of 1375 K, circular, monolayer pits form on the surface when exposed to 0.4 eV O_2. This suggests that the surface has enough energy to overwhelm any small energetic differences between armchair and zig-zag sites, which results in the two sites etching at approximately the same rate. This leads to the formation of circular pits, as seen in **Figure 3.4**. A similar transition was found in previous work under different experimental conditions.[56] As would be expected, the creation of circular etch pits was observed at the higher surface temperature of 1475 K when exposed to 0.4 eV O_2, although these pits grew at a much slower rate than those on a 1375 K surface.

Previous work with samples reacted in tube furnaces has demonstrated the diameter of etch pits growing linearly with exposure,[35–38] indicating that the total rate of carbon removal increases with O_2 exposure. This suggests that the surface becomes more reactive as etch features grow and edge carbons with unsaturated dangling bonds become more pervasive.

Interestingly, under all conditions examined here, the rate of carbon removal was constant with oxygen exposure, with no increase due to the proliferation of edge carbons. This suggests that

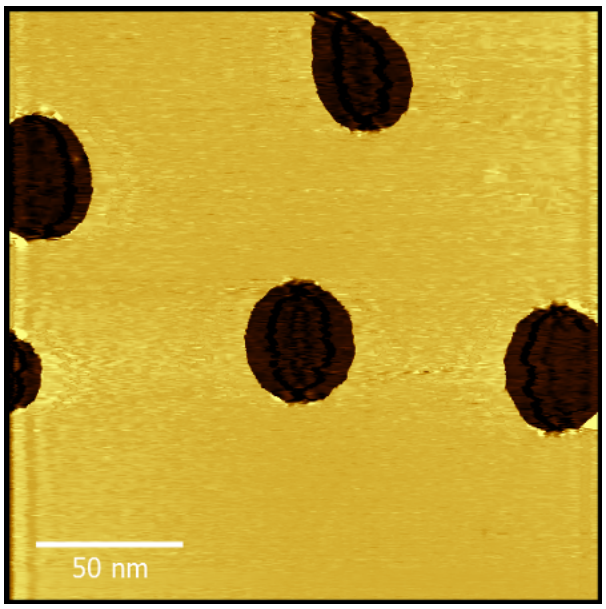


Figure 3.4: Formation of circular etch pits on an HOPG surface. STM image of representative etch pits formed on a sputtered HOPG sample after exposure to 0.4 eV O_2 at a surface temperature of 1375 K. Set point: 300 mV and 0.6 nA.

O_2 can adsorb at an arbitrary location and diffuse across the surface as adsorbed O to find a reactive edge carbon, such that the rate-limiting step of carbon removal from the surface is not sensitive to the density of edge carbons (as in the high O_2 flux conditions of previous experiments) but instead is dependent on the concentration of oxygen adsorbed on the surface. **Figure 3.5** demonstrates the constant rate of carbon removal on an HOPG surface at temperatures of 1275, 1375, and 1475 K. The slope of each linear fit corresponds to the probability of a given O_2 molecule removing a carbon atom from the surface. For 0.4 eV O_2 molecules, the values of these reaction probabilities are $3\times10^{-6} \pm 1\times10^{-6}$, $2\times10^{-4} \pm 1\times10^{-4}$, and $7\times10^{-6} \pm 3\times10^{-6}$ for surface temperatures of 1275 K, 1375 K, and 1475 K, respectively. Previous studies on graphite oxidation have demonstrated non-Arrhenius behavior with respect to surface temperature, and our findings exhibit similar behavior.[31,52] Our experiments in the 1275 K – 1475 K surface temperature range reached a maximum reaction probability at ~1375 K, which agrees well with previously reported values. This behavior is likely due to decreasing coverage of adsorbed O atoms with increased temperature.[50,51] The effect of oxygen energy on reactivity in the initial oxidation regime is clear in the normally-oriented beam experiments: when the beam energy was raised from 0.4 eV to 0.7 eV, the overall reactivity of the surface increased significantly for both the 1275 K and 1375 K surfaces. The reaction probability of impinging 0.7 eV O_2 is $4\times10^{-4} \pm 2\times10^{-4}$ and $5\times10^{-4} \pm 2\times10^{-4}$ for surface temperatures of 1275 K and 1375 K, respectively; this corresponds to an increase of a factor of over 100 for the 1275 K surface and of over 2 for the 1375 K surface, as seen in **Table 3.1**.

The dissociation probability of O_2 molecules impinging normal to a clean HOPG surface with sputter-induced vacancies demonstrate a marked dependence on kinetic energy. The relative dissociation probabilities under different experimental conditions were inferred by measuring the

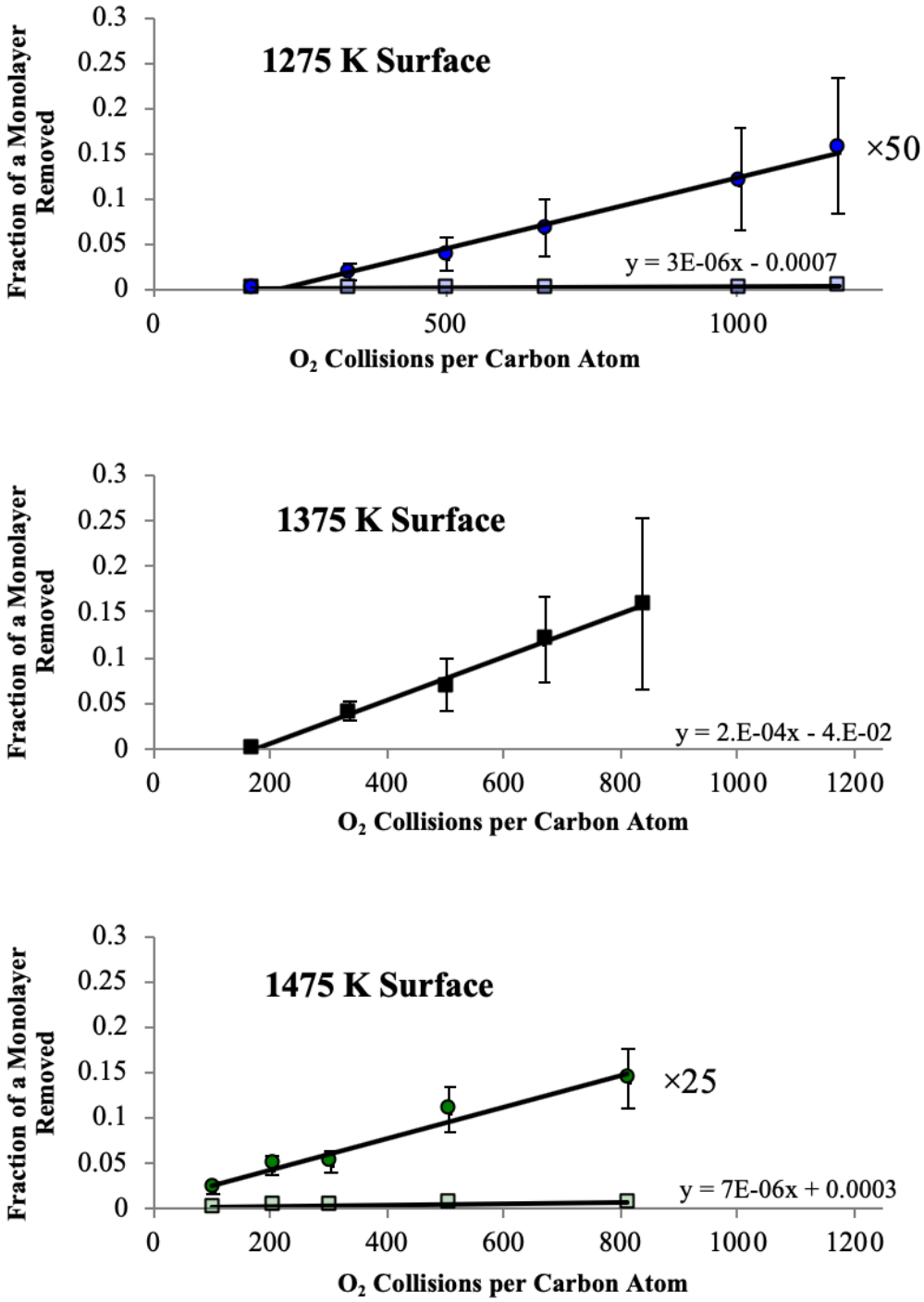


Figure 3.5: Reactivity plots of 0.4 eV O_2 on HOPG at different temperatures. Reactivity plots of 1275 K (top), 1375 K (middle), and 1475 K (bottom) HOPG surfaces exposed to 0.4 eV O_2, where the fraction of the surface monolayer reacted is plotted against the average number of collisions an individual carbon atom has with O_2 molecules. The linear fit to each of these plots corresponds to the probability of an O_2 molecule ultimately removing a carbon atom from the surface. The reactivity plots for the 1275 K and 1475 K surfaces are magnified by 50 and 25 times, respectively, to be visible on the same scale as the 1375 K surface.

Translational O_2 Energy Normal to the Surface (eV)	HOPG Grade	Impinging O_2 Angle (°)	Surface Temperature (K)	Reaction Probability
0.4	SPI-3	90	1275	$3\times10^{-6} \pm 1\times10^{-6}$
0.4	SPI-3	90	1375	$2\times10^{-4} \pm 1\times10^{-4}$
0.4	SPI-3	90	1475	$7\times10^{-6} \pm 3\times10^{-6}$
0.4	SPI-3	45	1375	$1.1\times10^{-4} \pm 5\times10^{-5}$
0.7	SPI-3	90	1275	$4\times10^{-4} \pm 2\times10^{-4}$
0.7	SPI-3	90	1375	$5\times10^{-4} \pm 2\times10^{-4}$
0.7	SPI-2	90	1375	$3\times10^{-5} \pm 1\times10^{-5}$
0.7	SPI-2	45	1375	$3\times10^{-5} \pm 1\times10^{-5}$

Table 3.1: O_2 reaction probabilities. A complete list of O_2 reaction probabilities for all sets of experimental conditions.

nucleation time, the amount of O_2 exposure necessary for product formation to begin and etching to occur. **Figure 3.6** shows the amount of carbon consumed by etching with molecular oxygen impinging at a normal angle on a 1375 K surface at both 0.4 eV and 0.7 eV kinetic energies. The nucleation time, graphically defined as the x-intercept of the linear trends, is about 2.5 times longer for 0.4 eV oxygen, in line with the difference in dissociation probabilities predicted theoretically.[60] Further, the nucleation time does not appear to be strongly related to the subsequent etching rate. The nucleation time for 0.7 eV O_2 remained comparatively short even when its etching rate was lowered through the use of a higher quality HOPG sample having a lower density of domain boundaries and intrinsic defects. Conversely, altering the impingement angle of the beam affected nucleation time but not etching rate, with more glancing angles producing longer nucleation times. Thus, molecular oxygen with higher energy and impingement angles closer to normal do indeed dissociate more readily on sputter vacancies, leading to a higher coverage of adsorbed O and the onset of product formation at smaller O_2 exposures.

In addition to increasing the reaction probability of impinging oxygen, raising the incident O_2 energy from 0.4 eV to 0.7 eV drastically changes the morphology of the etch features on the surface. 0.4 eV O_2 predominantly created symmetrical etch pits, with hexagonal pits formed at

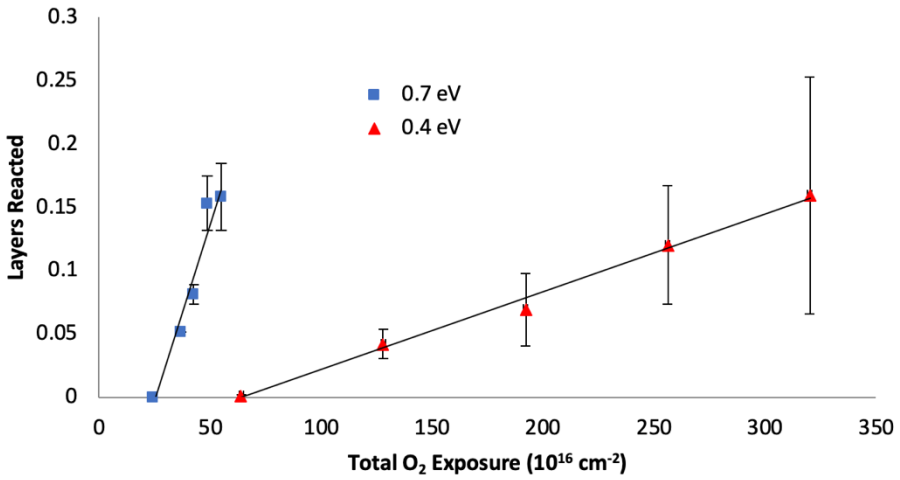


Figure 3.6: Nucleation time dependence on O_2 kinetic energy. Reactivity of HOPG samples in terms of layers of graphite reacted versus fluence of O_2 from a supersonic molecular beam. Vacancies were introduced by sputtering with 4 keV Ar^+ ions to provide nucleation sites. Samples exposed to molecular oxygen with kinetic energies of 0.4 eV (red) and 0.7 eV (blue) at a surface temperature of 1375 K and normal incident angle show marked differences in nucleation time (the x-intercept of the linear regressions) as well as subsequent overall reactivity (the slope). The nucleation time with 0.4 eV oxygen is roughly 2.5 times longer than that of 0.7 eV oxygen.

lower surface temperatures (<1325 K) and circular pits formed at higher surface temperatures. By contrast, at the higher beam energy of 0.7 eV, irregular, anisotropic etch channels dominated, as seen in **Figure 3.7**. This channeling phenomenon was observed at surface temperatures of both 1275 K and 1375 K, indicating that it is caused solely by the impinging oxygen energy. New pits appeared to remain mostly symmetrical up to a maximum radius of about 20 nm, by which point they spawned rapidly growing channels. The morphology of the pits prior to channeling was similar to those in the 0.4 eV experiments, although the 1275 K surface also formed unusual, nearly triangular pits in some areas (as shown in **Figure 3.7a**) which may result from locally decreased surface temperatures.[61]

It is interesting to note that the reaction probabilities with 0.7 eV O_2 at both surface temperatures are roughly equal, suggesting that the large influence of surface temperature over carbon removal rate seen with 0.4 eV oxygen is specific to the formation of circular and hexagonal

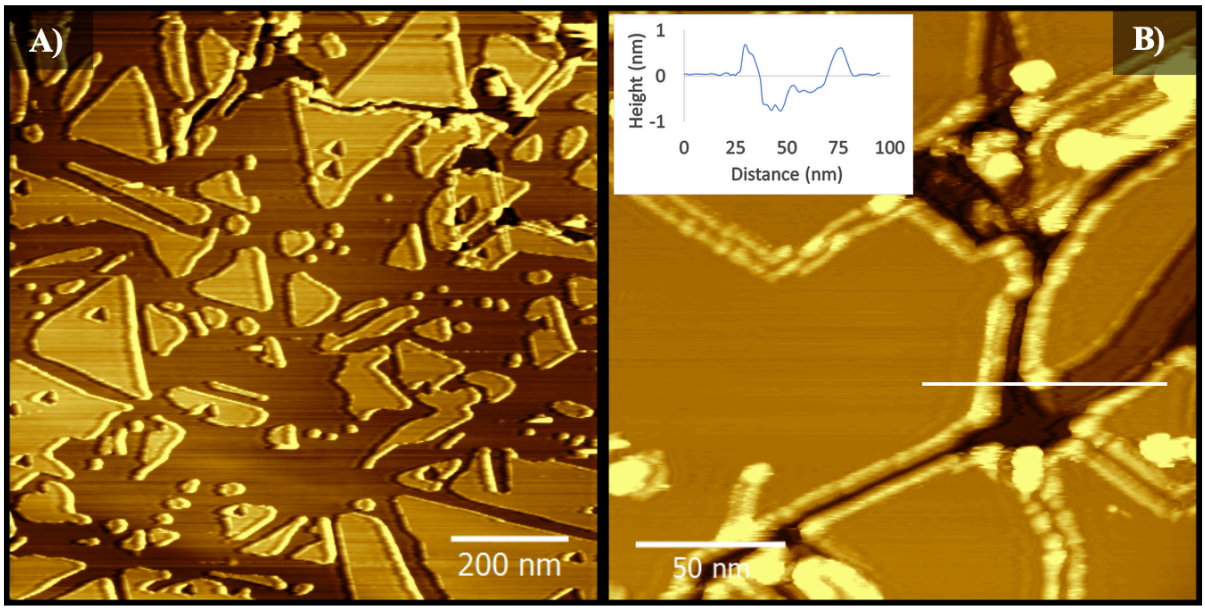


Figure 3.7: STM images of anisotropic etch features formed by 0.7 eV O_2. STM images of representative etch channels formed on a sputtered HOPG sample after exposure to 0.7 eV O_2 at a surface temperature of **A)** 1275 K (400mV, 0.6 nA) and **B)** 1375 K (300 mV, 0.6 nA); the inset line scan represents areas of single and double layer etching, with two negative contrast terraces at around 0.3 nm and 0.8 nm corresponding to one and two layer deep etch features, respectively. Multilayer etch features are much more abundant on a 1375 K surface in comparison to a 1275 K surface due to increased vertical etching. For example, multilayer etching was more pervasive on the surface shown in **(B)** despite it being exposed to about 1/3 as much O_2 as the surface in **(A)**. Faceted etch pits up to ~20 nm in diameter were also observed on the 1275 K surface as seen in **(A)**.

pits. The enhancement to the reaction probability at both surface temperatures at the higher beam energy can be attributed to the new anisotropic channeling mode that emerges, which is evidently not dependent on surface temperature and dominates over the symmetrical pit etching mode. The etching process giving rise to these channels is thus kinetically as well as morphologically distinct.

The observed increase in carbon removal rate is unlikely to stem from a direct abstraction mechanism whereby by the O_2 molecule removes a carbon atom from the surface through direct collision to form CO_2. Studies on systems with much higher incident O_2 energies suggest that there is no available reaction mechanism by which an O_2 molecule will directly abstract a carbon atom from the surface; the energy required is too great to render this a realistic possibility. Instead,

computational and experimental findings demonstrate that O_2 does not chemisorb as molecular oxygen but rather undergoes exothermic dissociative chemisorption, forming adsorbed O atoms.[42]

Results on higher grade HOPG samples indicate that channels may be following domain boundaries, explaining their irregular, elongated shape. Channels attributed to grain boundaries have been observed previously, although on a larger micron-scale and under different conditions.[62,63] On lower grade HOPG (SPI-3) with lateral grains no larger than 30-40 nm, most pits remain roughly circular up to a ~20 nm diameter before channeling. By contrast, on higher grade samples (SPI-2) with lateral grain sizes of 0.5-1.0 mm, only circular pits are found after exposure to 0.7 eV at a surface temperature of 1375 K, as seen in **Figure 3.8**. This result suggests that intrinsic surface properties dictate channel morphology, as the only significant reactive difference between the two samples is the difference in lateral grain sizes. Due to the absence of channeling, the reaction probability of 0.7 eV O_2 on a 1375 K surface drops from $5 \times 10^{-4} \pm 2\times10^{-4}$ on an SPI-3 HOPG surface to $3\times10^{-5} \pm 1\times10^{-5}$ on an SPI-2 HOPG surface, decreasing by over an order of magnitude. This once again demonstrates the connection between kinetics and morphology: the channeling process must be fundamentally faster than pit formation, and thus when the surface structure is not conducive to channeling the kinetic enhancement of 0.7 eV oxygen fails to materialize.

The relationship between vertical etching rates on 1275 K and 1375 K surfaces remained relatively unchanged with an increase in beam energy from 0.4 eV to 0.7 eV. On a 1375 K surface, large, two-layer etch features were observed after approximately 20% of the surface monolayer was removed, indicating that new etch features were nucleated on the clean second layer after it was unearthed. Additional multi-layer features up to over 20 layers deep, **Figure 3.9**, were observed on the 1375 K sample after an O_2 exposure of approximately 4×10^{18} cm^{-2}. In contrast,

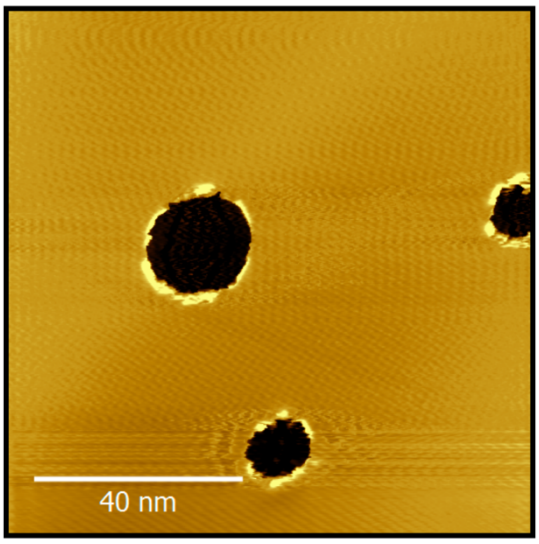


Figure 3.8: Symmetric etch pits formed on SPI-2 grade HOPG. STM image of representative etch pits formed on a sputtered SPI-2 HOPG sample after exposure to 0.7 eV O_2 at a surface temperature of 1375 K. Set point: 300 mV and 0.7 nA.

only limited two-layer etch features were observed on the 1275 K HOPG sample, even when about 30% of the surface monolayer was removed, and no etch features over 2 layers deep were observed. Thus, as with 0.4 eV oxygen, the increase in surface temperature allows new pits to nucleate on undefected graphite after the consumption of all initial surface defects. This suggests that the abstraction of carbon from the basal plane is limited by surface temperature and not dependent on incident O_2 energy.

Experiments conducted with an impinging O_2 angle of 45° from the surface normal with 1375 K surfaces suggest that the impact angle of O_2 may affect etch feature morphology while the total overall reactivity of the surface remains relatively unchanged. Exposure of 0.4 eV O_2 to an SPI-3 1375 K surface at 45° found a negligible decrease in overall reactivity to $1.1\times10^{-4} \pm 5\times10^{-5}$ compared to $2\times10^{-4} \pm 1\times10^{-4}$ with the beam directed normal to the surface. Etch pits were mostly circular as in the normal-angle case. Results from a SPI-2 surface heated to 1375 K and exposed to 0.7 eV O_2 at 45° indicate that O_2 impinging at that angle may form different etch features than normal-angle O_2. The exposed surface was dominated by the formation of faceted, monolayer-

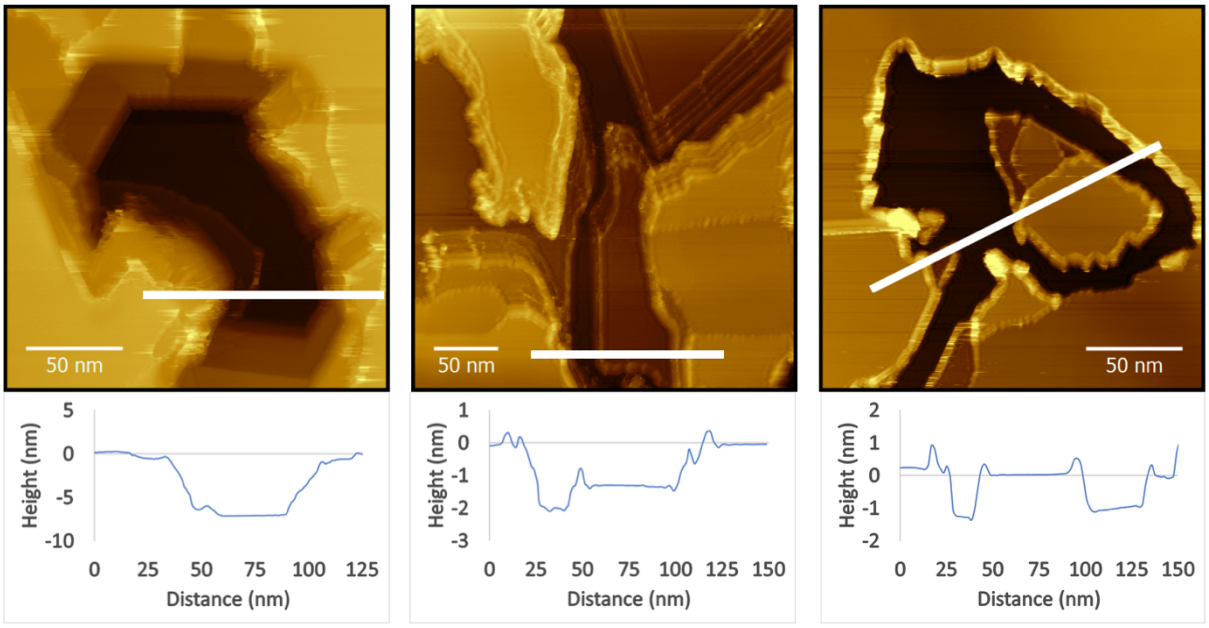


Figure 3.9: STM images of reactive multilayer etch pits. STM images of multilayer (10's of layers deep) etch pits formed on a sputtered SPI-3 HOPG sample after exposure to 0.7 eV O_2 at a surface temperature of 1375 K. Images taken at 300 mV, 0.7 nA; 100 mA, 0.7 nA; and 100 mA, 0.7 nA, respectively.

deep etch pits, shown in **Figure 3.10a**, in contrast to the circular pits found with 0.7 eV O_2 normal to a SPI-2 surface. However, more temperature-dependent studies are needed to conclusively say if and how the impingement angle affects the faceted to circular morphological transition. Interestingly, large elongated pits often nucleated on intrinsic linear defects, as shown in **Figure 3.10b**. While these lines clearly serve as nucleation sites and likely cause the pit elongation by facilitating etching along the defect, they do not form narrow channels like those found on a SPI-3 surface exposed to 0.7 eV oxygen. The measured overall reaction probability with a 1375 K SPI-2 surface exposed to 0.7 eV O_2 at a 45° impingement angle is $3\times10^{-5} \pm 1\times10^{-5}$, approximately the same as the normal angle experiment ($3\times10^{-5} \pm 1\times10^{-5}$) despite the $\sqrt{2}$ decrease in O_2 translational energy perpendicular the surface. The emergence of faceted pits at a more glancing angle might indicate slight changes in site-selective reactivity, but these differences did not cause

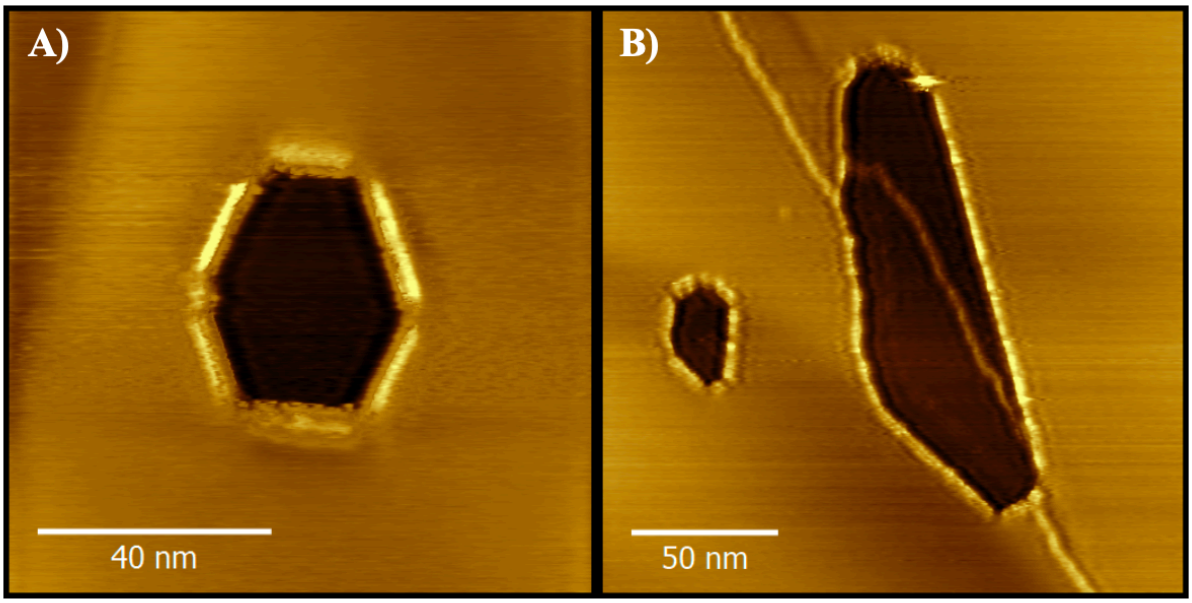


Figure 3.10: Etch pit formation resulting from O_2 impinging at 45°. Images of pits on a 1375 K SPI-2 surface exposed to 0.7 eV O_2 impinging at 45° relative to the surface plane. **A)** A faceted pit typical of those that dominated the surface. **B)** An example of a large, elongated pit that formed on a linear defect. Both images were taken at 100 mV and 0.6 nA.

a significant change in the overall rate of carbon removal from the surface. More studies need to be completed to determine the mechanistic differences between O_2 impinging at various angles.

3.4: Conclusions

We have demonstrated the efficacy of using STM and supersonic molecular beams in tandem to combine the realms of macroscopic interfacial kinetics with atomic, nano, and mesoscale morphology, allowing a more holistic examination of graphite oxidation. This novel approach allows us to directly link the time-evolving morphology of the reacting interface with the observed reaction kinetics, in essence, giving access to the spatio-temporal correlations that govern time-evolving interfacial reactivity. The results presented in this chapter have uncovered independent effects of oxygen energy, angle, and surface temperature on etching morphology, dictating the formation of hexagonal pits, circular pits, or anisotropic channels. Lower energy (0.4

eV) impinging oxygen produced pits faceted along crystallographic directions on a 1275 K surface that transitioned into circular pits with a 100 K temperature increase. Experiments with different incident angles that compared outcomes using normal versus 45 degrees found only limited kinetic and morphological changes. The reaction probability under a given set of experimental conditions remained constant as the etch features evolved, suggesting that the availability of reactive edge carbons is not the limiting factor in the oxidation rate. An increase in oxygen energy from 0.4 eV to 0.7 eV created anisotropic channels at all surface temperatures, with these features dominating the morphological landscape while other features, such as faceted, circular, and elliptical pits, still exist. Furthermore, the reaction probability increased with impinging oxygen energy, indicating a kinetically distinct process giving rise to the channels. Comparison of the relative reactivity of higher grade versus lower grade HOPG indicates that the formation of etched channels largely depends on the presence of grain boundaries. The fine control over the complete parameter space of surface temperature along with oxygen energy, angle, and flux afforded by this experimental technique has provided fresh insights into the oxidation mechanism for this important model system. Moreover, these findings are of further interest given current needs to perfect advanced carbon containing materials for high performance flight, reentry vehicles, and next generation propulsion systems that need to operate in aggressive oxidizing and high-temperature environments.

Chapter 4: Room Temperature Oxidation of GaAs(110) Using High Translational Kinetic Energy Molecular Beams of O_2 Visualized by STM

Summary

This study examines the reactive surface dynamics of GaAs(110) oxidation with molecular oxygen at room temperature over a range of impinging kinetic energies. Visualization of the surface by scanning tunneling microscopy (STM) after exposures to O_2 with kinetic energies of 0.4-1.2 eV provides morphological and kinetic data that were obtained utilizing a novel instrument that combines a supersonic molecular beam with an in-line, *in-situ* STM. Oxidation was found to proceed by two morphologically distinct, competing mechanisms: a spatially homogeneous process with randomly distributed chemisorbed oxygen atoms leading to layer-by-layer oxide growth, and a spatially heterogeneous process with oxides nucleating on structural surface defects and growing vertically and laterally with continued exposure. Both oxidation mechanisms exhibit enhanced reactivity with increasing kinetic energy. Only trace oxidation was observed with O_2 kinetic energies below 0.7 eV; a rapid increase in the rate of oxidation from 1.0-1.2 eV was found with homogeneous and heterogeneous oxidation proceeding simultaneously until full surface coverage was reached. In addition, the relative rates of the two mechanisms appear to change with O_2 kinetic energy: spatially homogeneous oxidation is expected to dominate at lower kinetic energies (<0.7 eV) while the heterogenous growth of oxide islands increasingly dominates with higher kinetic energies (≥1.0 eV). The results obtained in this study conclusively demonstrate that a heterogenous oxidation mechanism is activated on GaAs(110) at high O_2 kinetic energies, and reveal that thin oxide layers can be achieved with higher efficiency at room temperature using molecular beams of oxygen. These results provide vital information about the morphological

evolution of the surface in conjunction with the overall kinetics, and identify a controlled method of enhanced oxidation at moderate temperatures that could potentially improve abruptness at oxide interfaces and be used in the fabrication of GaAs semiconductor devices.

4.1: Introduction

III-V compound semiconductors may be the key to developing ever-faster electronic devices as silicon transistors reach their size limitations.[64] GaAs represents one of the most promising semiconductor materials due to an electron mobility five times that of silicon and a high radiation hardness valuable in aerospace and military applications such as integrated circuits and solar cells for spacecraft.[65] The performance and quality of gallium arsenide metal-oxide-semiconductor (MOS) devices depends critically on the ability to create ultra-thin oxide films on the substrate surface. Previous studies[66–73] on the oxidation of the GaAs substrate have utilized aggressive conditions involving high-temperature or electrochemical environments to overcome the low reactivity of O_2 on GaAs under ambient conditions.[74,75] Ideally, enhancement of GaAs oxidation could be achieved using relatively low surface temperatures and clean environments to maintain surface stoichiometry and reduce defects in the oxide film. A fundamental understanding of the O_2-GaAs interface is therefore required to probe new oxidation pathways of the GaAs surface and to ultimately improve the processing and manufacturing of GaAs MOS devices.

In this chapter, we present a marked enhancement of oxidation kinetics on the *p*-type GaAs(110) surface using impinging O_2 with high kinetic energies and incident angles oriented normal or 45° to the surface. We have utilized a unique approach to studying interfacial reaction dynamics by visualizing the oxidation of a *p*-type GaAs(110) surface at room temperature with energy- and angle-selected O_2 using a combination of supersonic molecular beam and ultra-high vacuum scanning tunneling microscopy (STM) techniques. This experimental approach has been used previously to successfully answer questions about the site-specific reactivity of O_2 on Si(111)-7x7[40] and HOPG[76] surfaces. The combination of supersonic molecular beam and STM techniques links time-evolving morphologies to reaction kinetics, providing spatio-temporal

correlations that govern the reactivity of surface reactions. By visualizing micrometer to sub-nanometer length-scales over time as oxidation proceeds, we have monitored the oxidation process from its initial phases to the formation of large-scale oxides on the surface. These results demonstrate two simultaneous oxidation mechanisms with distinct spatial distributions: the homogenous accumulation of randomly dispersed chemisorbed oxygen atoms as well as the heterogenous nucleation of oxide islands near defects.

Molecular oxygen starts to dissociatively chemisorb on the GaAs(110) surface at temperatures above 60 K.[77] The initial sticking coefficient for thermally dosed O_2 on a clean GaAs(110) surface is 2×10^{-5}, with oxygen initially adsorbing at a linear rate followed by a quasi-logarithmic uptake with continued exposure.[75] Results from AES and XPS studies indicate that the initial chemisorption (~3×10^5 L; 1 L = 10^{-6} Torr sec) of O_2 is slow and only increases the surface coverage to $\Theta = 0.05–0.1$ depending on the amount of surface defects present.[78] The main oxygen uptake onto the surface proceeds *via* activated adsorption followed by field-assisted growth of an oxide phase;[79–82] the formation of subsurface oxides is still disputed.[83–85] Subsequent oxidation appears to be layer-by-layer[79–81] and has been described by the Mott-Cabrera mechanism,[86] a phenomenon in which an electric field assists the oxidation process *via* electrons tunneling through the oxide film.[82] While the initial oxidation is generally assumed to be spatially homogeneous across the surface, there is some indication of spatially inhomogeneous oxidation with oxide islands nucleating on defects.[83,84]

Numerous AES and photoemission studies[87–92] have addressed the bonding coordination of the adsorbed oxygen, with results indicating varying bonding geometries during different stages of the oxidation process. At high oxygen coverages, experimental[83–85] and theoretical evidence[93] indicates O atoms are multicoordinated about equally between Ga and As atoms. In the initial

oxidation regime, conflicting evidence supports preferential bonding to surface As[88,94,95] and Ga[78,84,96,97] atoms, as well as bonding in bridge-bond positions with coordination to both Ga and As.[90,98] Experimental and theoretical studies on multiple GaAs(100) surfaces have demonstrated that the bonding of oxygen to surface Ga atoms is thermodynamically favored over bonding to surface As atoms.[99–101]

STM imaging of the clean GaAs(110) surface exhibits atom-selective behavior in which positive sample biases with respect to the STM tip (unoccupied surface state imaging) visualize the Ga atoms while negative sample biases (occupied surface state imaging) visualize the As atoms.[102] Investigations using STM have demonstrated spatially homogeneous oxidation with the stochastic appearance of scattered oxidized sites on the GaAs(110) surface,[98,103] while the spatially heterogenous nucleation and growth of oxide islands has also been observed by STM on the GaAs(100) surface.[104] The presence of spatially homogeneous chemisorbed oxygen atoms on a *p*-type GaAs(110) surface was found on defect-free terraces as shown by subsequent imaging in the same ~225 nm^2 area after exposure, and the imaging suggests that the chemisorbed oxygen sits in an interchain bridging site aligned in the $[1\bar{1}0]$ direction with respect to the surface As atoms.[98] The chemisorbed O atoms demonstrate slight variations in topographical height and width with changes in imaging conditions but always appear as small isolated protrusions on the surface with a lateral size of 4-6 Å at full-width half-maximum (FWHM) on a *p*-type sample. This differs significantly from the delocalized nature of oxygen adsorbates on an *n*-type sample that results from the negatively-charged nature of the chemisorbed O atom, as opposed to the neutral adsorbates on *p*-type samples.[103,105] Spatially heterogenous oxidation was observed on a *n*-type GaAs(100) surface, with nucleation centers growing to cover the surface in a manner similar to the oxidation mechanism found on InP.[104,106] 100 nm × 100 nm STM images of the surface with

continued exposure to air revealed the nucleation of oxide islands, which grew laterally to cover the surface in a uniform oxide layer ~2 nm thick. This stands in contrast with previous findings indicating that GaAs oxidation is homogenous across the surface and proceeds layer-by-layer.

The results of this chapter will detail the reactive oxidation of a GaAs(110) sample at room temperature using high kinetic energy impinging O_2 while visualizing the corresponding morphological evolution of the surface during exposures. By employing a combination of molecular beam and STM techniques, we have explored the energetic barriers to reaction using monoenergetic O_2 and have illustrated two kinetically and morphologically distinct mechanisms of oxide growth: the heterogeneous nucleation and growth of oxide-islands at O_2 kinetic energies ≥1.0 eV, and the homogenous accumulation of randomly distributed oxidized sites leading to layer-by-layer oxide growth. Characterization of the kinetics and surface evolution of both modes of oxide formation will be detailed, and a comprehensive overview of the high kinetic energy oxidation of the GaAs(110) surface will be presented.

4.2: Experimental

The results reported here were obtained using a new UHV instrument combining supersonic molecular beam and STM/AFM techniques. The instrument is composed of a triply differentially pumped beamline, a surface preparation/characterization chamber, and an SPM chamber containing a variable temperature SPM based on the ultra-stable design of Shuheng Pan, built in collaboration with RHK. As described in previous publications,[40,76] the custom-built Pan STM has been designed with the surface plane vertical such that the sample can be exposed to the supersonic molecular beam with the STM tip still in contact, and includes the capability for exploring variable angles of incidence. This unique configuration and the high stability of the

microscope allow given nanoscopic areas to be revisited after exposure to the molecular beam, tracking the progression of surface oxidation over time.

Supersonic molecular beams were generated by the expansion of a 5% O_2/95% He gas mixture through a 30 μm molybdenum pinhole at pressures from 20-80 psi and nozzle temperatures ranging from 300-975 K (± 5%). The translational kinetic energy of the molecular beam at each nozzle temperature was measured using time-of-flight (TOF), and values of 0.38 ± 0.04 eV, 0.73 ± 0.08 eV, 0.97 ± 0.15 eV, 1.10 ± 0.12 eV, and 1.22 ± 0.17 eV were found for nozzle temperatures of 300, 575, 775, 875, and 975 K, respectively. The uncertainty values in these energies represent the FWHM of each energy distribution. The molecular beam flux for all beam conditions was on the order of 10^{13} O_2 molecules cm^{-2} s^{-1}, as determined by the King and Wells method.[107] The GaAs(110) sample was positioned in the SPM chamber during exposures, with a 4 mm diameter beam spot on the crystal. The sample was held at room temperature for all experiments and the surface plane was oriented either normal or at 45° with respect to the impinging beam. The kinetic energy of oxygen in each beam therefore exceeds the thermal energy of the room temperature surface by over an order of magnitude. Imaging was performed between beam exposures. Same-spot visualization experiments, whereby the same set of atoms could be revisited after exposure to high kinetic energy O_2, were completed by moving the STM tip laterally multiple micrometers downrange (away from the O_2 beam) from the reference area during each exposure to mitigate tip shadowing while keeping the tip in contact with the surface. The STM tip was then moved back to the reference area after the exposure and the set of reference atoms were located using topographical markers on the surface. Only areas of the sample with direct line of sight to the beam were reacted after exposure, confirming that thermalized O_2 reflected from the STM tip and/or chamber did not significantly affect the oxidation of the surface.

GaAs(110) crystals (*p*-type Zn-doped, VGF grown, MTI Corporation) were used for all experiments, and were cut into approximately 5 mm × 1 cm strips for appropriate fit onto the sample mounts. Samples were cleaned in a UHV chamber ($<5\times10^{-11}$ Torr base pressure) by repeated cycles of ion sputtering at room temperature using 0.5-1.0 keV Ar^+ ions followed by subsequent annealing at 700 K ± 30 K to form the well-ordered GaAs(110) surface.[108–110] The surface was heated by applying current directly through the sample and the temperature was monitored using a Mikron infrared pyrometer ($\varepsilon = 0.69$) during the annealing process. An ion flux of ~7 μA/cm^2 was measured during the sputtering cycles. STM images were taken using etched or cut $Pt_{0.8}Ir_{0.2}$ tips.

4.3: Results and Discussion

A representative clean GaAs(110) surface as imaged by STM is shown in **Figure 4.1**, which was achieved after multiple cycles of ion sputtering with 0.5-1.0 keV Ar^+ ions and subsequent annealing to ~700 K. **Figure 4.1A** demonstrates both the overall terrace size and topography of the surface on a larger, mesoscopic scale. **Figure 4.1B** and **4.1C** illustrate the row structure on the terraces, along with individual bright site surface defects. The observed row structure in the nanoscopic images matches the expected periodicity of the GaAs(110) surface, scales appropriately with images of different sizes, and does not change with varying scanning conditions.

No significant oxidation was observed with exposures up to 6×10^{17} cm^{-2} using O_2 with kinetic energies of 0.4 eV, while 0.7 eV O_2 demonstrated only minimal surface oxidation. A critical threshold in reactivity was reached around 1.0 eV, as shown in **Figure 4.2**. After this point, reactivity increased at a greater than linear rate with kinetic energy, reaching a value at 1.2 eV

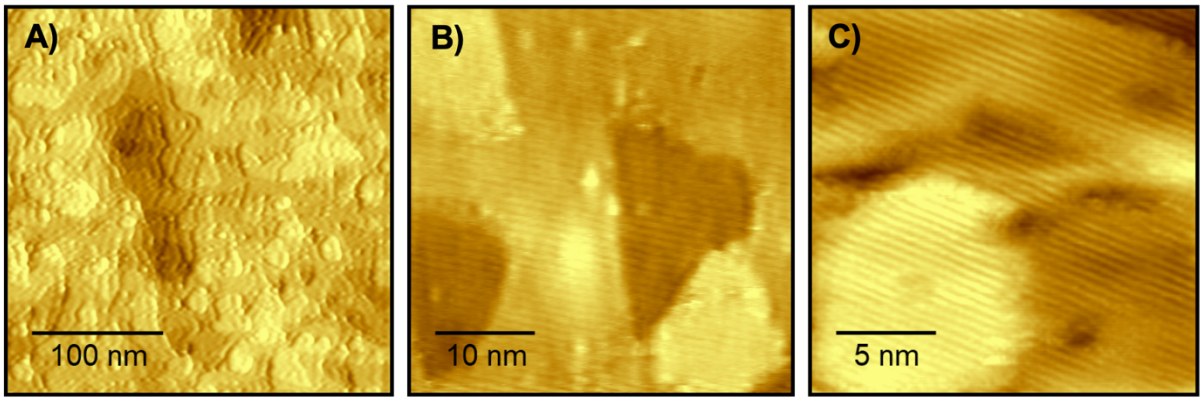


Figure 4.1: Representative STM images of the GaAs(110) surface. A) 300 nm × 300 nm (-2.8 V, -0.6 nA), **B)** 40 nm × 40 nm (2.8 V, 0.6 nA), and **C)** 20 nm × 20 nm (-3.0 V, -0.3 nA) STM images of representative clean GaAs(110) surfaces obtained after multiple sputter/anneal cycles. The terrace sizes and overall roughness of the surface are illustrated in **A)**, while the row structure can be seen running horizontally (and slightly down moving left to right) across **B)** and **C)**, along with the presence of natural bright site defects.

about four orders of magnitude higher than what has been observed previously with background exposure to room temperature oxygen.[74] The observed increase in reactivity is likely due in large part to the activation of the heterogenous oxidation mechanism with oxygen energies ≥0.7 eV. As shown in **Figure 4.3**, STM imaging has revealed the nucleation and growth of "oxide islands" after exposure to ~7×10^{16} cm^{-2} of 0.7 eV O_2 normal to the surface that appear to nucleate on or near pit defects. The oxide islands have a height profile of ~5-10 Å above the surface with both positive and negative scanning bias, consistent with a thin oxide film.[111,112] The oxide islands completely replace the row structure seen on clean terraces and are morphologically distinct from the clean GaAs(110) surface. Given that the surface in all cases was dominated by such ~5-10 Å tall oxide islands, the reactivity shown in **Figure 4.2** was calculated by approximating the fully oxidized surface as consisting of a uniform 10 Å thick sheet of β-Ga_2O_3, as any As_2O_3 formed at the interface with GaAs is expected to react to form Ga_2O_3 and As.[113] This 10 Å thickness value represents an upper bound on the probable thickness of the oxide layer at full coverage. Reaction probability per impinging O_2 molecule, P, is then given by

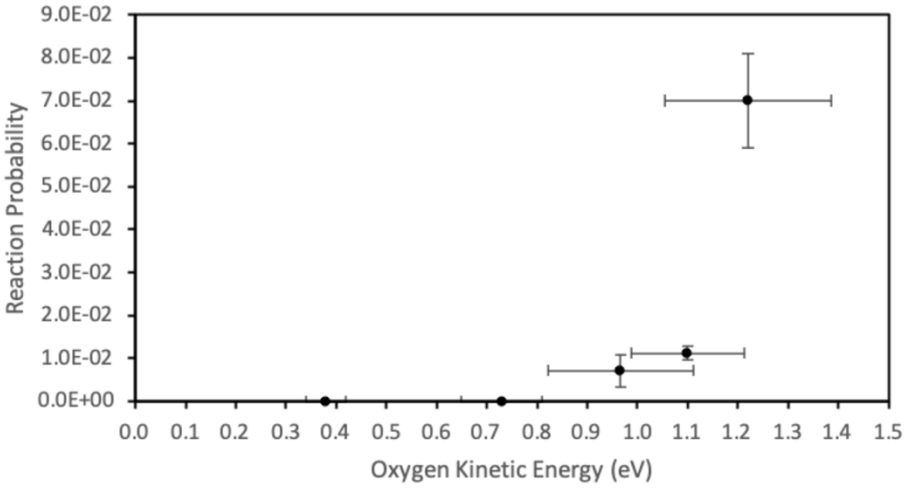


Figure 4.2: GaAs(110) reactivity dependence on O_2 kinetic energy. Overall reaction probability vs O_2 kinetic energy for exposure to oxygen impinging normal to the surface with kinetic energies between 0.4 eV and 1.2 eV. Reactivity sharply increases after a critical threshold energy is reached between 0.7 eV and 1.0 eV, showing a nonlinear relationship between O_2 energy and reactivity. The horizontal error bars are derived from the TOF measurements at each beam energy to show the width of the distribution of O_2 kinetic energies.

$$P = \frac{3\,h\,N_A \rho_{Ga_2O_3}}{2\,M_{Ga_2O_3} \Phi_{O_2} t}, \qquad \textbf{(E4-3)}$$

for oxide thickness $h = 10$ Å, density $\rho_{Ga_2O_3}$, Avogadro's number N_A, molar mass $M_{Ga_2O_3}$, stoichiometric factor $\frac{3}{2}$, flux of impinging oxygen Φ_{O_2}, and time to fully oxidize the surface t. The reaction probability is therefore here defined as the ratio of the number of impinging O_2 molecules that contribute to the 10 Å thick oxide layer to the total fluence of O_2 molecules. This calculation allows a reasonable comparison of relative reactivities in order to determine the effect of impinging O_2 energy on the reactivity of the GaAs(110) surface.

Infrequent oxide islands grew to a maximum area on the order of 10^4 nm^2 with exposures up to 5×10^{17} cm^{-2} of 0.7 eV oxygen, and cumulatively covered a very small percentage of the surface. At higher energies (≥1.0 eV), the islands expanded laterally with continued exposure until they consumed the entire surface. In some cases, islands grew vertically as well as laterally, with

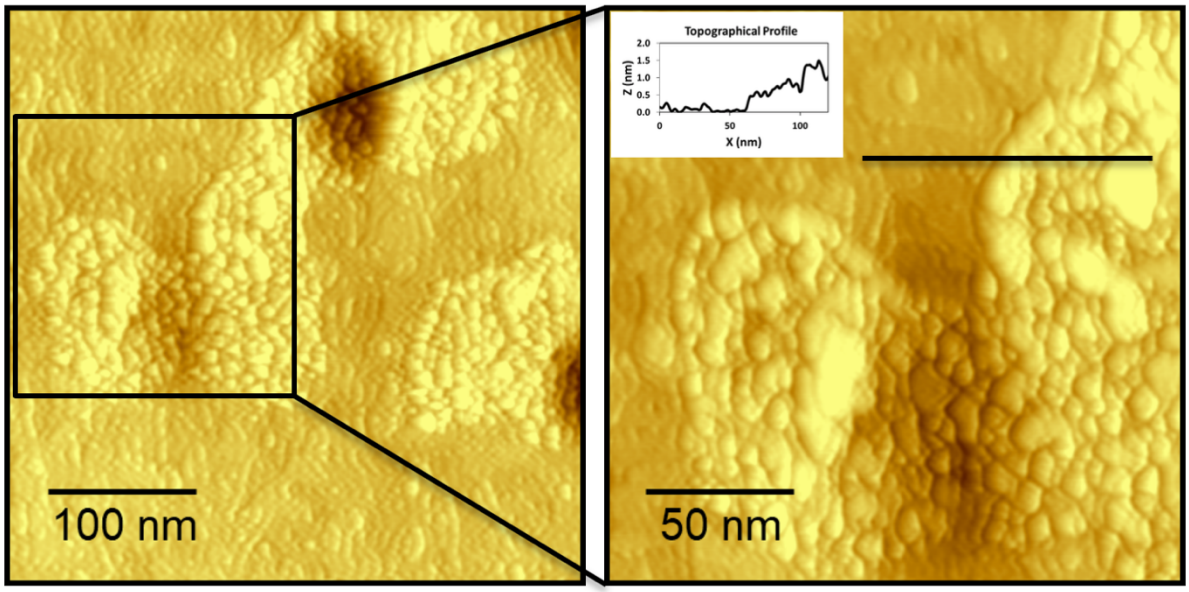


Figure 4.3: STM image of representative GaAs(110) oxide island. A 400 nm × 400 nm STM image (-2.0 V, -0.6 nA) of an oxide island on a GaAs(110) surface after exposure to ~7×10^{16} cm^{-2} of 0.7 eV kinetic energy O_2 with a magnified image (200 × 200 nm; -2.0 V, -0.6 nA) showing a more detailed view of the same area. The topographical profile on the magnified image demonstrates the corrugation and height of the oxide island. Spatially heterogeneous oxidation creates patches of oxide that nucleate on surface defects, such as the pit shown here, and grow laterally to cover the surface with further oxygen exposure.

STM visualization revealing the presence of tall, multilayer oxide islands spanning >1 μm in diameter, such as the one shown in **Figure 4.4**. The dramatic vertical growth of these islands likely indicates multilayer/subsurface oxidation near intrinsic large-scale surface defects (*i.e* microfissures, dislocations, *etc.*) as previously suggested in the literature,[84] which then cause the surface to "blister" as a result of the lattice expansion resulting from the formation of subsurface Ga_2O_3 and/or As_2O_3. **Figure 4.5** shows the uplift of clean GaAs terraces after exposure to 1.2 eV oxygen, possibly as a result of subsurface oxidation. This area of the surface is adjacent to a large-scale surface defect, which comports with the idea that subsurface oxidation occurs through the exploitation of deep surface fissures. This blistering mechanism explains the vertical growth of the islands without the need for mass transport of gallium and arsenic atoms, which at room temperature would be too slow to represent a realistic possibility.

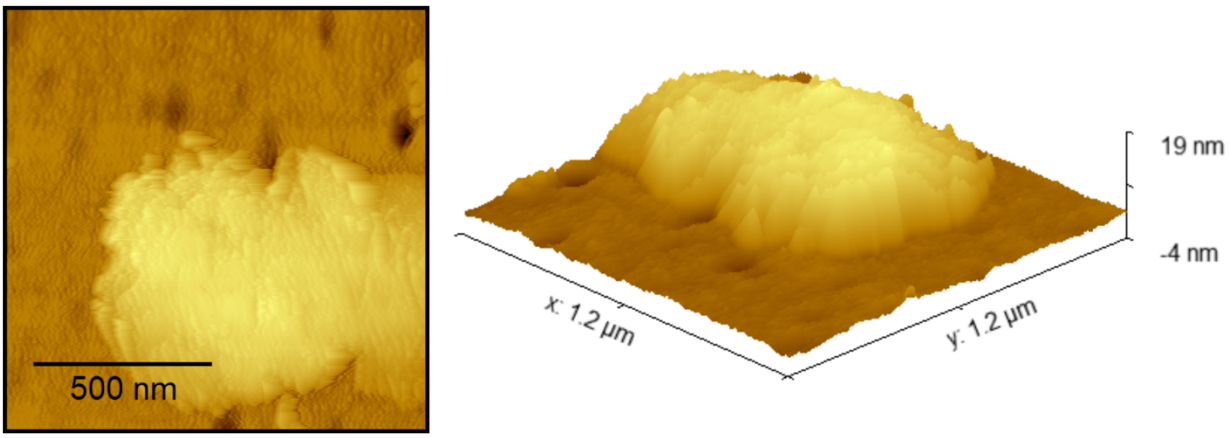


Figure 4.4: Visualization of dramatic vertical growth of GaAs(110) oxide island. A 1.2 µm × 1.2 µm image (-2.8 V, -0.6 nA) STM image of an elevated oxide island on a GaAs(110) surface formed after a total exposure of ~1×10^{17} cm^{-2} of O_2 with a kinetic energy of 1.0 eV. A 3D representation of the STM image is shown at right to emphasize the height and roughness of the oxide island. The high vertical elevation of such islands may indicate subsurface oxidation and "blistering" of the surface.

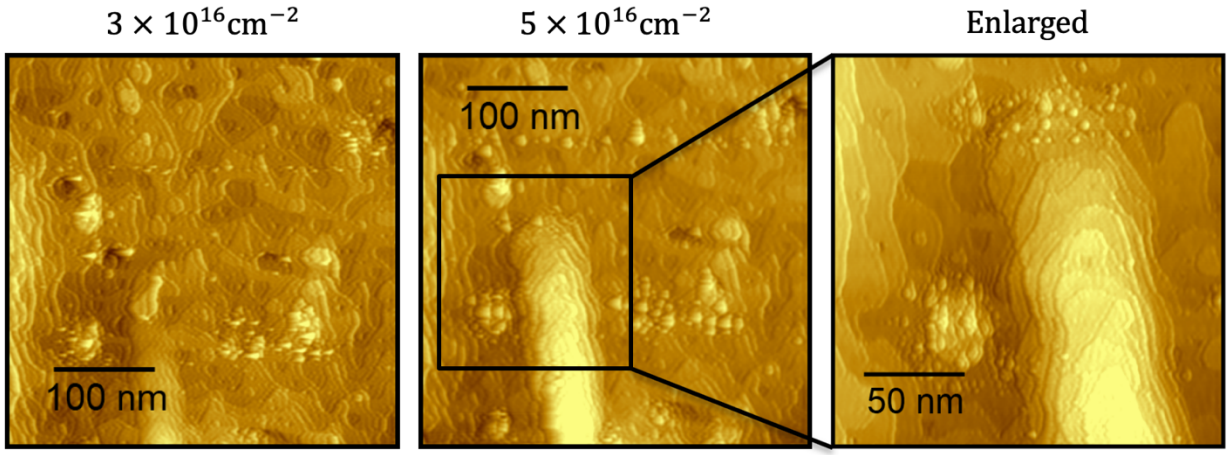


Figure 4.5: STM visualization of terrace elevation. Sequential STM images (-2.8 V, -0.6 A) in the same local area illustrating the elevation of clean terraces on a room temperature GaAs(110) surface after exposure to 1.2 eV O_2 impinging 45° from normal to the surface. Two 400 nm × 400 nm images show the area after 3×10^{16} O_2 exposure (left) and after 5×10^{16} O_2 exposure (center). The morphological change is likely due to subsurface oxidation and subsequent lattice expansion resulting in the "blistering" of the surface. The magnified 200 nm × 200 nm image at right highlights the raised terraces seen in the middle image.

Using our unique ability to monitor a single nanoscopic area while it is exposed to high energy oxygen, we have directly observed the growth of oxide islands with exposure to 1.2 eV O_2 impinging at a 45° angle (0.8 eV kinetic energy normal to the surface) as shown in **Figure 4.6**, providing explicit evidence of the spatially heterogeneous oxidation mechanism. This figure

illustrates representative examples of the spatially heterogeneous growth of patches of oxide in otherwise clean areas on the GaAs surface. Each set of images shows a single nanoscopic area as it is exposed to oxygen, demonstrating spatially heterogeneous oxide islands nucleating near defects and growing across the surface. There is a sharp divide between oxidized and unoxidized areas in these images, with the terraces not overtaken by oxide islands remaining clean. These images demonstrate conclusively that the heterogenous oxidation mechanism is activated at high

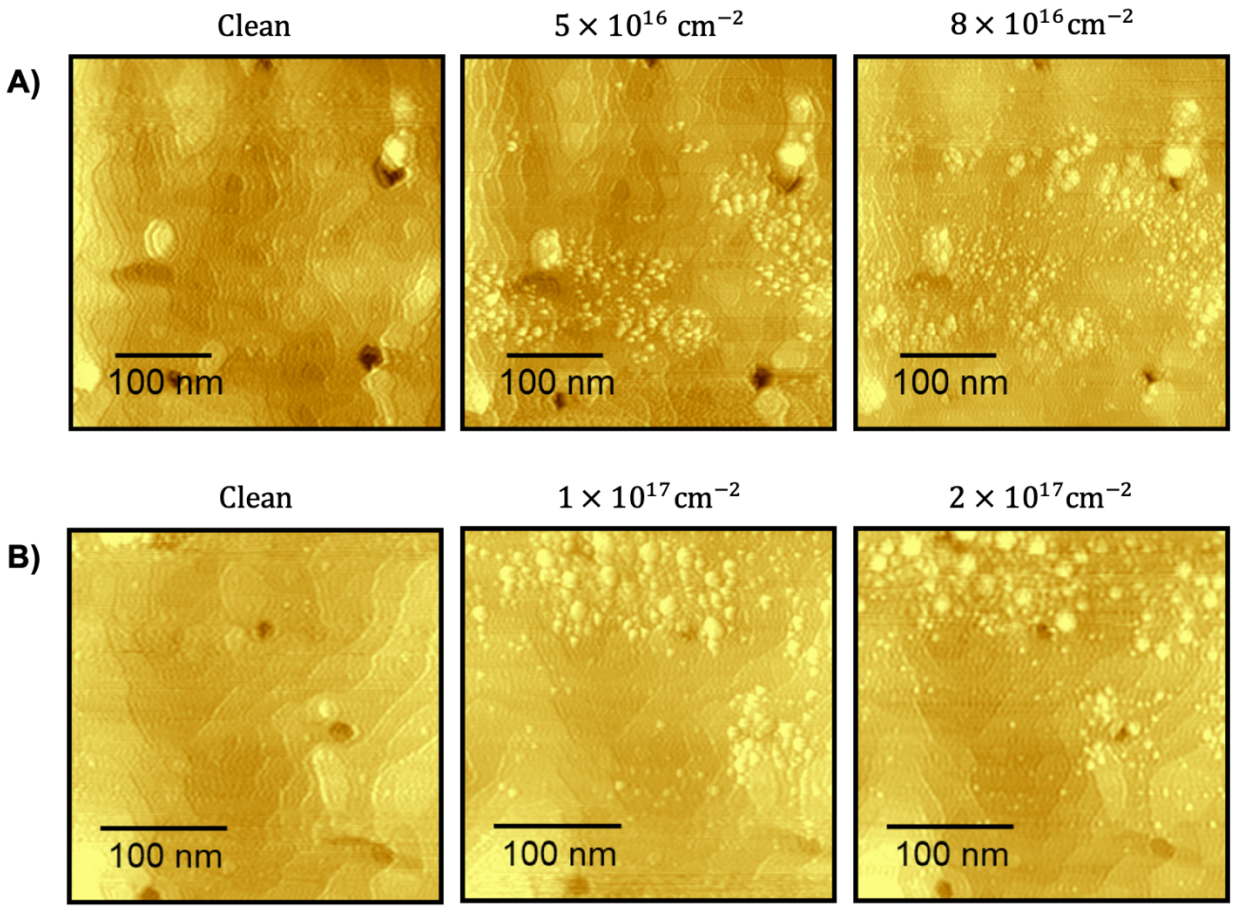


Figure 4.6: Same-spot STM imaging of oxide formation on the GaAs(110) surface. Multiple examples of sequential STM images (-2.8 V, -0.6 A) in which the same local area is revisited after each exposure, directly demonstrating the growth of spatially heterogeneous oxide structures on a room temperature GaAs(110) surface with exposure to 1.2 eV O_2 impinging 45° from normal to the surface. Total exposures of O_2 are given above each STM image. **A)** A sequence of 400 nm × 400 nm images in a single area. **B)** A sequence of 300 nm × 300 nm images in another area with longer exposures. Both **A)** and **B)** demonstrate the emergence of spatially heterogeneous oxide patches (seen as clusters of large bright features on the surface) while nearby terraces remain largely unoxidized.

oxygen energies, with oxide islands nucleating and growing laterally across the surface while surrounding areas remain unoxidized.

STM imaging with a variety of different surface bias values indicates that the observed elevation of the oxide islands is reflective of the surface topography, not electronic effects. The exact coordination of the chemisorbed oxygen atoms within the oxide cannot be determined by STM, but due to the inherent instability of the GaAs-As_2O_3 interface, the oxides are assumed to largely consist of Ga_2O_3.[113] The observed spatial heterogeneity suggests that the activated dissociative chemisorption of the high kinetic energy O_2 is favored on intrinsic surface defect sites, consistent with previous findings.[83,84] Subsequent three-dimensional oxide growth might then occur at these nucleation sites, which would lead to the formation of the spatially heterogeneous oxide islands. The results of this study conclusively demonstrate the activation of a distinct heterogeneous oxidation process, adding to the knowledge base on the oxidation of this important electronic material.

Although heterogenous oxidation is the dominant mechanism at high oxygen kinetic energies, the homogenous mechanism was also found to occur simultaneously, indicating competition between the two mechanisms. Representative examples of a surface before and after exposure to normal-angle 1.0 eV O_2 are shown in **Figure 4.7**, with the randomly distributed bright features corresponding to individual oxidized sites.[98] An analysis of the x and y coordinates of the bright protrusions in seven 40 nm × 40 nm images of a surface exposed to 4×10^{17} cm^2 of 1.0 eV oxygen, including the one shown in **Figure 4.7B,** finds an average nearest neighbor separation of 2.2 ± 0.1 nm, which matches the separation of 2.2 ± 0.1 nm expected for a stochastic process once the presence of image boundaries is taken into consideration.[114] The density of oxidized sites grows linearly with exposure, as shown in **Figure 4.8** for exposure to 1.1 eV oxygen. The slope of this

plot corresponds to the reaction probability of the homogenous mechanism at this oxygen kinetic energy. The linear trend therefore indicates a constant reaction probability with exposure, suggesting that in the low coverage limit, the homogeneous chemisorption of oxygen atoms to the GaAs(110) surface does not affect the subsequent reactivity of the surrounding surface sites. The spatially homogeneous oxidation mechanism therefore represents a stochastic process in the low coverage limit whereby oxygen molecules dissociatively chemisorb on unreacted surface sites with

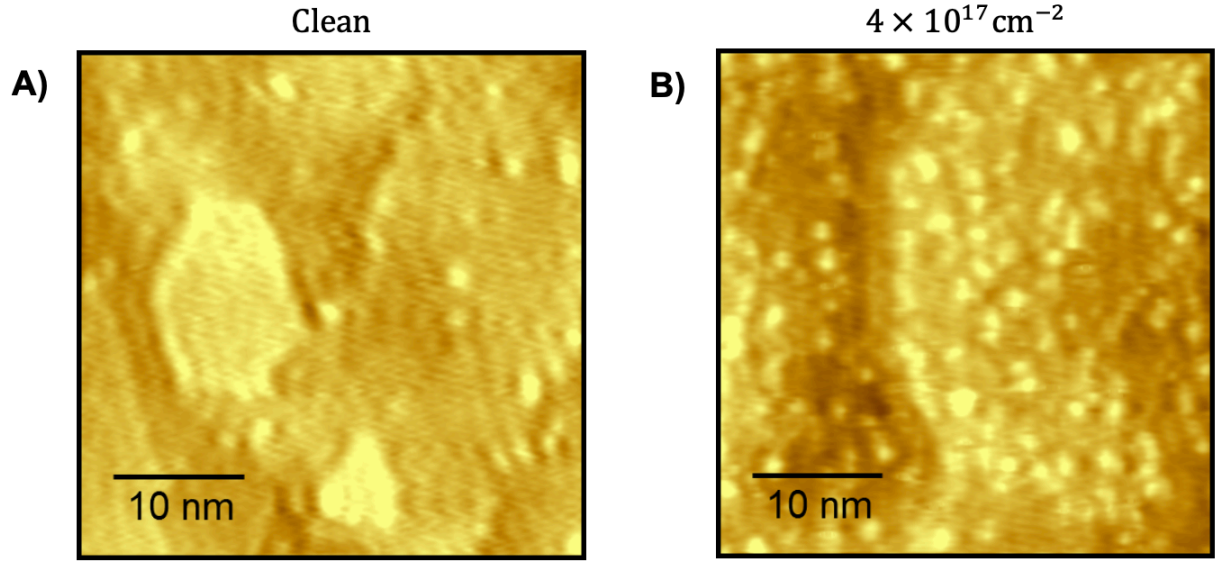


Figure 4.7: Representative STM images of homogenous oxidation. STM images in different local areas of the surface, representative of the **A)** clean GaAs(110) surface (40 nm × 40 nm; -3.0 V, -0.6 nA) and **B)** a surface after exposure to ~4×10^{17} cm^{-2} of O_2 with a kinetic energy of 1.0 eV (40 nm × 40nm, -2.0 V, -0.6 nA). Comparison of these two images demonstrates the difference in the density of chemisorbed oxygen atoms (the bright protrusions) before and after exposure to 1.0 eV O_2 as the surface undergoes homogeneous oxidation. The spacing between nearest neighbors matches that of a stochastic process, indicating that the presence of the oxidized sites does not significantly affect the reactivity of surrounding surface atoms.

a constant reaction probability. The reaction probability of the homogeneous oxidation mechanism at higher coverages could not be measured due to the complete consumption of the surface in an oxide layer resulting from the kinetically dominant heterogeneous oxidation process.

Measurements of oxide formation with oxygen impinging normal to the GaAs(110) surface demonstrate that increasing O_2 kinetic energy greatly enhances the reactivity of both the spatially heterogeneous and homogeneous mechanisms of oxidation above the observed energy threshold

of 0.7-1.0 eV. The comparative kinetics for the heterogeneous and homogeneous oxidation mechanisms are plotted in **Figure 4.9** for impinging O_2 energies from 1.0-1.2 eV; this plot demonstrates the strong correlation for both mechanisms between impinging O_2 kinetic energy and the reactivity of a room temperature GaAs(110) surface. The heterogeneous reaction probability was calculated indirectly by subtracting the contribution of the homogeneous mechanism from the overall reaction probability. The figure demonstrates that the fast kinetics of the heterogeneous mechanism completely dominate surface oxidation at O_2 kinetic energies ≥1.0

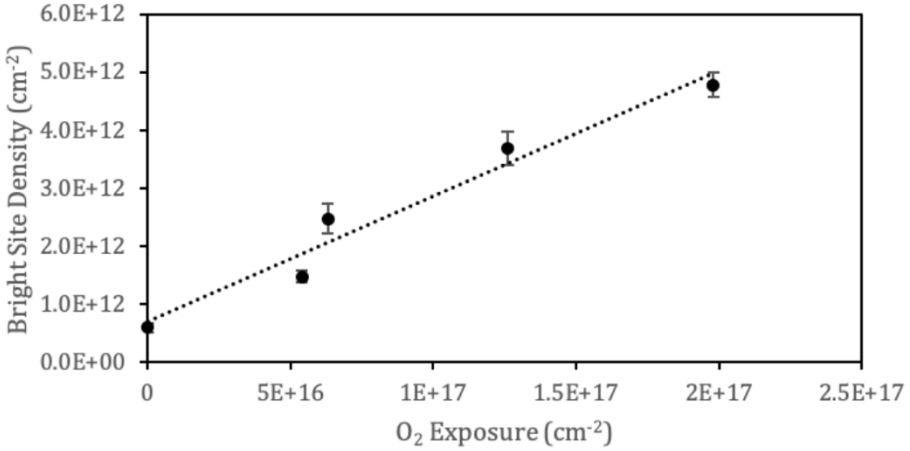


Figure 4.8: Homogeneous oxidation reactivity plot. A reactivity plot demonstrating the increasing areal density of homogeneous oxidation sites on a room temperature GaAs(110) surface after continued exposure to O_2 with a kinetic energy of 1.1 eV. The slope of the linear fit represents the probability of an O_2 molecule colliding with the GaAs(110) surface and forming an individual bright protrusion as imaged by STM. The linearity of the fit indicates that oxidized sites do not influence the reactivity of the surface to subsequent oxidation in the low coverage limit.

eV. The homogeneous oxidation reaction rate also increases with increasing O_2 kinetic energy, similar to the heterogeneous reaction rate, but the values for the reaction probability of the homogeneous mechanism at each energy are 3-4 orders of magnitude lower than those of the heterogeneous growth mechanism. The dominant oxidation mechanism at high oxygen energies is therefore the heterogenous nucleation of oxide islands on surface defects that grow laterally to

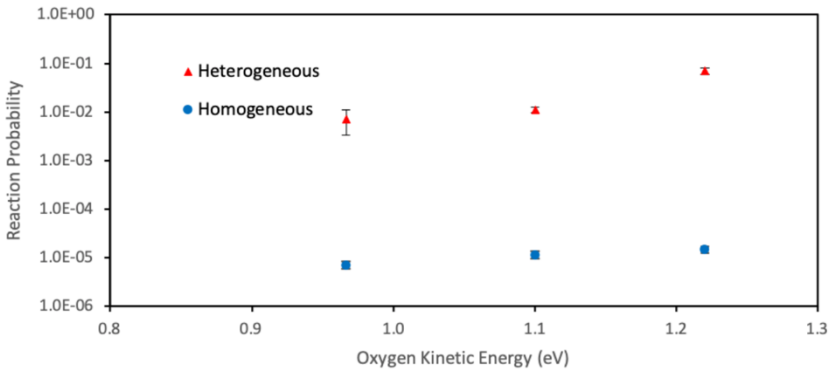


Figure 4.9: Heterogeneous and homogeneous comparative reactivity. A reactivity plot illustrating the O_2 impinging kinetic energy dependence of the reaction probabilities of the heterogeneous and homogeneous oxidation mechanisms on a room temperature GaAs(110) surface. The data show that the reactivities of both mechanisms increase with oxygen kinetic energy, and that the heterogeneous mechanism dominates over the homogenous mechanism at each energy. The reaction probability is plotted on a logarithmic scale on the y-axis, and is calculated as the ratio of the number of individual bright oxidized sites to the total number of O_2 collisions for the homogeneous mechanism, and as ratio of the number of impinging O_2 molecules that contribute to a 10 Å thick oxide layer to the total fluence of O_2 molecules (minus the contribution of the homogeneous mechanism) for the heterogeneous mechanism.

consume the surface, outcompeting the homogenous accumulation of oxidized sites and subsequent layer-by-layer growth.

4.4: Conclusions

The results of this study demonstrate the enhanced oxidation of a room temperature GaAs(110) surface using impinging O_2 with high kinetic energies (≥1.0 eV), representing an enhanced method of oxidizing a GaAs surface at moderate temperatures. Surface dynamics and energetic dependencies at the atomic scale were examined by monitoring the *in-situ* evolution of the GaAs(110) surface during exposures to tightly controlled energy- and angle-selected O_2. Increasing the kinetic energy of the impinging O_2 dramatically increases the probability for dissociative chemisorption, while also markedly altering the morphology of the resulting oxides. Oxidation proceeds through multiple competing mechanisms, with the dominant oxidation

mechanism dependent upon the incident O_2 kinetic energy. While the homogenous mechanism with randomly distributed oxidized sites leading to layer-by-layer growth is expected to dominate at low oxygen kinetic energies, at high kinetic energies the heterogenous mechanism dominates, with oxide islands nucleating on surface defects and growing laterally and vertically. Results suggest that the oxide islands can be physically uplifted by subsurface oxidation that nucleates at defect sites and induces lattice expansion that forces the surface to grow vertically in a "blistering" fashion. Homogeneous oxidation was observed occurring simultaneously but at a lower rate, resulting in the domination of the heterogeneous mechanism. The heterogeneous formation and growth of oxide islands was observed at all impinging O_2 kinetic energies at or above 1.0 eV, with the reaction probabilities of both mechanisms increasing with oxygen kinetic energy. The results of this study reveal spatio-temporal correlations that link the varying oxidation kinetics on the GaAs(110) surface to specific surface morphologies on a broad range of length scales. This provides new insight into the initial oxidation stages of GaAs surfaces that is vital to better controlling oxidation during material processing, represents a possible method of creating crucial ultra-thin oxide films with enhanced efficiency at lower surface temperatures, and offers a potential route to enabling a high degree of interfacial abruptness. A greater understanding of the dynamics of GaAs oxidation holds the potential for new techniques allowing passivation and modification of GaAs at moderate surface temperatures for the effective manufacturing and optimal functioning of this high-performance semiconductor.

Chapter 5: STM Visualization of N_2 Dissociative Chemisorption on Ru(0001) at High Impinging Kinetic Energies

Summary

This chapter examines the reactive surface dynamics of energy- and angle-selected N_2 dissociation on a clean Ru(0001) surface. Presented herein are the first STM images of highly energetic N_2 dissociation on terrace sites utilizing a novel UHV instrument that combines a supersonic molecular beam with an *in-situ* STM that is in-line with the molecular beam. Results of the study demonstrate that increasing kinetic and vibrational energy of the impinging N_2 activates and increases the sticking probability on terrace sites, matching previous experimental results. Atomically-resolved visualization of individual N_2 dissociation events elucidates the fundamental reactive dynamics of the N_2/Ru(0001) system by providing a detailed understanding of many important properties: the distance and angle between previously paired nitrogen atoms, site-specificity and coordination of binding on terrace sites, and the local evolution of surrounding nanoscopic areas. These properties are precisely measured over a range of impinging N_2 kinetic energies and angles, revealing previously unattainable information about the energy dissipation channels that govern the reactivity of the system. The preliminary results presented in this chapter will provide critical experimental insight into the fundamental N_2 dissociation mechanism that, in conjunction with theoretical modeling, will help determine the role of important dynamical processes such as energy transfer to surface phonons and nonadiabatic excitation of electron-hole pairs (ehps). These results will not only help uncover the underlying chemistry and physics that give rise to the unique behavior of this activated dissociative chemisorption system but represent an exciting new approach to understanding non-traditional gas-surface reactive dynamics.

5.1: Introduction

The interaction of gaseous species on ruthenium surfaces has been studied extensively due to the importance of ruthenium as a catalyst for a wide variety of applications.[115,116] Notably, Ru-based systems represent an important class of potential second-generation catalysts for synthetic ammonia production through the Haber-Bosch process, due to the higher activity under milder conditions of ruthenium as compared to iron catalysts.[117–124] The rate limiting step of this process is the dissociative chemisorption of N_2,[125] due to the high amounts of energy required to break its strong triple bond. A fundamental understanding of N_2 dissociation onto ruthenium surfaces is therefore of great technological and economic importance.

In addition to its relevance to ammonia synthesis, N_2 dissociation onto Ru(0001) is a prototypical activated dissociative chemisorption process, and understanding the mechanistic features of this process would have a considerable impact on the field of heterogeneous catalysis. Compared to other activated dissociation benchmark systems–namely H_2 on Cu[126,127] or CH_4 on transition metals–that have dissociation probabilities (s_0) that approach unity at normal incident kinetic energies (E_N) much greater than the potential barrier (V^*),[128,129] N_2 exhibits substantially different adsorption behavior, demonstrating $s_0 \ll 1$ at $E_N \gg V^*$.[130–132] Nonadiabatic coupling/tunneling mechanisms[130,133–138] and energy transfer to surface phonons,[139,140] along with theoretical formulations using only adiabatic treatments,[141–143] have all been proposed to describe the odd dissociation behavior of N_2 on Ru(0001). Further experimental work is required to answer questions that remain about the fundamental reactive surface dynamics of this important system.

In this chapter, I will present preliminary results detailing the reactive dynamics of N_2 on a clean, room temperature Ru(0001) surface. Atomically-resolved visualization of individual dissociation events at different impinging energies and angles provide a detailed understanding of

the spacing and angle of previously paired nitrogen atoms, site-specificity of terrace binding, and local, nanoscopic information about the reactive evolution of the Ru(0001) surface in the low-coverage regime. In conjunction with theoretical studies, these results will reveal detailed insight into the role of both energy transfer to surface phonons and nonadiabatic coupling to ehps during the dissociation event. By monitoring the nanoscopic evolution of the Ru(0001) surface during exposure to energy- and angle-selected N_2, this work elucidates previously unattainable information about the mechanisms of energy dissipation into the surface of this important gas-surface interface, and more generally represents a powerful new approach to exploring fundamental reactive surface dynamics.

The dissociation probability of N_2 on a clean Ru(0001) surface under ambient conditions is very low ($s_0 \approx 10^{-12}$),[144–146] due to a high activation barrier that occurs late in the dissociation process and requires significant stretching of the N_2 bond.[131,135,143,147] Thermal sticking occurs exclusively at crystal steps, due to a 1.5 eV difference between the activation barrier at terrace (~1.9 eV) and step (~0.4 eV) sites.[131,148,149] Molecular beam studies[130–132,134–136,150] demonstrate that high impinging kinetic energies of N_2 activate dissociation on terrace sites, with no dependence on surface temperature. The dissociation probability increases slowly with increasing N_2 kinetic energy, and plateaus at $s_0 \approx 10^{-2}$ for kinetic energies much higher than the activation barrier;[130–132] vibrational excitation of the impinging N_2 also increases the dissociation probability markedly.[130]

STM studies,[151,152] in conjunction with theoretical calculations,[115,148,149] have helped elucidate the spatial properties, adsorbate-adsorbate interactions, and binding structures of adsorbed nitrogen atoms with atomic resolution. STM visualization images adsorbed nitrogen atoms as triangular depressions 5 Å wide in topographical scans.[151,152] N adsorbates occupy the

hcp threefold hollow site on terraces[151] and bridge site on steps[149] of the Ru(0001) surface. Interactions between N adsorbates are repulsive at nearest neighbor and second nearest neighbor sites, and slightly attractive at third nearest neighbor sites, resulting in an approximate pair potential of hard spheres that blocks the first and second nearest neighbor sites at room temperature and in the low coverage regime.[151] Experimental[152] and theoretical[115] barriers to diffusion of 0.9 eV and ~1.1 eV, respectively, have been observed for N adsorbates on the Ru(0001) surface. This allows adsorbate movement to be frozen out kinetically at moderate temperatures after the dissociation event occurs.

The preliminary results in this chapter represent the first STM images of energy- and angle-selected N_2 dissociation on Ru(0001) terrace sites. These images reveal spatio-temporal information about the reacting Ru(0001) interface that will help uncover the role of multiple energy dissipation channels–such as nonadiabatic coupling to ehps–in the dissociation process. This work will provide a deeper understanding of N_2 dissociation on ruthenium surfaces that can directly contribute to the design and manufacture of more efficient industrial catalysts for industrial NH_3 production. Furthermore, the results presented herein are not only important to industrial heterogeneous catalysis, but in collaboration with theoretical exploration, contribute a more fundamental understanding of activated dissociative adsorption systems and heterogeneous catalysis as a whole.

5.2: Experimental

The results reported in this chapter were acquired utilizing a new UHV instrument that contains both supersonic molecular beam and STM/AFM techniques. As reported in previous publications,[40,76,153] the instrument is comprised of a triply differentially pumped beamline, a

surface characterization/preparation chamber that contains Auger electron spectroscopy (AES) and low-energy electron diffraction (LEED) capabilities, and a scanning probe microscope (SPM) chamber that holds the variable temperature SPM based on the ultra-stable design of Shuheng Pan, built in collaboration with RHK. The custom-built PAN STM was built with a vertical plane, therefore allowing the Ru(0001) surface to be exposed to the supersonic molecular beam at variable angles of incidence with the STM tip still in contact. In conjunction with the high stability of the microscope, this unique configuration allows nanoscopic areas of the Ru(0001) surface to be revisited during exposures to high kinetic energy N_2 to provide previously unattainable information about the reactive spatiotemporal evolution of the surface.

Supersonic molecular beams were generated by the expansion of a 3% N_2/97% He gas mixture through a 30 μm molybdenum pinhole at pressures from 20 to 100 psi and nozzle temperatures ranging from 300 to 1150 K (± 5%). The translational kinetic energy of the molecular beam at each nozzle temperature was measured using time-of-flight (TOF), and values of 0.8 ± 0.3, 1.1 ± 0.4, and 1.3 ± 0.6 eV were found for nozzle temperatures of 730, 1000, and 1150 K, respectively. The uncertainty values in these energies represent the FWHM of each energy distribution. The molecular beam flux for all beam conditions was on the order of 10^{13} N_2 molecules cm^{-2} s^{-1}, as determined by the King and Wells method.[107]

All N_2 molecular beam exposures onto the Ru(0001) surface were performed with the sample in the SPM chamber, which corresponds to a 4 mm diameter beam spot on the crystal. The sample was either held at room temperature or cryocooled statically with liquid nitrogen during imaging/exposures; the temperature of the sample was monitored using a cryostat thermocouple attached to the STM assembly. The surface plane can be oriented from 0 to 45° during exposures to the N_2 molecular beam. Same-spot visualization experiments, which capture the evolution of

the same set of surface atoms as they are exposed to energy- and angle-selected N_2, were achieved by laterally positioning the STM tip multiple micrometers downrange (away from the molecular beam) from the reference atoms during exposures to the N_2 beam. The STM tip was then moved back to the reference area using topographical markers on the surface after the exposure, therefore allowing local, nanoscale evolution to be observed. The STM tip was moved to reduce tip shadowing but maintained tunneling contact with the surface throughout exposures, significantly reducing drift and allowing the reference area to be routinely found after exposures to the N_2 beam. Reactive evolution of the surface only arose due to exposure to the N_2 molecular beam, and not as a result of trace thermalized N_2 reflected from the tip/chamber, which was confirmed by the fact that only areas of the surface with direct line of sight to the N_2 beam were reacted.

The Ru(0001) crystal (Surface Preparation Laboratory, 99.99% purity) was cleaned in the characterization/preparation chamber ($< 1 \times 10^{-10}$ Torr base pressure) by multiple sputter/anneal cycles, similar to those reported previously.[154,155] The Ru(0001) surface was sputtered at room temperature using 0.5 keV Ar^+ ions generated by a PHI 04-150 ion gun resulting in a current of 10-50 nA cm^{-2} on the sample; the sample was flash annealed by electron beam bombardment to ~1500 K for ~10 s after sputtering cycles. The temperature was monitored using a Mikron infrared pyrometer ($\varepsilon = 0.35$) during annealing. Hundreds of cleaning cycles were necessary to produce a clean and ordered Ru(0001) surface. An Omicron NGL 10 SPECTALEED with both LEED and AES capabilities was used to determine if the Ru(0001) surface was ordered and free of impurities. Sputter/anneal cycles were performed until a sharp, hexagonal LEED pattern, clean AES spectrum, and STM images of clean terraces, step edges, and a hexagonal lattice were obtained.[151,152,154,155] STM images were taken using etched or cut $Pt_{0.8}Ir_{0.2}$ tips.

5.3: Results and Discussion

Hundreds of ion sputtering/annealing cycles were required to produce a clean and ordered Ru(0001) surface. Initially, lower energy (0.5 keV) Ar+ sputtering cycles followed by longer anneal cycles (>1 min) at slightly lower temperatures (<1400 K) were used and produced a partially clean surface. Local areas of clean and ordered Ru(0001) surface were produced from these procedures, but subsequent STM imaging revealed the presence of moiré patterns indicative of monolayer and bilayer graphene formation (**Figure 5.1**).[156] Subsequent higher energy (3 keV) Ar^+ sputtering cycles followed by shorter (~5 s) and higher temperature (~1500 K) annealing cycles produced a clean, ordered Ru(0001) surface, characterized by AES, LEED, and STM visualization in **Figure 5.2**. Once a clean Ru(0001) surface was achieved and characterized, the surface was exposed to N_2. As shown in **Figure 5.3**, adsorbed nitrogen atoms are imaged as triangular depressions approximately 5 Å wide and 0.5-1 Å deep in topographical scans, closely matching literature values;[151,152] the three-fold symmetry of the adsorbate suggests binding at either the fcc or hcp sites, with previous experimental and theoretical studies indicating binding at hcp sites is most favorable.[115,151,157]

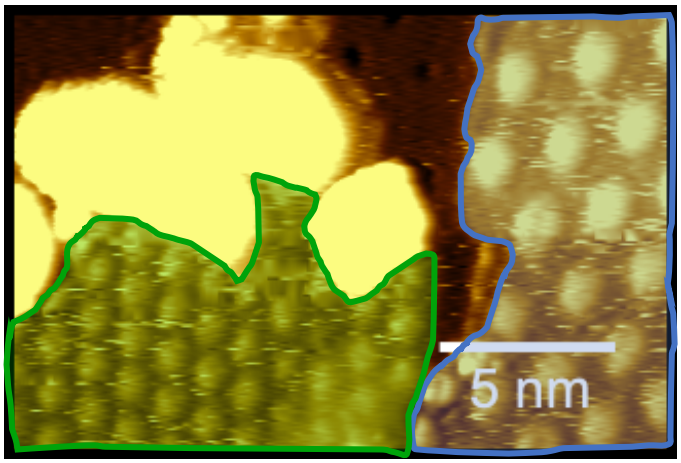


Figure 5.1: Representative STM image of monolayer and bilayer graphene on the Ru(0001) surface. STM image (-1.5 V, -250 pA) of monolayer (green) and bilayer (blue) graphene formation on the Ru(0001) surface.

STM imaging of the same nanoscopic area revealed no observable diffusion of the nitrogen adsorbates (**Figure 5.4**). Contrary to a previous STM study,[152] these "diffusion" experiments were performed multiple times on the room temperature Ru(0001) surface and no observable diffusion was ever observed

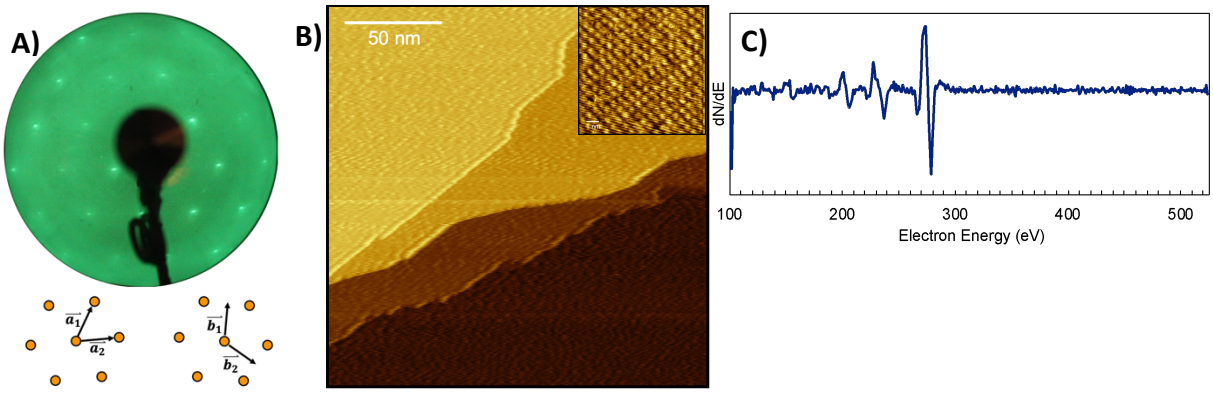


Figure 5.2: Characterization of a clean and ordered Ru(0001) surface. A) A LEED pattern of the clean Ru(0001) surface demonstrating a sharp, hexagonal pattern with higher order diffraction peaks; a schematic of the reciprocal ($\overrightarrow{a_1}$ and $\overrightarrow{a_2}$) and real ($\overrightarrow{b_1}$ and $\overrightarrow{b_2}$) space lattice vectors are given, corresponding to the interpretation of the LEED pattern and STM images, respectively. **B)** STM image (-1.5 V, -250 pA) of the clean Ru(0001) surface revealing multiple clean terraces and step edges; an inset of the bare lattice is in the top right. **C)** A differentiated AES spectrum (3 keV) of the clean Ru(0001) surface showing no contaminant peaks.

over the course of hours. The results can be explained most likely by the use of a tunneling current in this study that is less than 100 times of that used previously, therefore minimizing tip interactions with the adsorbates that can influence their movement upon the surface. Notably, the lack of diffusion enables the N_2 dissociation event to be directly investigated at room temperature

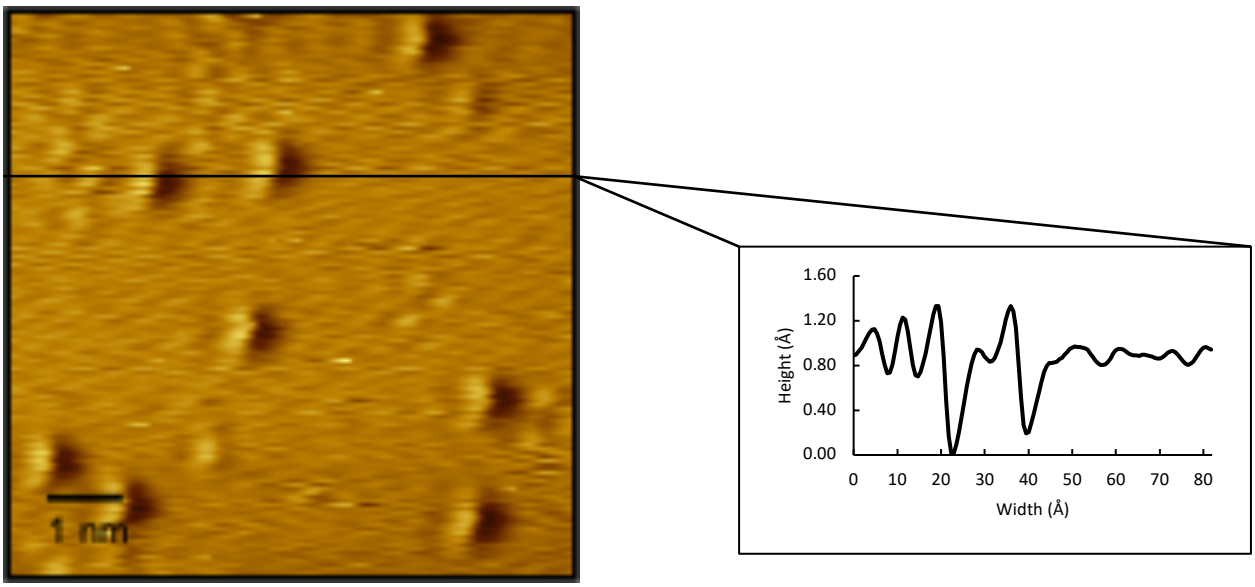


Figure 5.3: Representative STM image of adsorbed nitrogen atoms. A representative STM image (-1.5 V, -250 pA) of 8 adsorbed nitrogen atoms, imaged as dark triangles. A line scan is shown to demonstrate the average width and depth of the visualized nitrogen complexes.

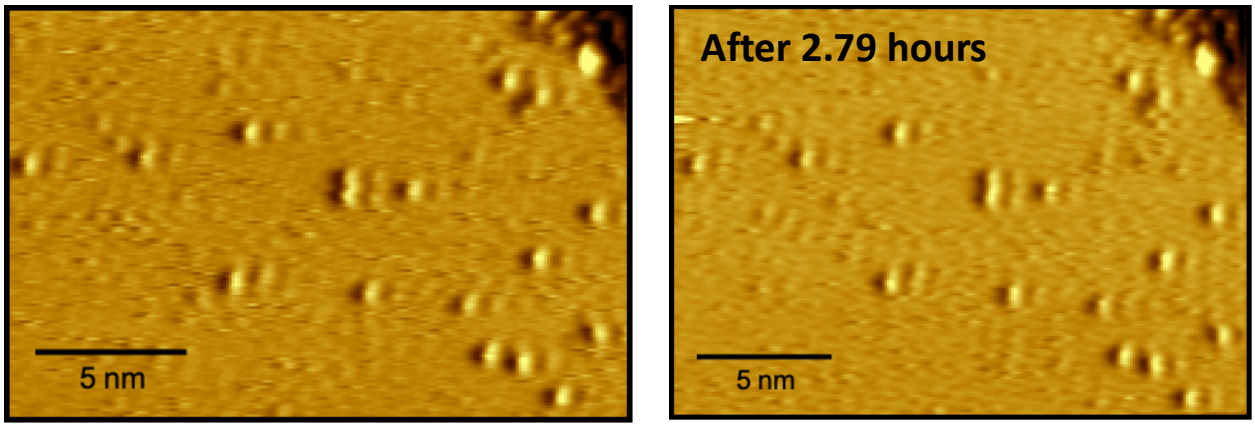


Figure 5.4: Negligible diffusion of nitrogen adsorbates. STM images (-1.5 V, -250 pA) of the same nanoscopic area, taken 2.79 hours apart. No observable diffusion of any of the nitrogen adsorbates (dark triangles) was observed in relation to the step edge or one another on the room temperature Ru(0001) surface.

by measuring the distance between and location of the resulting nitrogen atom adsorbates. If the nitrogen atoms were to diffuse at room temperature, the resulting spacing and location of the nitrogen adsorbates would reflect a combination of the interactions of the impinging N_2 with the Ru(0001) surface as well as subsequent thermal diffusion of the adsorbates, thus yielding random information. Since diffusion is frozen out over appropriate time frames at room temperature, the spacing and binding of the nitrogen atoms provides direct insight into the energy transfer of the impinging N_2 with the surface and the liberated energy during the dissociation event.

Shown in **Figure 5.5** are representative STM images of the room temperature Ru(0001) surface before and directly after exposure to ~1.1 eV N_2 impinging normal to the surface; the identified nitrogen adsorbates are circled in red for clarity (19 total). By scanning multiple nanoscopic areas of the surface after exposures, the reactivity of the surface and resulting sticking coefficient for the N_2 on Ru(0001) terraces can be calculated in extremely low coverage (<0.1%) regimes for different N_2 energies. For each study, 9000 nm^2 of the surface or more were imaged and subsequently used to calculate the sticking probability of the system. **Figure 5.6** demonstrates the sticking probability of N_2 with an impinging kinetic energy of 1.1 eV (assuming all nitrogen

atoms originate from a N_2 dissociation event) as a function of total exposure; the x-axis is in units of Langmuirs (L), which is defined as the N_2 fluence necessary to form a complete monolayer assuming a unity sticking probability. Notably, even at coverages less than 0.2% of the surface, the reactivity of the surface significantly decreases with increasing exposure. This result likely suggests that either a very limited number of favorable binding terrace sites exist on the surface, or that the binding of nitrogen adsorbates on the Ru(0001) terrace affects the local geometry, electronic structure, and/or reactivity of those sites, subsequently decreasing the overall reactivity of the surface as it evolves due to N_2 exposure. Theoretical study of this system may provide insight into the fundamental mechanism by which the reactivity decreases and is being explored. These preliminary results highlight the utility of the experimental approach described herein, and demonstrate the dynamic nature of the Ru(0001) surface during its reactive evolution.

Furthermore, the reactivity of 1.1 eV N_2 impinging normal to the Ru(0001) surface does not significantly differ from the reactivity of the same energy N_2 impinging 45° with respect to the surface plane, suggesting that the reactivity scales with total N_2 energy. Additional studies at

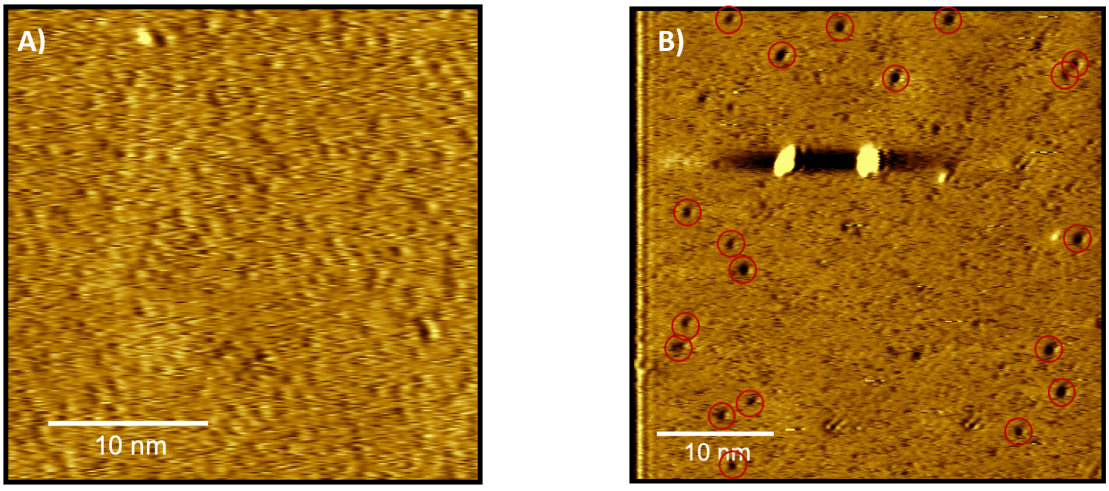


Figure 5.5: Representative STM images of the Ru(0001) surface before and after exposure to 1.1 eV N_2. Representative room temperature STM images (-1.5 V, -250 pA) of a **A)** clean Ru(0001) surface and **B)** a Ru(0001) surface directly after exposure to 3×10^{15} cm^{-2} of 1.1 eV N_2 impinging normal to the surface. Nitrogen adsorbates are circled in red for clarity.

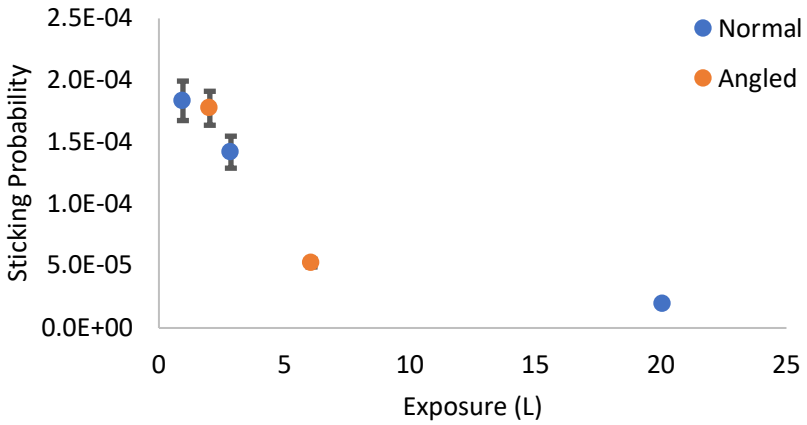


Figure 5.6: Sticking probability of 1.1 eV N_2 on a room temperature Ru(0001) surface as a function of exposure. A plot of the sticking probability of 1.1 eV N_2 impinging normal (blue) and 45° from the surface plane (orange) on a room temperature Ru(0001) surface as a function of the total exposure (in Langmuirs).

different impinging kinetic energies and angles will be performed to understand this system in much more depth. The reported sticking probabilities are in qualitative agreement with previous molecular beam studies.[130,131,150]

Uncovering the pair distance(s) and relative angle(s), and whether or not the impinging N_2 kinetic energy and angle affect these values, is crucial to uncovering how the N_2 interacts with the surface and what energy transfer mechanisms govern the reaction. Determination of the pair distance(s) and relative angle(s) of nitrogen pairs will be accomplished through two experimental approaches, which are both currently in progress. The first method will be to expose the Ru(0001) surface at extremely low coverages (<0.05%); by reducing the total number of nitrogen atom pairs, the spacing between dissociation events will be very large and the identity of the nitrogen atom pairs can become evident. Representative STM images of these low coverage exposures are shown in **Figure 5.7** for 1.1 eV N_2 impinging normal to the Ru(0001) surface that clearly highlight individual nitrogen pairs–circled in red for clarity–formed from singular dissociation events. STM images that revealed multiple dissociation events in the same nanoscopic area were not included in any data analysis in order to avoid misidentification of nitrogen pairs.

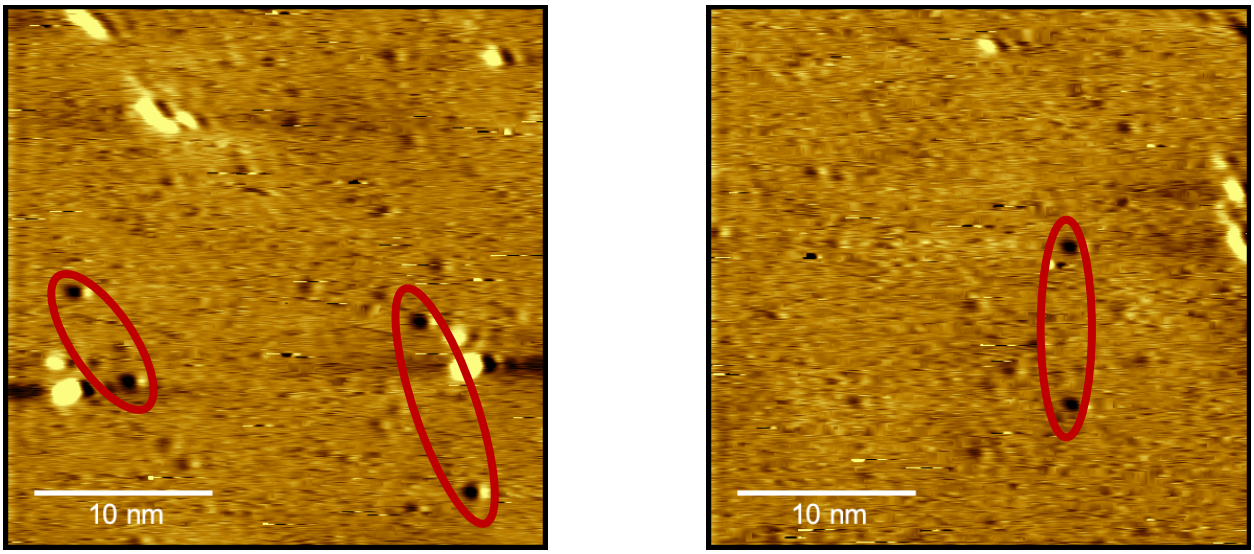


Figure 5.7: Representative STM images of low coverage 1.1 eV N_2 normal exposures. Two representative STM images (-1.5 V, -250 pA) of a room temperature Ru(0001) surface after exposure to 0.3 L of 1.1 eV N_2 impinging normal to the surface; the nitrogen pairs are circled in red for clarity.

Figure 5.8 demonstrates preliminary experimental measurements of individual nitrogen atom pair distances for 1.1 eV N_2 impinging (**A**) normal to the and (**B**) 45° with respect to surface normal at extremely low coverages on a room temperature Ru(0001) surface. These preliminary results suggest an average nitrogen pair distance for the normal and 45° studies of 8.4 ± 0.5 nm and 9.4 ± 0.7 nm, respectively; these distances are extremely large considering that these values are over 30 times larger than the lattice constant of ruthenium. No conclusions can yet be made about significant differences in the pair distances or relative angles between the angled and normal

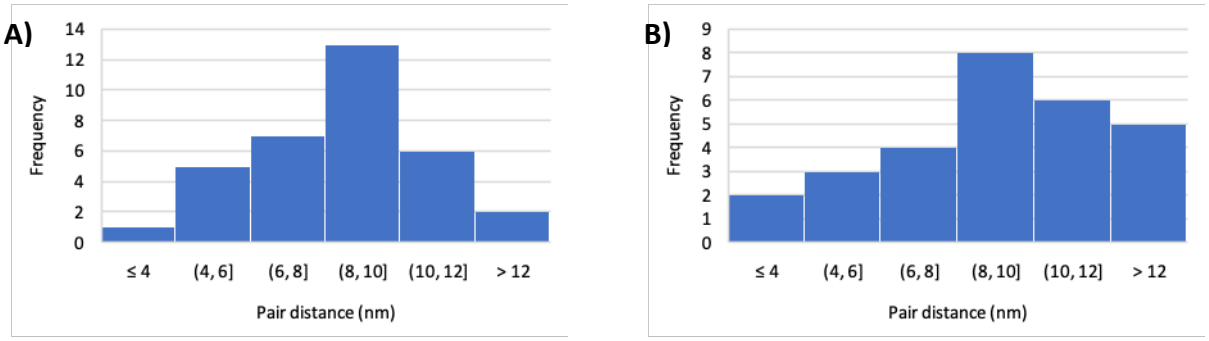


Figure 5.8: Nitrogen pair distances for 1.1 eV N_2 impinging A) normal to the and B) 45° with respect to surface normal. Preliminary histogram data showing measured pair distances for 1.1 eV N_2 impinging **A)** normal to the surface and **B)** at 45° with respect to surface normal.

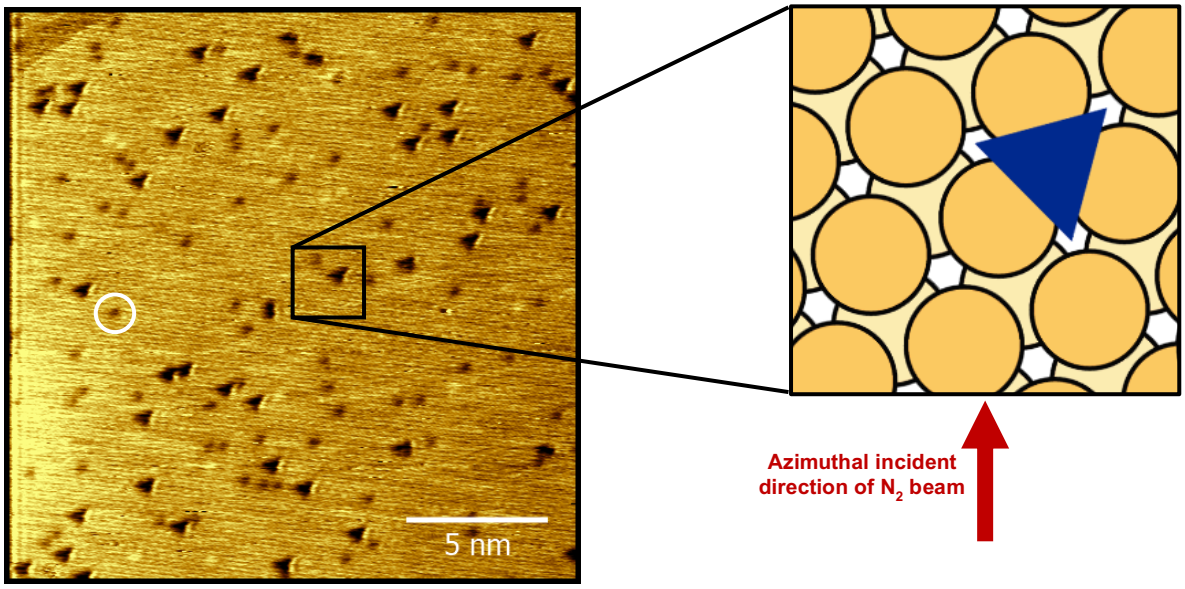


Figure 5.9: Azimuthal incident direction of N_2 beam during angled exposures. STM image (-1.5 V, -250 pA) of the Ru(0001) surface with nitrogen (dark triangles) along with oxygen (example circled in white) adsorbates. The schematic on the right highlights the orientation of the Ru(0001) lattice with the nitrogen adsorbate sitting in an hcp site and the azimuthal orientation (angled with respect to surface normal) of the N_2 beam with respect to the ruthenium lattice during angled exposures.

1.1 eV studies, although future results will provide more definitive insight into how impinging angle affects the subsequent binding of nitrogen pairs. **Figure 5.9** illustrates the orientation of the N_2 molecular beam with respect to the Ru(0001) lattice–confirmed by STM imaging of the nitrogen adsorbates[151,158] as well as LEED and STM characterization of the Ru(0001) lattice (**Figure 5.2**)–which will be critical in determining correlations between the incident angle of N_2 and the resulting nitrogen pair spacing, relative angle, and binding sites. A comprehensive discussion of the orientation of the crystal with respect to LEED patterns and STM images can be found in **Chapter 2.6**. Additional studies at different N_2 kinetic energies and impinging angles are forthcoming.

The second experimental approach being used to determine the pair distance(s) and relative angle(s) of nitrogen pairs utilizes the unique experimental setup described previously, whereby the same nanoscopic area of the Ru(0001) surface can be visualized *during* exposures,

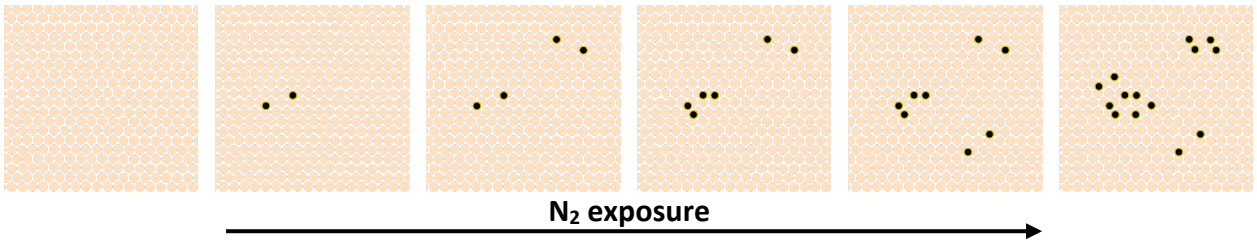


Figure 5.10: Schematic of N_2 dissociation events imaged in real time. A pictorial representation of how real time imaging of a surface can help determine nitrogen pairs; individual pairs of nitrogen atoms are imaged in real time as they adsorb to the surface, culminating in the final image on the right.

allowing the evolution of the surface to be imaged in real time. An example of these potential results is shown in **Figure 5.10**, which clearly shows how real time atomically-resolved STM imaging can identify each pair of nitrogen atoms as the surface reactively evolves. In each successive image, a new pair of nitrogen adsorbates binds to the surface; by visualizing the surface in real time during exposure to high energy N_2, the addition of each pair of nitrogen atoms would be clearly observed, as opposed to imaging a convolution of all of these pairs represented by the final image of the sequence. This same-spot reactive imaging poses greater experimental challenges but provides unique and previously unattainable information about the evolution of this reactive interface.

The preliminary results of this chapter and the data that will be obtained in the aforementioned in progress experiments represent powerful insight into the fundamental dynamics of N_2 activated dissociative adsorption on Ru(0001). STM visualization of individual dissociation events identifies the site and location of the resulting nitrogen adsorbates with angstrom level precision. The spacing of the adsorbates directly correlates to the energy transfer mechanisms involved in the dissociation process and will help uncover the importance of nonadiabatic excitation of ehps in these reactive events. Additionally, the relative angle between the resulting adsorbates will reveal, among others: the presence of a metastable molecular state, influence of N_2 kinetic energy and impinging angle, and site specificities. Paired with theoretical insight from

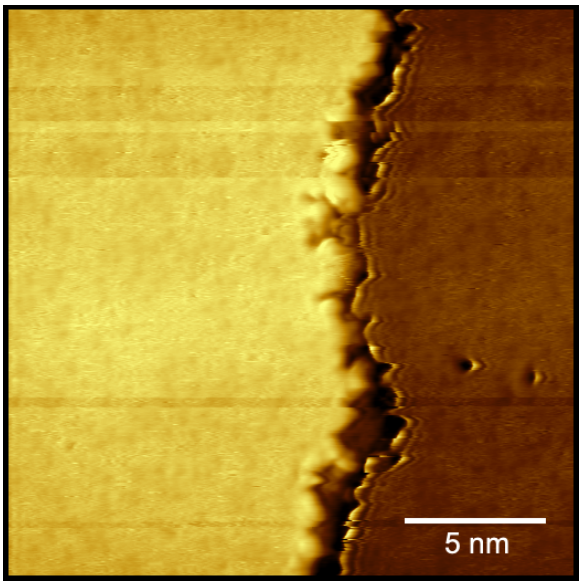


Figure 5.11: N_2 binding at step edges. STM image (-1.5 V, -250 pA) of nitrogen binding at step edges after exposure to ~30 L of 0.3 eV N_2.

ongoing collaborations with Professor Hua Guo's research group, these previously unattainable experimental results will help to answer many of the unsolved questions about this unique activated dissociative adsorption process.

While the focus of this study is the dissociative adsorption of N_2 on terrace sites, the dissociative adsorption of N_2 at step edges was also observed. Exposure of the room temperature Ru(0001) surface to ~30 L 0.3 eV N_2 impinging normal to the surface resulted in negligible N_2 binding to terrace sites, however STM imaging (**Figure 5.11**) revealed evidence of extensive nitrogen atom binding at step edges, matching previous studies that prove that the reactivity of N_2 on the Ru(0001) surface is completely dominated at steps.[131,148,149] The total reactivity at the step edges could not be precisely quantified, but this observation further confirms the large difference in reactivity between the step and terrace sites.

The enhanced reactivity of N_2 on terrace sites with a translational kinetic energy of 1.1 eV, due to expansion of the 3% N_2/97% He gas mixture through a heated beam nozzle at varying temperatures, is likely a result of both increased translational kinetic energy and vibrational excitation of the impinging N_2, as seen previously.[130] **Table 2.3** demonstrates percentages of the N_2 flux that occupy the first ($\nu = 1$) and second ($\nu = 2$) vibrationally excited states at varying nozzle temperatures: the percentage of N_2 molecules in $\nu = 1$ is 0.8%, 1.5%, 2.3%, 3.4%, 4.7%, and 6.0% for nozzle temperatures of 700, 800, 900, 1000, 1100, and 1200 K, respectively, and the

percentage of N_2 molecules in $\nu = 2$ is ≥0.1% at nozzle temperatures ≥1000 K. Theoretical insight into this system will be critical to understand how vibrationally excited N_2 molecules contribute to the reactivity of the system and morphological evolution of the surface.

5.4: Conclusions

Presented in this chapter are the first STM images of energy- and angle-selected N_2 dissociation on Ru(0001) terraces sites. The preliminary results of this chapter demonstrate the dynamic reactivity of 1.1 eV N_2 on the room temperature surface, and clearly illustrate the increased reactivity of step edges in comparison to terraces at lower (≤0.3 eV) N_2 kinetic energies. Additionally, initial investigations of the spacing and relative angle between nitrogen adsorbate pairs at N_2 kinetic energies of 1.1 eV at various impinging angles are provided. A proven research plan for experimentally isolating and analyzing individual nitrogen pairs is given. The effect of N_2 impinging energy and angle on the reactivity and subsequent reactive evolution of the surface in a low coverage limit are discussed. The results from these studies provide direct experimental insight into the energy transfer mechanisms that govern the dissociation process and uncover detailed aspects of the dynamics of the dissociation event. In conjunction with theoretical collaboration, the importance of nonadiabatic interaction in N_2 dissociation on Ru(0001) terrace sites will be directly addressed. This chapter details a unique new method of studying reactive surface dynamics and will help answer important and unresolved questions surrounding this fundamentally and technologically important activated dissociative adsorption process.

Appendix A

Appendices

This appendix contains the raw data and STM images used for all figures and arguments presented in this thesis. The filenames of the STM images, along with the figure that they support, are included with each figure; the complete contents of the appendix were submitted electronically to Professor Sibener.

A1: Atomically-Resolved Oxidative Erosion and Ablation of Basal Plane HOPG Graphite Using Supersonic Beams of O_2 with Scanning Tunneling Microscopy

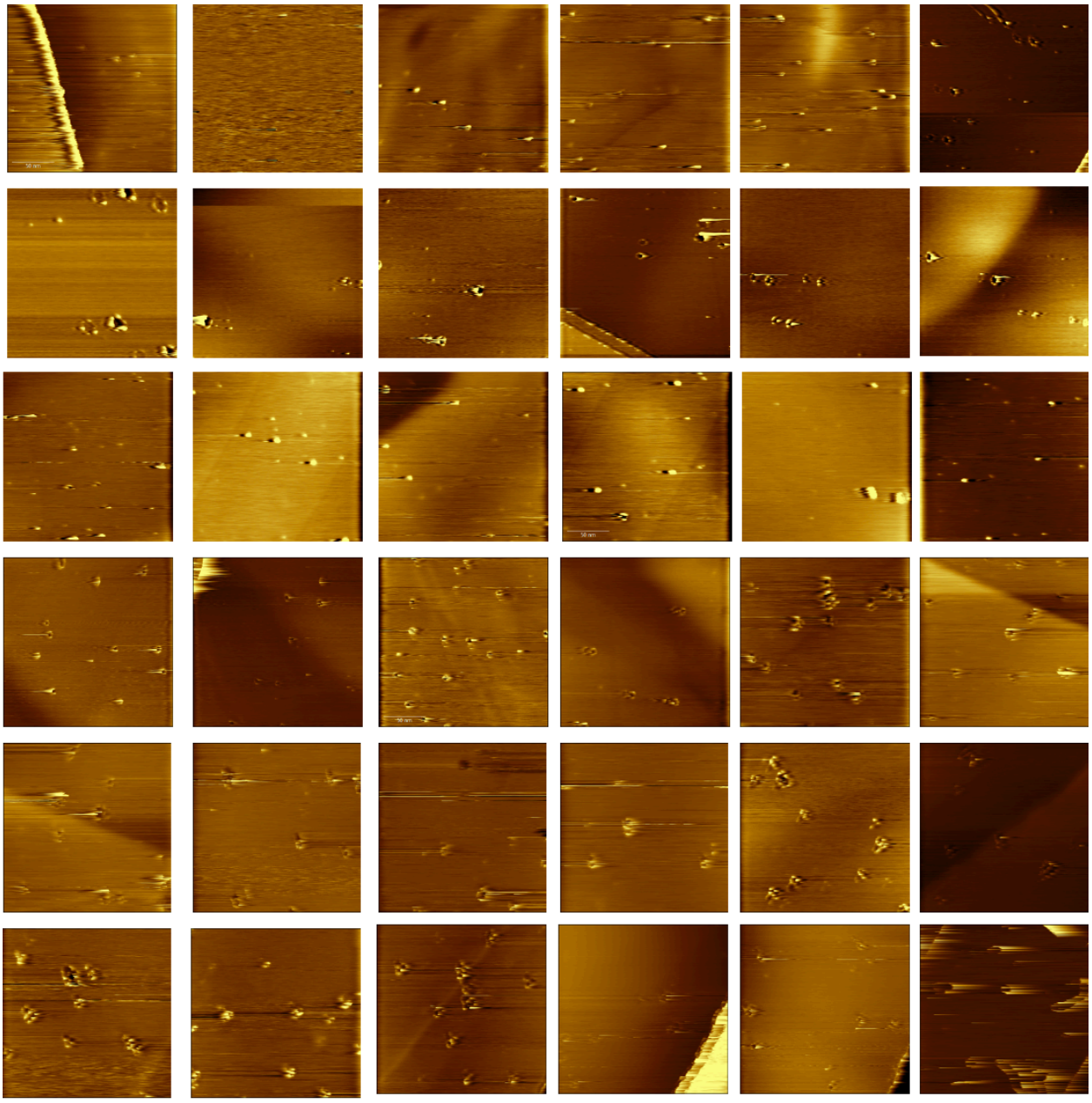


Figure A1.1: First set of 36 images used in Figure 3.2.

Filenames for **Figure A1.1** from top left to bottom right:

Directory: Appendix\A1-2\ Sputtered, Leak O2 15min
081716_0019

Directory: Appendix\A1-2\ Sputtered, Leak O2 30min
081916_0002, 081916_0003, 081916_0004, 081916_0007, 081916_0010, 081916_0011, 081916_0012, 081916_0013, 081916_0014, 081916_0015, 081916_0016, 081916_0018, 081916_0019, 081916_0020, 081916_0021, 081916_0022, 081916_0023

Directory: Appendix\A1-2\ Sputtered, Leak O2 45min
081916_0024, 081916_0025, 081916_0026, 081916_0027, 081916_0028, 081916_0029, 081916_0030, 081916_0031, 081916_0032, 081916_0033, 081916_0034, 081916_0035, 081916_0036, 081916_0037, 081916_0038, 081916_0040, 081916_0041, 081916_0042

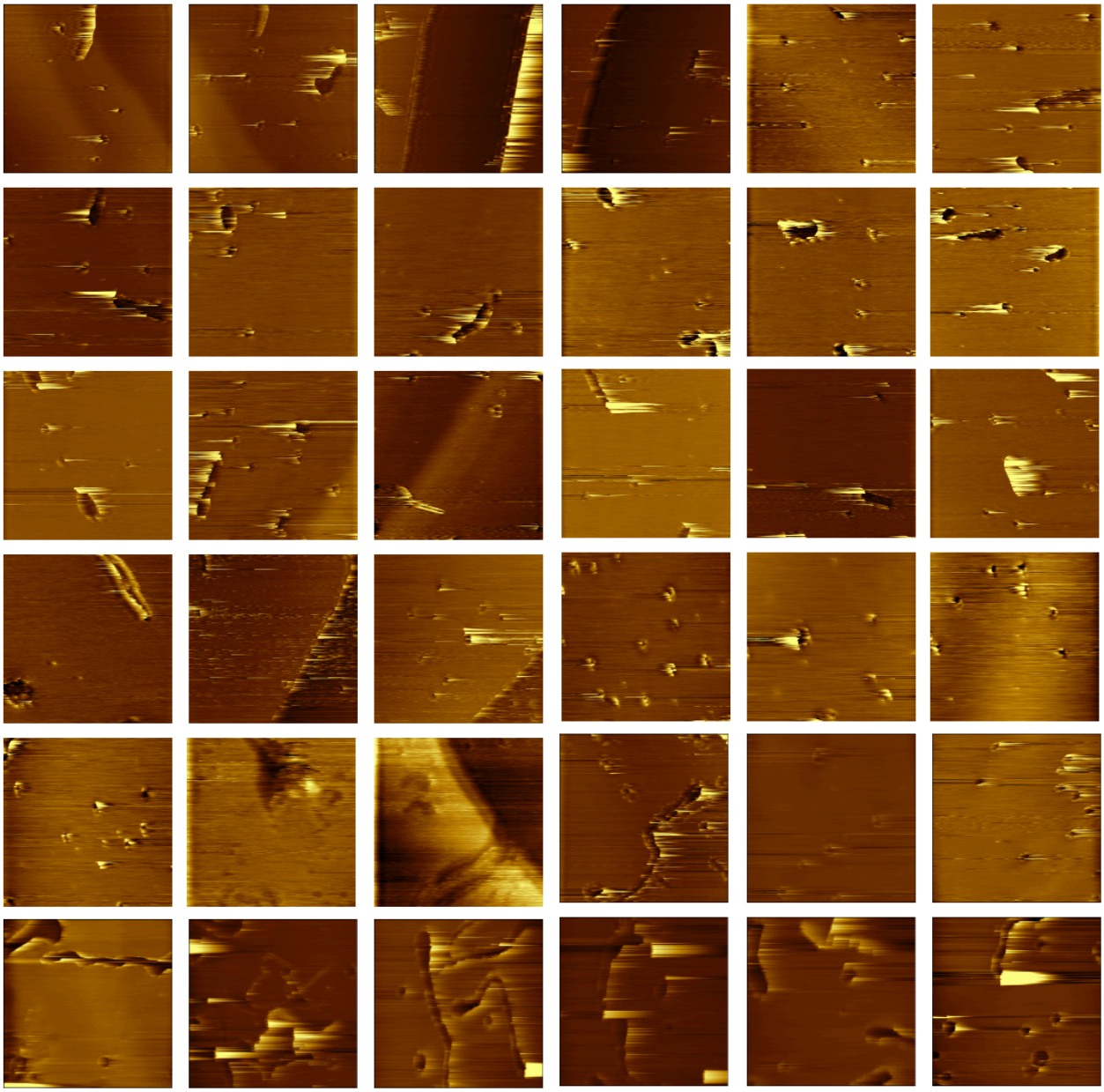


Figure A1.2: Second set of 36 images used in Figure 3.2.

Filenames for **Figure A1.2** from top left to bottom right:
Directory: Appendix\A1-3\Sputtered, Leak O2 45 min
082116_0001, 082116_0002, 082116_0003, 082116_0004

Directory: Appendix\A1-3\ Sputtered, Leak O2 60min
082216_0002, 082216_0003, 082216_0004, 082216_0005, 082216_0006, 082216_0007, 082216_0008, 082216_0009, 082216_0010, 082216_0011, 082216_0012, 082216_0013, 082216_0014, 082216_0015, 082216_0016, 082216_0017, 082216_0018, 082216_0019, 082216_0020, 082216_0022

Directory: Appendix\A1-3\ Sputtered, Leak O2 90min
082216_0023, 082216_0024, 082216_0027, 082216_0029, 082216_0031, 082316_0001, 082316_0002, 082316_0003, 082316_0004, 082316_0005, 082316_0006

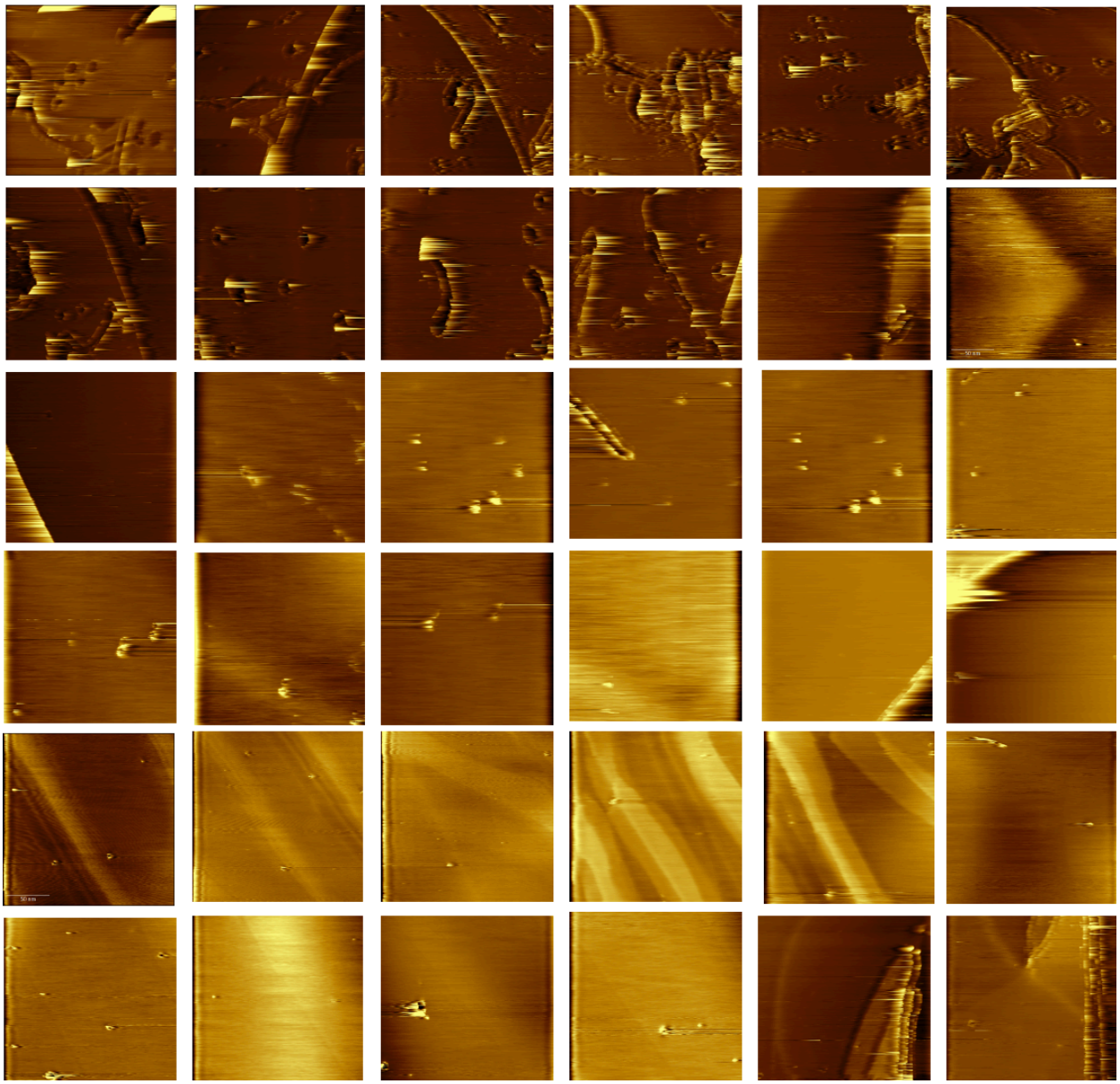


Figure A1.3: Third set of 36 images used in Figure 3.2.

Filenames for **Figure A1.3** from top left to bottom right:

Directory: Appendix\A1-4\Sputtered, Leak O2 90 min
082316_0007, 082316_0008, 082316_0009, 082316_0010, 082316_0011, 082316_0012, 082316_0013, 082316_0014, 082316_0015, 082316_0016

Directory: Appendix\A1-4\Unsputtered, Leak O2 15 min
082316_0020, 082316_0024

Directory: Appendix\A1-4\Unsputtered, Leak O2 30 min
082416_0013, 082416_0018

Directory: Appendix\A1-4\Unsputtered, Leak O2 45 min
082416_0022, 082416_0023, 082416_0024, 082416_0025, 082416_0026, 082416_0028, 082416_0029, 082416_0030, 082416_0031, 082416_0032, 082416_0035, 082416_0036, 082416_0037, 082416_0038, 082416_0039, 082416_0040, 082416_0041, 082416_0042, 082416_0043, 082416_0044

Directory: Appendix\A1-4\Unsputtered, Leak O2 60 min
082516_0001, 082516_0002

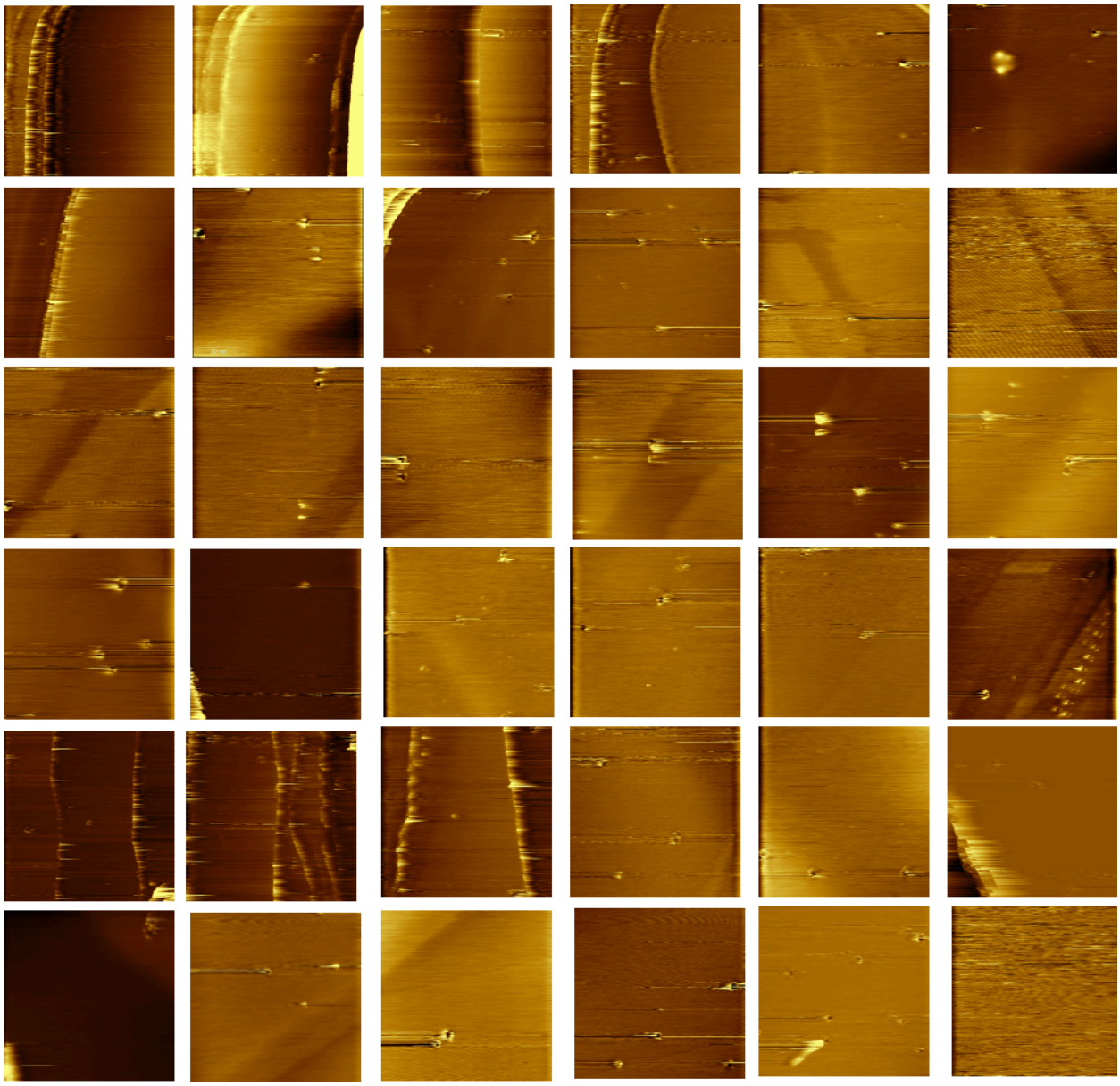


Figure A1.4: Fourth set of 36 images used in Figure 3.2.

Filenames for **Figure A1.4** from top left to bottom right:

Directory: Appendix\A1-5\Unsputtered, Leak O2 60 min
082516_0003,082516_0004, 082516_0005, 082516_0006, 082516_0007, 082516_0008, 082516_0009, 082516_0010, 082516_0012, 082516_0013, 082516_0014, 082516_0015, 082516_0016, 082516_0017, 082516_0018, 082516_0019, 082516_0020, 082516_0021

Directory: Appendix\A1-5\Unsputtered, Leak O2 75 min
082516_0022, 082516_0023, 082516_0024, 082516_0025, 082516_0026, 082516_0027, 082516_0028, 082516_0029, 082516_0030, 082516_0031, 082516_0033, 082516_0034, 082516_0035, 082516_0036, 082516_0037, 082516_0038, 082516_0039, 082516_0040

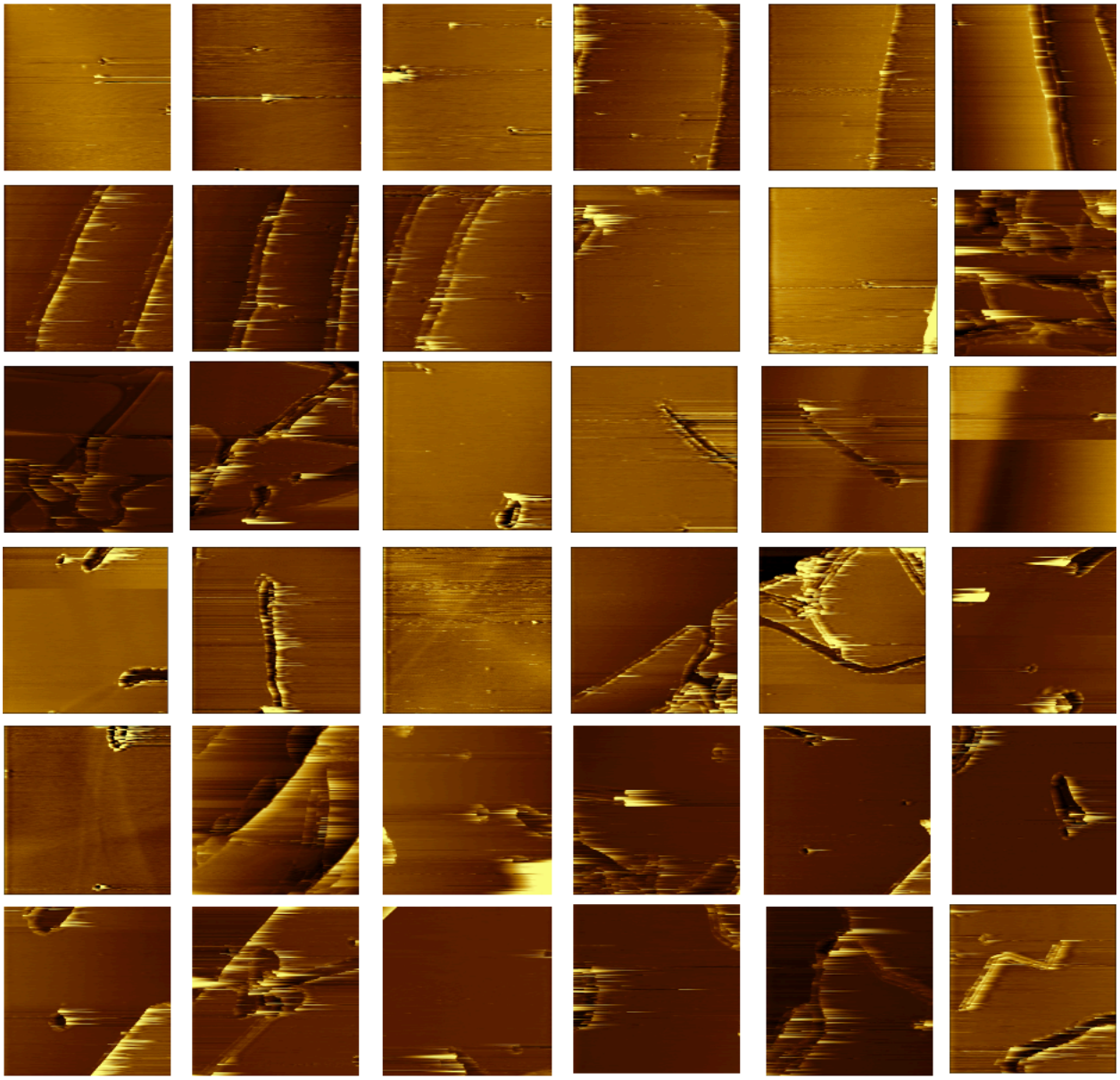


Figure A1.5: Fifth set of 36 images used in Figure 3.2.

Filenames for **Figure A1.5** from top left to bottom right:

Directory: Appendix\A1-6\Unsputtered, Leak O2 75 min
082516_0041, 082516_0042, 082516_0043

Directory: Appendix\A1-6\Unsputtered, Leak O2 90 min
082516_0044, 082516_0045, 082516_0046, 082516_0047, 082516_0048, 082516_0049, 082516_0050, 082516_0051, 082516_0052, 082516_0053, 082516_0054, 082616_0001, 082616_0002, 082616_0003, 082616_0004, 082616_0005, 082616_0006, 082616_0007, 082616_0008, 082616_0009, 082616_0010, 082616_0011

Directory: Appendix\A1-6\Unsputtered, Leak O2 120 min
082616_0012, 082616_0013, 082616_0014, 082616_0015, 082616_0016, 082616_0017, 082616_0018, 082616_0019, 082616_0020, 082616_0021, 082616_0022

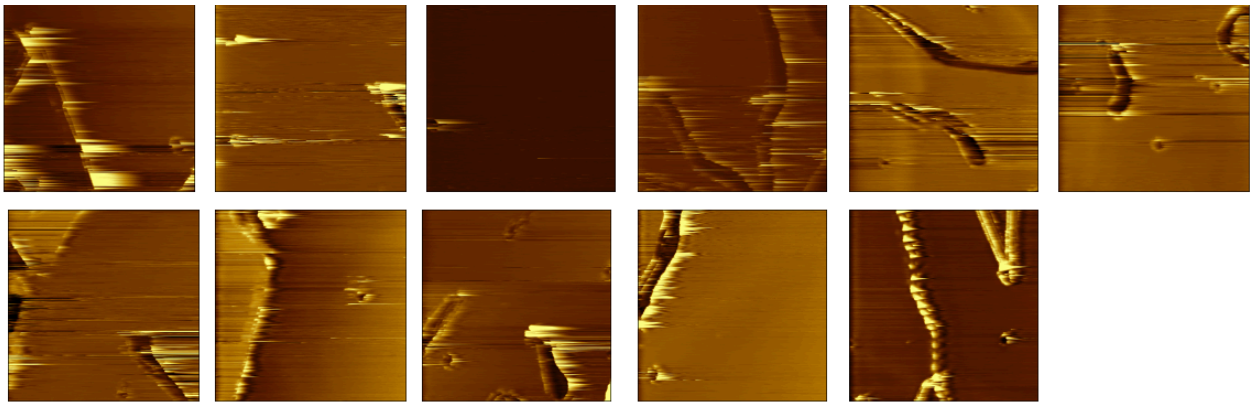


Figure A1.6: Last set of 11 images used in Figure 3.2.

Filenames for **Figure A1.6** from top left to bottom right:

Directory: Appendix\ Unsputtered, Leak O2 120min
082616_0023, 082616_0024, 082616_0025, 082616_0026, 082916_0001, 082916_0002, 082916_0003, 082916_0004, 082916_0005, 082916_0006, 082916_0007

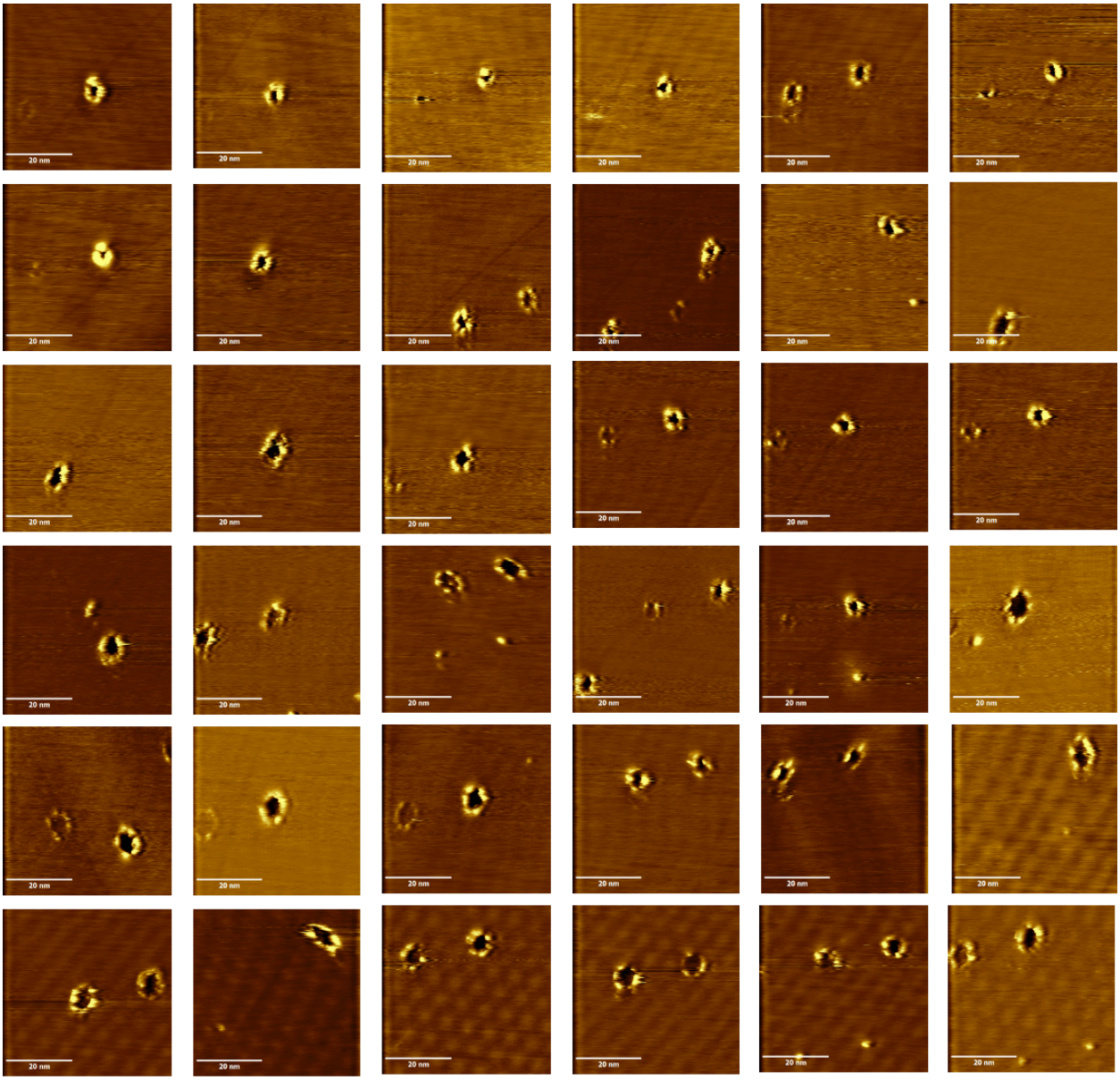


Figure A1.7: First set of 36 images used in the top graph of Figure 3.5 and the first row of Table 3.1.

Filenames for **Figure A1.7** from top left to bottom right:

Directory: Appendix\A1-8\1000C, 0.4eV Beam 7hrs
022817_0002, 022817_0005, 022817_0007, 022817_0010, 022817_0014, 022817_0016, 022817_0018, 022817_0019

Directory: Appendix\ A1-8\1000C, 0.4eV Beam 10.5hrs
030117_0007, 030117_0008, 030117_0009, 030117_0012, 030117_0013, 030117_0016, 030117_0018, 030117_0020, 030117_0021, 030117_0022, 030117_0024, 030217_0001, 030217_0006, 030217_0011, 030217_0013

Directory: Appendix\ A1-8\1000C, 0.4eV Beam 14hrs
030217_0016, 030217_0019, 030217_0021, 030217_0022, 030217_0026, 030217_0027, 030217_0029, 030217_0030, 030217_0031, 030217_0032, 030217_0033, 030217_0034, 030217_0035

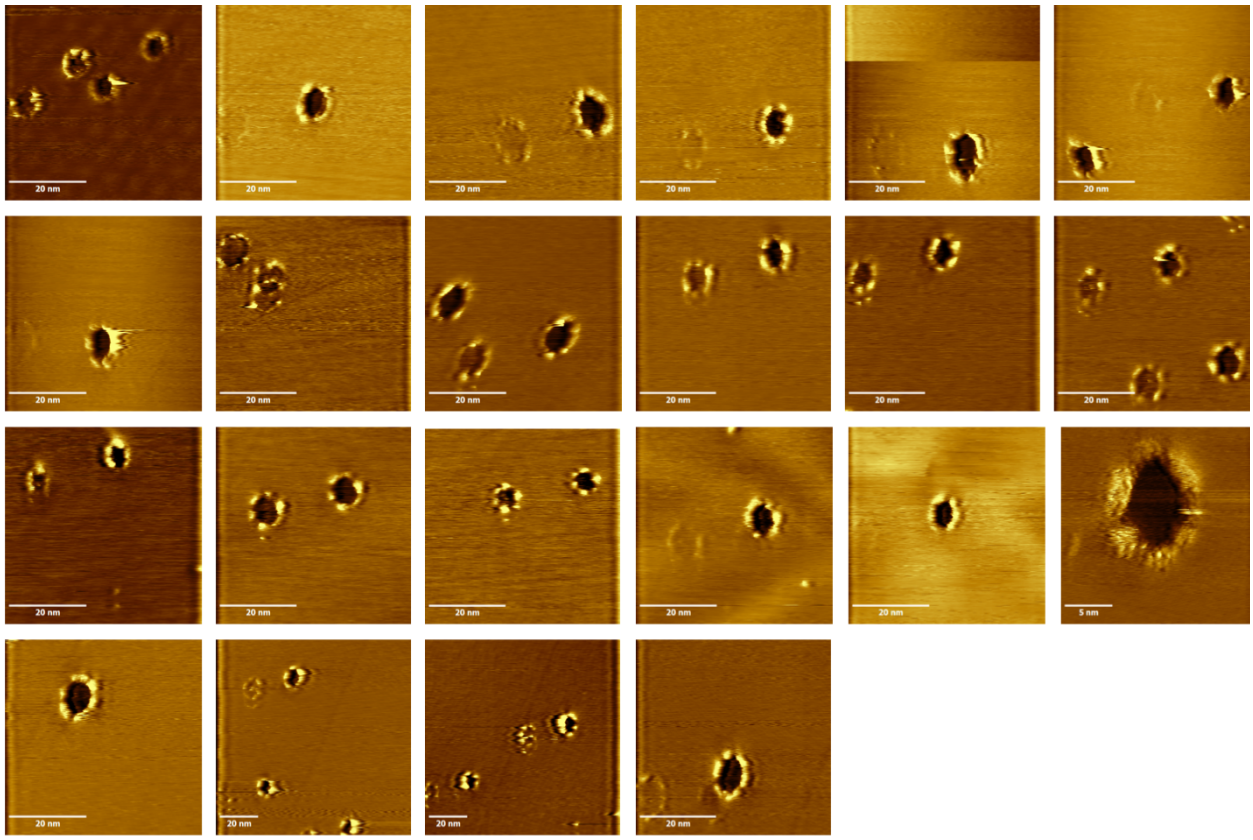


Figure A1.8: Last set of 22 images used in the top graph of Figure 3.5 and the first row of Table 3.1.

Filenames for **Figure A1.8** from top left to bottom right:

Directory: Appendix\A1-9\1000C, 0.4eV Beam 14hrs
030217_0036

Directory: Appendix\A1-9\1000C, 0.4eV Beam 21hrs
030817_0002, 030817_0006, 030817_0007, 030817_0009, 030817_0011, 030817_0012, 030817_0013, 030917_0001, 030917_0002, 030917_0003, 030917_0004, 030917_0005, 030917_0006, 030917_0007, 030917_0010, 030917_0011

Directory: Appendix\A1-9\1000C, 0.4eV Beam 24.5hrs
030917_0013, 030917_0015, 030917_0017, 030917_0018 030917_0020

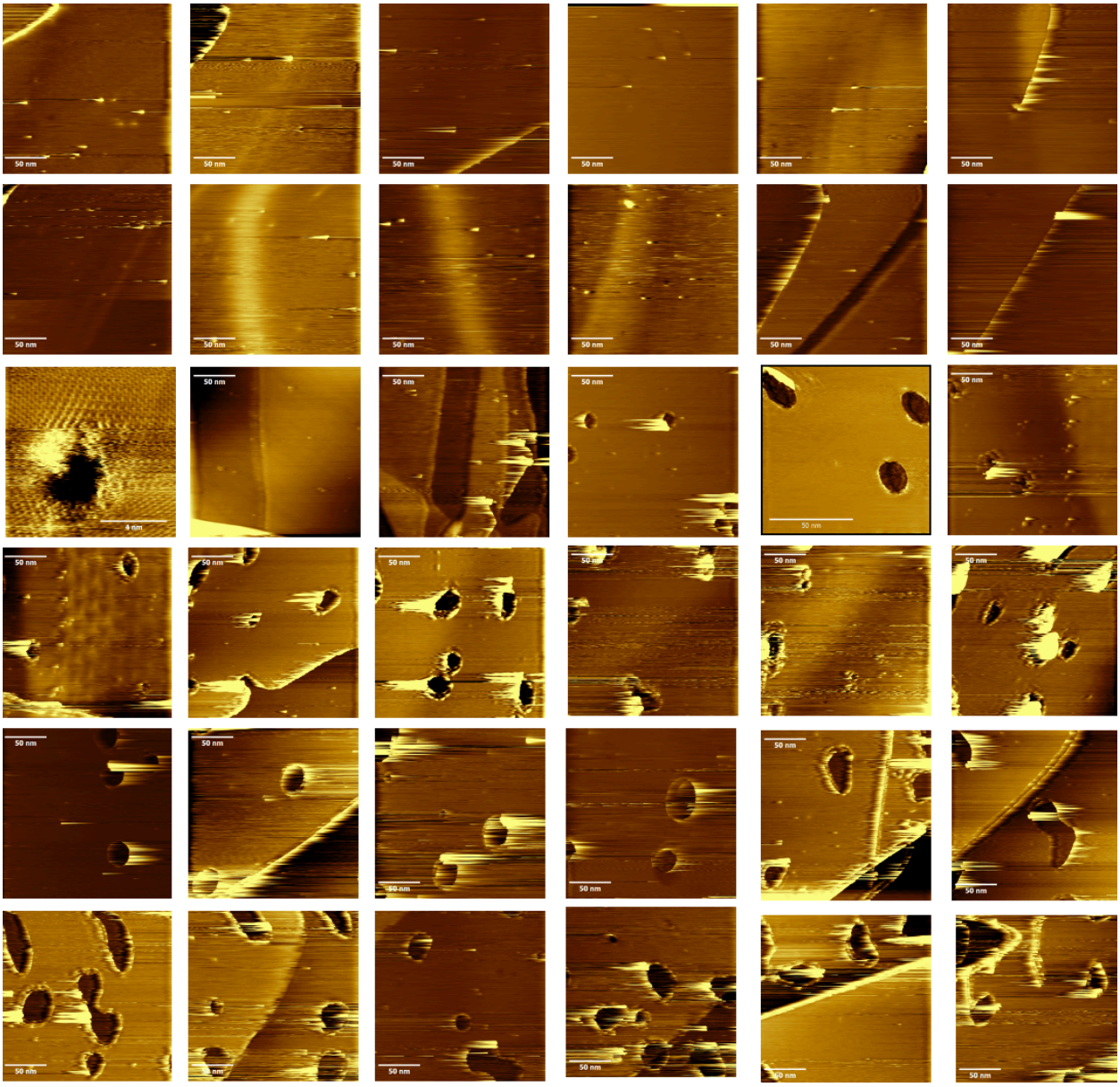


Figure A1.9: First set of 36 images used in the middle graph of Figure 3.5, Figure 3.6, and the second row of Table 3.1.

Filenames for **Figure A1.9** from top left to bottom right:

Directory: Appendix\A1-10\ 1100C, 0.4eV Beam Trial 1, 3.5hrs
091616_0001, 091616_0003, 091616_0006, 091616_0007, 091616_0008, 091616_0009, 091916_0001, 091916_0002, 091916_0003, 091916_0004, 091916_0006, 091916_0008, 091916_0015, 091916_0018, 091916_0030

Directory: Appendix\A1-10\ 1100C, 0.4eV Beam Trial 1, 7hrs
092116_0033, 092116_0034, 092116_0045, 092116_0047

Directory: Appendix\A1-10\ 1100C, 0.4eV Beam Trial 1, 9.5hrs
092216_0001, 092216_0002, 092216_0005, 092216_0006, 092216_0008, 092216_0009, 092216_0011, 092216_0012, 092216_0013, 092316_0001, 092316_0002, 092316_0003, 092316_0004, 092316_0005, 092316_0006, 092316_0009, 092316_0010

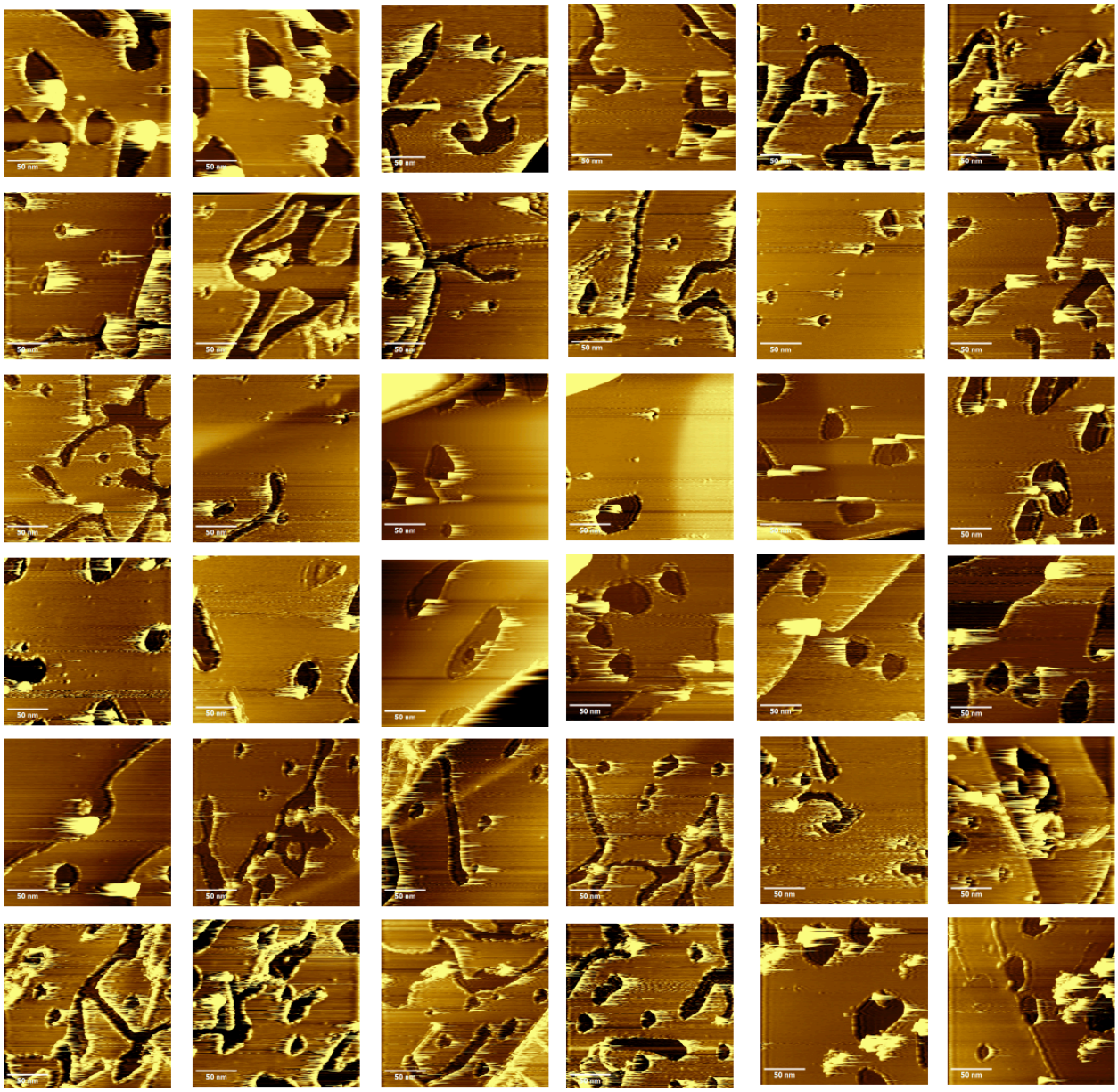


Figure A1.10: Second set of 36 images used in the middle graph of Figure 3.5, Figure 3.6, and the second row of Table 3.1.

Filenames for **Figure A1.10** from top left to bottom right:

Directory: Appendix\A1-11\ 1100C, 0.4eV Beam Trial 1, 14hrs
092616_0005, 092616_0006, 092716_0001, 092716_0002, 092716_0003, 092716_0004, 092716_0010, 092716_0011, 092716_0014, 092716_0015, 092716_0016, 092716_0017, 092716_0018, 092716_0019, 092716_0021, 092716_0022, 092716_0023, 092716_0025, 092716_0026, 092716_0027, 092716_0028, 092816_0001, 092816_0002, 092816_0003, 092816_0004, 092816_0020, 092816_0021, 092816_0022, 092916_0001, 092916_0002, 092916_0003, 092916_0004, 092916_0005, 092916_0006

Directory: Appendix\A1-11\ 1100C, 0.4eV Beam Trial 1, 17.5hrs
093016_0006, 093016_0007

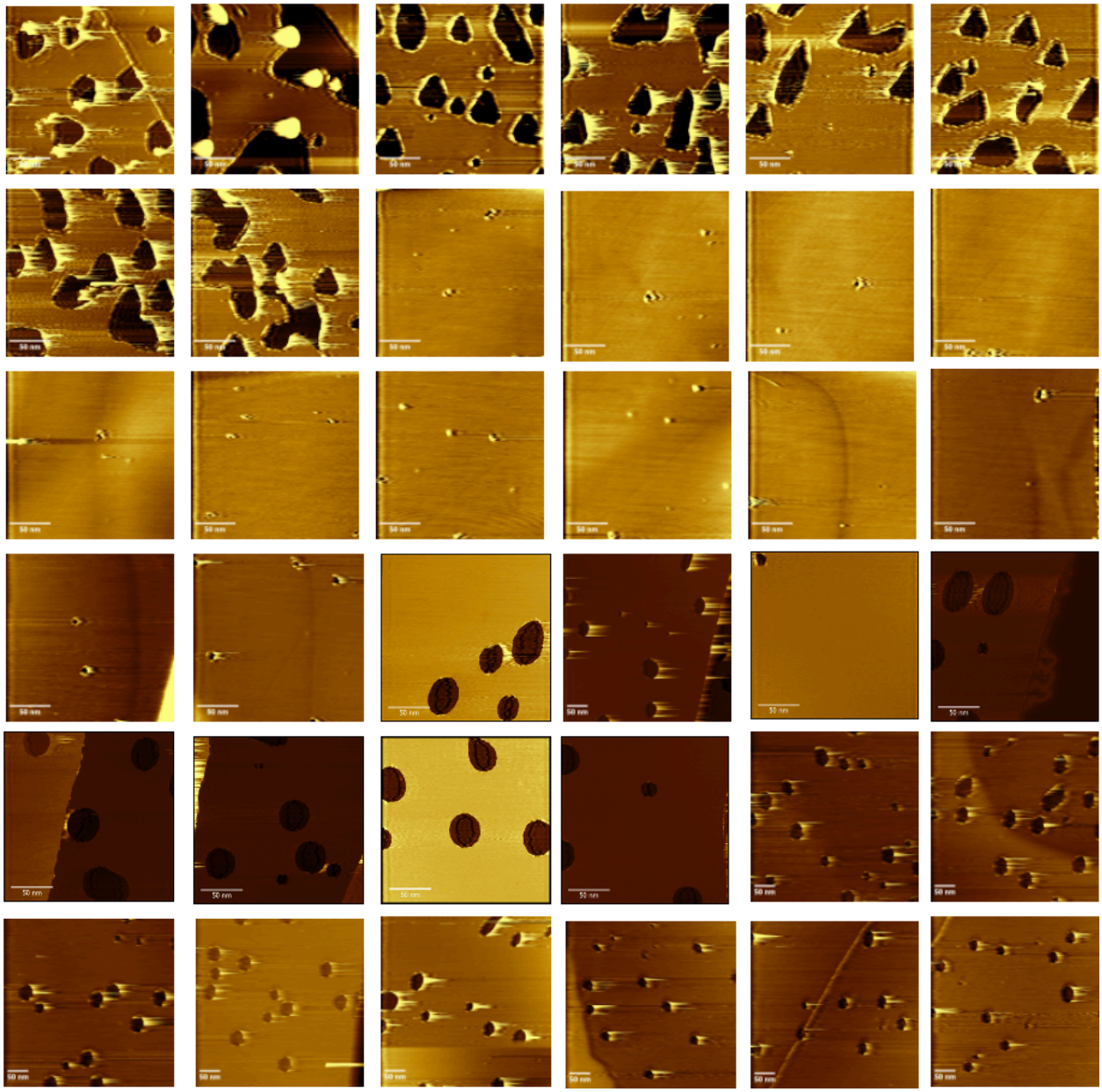


Figure A1.11: Third set of 36 images used in the middle graph of Figure 3.5, Figure 3.6, and the second row of Table 3.1.

Filenames for **Figure A1.11** from top left to bottom right:

Directory: Appendix\A1-12\ 1100C, 0.4eV Beam Trial 1, 17.5hrs
093016_0008, 093016_0009, 093016_0022, 093016_0023, 093016_0024, 093016_0025, 093016_0026, 093016_0027

Directory: Appendix\A1-12\ 1100C, 0.4eV Beam Trial 2, 3.5hrs
012717_0001, 012717_0006, 012717_0009, 012717_0011, 012717_0013, 012717_0015, 012717_0018, 012717_0021, 012717_0022, 012717_0024, 012717_0028, 012717_0030

Directory: Appendix\A1-12\ 1100C, 0.4eV Beam Trial 2, 7hrs
013017_0001, 013017_0002, 013017_0003, 013017_0004, 013017_0005, 013017_0006, 013017_0007, 013017_0008, 013017_0009, 013017_0010, 013017_0011, 013017_0012, 013017_0013, 013017_0014, 013017_0015, 013017_0016

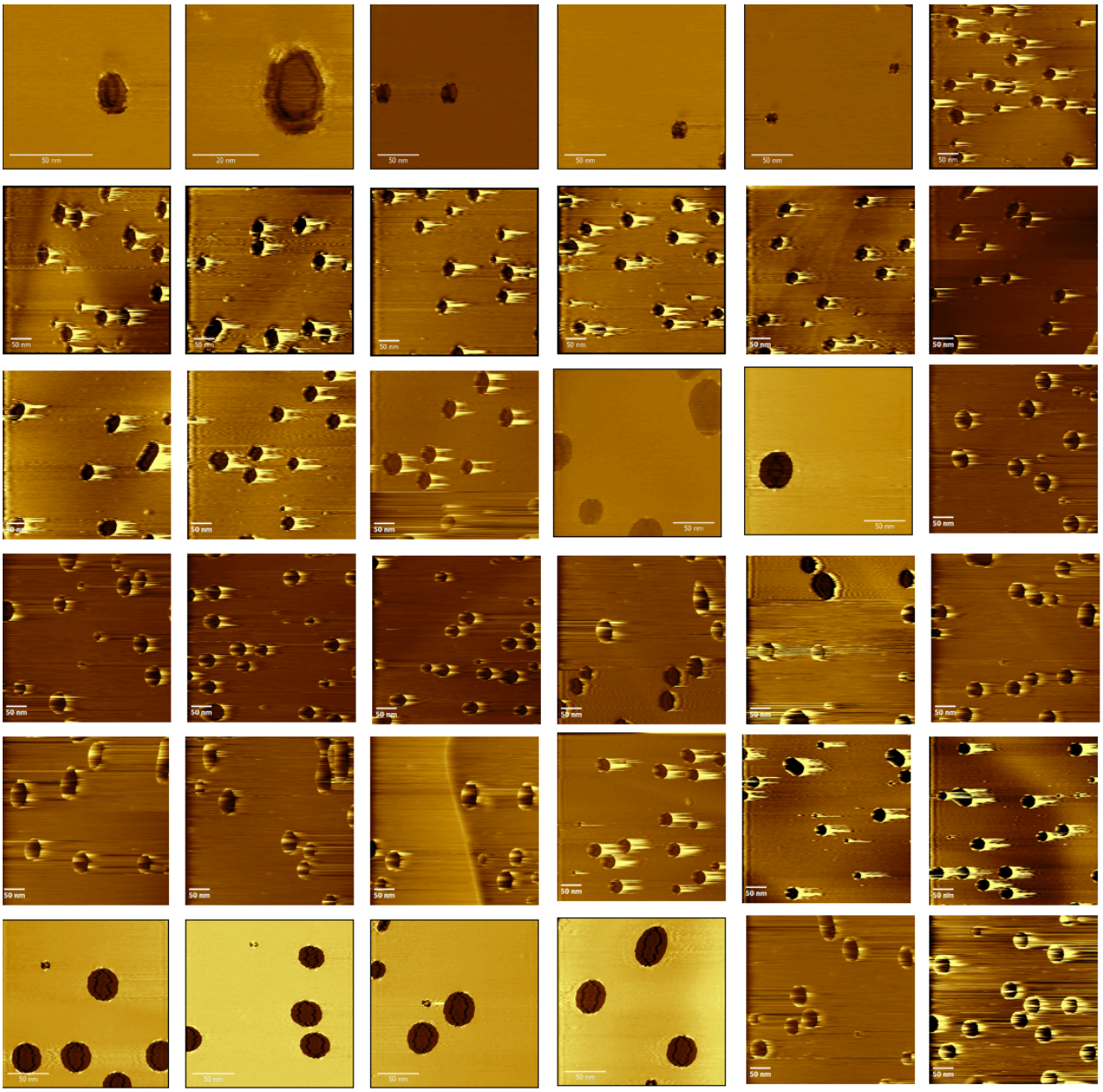


Figure A1.12: Fourth set of 36 images used in the middle graph of Figure 3.5, Figure 3.6, and the second row of Table 3.1.

Filenames for **Figure A1.12** from top left to bottom right:

Directory: Appendix\A1-13\ 1100C, 0.4eV Beam Trial 2, 7hrs
013017_0018, 013017_0019, 013017_0020, 013017_0021, 013017_0022

Directory: Appendix\A1-13\ 1100C, 0.4eV Beam Trial 2, 10.5hrs
013117_0008, 013117_0009, 013117_0010, 013117_0011, 013117_0012, 020117_0001, 020117_0002, 020117_0003, 020117_0004, 020117_0005, 020117_0007, 020117_0008

Directory: Appendix\A1-13\ 1100C, 0.4eV Beam Trial 2, 14hrs
020117_0009, 020117_0010, 020117_0011, 020117_0012, 020117_0013, 020117_0014, 020117_0015, 020117_0016, 020117_0017, 020117_0018, 020217_0001, 020217_0002, 020217_0003, 020217_0004, 020217_0005, 020217_0006, 020217_0007

Directory: Appendix\A1-13\ 1100C, 0.4eV Beam Trial 2, 14hrs
020217_0014, 020217_0015

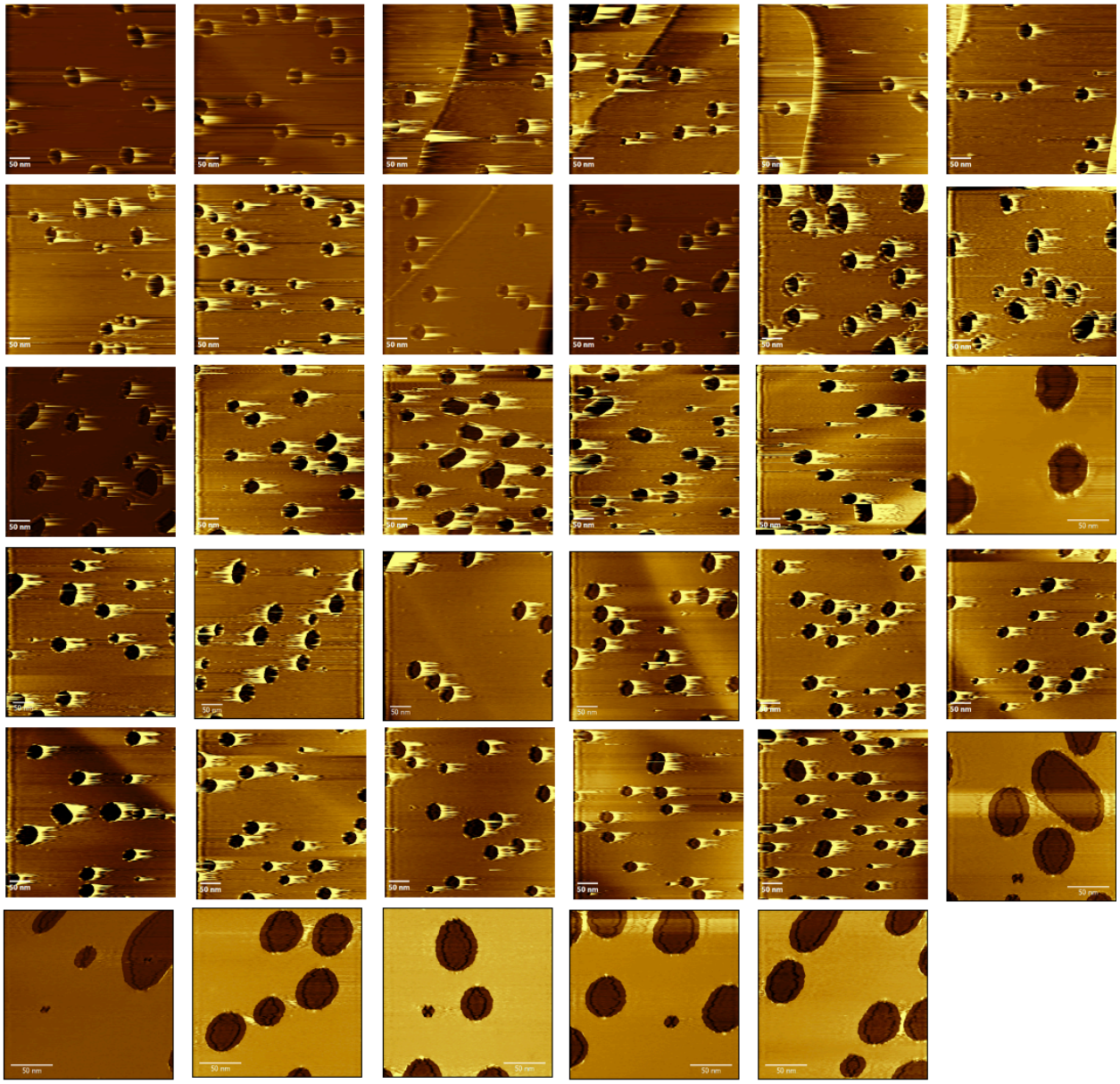


Figure A1.13: Last set of 35 images used in the middle graph of Figure 3.5, Figure 3.6, and the second row of Table 3.1.

Filenames for **Figure A1.13** from top left to bottom right:

Directory: Appendix\A1-14\ 1100C, 0.4eV Beam Trial 2, 17.5hrs
020217_0016, 020217_0017, 020317_0001, 020317_0002, 020317_0003, 020317_0004, 020317_0005, 020317_0006, 020317_0007, 020317_0008, 020317_0009, 020317_0010, 020317_0011, 020317_0012, 020317_0013, 020317_0014, 020317_0015, 020317_0017

Directory: Appendix\A1-14\ 1100C, 0.4eV Beam Trial 2, 21hrs
020617_0018, 020617_0019, 020617_0020, 020617_0021, 020617_0022, 020617_0023, 020617_0024, 020617_0025, 020617_0026, 020617_0027, 020617_0028, 020717_0001, 020717_0002, 020717_0003, 020717_0004, 020717_0005, 020717_0006

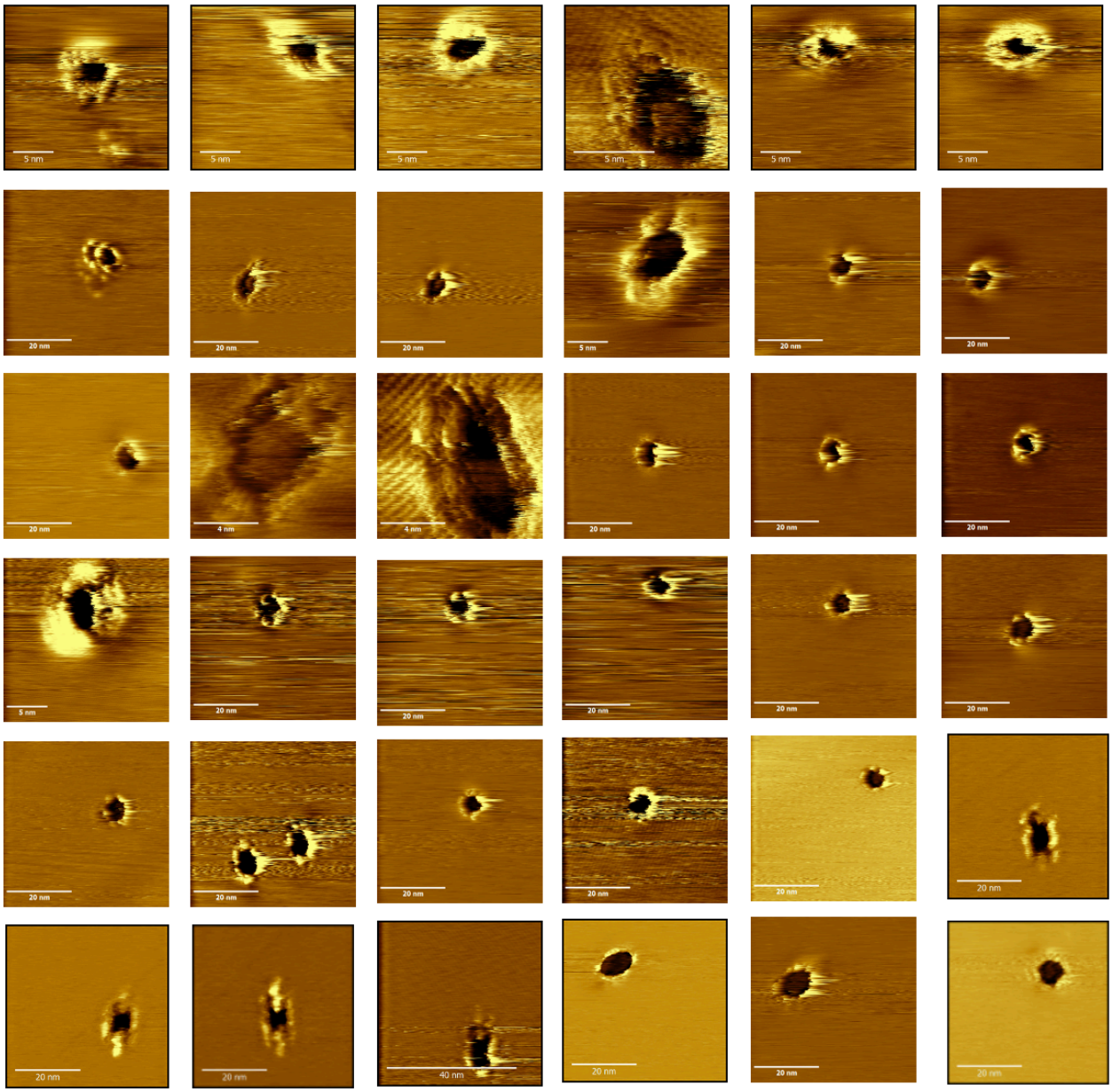


Figure A1.14: First set of 36 images used in the bottom graph of Figure 3.5 and the third row of Table 3.1.

Filenames for **Figure A1.14** from top left to bottom right:

Directory: Appendix\A1-15\ 1200C, 0.4eV Beam, 3hrs
080817_0007, 080817_0008, 080817_0009, 080817_0010, 080817_0011, 080817_0012

Directory: Appendix\A1-15\ 1200C, 0.4eV Beam, 6hrs
080917_0002, 080917_0004, 080917_0005, 080917_0006, 080917_0007, 080917_0008, 080917_0009, 080917_0014, 080917_0015, 080917_0016, 080917_0018, 080917_0019, 080917_0020

Directory: Appendix\A1-15\ 1200C, 0.4eV Beam, 9hrs
081017_0000, 081017_0001, 081017_0002, 081017_0003, 081017_0004, 081017_0005, 081017_0006, 081017_0007, 081017_0008, 081017_0009

Directory: Appendix\A1-15\ 1200C, 0.4eV Beam, 9hrs
081117_0002, 081117_0003, 081117_0005, 081117_0007, 081117_0008, 081117_0009, 081117_0010

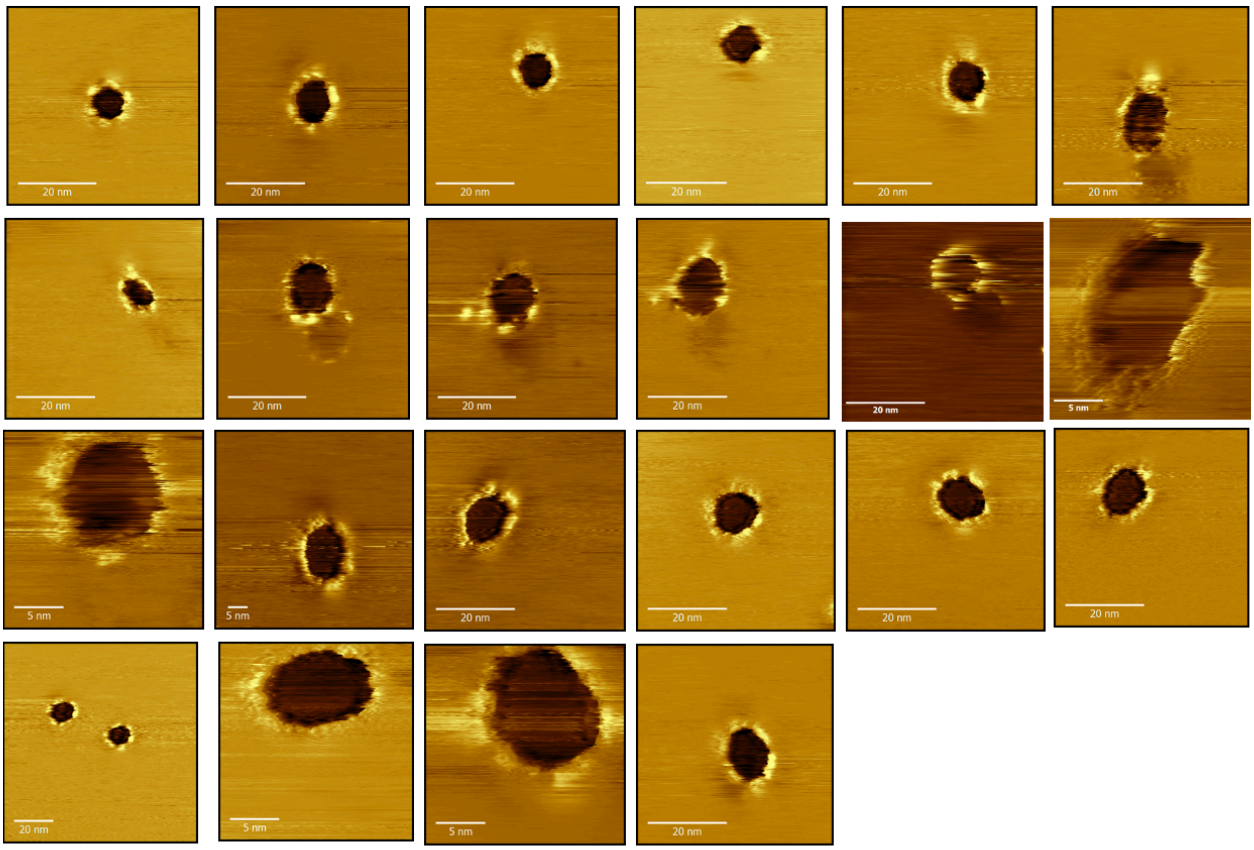


Figure A1.15: Last set of 22 images used in the bottom graph of Figure 3.5 and the third row of Table 3.1.

Filenames for **Figure A1.15** from top left to bottom right:

Directory: Appendix\A1-16\1200C, 0.4eV Beam, 15hrs
081117_0012, 081117_0014, 081117_0015, 081117_0017 081117_0019

Directory: Appendix\A1-16\1200C, 0.4eV Beam, 24hrs
081417_0001, 081417_0002, 081417_0003, 081417_0004, 081417_0005, 081417_0007, 081417_0009, 081417_0010, 081417_0011, 081417_0012, 081417_0013, 081417_0015, 081417_0016, 081417_0018, 081417_0020, 081417_0021, 081417_0022

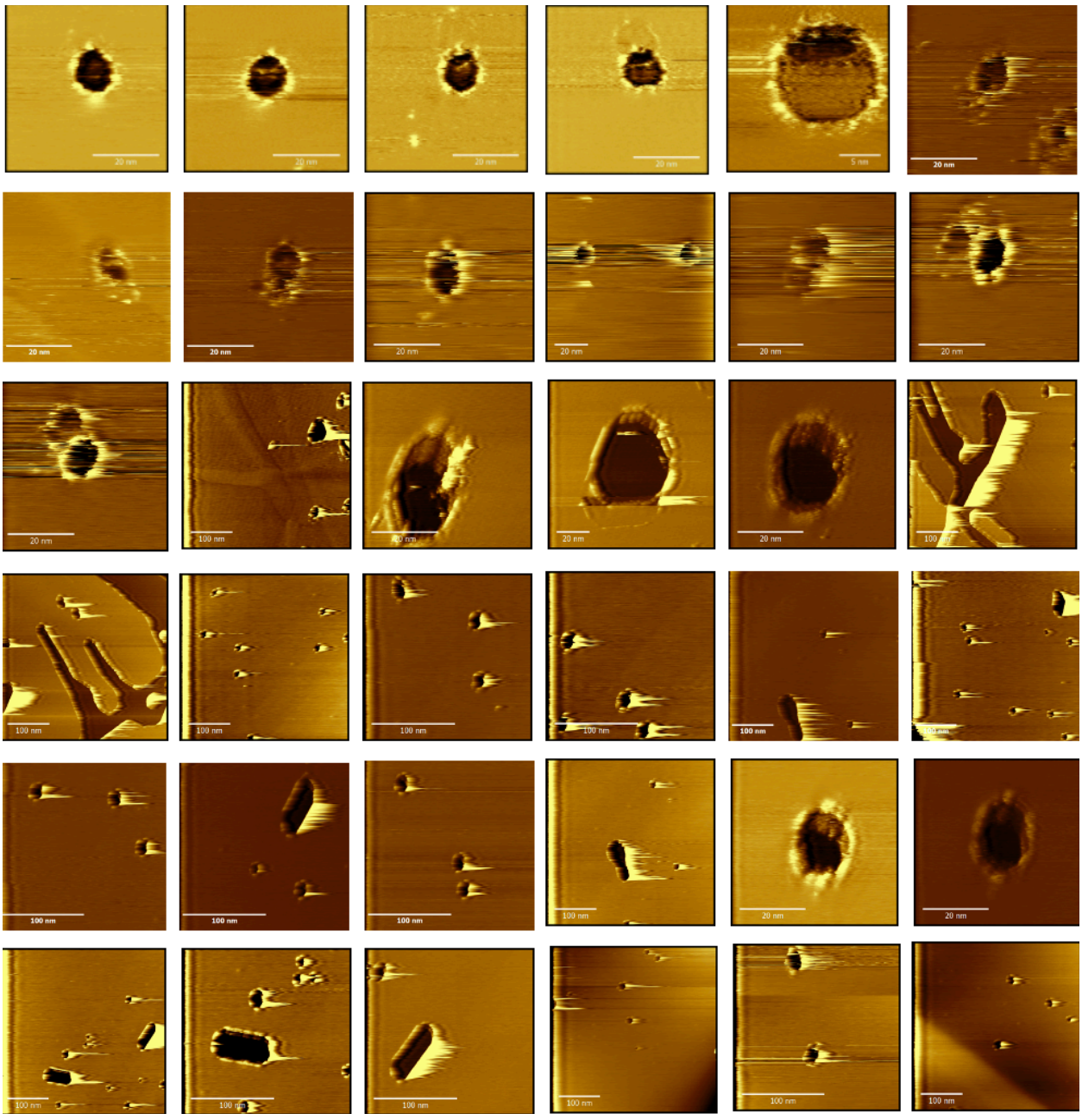


Figure A1.16: First set of 36 images used in the fourth row of Table 3.1.

Filenames for **Figure A1.16** from top left to bottom right:

Directory: Appendix\A1-17\ 45 Degree, 1100C, 0.4eV Beam, 12hrs
051517_0008, 051517_0009, 051517_0011, 051517_0012, 051517_0013, 053117_0001, 053117_0003, 053117_0004, 053117_0006, 053117_0007, 053117_0008, 053117_0009, 053117_0010

Directory: Appendix\A1-17\ 45 Degree, 1100C, 0.4eV Beam, 16hrs
060117_0027, 060117_0028, 060117_0029, 060117_0030, 060117_0031, 060117_0032, 060217_0001, 060217_0002, 060217_0003, 060217_0004, 060217_0005, 060217_0006, 060217_0007, 060217_0011, 060217_0012, 060217_0014, 060217_0015, 060217_0016, 060217_0017, 060217_0018, 060217_0021, 060217_0022, 060217_0024

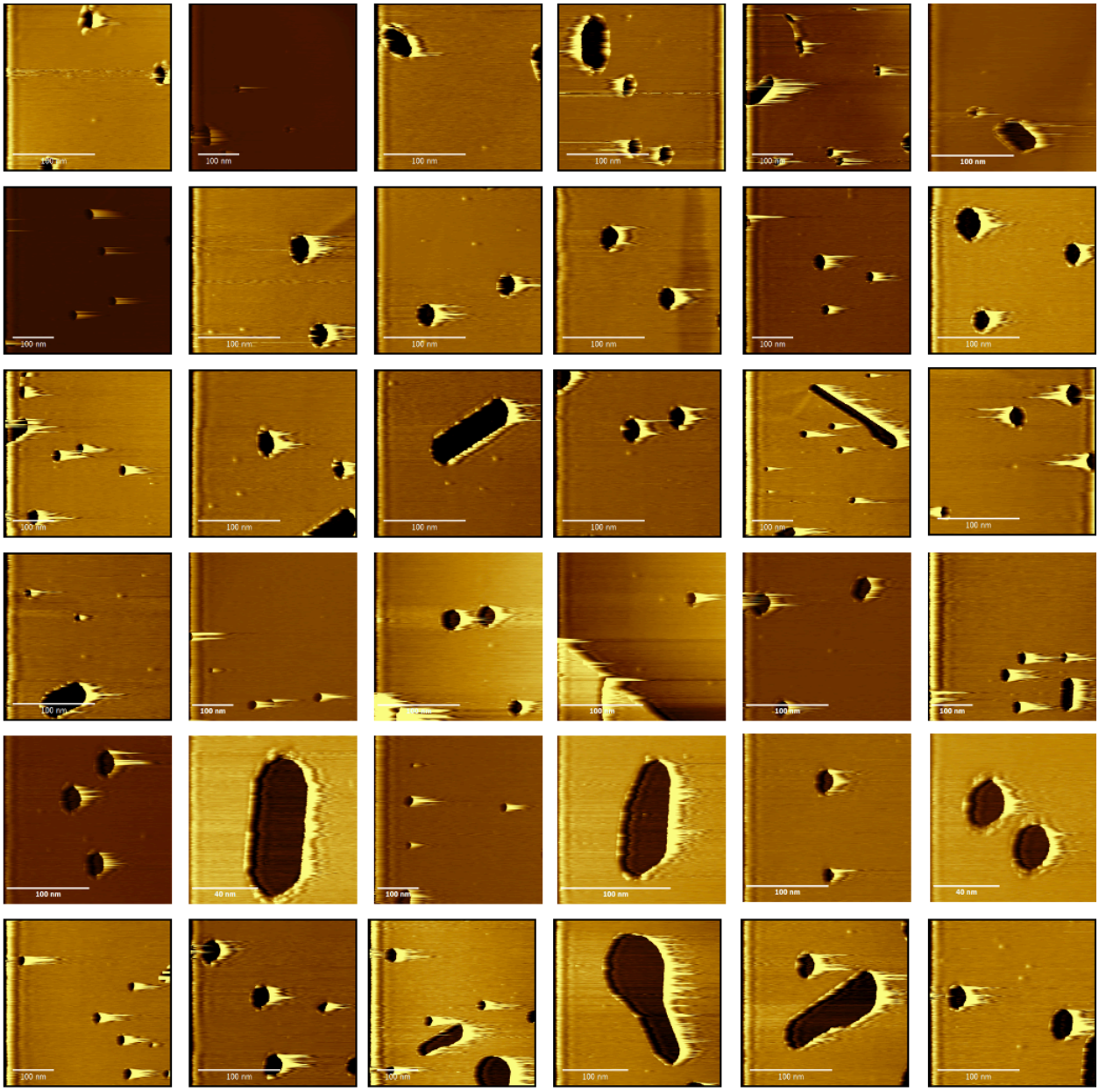


Figure A1.17: Second set of 36 images used in the fourth row of Table 3.1.

Filenames for **Figure A1.17** from top left to bottom right:

Directory: Appendix\ A1-18\ 45 Degree, 1100C, 0.4eV Beam, 16hrs
060217_0025,
060217_0026,
060217_0027,
060217_0028, 060217_0029, 060217_0030
Directory: Appendix\ A1-18\ 45 Degree, 1100C, 0.4eV Beam, 19hrs
060317_0001,
060317_0002,
060317_0003,
060317_0004, 060317_0005, 060317_0006, 060317_0007, 060317_0008, 060317_0009, 060317_0010, 060317_0011, 060317_0012, 060317_0013, 060317_0014, 060517_0001, 060517_0002, 060517_0003, 060517_0004, 060517_0005, 060517_0008, 060517_0009, 060517_0010, 060517_0011, 060517_0012, 060517_0013, 060517_0014, 060517_0015, 060517_0017, 060517_0018, 060517_0019

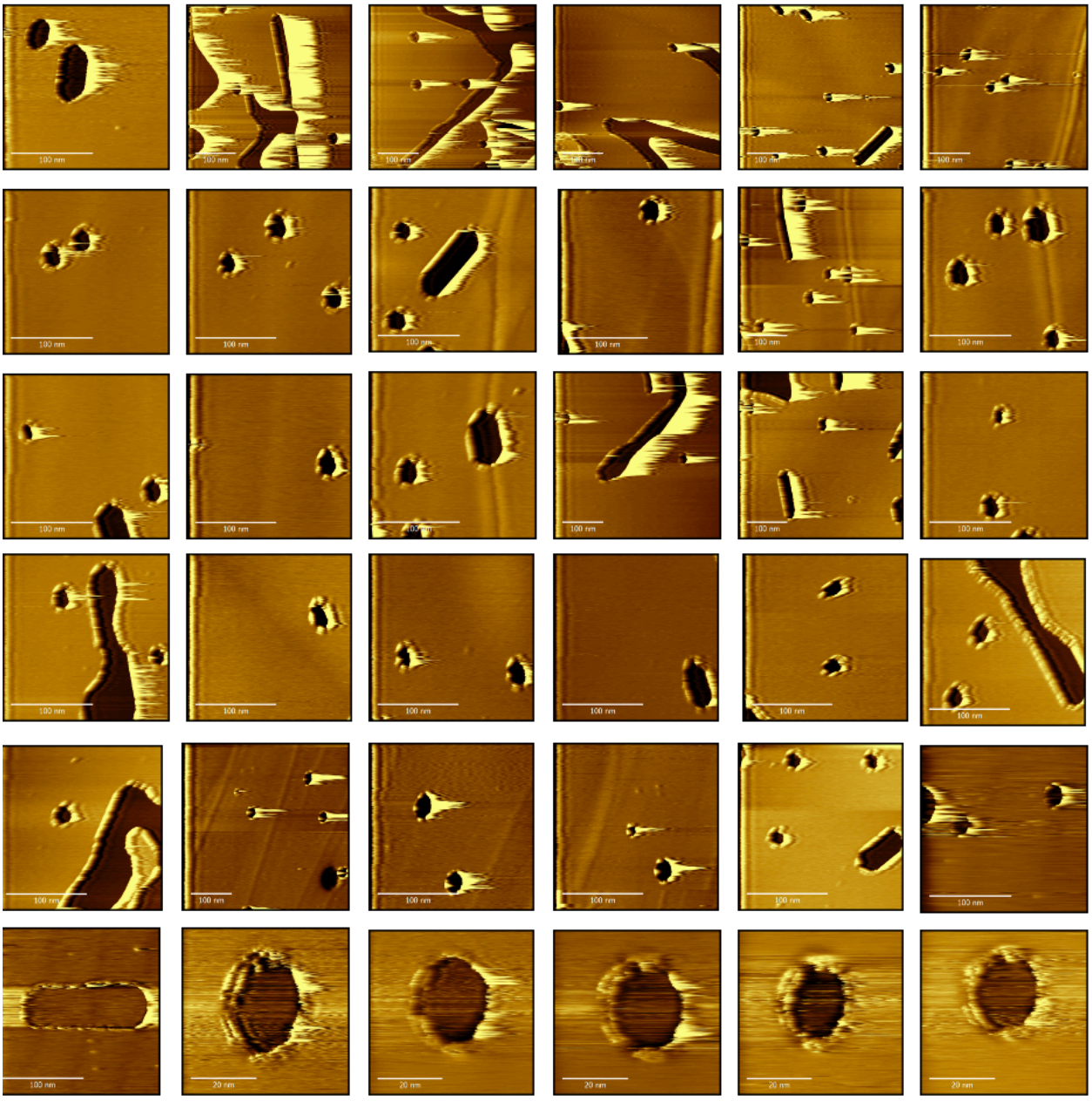


Figure A1.18: Third set of 36 images used in the fourth row of Table 3.1.

Filenames for **Figure A1.18** from top left to bottom right:

Directory: Appendix\ A1-19\ 45 Degree, 1100C, 0.4eV Beam, 19hrs
060517_0020

Directory: Appendix\ A1-19\ 45 Degree, 1100C, 0.4eV Beam, 22hrs
060517_0021, 060517_0022, 060517_0023, 060517_0024, 060517_0025, 060517_0026, 060517_0027, 060517_0028, 060517_0029, 060517_0030, 060517_0031, 060517_0032, 060517_0033, 060517_0034, 060517_0035, 060517_0036, 060517_0037, 060517_0038, 060517_0039, 060517_0040, 060517_0041, 060517_0042, 060517_0043, 060517_0044, 060517_0045, 060517_0046, 060517_0047, 060517_0048, 060617_0001, 060617_0002, 060617_0003, 060617_0004, 060617_0005, 060617_0006, 060617_0007

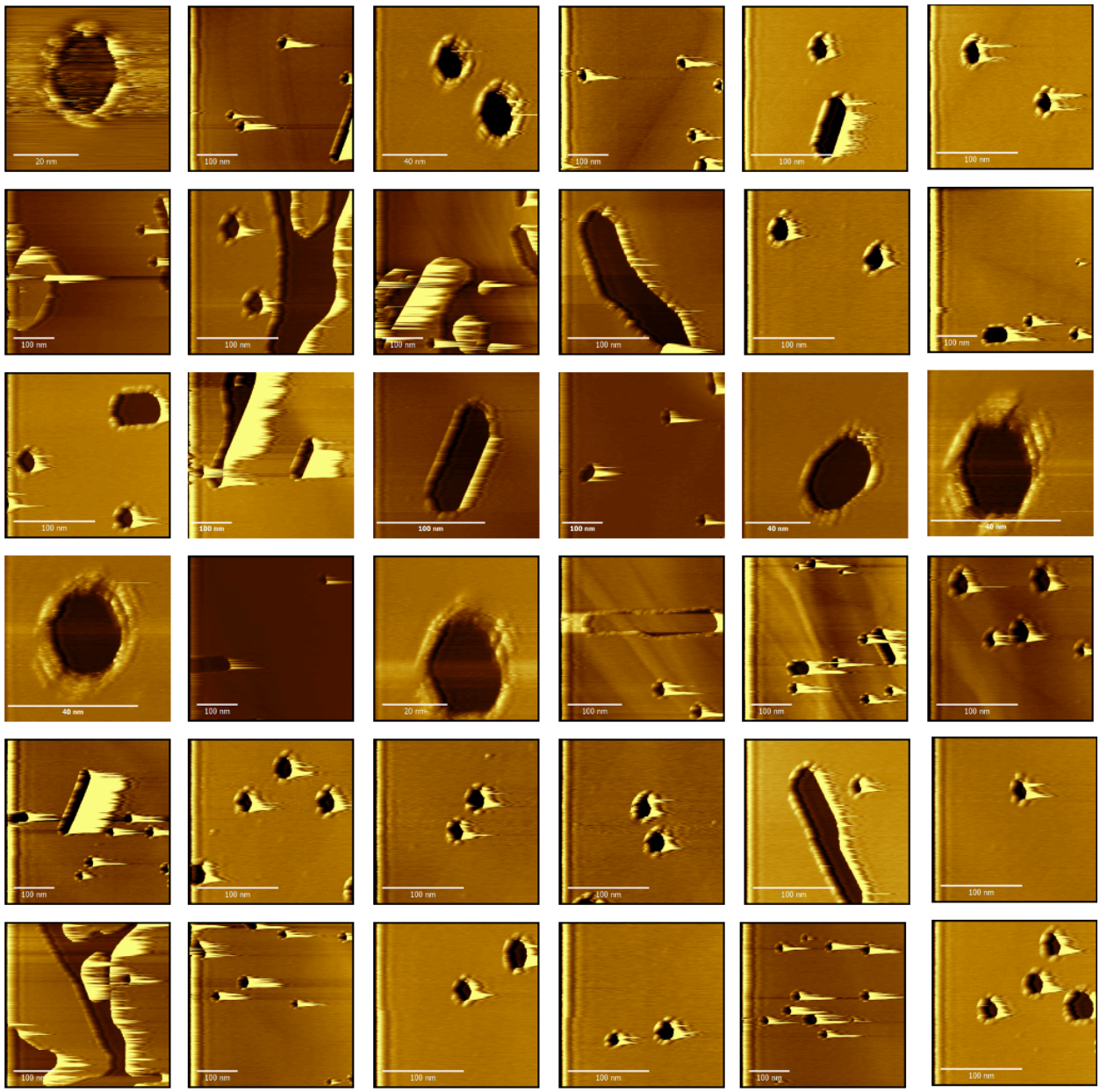


Figure A1.19: Fourth set of 36 images used in the fourth row of Table 3.1.

Filenames for **Figure A1.19** from top left to bottom right:

Directory: Appendix\ A1-20\ 45 Degree, 1100C, 0.4eV Beam, 22hrs
060617_0008

Directory: Appendix\ A1-20\ 45 Degree, 1100C, 0.4eV Beam, 26hrs
060617_0009, 060617_0010, 060617_0013, 060617_0014, 060617_0015, 060717_0001, 060717_0002, 060717_0003, 060717_0004, 060717_0005, 060717_0006, 060717_0007, 060717_0008, 060717_0009, 060717_0010, 060717_0011, 060717_0012, 060717_0013, 060717_0014, 060717_0015, 060717_0016, 060717_0017, 060717_0018, 060717_0019, 060717_0020, 060717_0021, 060717_0022, 060717_0023, 060717_0024, 060717_0025, 060717_0026, 060717_0027, 060717_0028, 060717_0029, 060717_0030

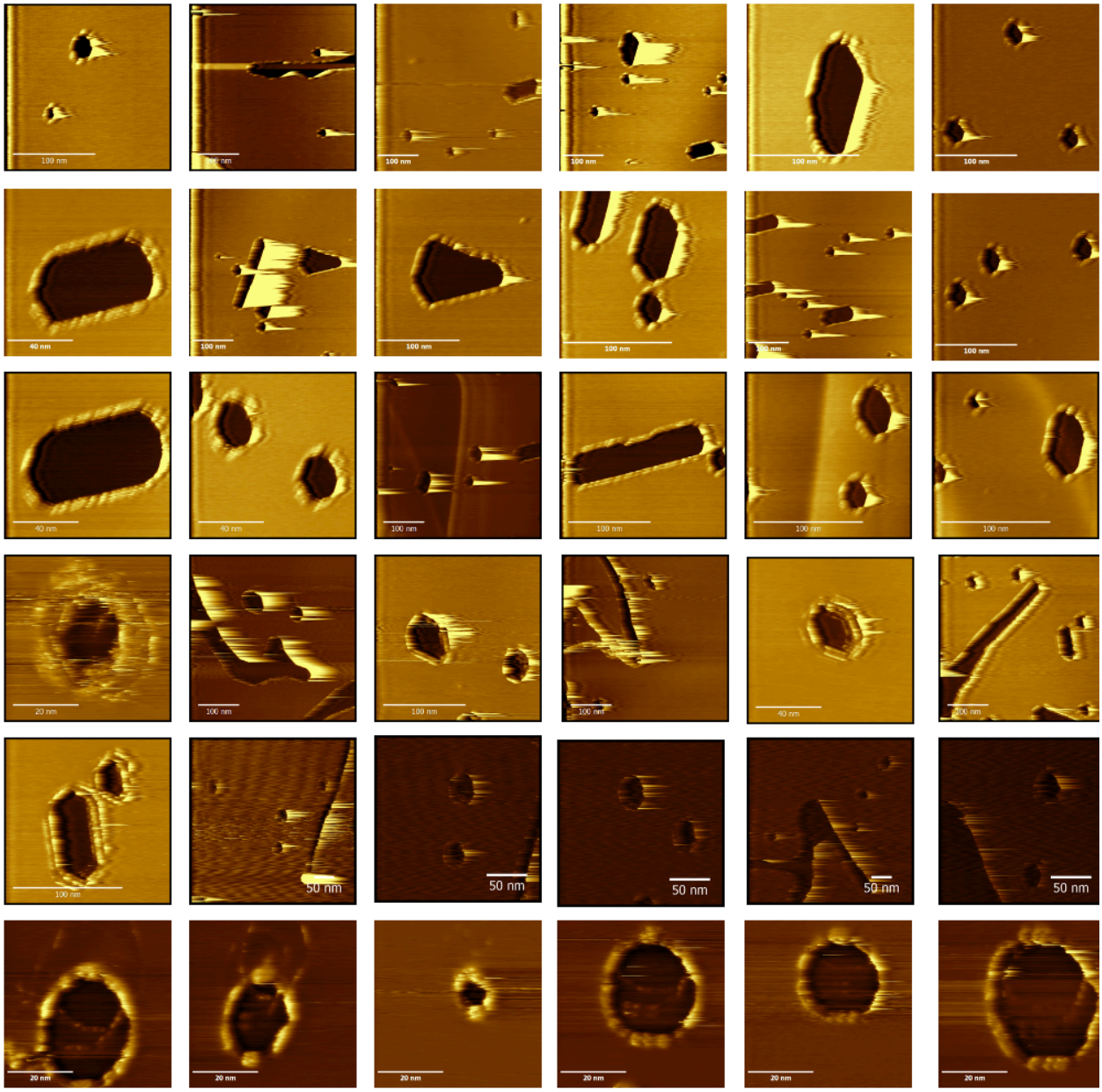


Figure A1.20: Fifth set of 36 images used in the fourth row of Table 3.1.

Filenames for **Figure A1.20** from top left to bottom right:

Directory: Appendix\ A1-21\ 45 Degree, 1100C, 0.4eV Beam, 26hrs
060717_0031, 060717_0032, 060717_0033, 060717_0035, 060717_0036, 060717_0037, 060717_0038, 060717_0039, 060717_0040, 060717_0041, 060717_0042, 060717_0043, 060717_0044, 060717_0045, 060717_0046, 060717_0047, 060717_0048, 060717_0049

Directory: Appendix\ A1-21\ 45 Degree, 1100C, 0.4eV Beam, 31hrs
060817_0002, 060817_0003, 060817_0004, 060817_0005, 060817_0006, 060817_0007, 060817_0008, 061217_0001, 061217_0002, 061217_0003, 061217_0004, 061217_0005, 061217_0006, 061217_0007, 061217_0008, 061217_0009, 061217_0010, 061217_0011

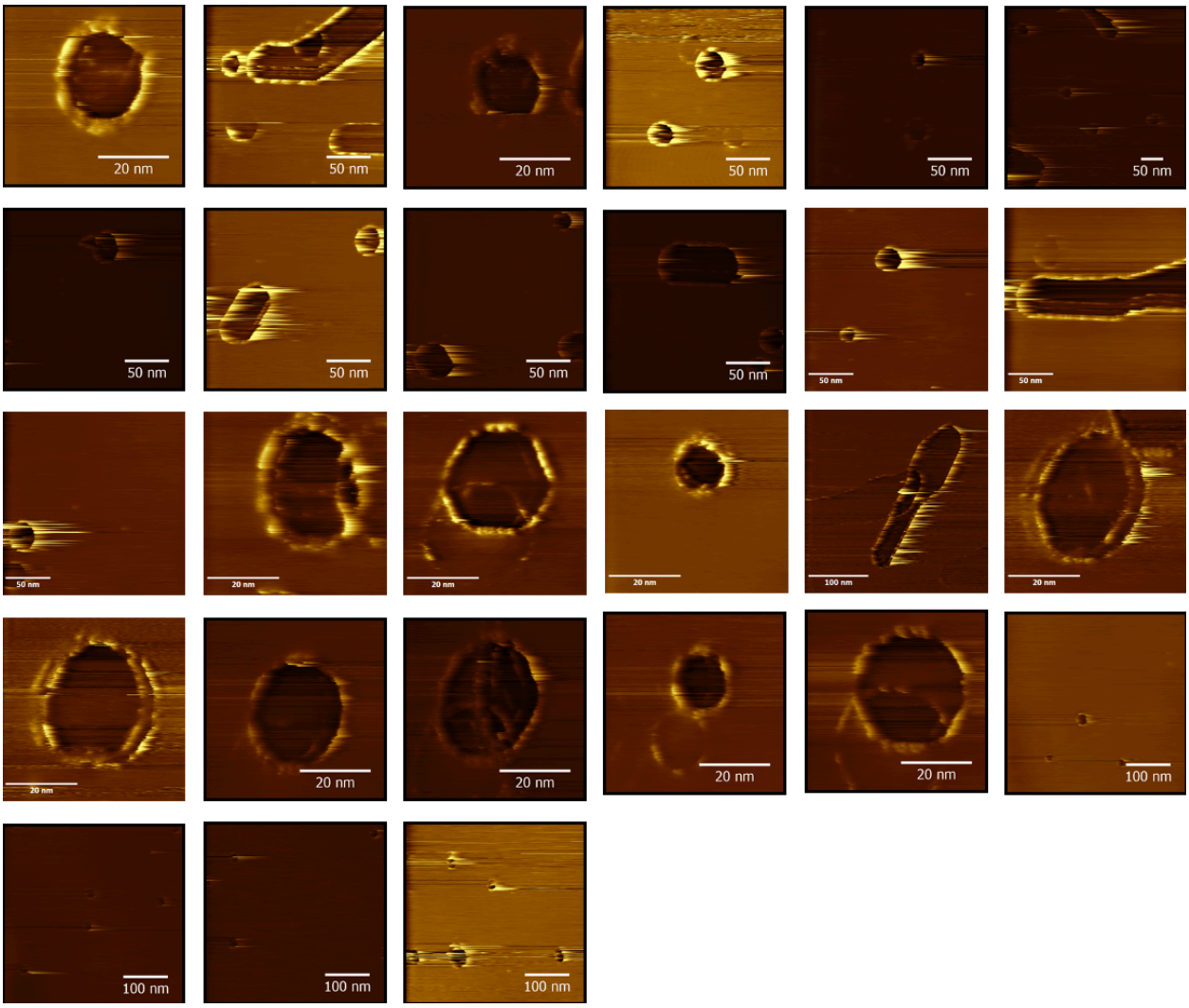


Figure A1.21: Last set of 27 images used in the fourth row of Table 3.1.

Filenames for **Figure A1.21** from top left to bottom right:

Directory: Appendix\ A1-22\ 45 Degree, 1100C, 0.4eV Beam, 31hrs
061217_0013, 061217_0015, 061217_0016, 061217_0018, 061217_0019, 061217_0020, 061217_0021, 061217_0022, 061217_0023 061217_0024, 061217_0026, 061217_0030, 061217_0032, 061217_0033, 061217_0034 061217_0036, 061217_0037, 061217_0039, 061217_0040, 061217_0042, 061217_0043 061217_0044, 061217_0045, 061317_0001, 061317_0002, 061317_0003, 061317_0004

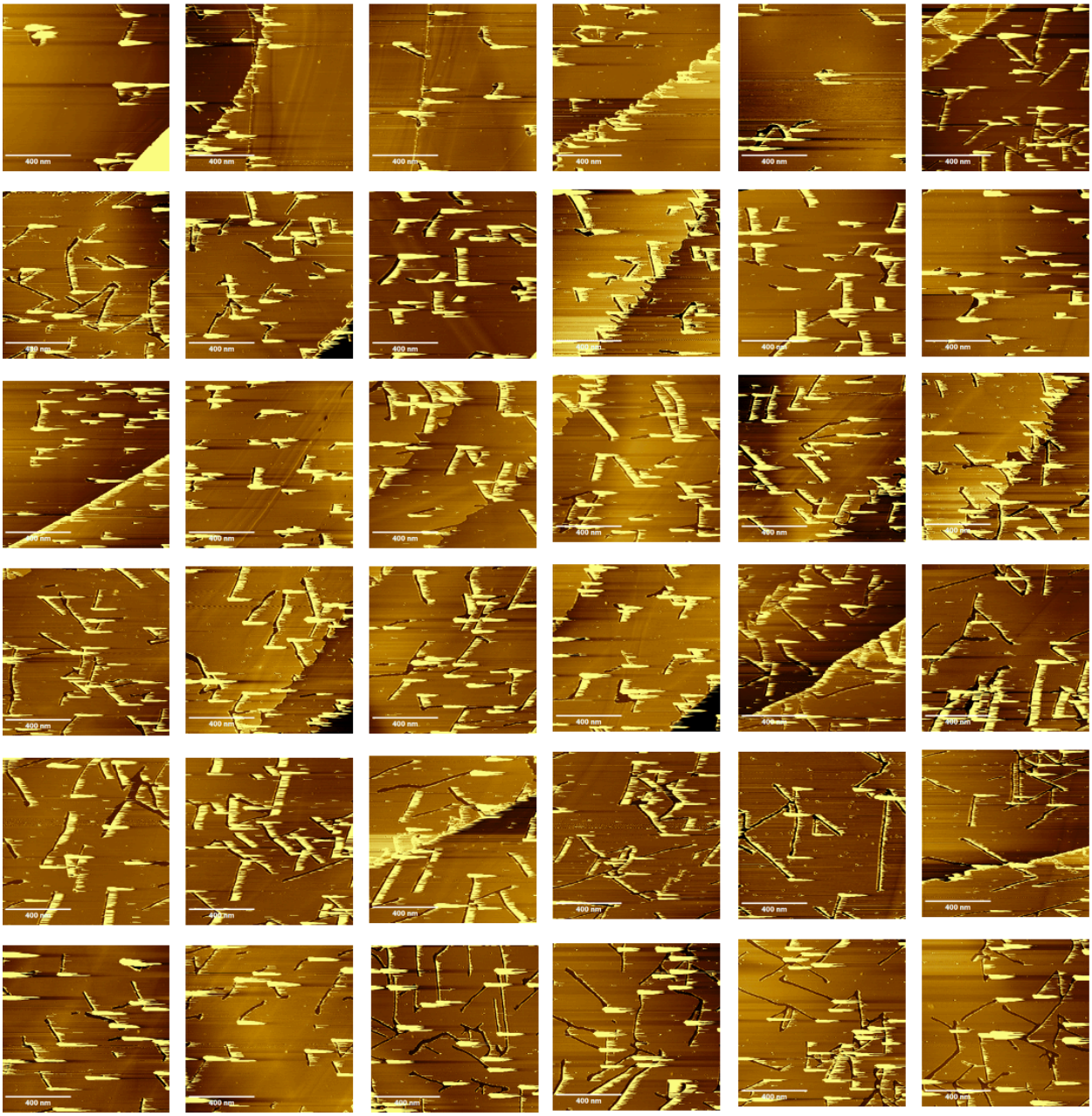


Figure A1.22: First set of 36 images used in the fifth row of Table 3.1.

Filenames for **Figure A1.22** from top left to bottom right:

Directory: Appendix\ A1-22\ 1000C, 0.7eV Beam, 2.5hrs
110617_0001, 110617_0002, 110617_0003, 110617_0004, 110617_0005, 110617_0007, 110617_0008

Directory: Appendix\ A1-22\ 1000C, 0.7eV Beam, 3.5hrs
110717_0001, 110717_0002, 110717_0003, 110717_0004, 110717_0005, 110717_0006, 110717_0007, 110717_0008, 110717_0009, 110717_0010, 110717_0011, 110717_0012, 110717_0013, 110717_0014

Directory: Appendix\ A1-22\ 1000C, 0.7eV Beam, 5.5hrs
110817_0001, 110817_0002, 110817_0003, 110817_0004, 110817_0005, 110817_0006, 110817_0007, 110817_0008, 110817_0009, 110817_0011, 110817_0012

Directory: Appendix\ A1-22\ 1000C, 0.7eV Beam, 8.5hrs
110917_0001, 110917_0002, 110917_0003, 110917_0004

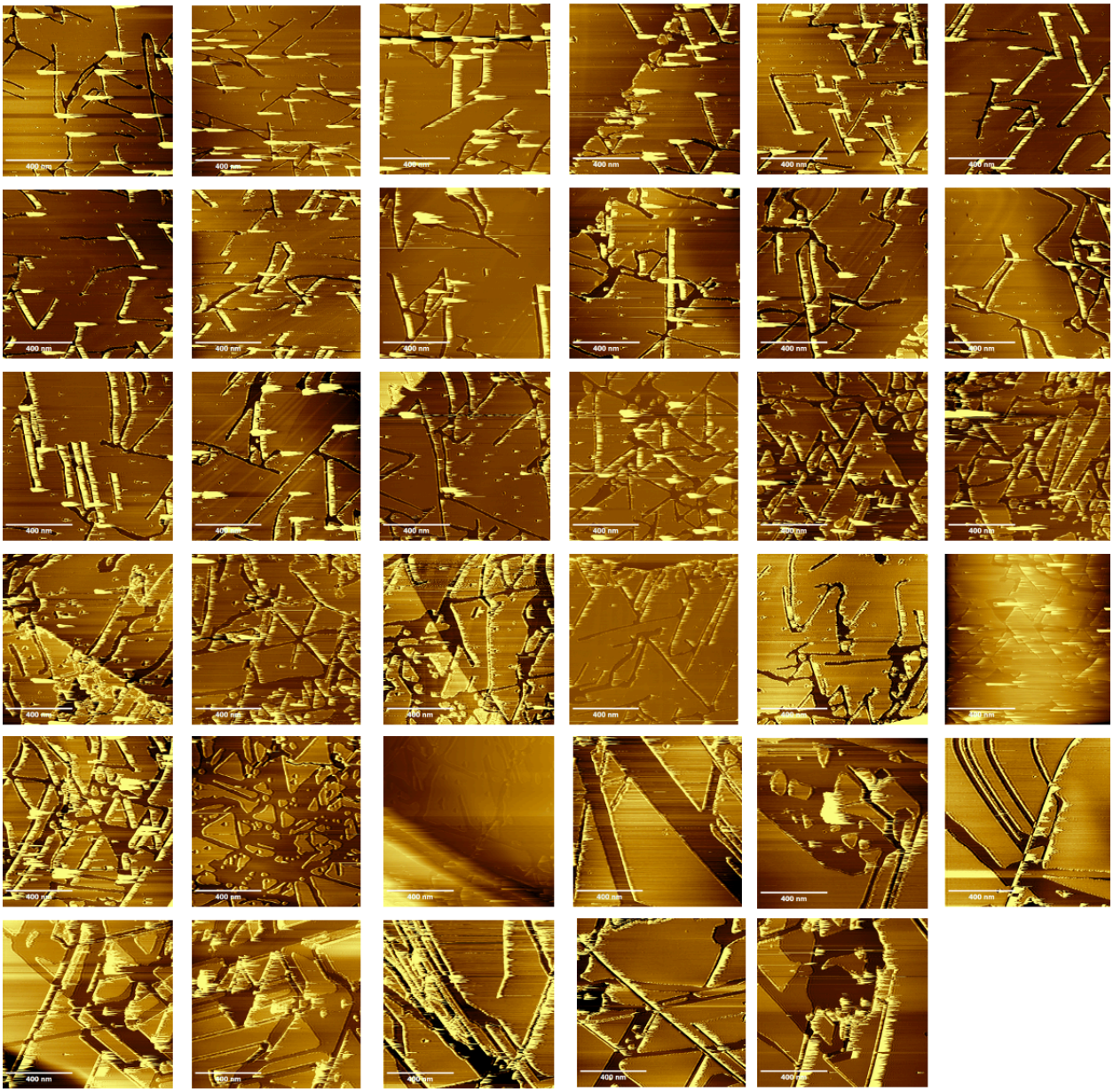


Figure A1.23: Last set of 35 images used in the fifth row of Table 3.1.

Filenames for **Figure A1.23** from top left to bottom right:

Directory: Appendix\ A1-23\ 1000C, 0.7eV Beam, 8.5hrs
110917_0005, 110917_0006, 110917_0007, 110917_0010, 110917_0011, 110917_0012, 110917_0013, 110917_0014

Directory: Appendix\ A1-23\ 1000C, 0.7eV Beam, 13.5hrs
111017_0001, 111017_0002, 111017_0003, 111017_0004, 111017_0005, 111017_0006, 111017_0007, 111017_0008, 111317_0001, 111317_0002, 111317_0003, 111317_0004, 111317_0005, 111317_0006, 111317_0007, 111317_0008

Directory: Appendix\ A1-23\ 1000C, 0.7eV Beam, 18.5hrs
111417_0001, 111417_0007, 111417_0008, 111517_0001, 111517_0002, 111517_0003, 111517_0004, 111517_0005, 111517_0006, 111517_0007, 111517_0008

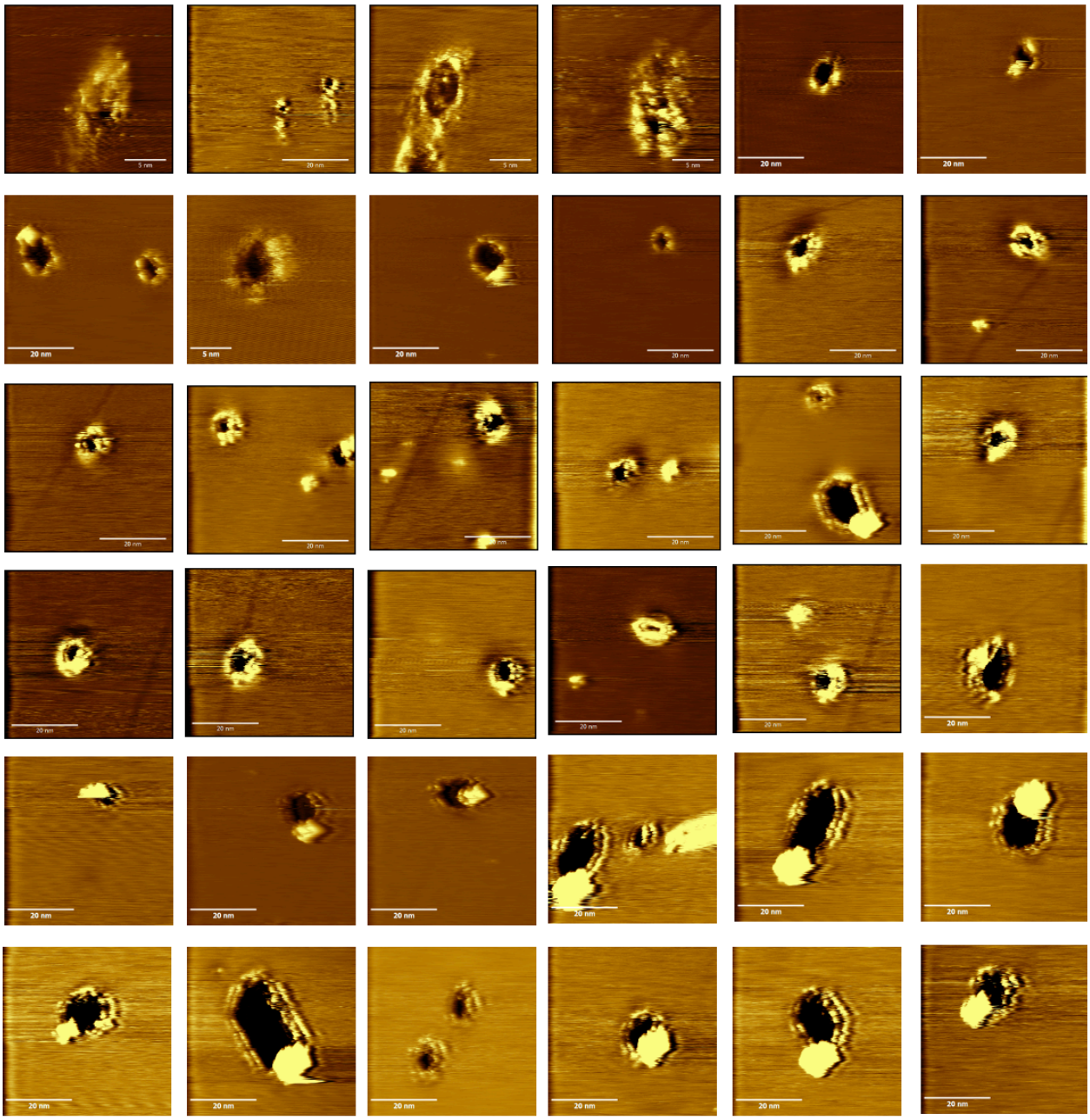


Figure A1.24: First set of 36 images used in Figure 3.6 and the sixth row of Table 3.1.

Filenames for **Figure A1.24** from top left to bottom right:

Directory: Appendix\A1-25\1100C, 0.7eV Beam Trial 2, 30min
072117_0004, 072117_0005, 072117_0008, 072117_0009

Directory: Appendix\A1-25\1100C, 0.7eV Beam Trial 2, 60min
072117_0011, 072117_0012, 072117_0013, 072117_0014, 072117_0015, 072117_0016, 072317_0001, 072317_0002, 072317_0003, 072317_0005, 072317_0006, 072317_0008, 072317_0010, 072317_0011, 072317_0012, 072317_0014, 072317_0015, 072317_0016, 072317_0017

Directory: Appendix\A1-25\1100C, 0.7eV Beam Trial 2, 90min
072417_0002, 072417_0003, 072417_0005, 072417_0006, 072417_0007, 072417_0009, 072417_0010, 072417_0012, 072417_0014, 072417_0015, 072417_0016, 072417_0018, 072417_0019

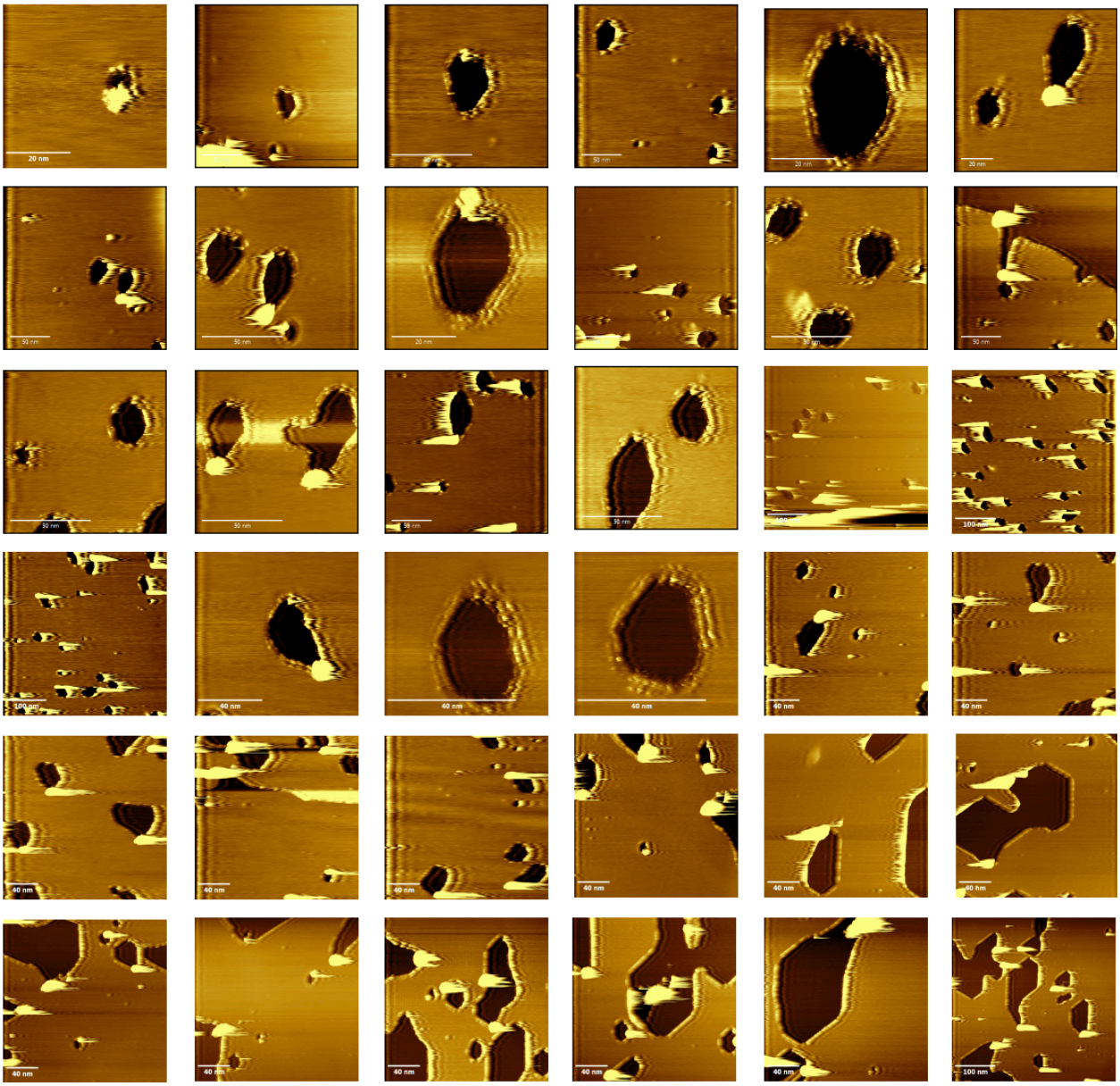


Figure A1.25: Second set of 36 images used in Figure 3.6 and the sixth row of Table 3.1.

Filenames for **Figure A1.25** from top left to bottom right:

Directory: Appendix\A1-26\1100C, 0.7eV Beam Trial 2, 90min
072417_0021, 072417_0022, 072417_0023, 072417_0024, 072417_0025, 072417_0026, 072417_0027, 072417_0028, 072417_0029, 072417_0030, 072417_0031, 072417_0032, 072417_0033, 072417_0034, 072417_0035, 072417_0036, 072417_0037, 072417_0038, 072417_0039, 072417_0040, 072417_0041, 072417_0042, 072417_0043, 072417_0044, 072417_0045, 072417_0046, 072417_0047

Directory: Appendix\A1-26\1100C, 0.7eV Beam Trial 2, 120min
072517_0006, 072517_0007, 072517_0008, 072517_0009, 072517_0010, 072517_0013, 072517_0014, 072517_0016, 072517_0017

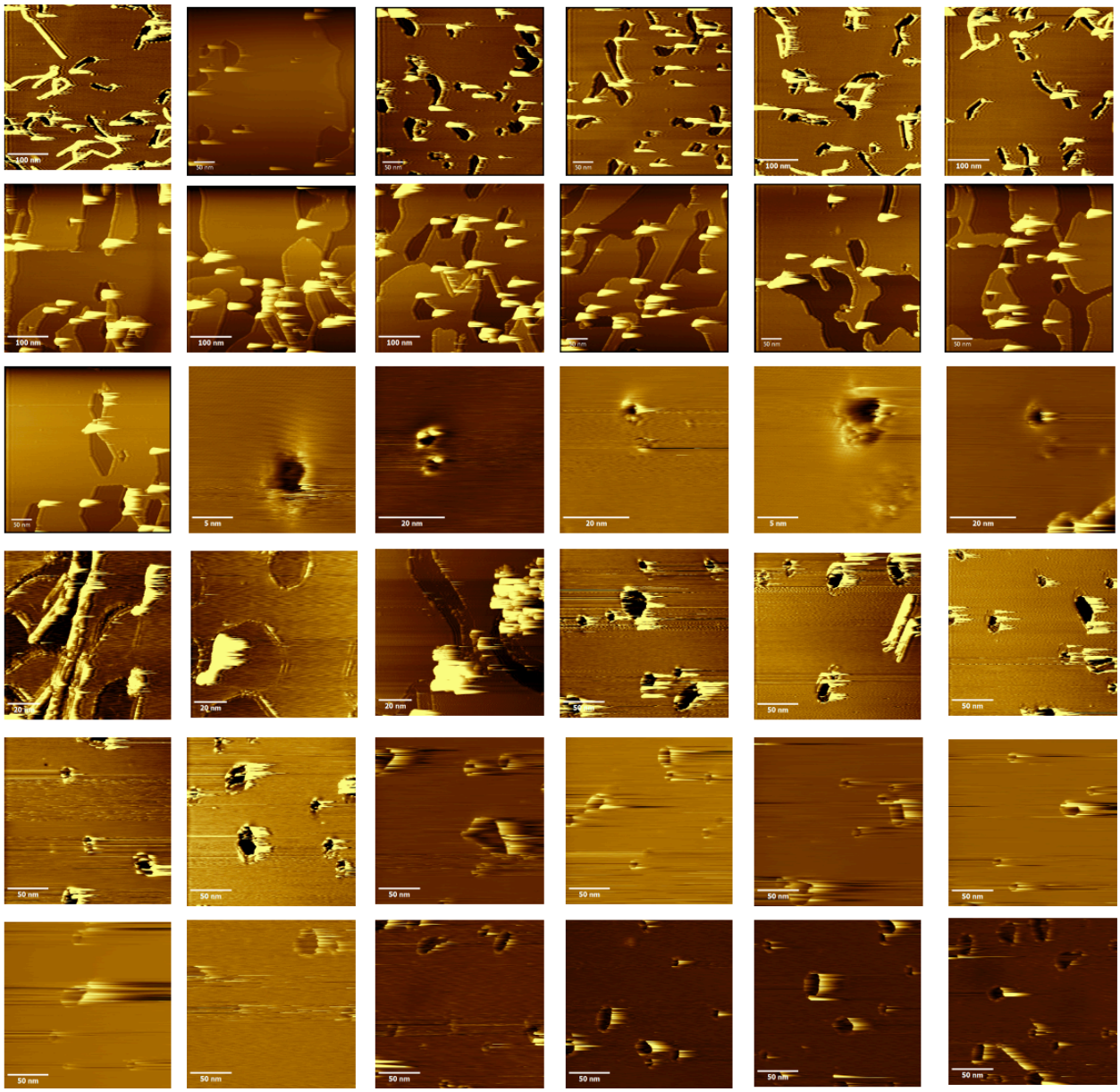


Figure A1.26: Third set of 36 images used in Figure 3.6 and the sixth row of Table 3.1.

Filenames for **Figure A1.26** from top left to bottom right:

Directory: Appendix\A1-27\1100C, 0.7eV Beam Trial 2, 120min
072517_0018, 072517_0020, 072517_0021

Directory: Appendix\A1-27\1100C, 0.7eV Beam Trial 2, 150min
072517_0022, 072517_0023, 072517_0024, 072517_0026, 072517_0027, 072517_0028, 072517_0029, 072517_0030, 072517_0031, 072517_0032

Directory: Appendix\A1-27\1100C, 0.7eV Beam Trial 3, 30min
081717_0001, 081717_0003, 081717_0004, 081717_0005, 081717_0006

Directory: Appendix\A1-27\1100C, 0.7eV Beam Trial 3, 90min
081817_0001, 081817_0002, 081817_0003, 081817_0004, 081817_0005, 081817_0006, 081817_0007, 081817_0008, 082117_0004, 082117_0006, 082117_0008, 082117_0009, 082117_0011, 082117_0013, 082117_0014, 082117_0016, 082117_0017, 082117_0018

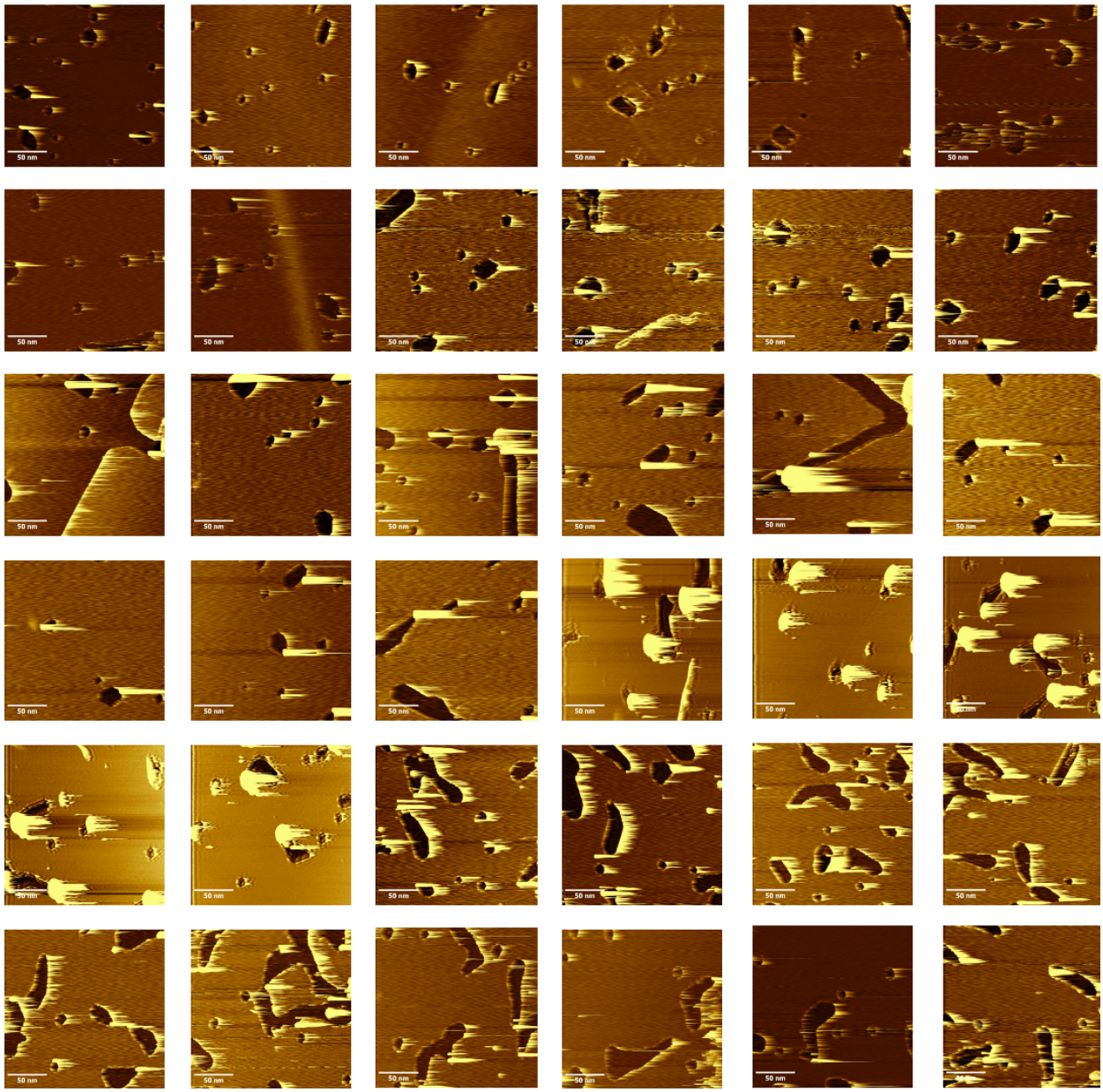


Figure A1.27: Fourth set of 36 images used in Figure 3.6 and the sixth row of Table 3.1.

Filenames for **Figure A1.27** from top left to bottom right:

Directory: Appendix\A1-28\1100C, 0.7eV Beam Trial 3, 90min
082117_0019, 082117_0020, 082117_0021, 082117_0022, 082117_0023

Directory: Appendix\A1-28\1100C, 0.7eV Beam Trial 3, 105min
082217_0001, 082217_0006, 082217_0007, 082217_0008, 082217_0009, 082217_0010, 082217_0011, 082217_0012, 082217_0013, 082217_0014, 082217_0015, 082217_0016, 082217_0017, 082217_0018, 082217_0019, 082217_0020

Directory: Appendix\A1-28\1100C, 0.7eV Beam Trial 3, 120min
082317_0001, 082317_0002, 082317_0003, 082317_0004, 082317_0005, 082317_0014, 082317_0015, 082317_0016, 082317_0017, 082317_0018, 082317_0019, 082317_0020, 082317_0021, 082317_0022, 082317_0023

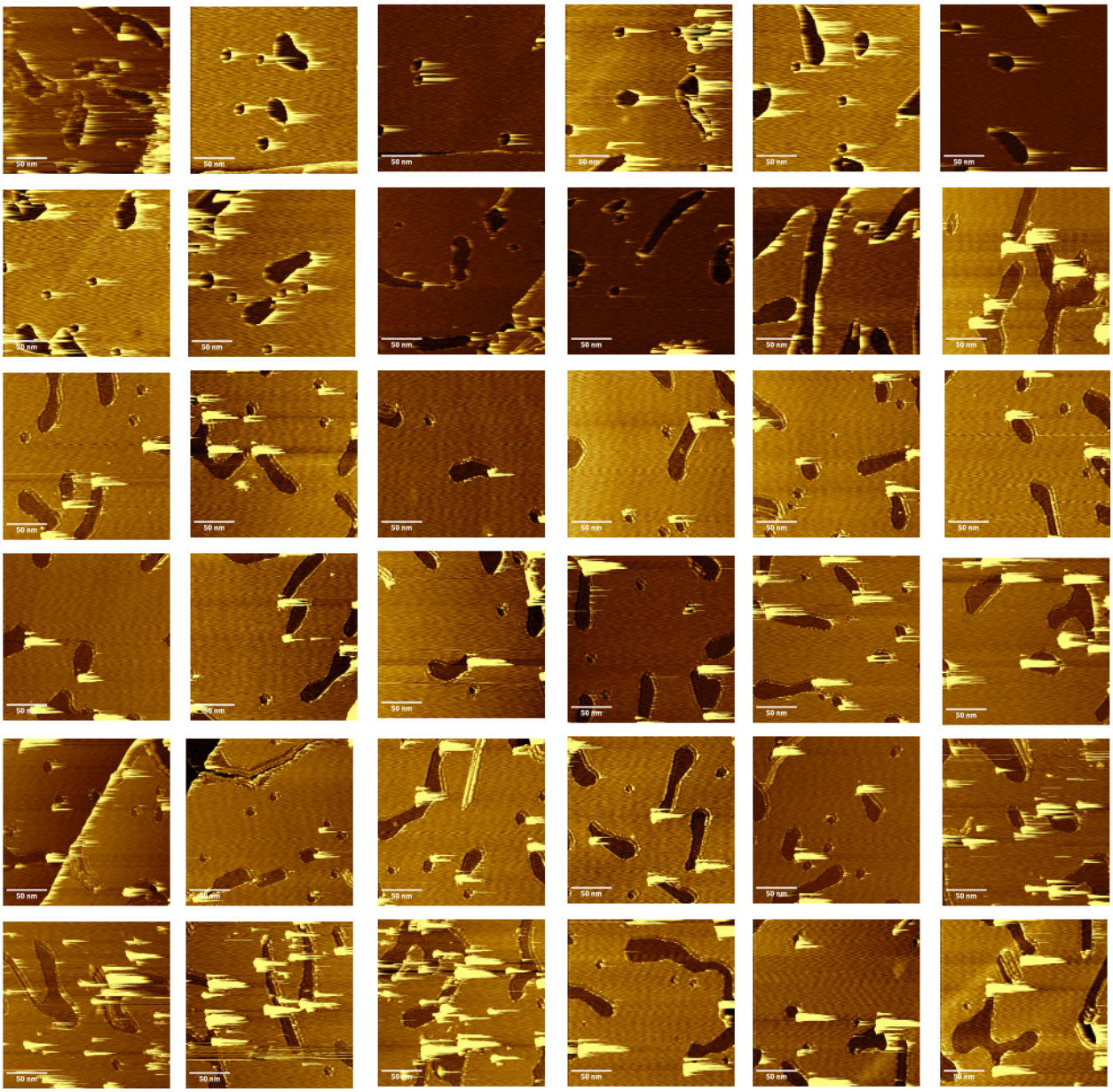


Figure A1.28: Fifth set of 36 images used in Figure 3.6 and the sixth row of Table 3.1.

Filenames for **Figure A1.28** from top left to bottom right:

Directory: Appendix\A1-29\1100C, 0.7eV Beam Trial 3, 120min
082317_0024, 082317_0025, 082317_0026, 082317_0027, 082317_0028, 082317_0029, 082317_0030, 082317_0031

Directory: Appendix\A1-29\1100C, 0.7eV Beam Trial 3, 135min
082417_0001, 082417_0002, 082417_0003, 082417_0007, 082417_0008, 082417_0009, 082417_0010, 082417_0011, 082417_0012, 082417_0013, 082417_0014, 082417_0015, 082417_0016, 082417_0017, 082417_0018, 082417_0019, 082417_0020, 082417_0021, 082417_0022, 082417_0023, 082417_0024, 082417_0025, 082417_0026, 082417_0027, 082417_0028

Directory: Appendix\A1-29\1100C, 0.7eV Beam Trial 3, 150min
082517_0001, 082517_0002, 082517_0003

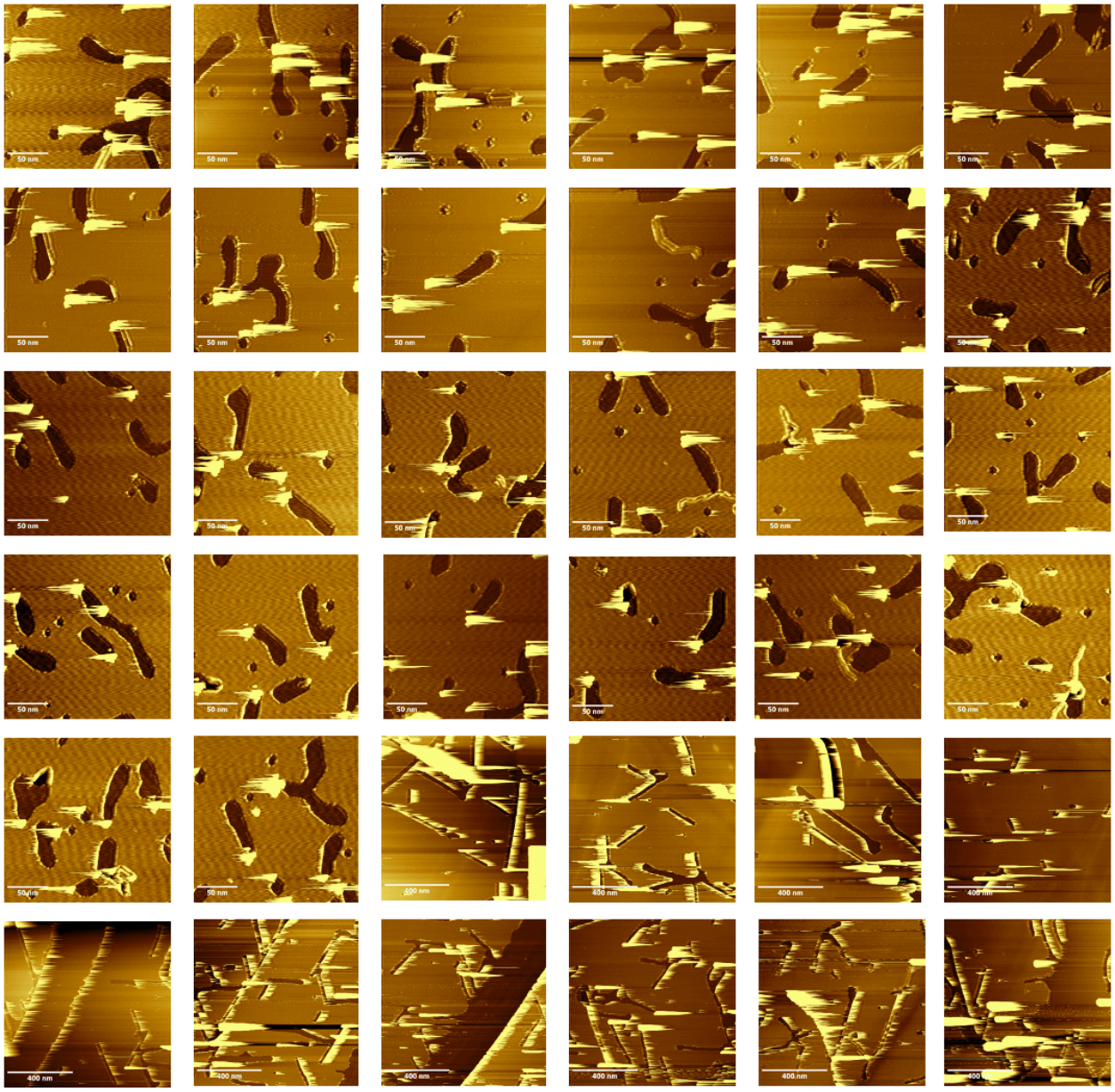


Figure A1.29: Sixth set of 36 images used in Figure 3.6 and the sixth row of Table 3.1.

Filenames for **Figure A1.29** from top left to bottom right:

Directory: Appendix\A1-30\1100C, 0.7eV Beam Trial 3, 150min
082517_0004, 082517_0005, 082517_0006, 082517_0007, 082517_0008, 082517_0009, 082517_0010, 082517_0011, 082517_0012, 082517_0013, 082517_0014, 082817_0001, 082817_0002, 082817_0003, 082817_0004, 082817_0005, 082817_0006, 082817_0007, 082817_0008, 082817_0009, 082817_0010, 082817_0011, 082817_0012, 082817_0013, 082817_0014, 082817_0016

Directory: Appendix\A1-30\1100C, 0.7eV Beam Trial 4, 90min
100917_0003, 100917_0004, 100917_0005, 100917_0008, 100917_0011, 100917_0012, 100917_0013, 100917_0014, 100917_0015, 100917_0017

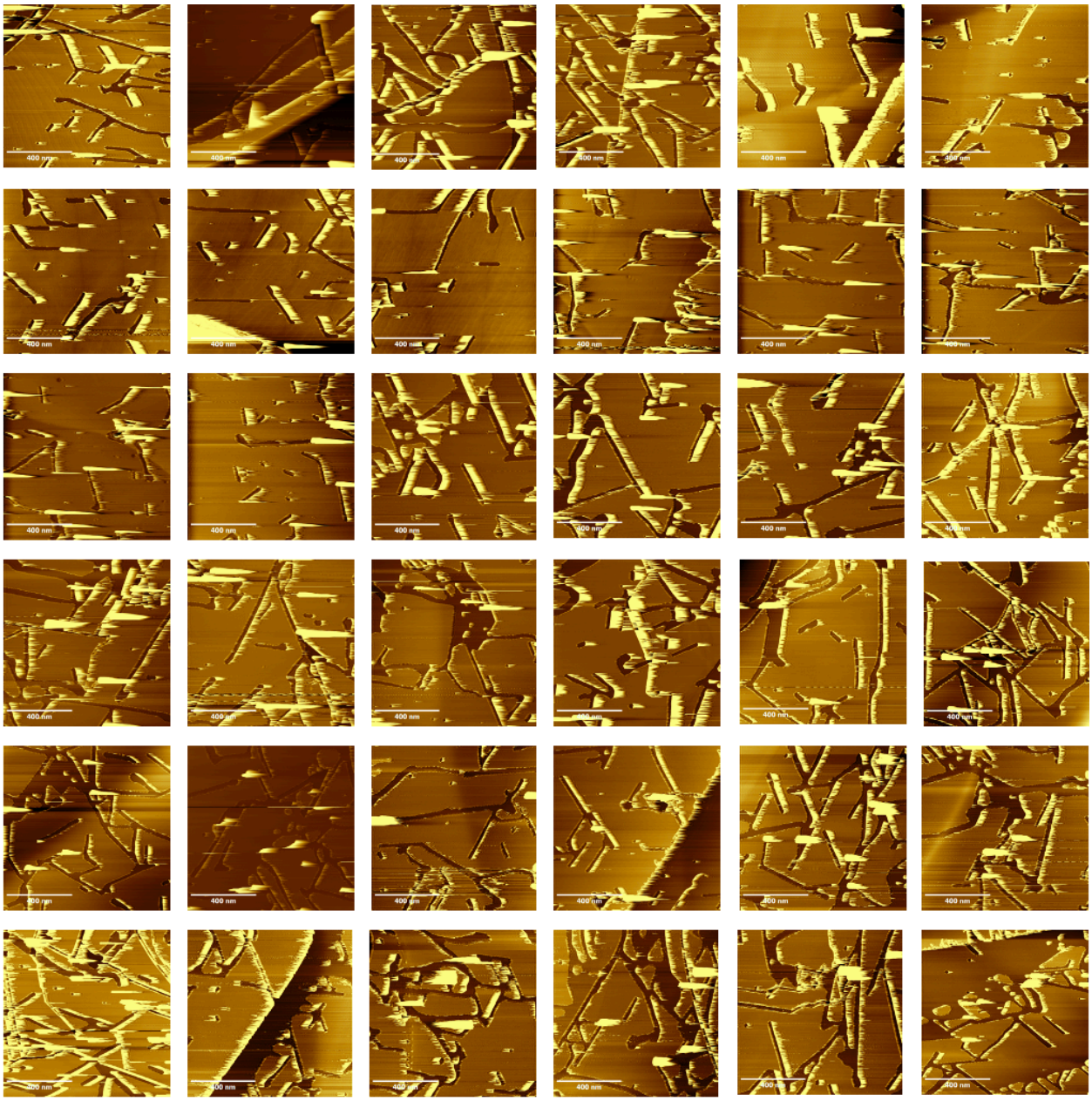


Figure A1.30: Seventh set of 36 images used in Figure 3.6 and the sixth row of Table 3.1.

Filenames for **Figure A1.30** from top left to bottom right:

Directory: Appendix\A1-31\1100C, 0.7eV Beam Trial 4, 120min
101017_0001, 101017_0002, 101017_0003, 101017_0004, 101017_0005, 101017_0006, 101017_0010, 101017_0011, 101017_0012, 101017_0013, 101017_0014, 101017_0015, 101017_0016, 101017_0017, 101017_0018, 101017_0019, 101017_0020

Directory: Appendix\A1-31\1100C, 0.7eV Beam Trial 4, 150min
101117_0001, 101117_0002, 101117_0003, 101117_0004, 101117_0005, 101117_0006, 101117_0007, 101117_0008, 101117_0009, 101117_0010, 101117_0011, 101117_0012, 101117_0013

Directory: Appendix\A1-31\1100C, 0.7eV Beam Trial 4, 210min
101217_0001, 101217_0002, 101217_0003, 101217_0004, 101217_0005, 101217_0006

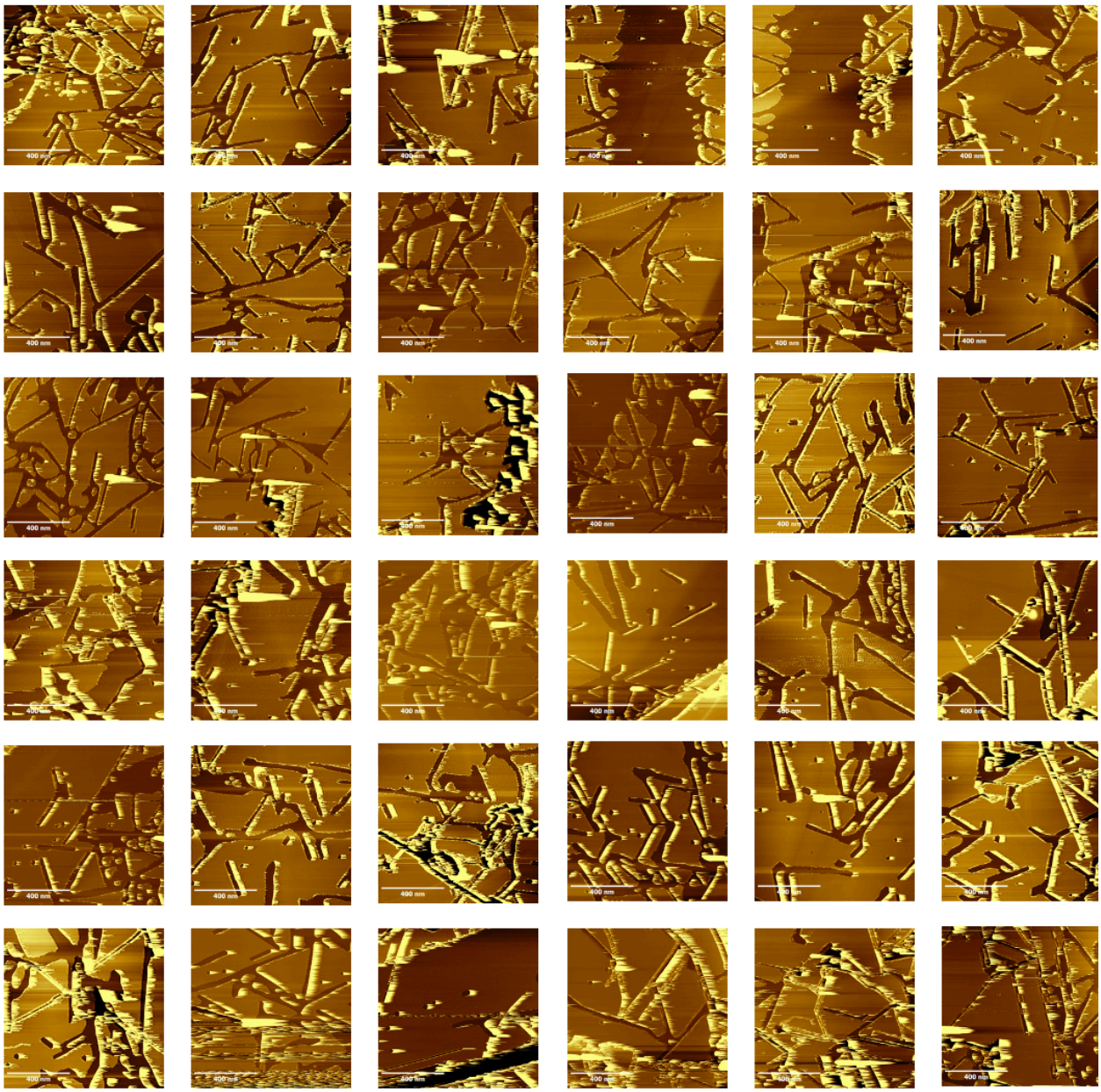


Figure A1.31: Eighth set of 36 images used in Figure 3.6 and the sixth row of Table 3.1.

Filenames for **Figure A1.31** from top left to bottom right:

Directory: Appendix\A1-32\1100C, 0.7eV Beam Trial 4, 210min
101217_0007, 101217_0008, 101217_0009, 101217_0012, 101217_0013, 101217_0014, 101217_0015

Directory: Appendix\A1-32\1100C, 0.7eV Beam Trial 4, 270min
101317_0001, 101317_0002, 101317_0003, 101317_0004, 101317_0005, 101317_0006, 101317_0007, 101317_0009, 101317_0011, 101317_0012, 101317_0013

Directory: Appendix\A1-32\1100C, 0.7eV Beam Trial 4, 360min
101617_0001, 101617_0002, 101617_0005, 101617_0007, 101617_0008, 101617_0009, 101617_0011, 101617_0012, 101617_0013, 101617_0015, 101617_0016

Directory: Appendix\A1-32\1100C, 0.7eV Beam Trial 4, 480min
101717_0001, 101717_0002, 101717_0003, 101717_0004, 101717_0005, 101717_0006

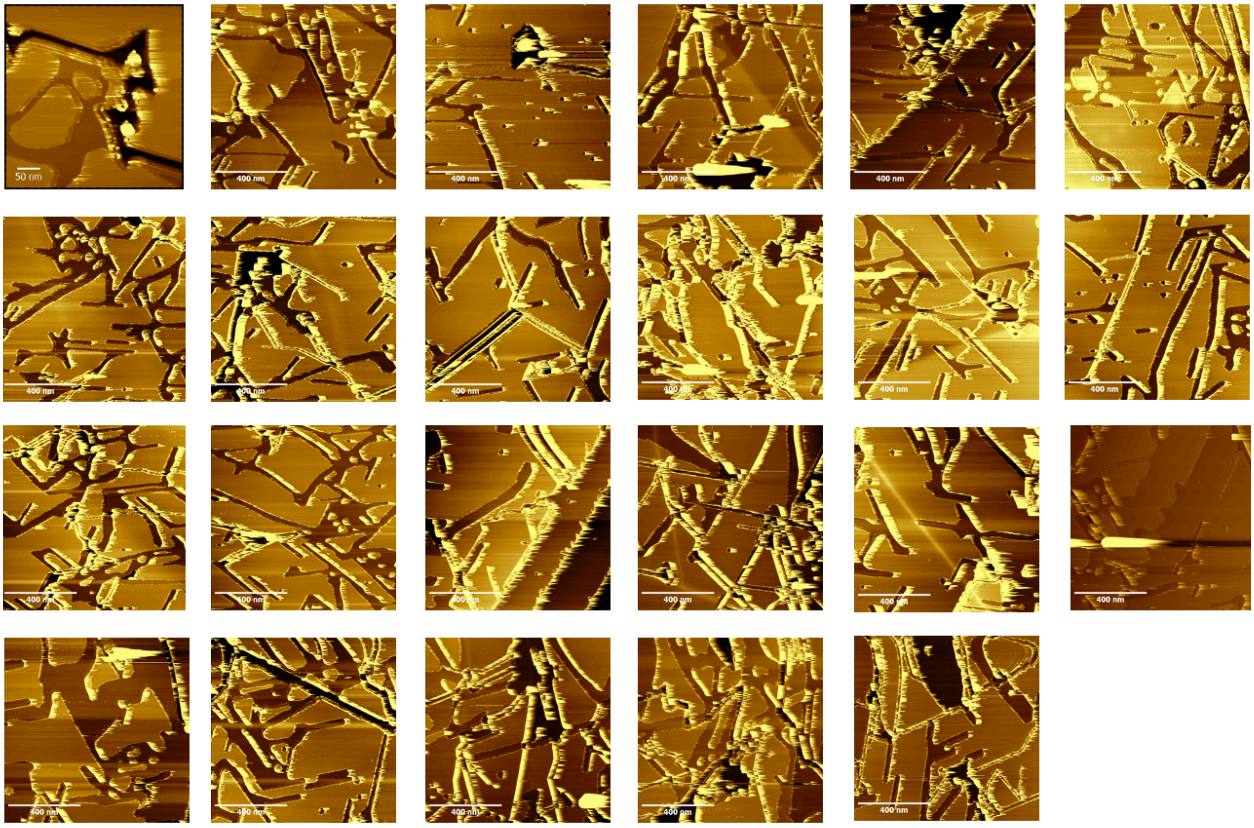


Figure A1.32: Last set of 23 images used in Figure 3.6 and the sixth row of Table 3.1.

Filenames for **Figure A1.32** from top left to bottom right:

Directory: Appendix\A1-33\1100C, 0.7eV Beam Trial 4, 480min
101717_0008, 101717_0009, 101717_0010, 101717_0012, 101717_0013, 101817_0001, 101817_0002, 101817_0003

Directory: Appendix\A1-33\1100C, 0.7eV Beam Trial 4, 600min
101817_0004, 101817_0006, 101817_0007, 101817_0008, 101817_0009, 101817_0010, 101817_0011, 101817_0012, 101817_0013, 101917_0001, 101917_0002, 101917_0003, 101917_0004, 101917_0005, 101917_0006

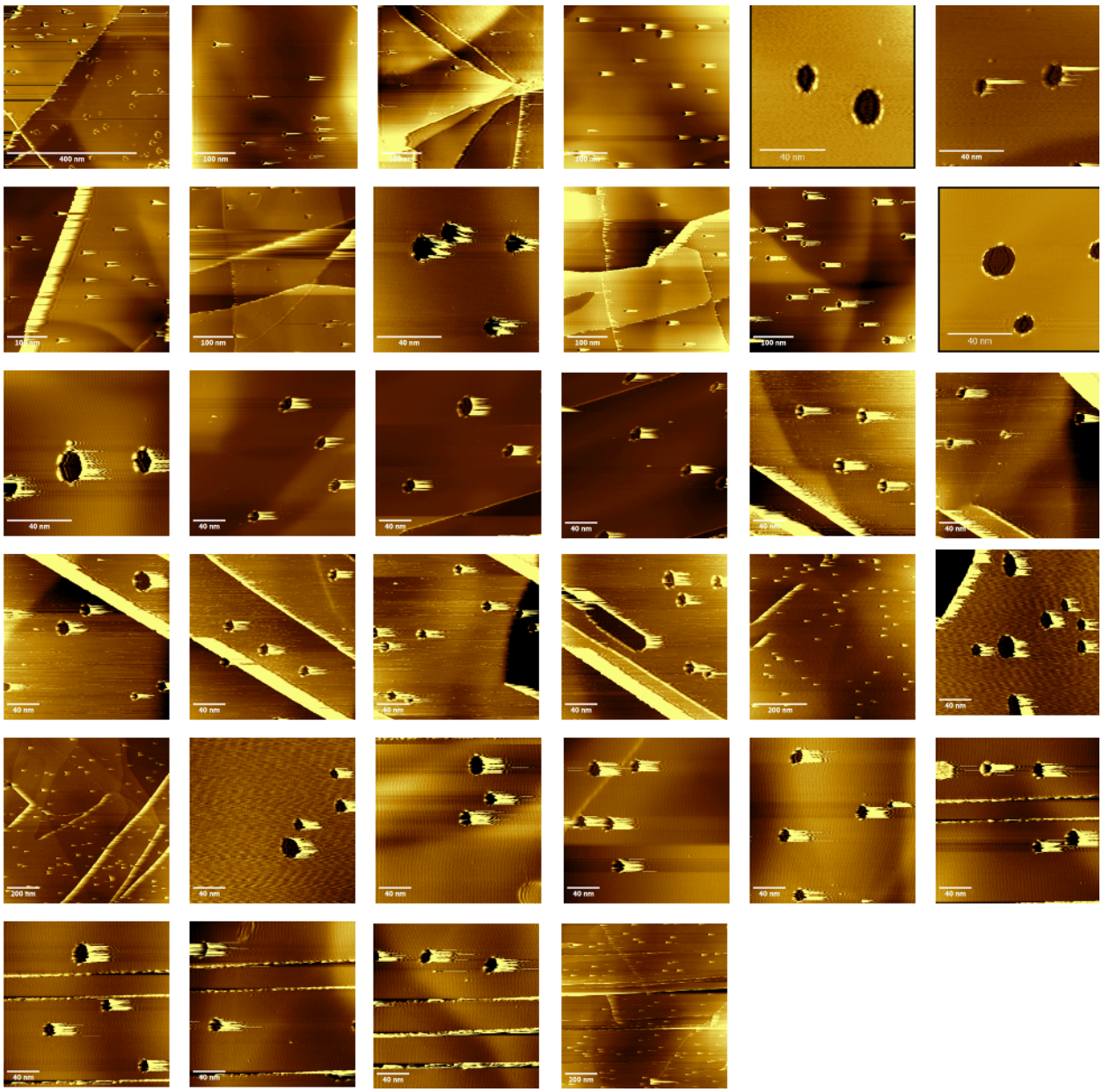


Figure A1.33: First set of 34 images used in the seventh row of Table 3.1.

Filenames for **Figure A1.33** from top left to bottom right:

Directory: Appendix\A1-34\ 1100C, 0.7eV Beam, Grade 2, 2hr
102417_0002, 102417_0003, 102417_0006

Directory: Appendix\A1-34\ 1100C, 0.7eV Beam, Grade 2, 3hr
102417_0010, 102417_0011, 102417_0012, 102417_0013, 102517_0001, 102517_0002, 102517_0003

Directory: Appendix\A1-34\ 1100C, 0.7eV Beam, Grade 2, 8hr
102617_0014, 102617_0015, 102617_0016, 102617_0021, 102617_0022, 102617_0023, 102717_0002, 102717_0003, 102717_0005, 102717_0006, 102717_0007, 102717_0009

Directory: Appendix\A1-34\ 1100C, 0.7eV Beam, Grade 2, 11.5hr
102717_0015, 102717_0017, 102717_0019, 102717_0020, 103017_0002, 103017_0003, 103017_0004, 103017_0006, 103017_0007, 103017_0008, 103017_0009, 103017_0010

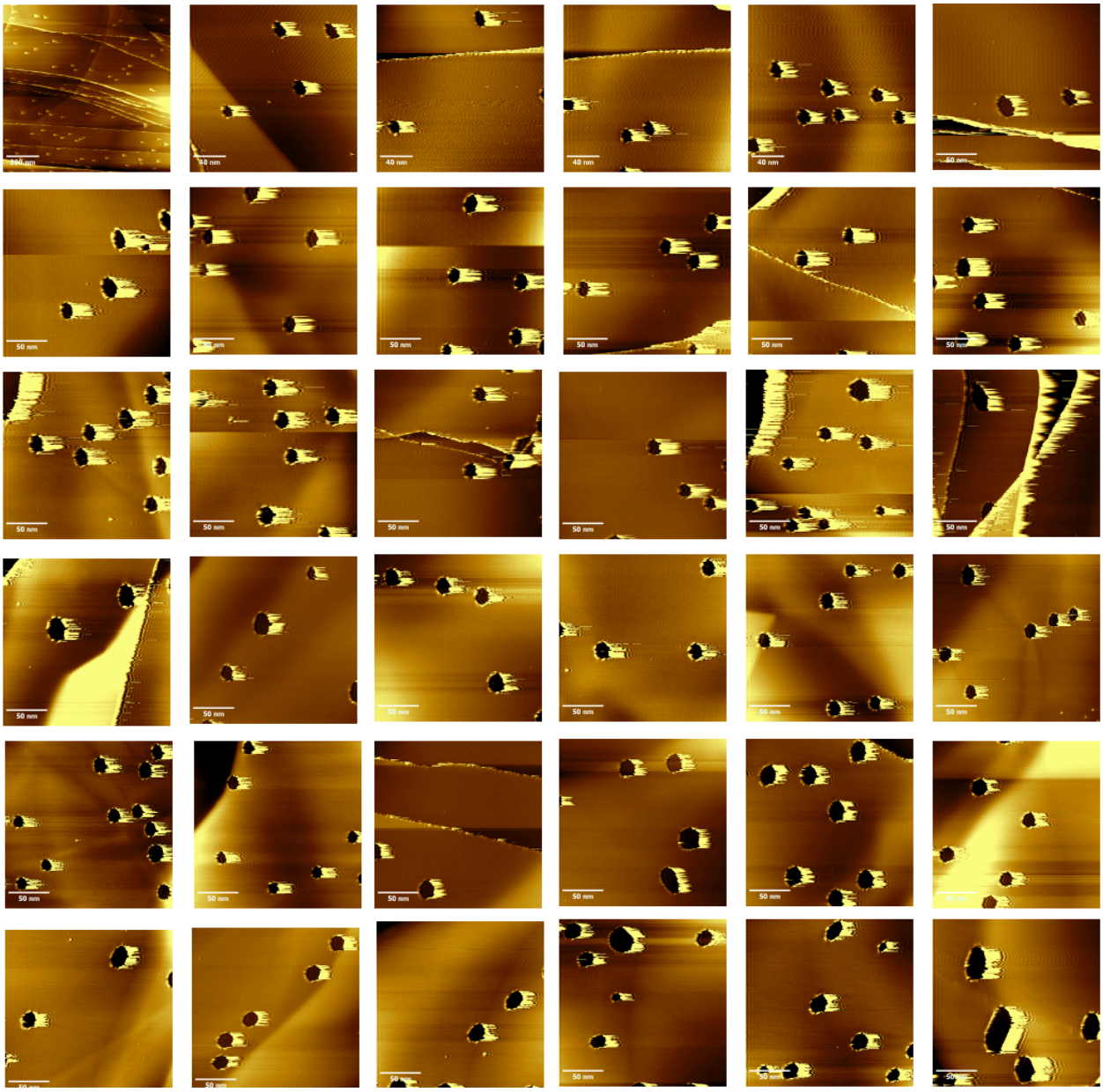


Figure A1.34: Second set of 36 images used in the seventh row of Table 3.1.

Filenames for **Figure A1.34** from top left to bottom right:

Directory: Appendix\A1-35\ 1100C, 0.7eV Beam, Grade 2, 11.5hr
103017_0012, 103017_0013, 103017_0015, 103017_0016, 103017_0017, 103017_0018

Directory: Appendix\A1-35\ 1100C, 0.7eV Beam, Grade 2, 16hr
103017_0021, 103017_0022, 103017_0023, 103017_0024, 103017_0025, 103017_0026, 103117_0002, 103117_0003, 103117_0004, 103117_0005, 103117_0006, 103117_0008, 103117_0009, 103117_0010, 103117_0011, 103117_0012, 103117_0013, 103117_0015, 103117_0016, 103117_0017

Directory: Appendix\A1-35\ 1100C, 0.7eV Beam, Grade 2, 25.5hr
110117_0002, 110117_0003, 110117_0004, 110117_0005, 110117_0006, 110117_0007, 110117_0008, 110117_0009, 110117_0010, 110117_0012

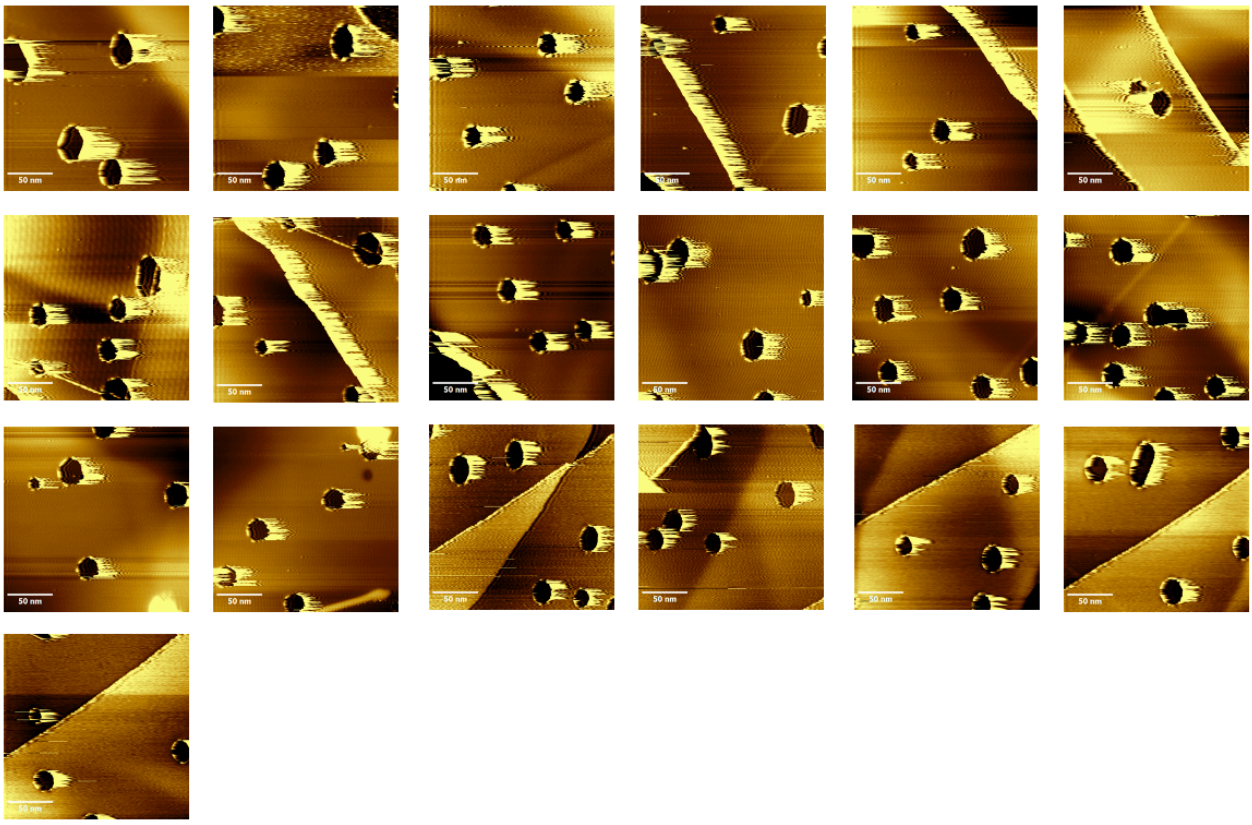


Figure A1.35: Last set of 19 images used in the seventh row of Table 3.1.

Filenames for **Figure A1.35** from top left to bottom right:

Directory: Appendix\A1-36\ 1100C, 0.7eV Beam, Grade 2, 25.5hr
110117_0013, 110217_0002, 110217_0003, 110217_0004, 110217_0005, 110217_0006, 110217_0008, 110217_0009, 110217_0010, 110217_0012, 110217_0013, 110217_0014, 110217_0015, 110217_0016, 110217_0018, 110217_0019, 110217_0020, 110217_0021, 110217_0022

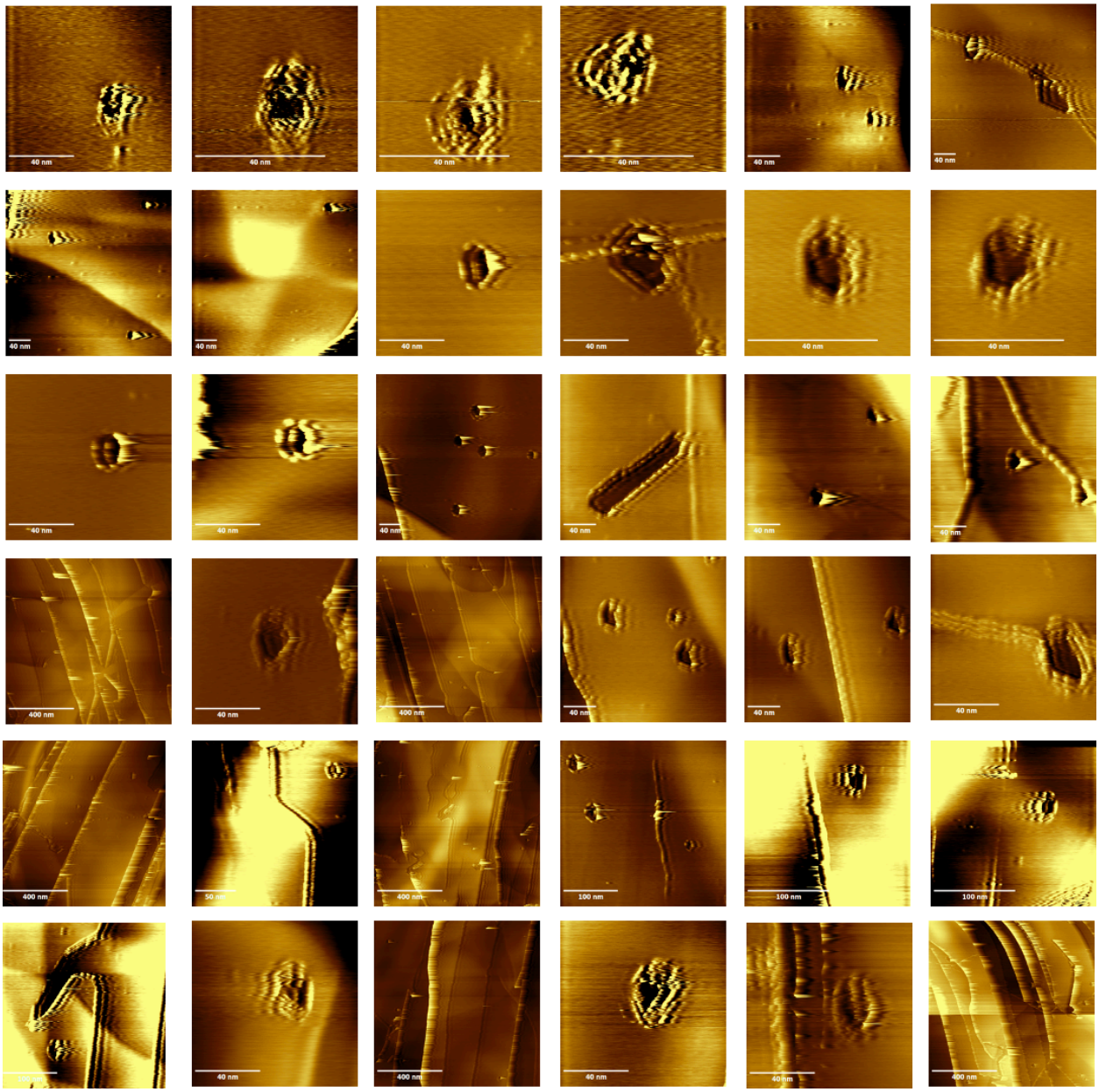


Figure A1.36: First set of 36 images used in the eighth row of Table 3.1.

Filenames for **Figure A1.36** from top left to bottom right:

Directory: Appendix\A1-37\ 45 Degrees, 1100C, 0.7eV Beam, Grade 2, 3.5hr
120117_0002, 120117_0003, 120117_0004, 120117_0005

Directory: Appendix\A1-37\ 45 Degrees, 1100C, 0.7eV Beam, Grade 2, 7hr
120417_0002,
120417_0003,
120417_0004,
120417_0006, 120417_0009, 120417_0010, 120417_00103, 120417_0014, 120417_0016, 120417_0017, 120417_0019, 120417_0021, 120417_0023, 120417_0025

Directory: Appendix\A1-37\ 45 Degrees, 1100C, 0.7eV Beam, Grade 2, 12hr
120517_0003, 120517_0004, 120517_0005, 120517_0006, 120517_0007, 120517_0008, 120517_0011, 120617_0001, 120617_0002, 120617_0003, 120617_0004, 120617_0005, 120617_0006, 120617_0007, 120617_0008, 120617_0009, 120617_0010, 120617_0011

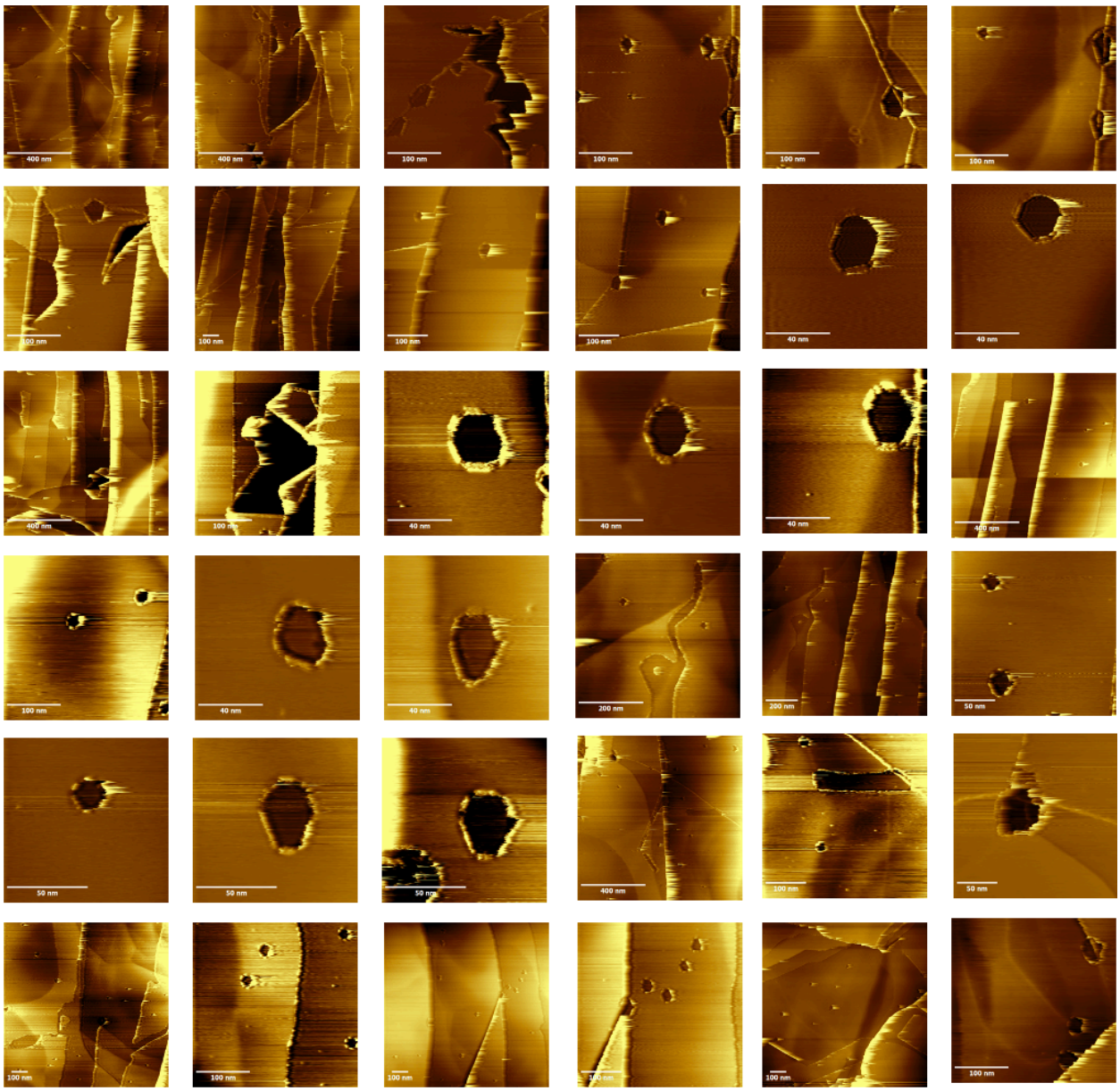


Figure A1.37: Second set of 36 images used in the eighth row of Table 3.1.

Filenames for **Figure A1.37** from top left to bottom right:

Directory: Appendix\A1-38\ 45 Degrees, 1100C, 0.7eV Beam, Grade 2, 17hr
120617_0012, 120717_0001, 120717_0002, 120717_0003, 120717_0004, 120717_0005, 120717_0006, 120717_0007, 120717_0008, 120717_0009, 120717_0010, 120717_0011, 120717_0012, 120717_0013, 120717_0014, 120717_0015, 120717_0016, 120717_0017, 120717_0018, 120717_0019, 120717_0020, 120717_0021, 120717_0022, 120717_0023, 120717_0024, 120717_0025, 120717_0026, 120717_0028, 120717_0029, 120717_0030, 120717_0031, 120717_0032, 120717_0033, 120717_0034

Directory: Appendix\A1-38\ 45 Degrees, 1100C, 0.7eV Beam, Grade 2, 22hr
120817_0001, 120817_0002

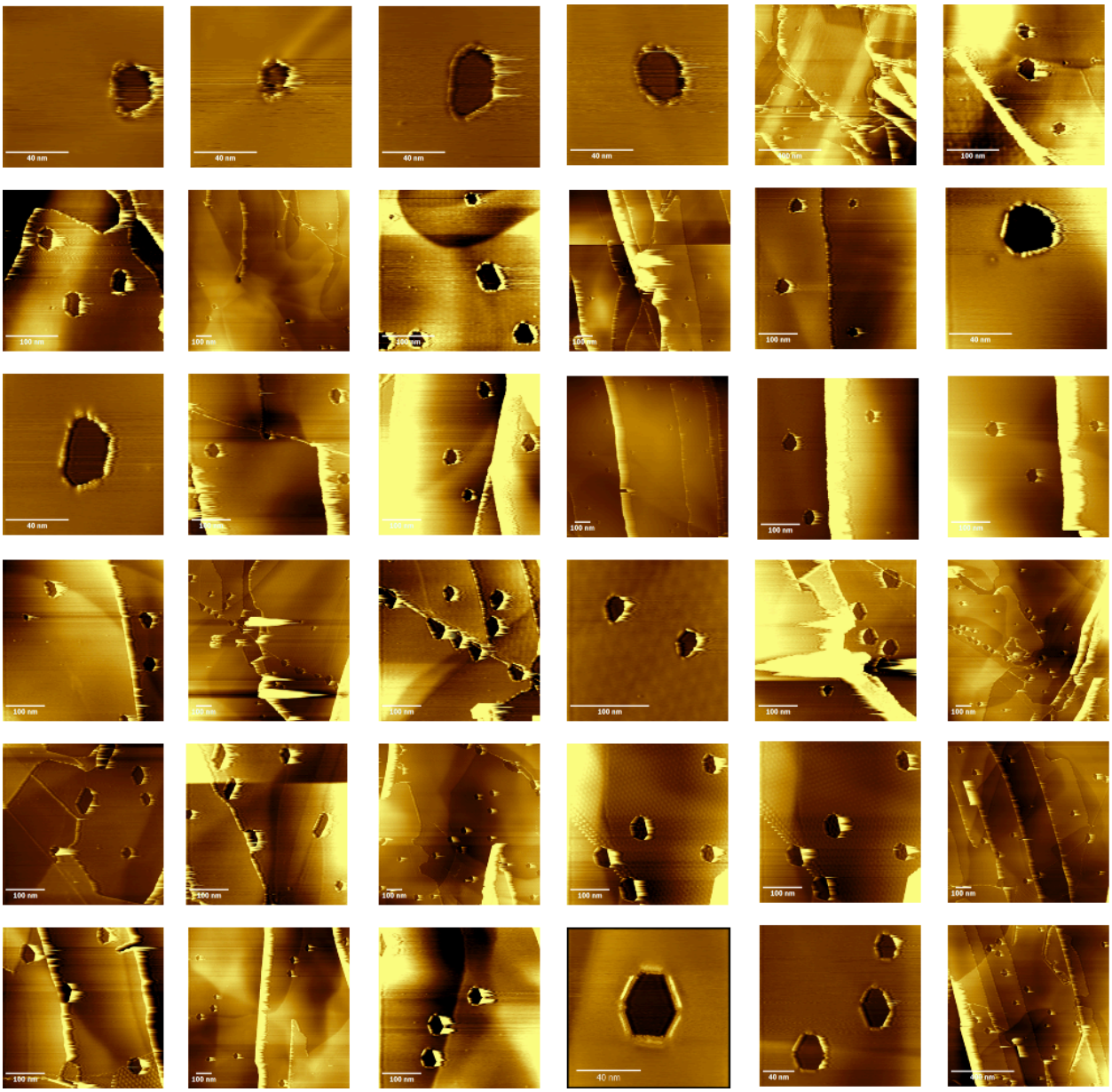


Figure A1.38: Third set of 36 images used in the eighth row of Table 3.1.

Filenames for **Figure A1.38** from top left to bottom right:

Directory: Appendix\A1-39\ 45 Degrees, 1100C, 0.7eV Beam, Grade 2, 22hr
120817_0003, 120817_0004, 120817_0005, 120817_0006, 120817_0007, 120817_0008, 120817_0009, 120817_0010, 120817_0011, 121117_0001, 121117_0002, 121117_0004, 121117_0005, 121117_0006, 121117_0007, 121117_0008, 121117_0009, 121117_0010, 121117_0011, 121117_0012, 121117_0013, 121117_0014, 121117_0015, 121117_0016, 121117_0017, 121117_0018

Directory: Appendix\A1-39\ 45 Degrees, 1100C, 0.7eV Beam, Grade 2, 31hr
121217_0001, 121217_0002, 121217_0003, 121217_0004, 121217_0005, 121217_0006, 121217_0007, 121217_0008, 121217_0009, 121217_0010

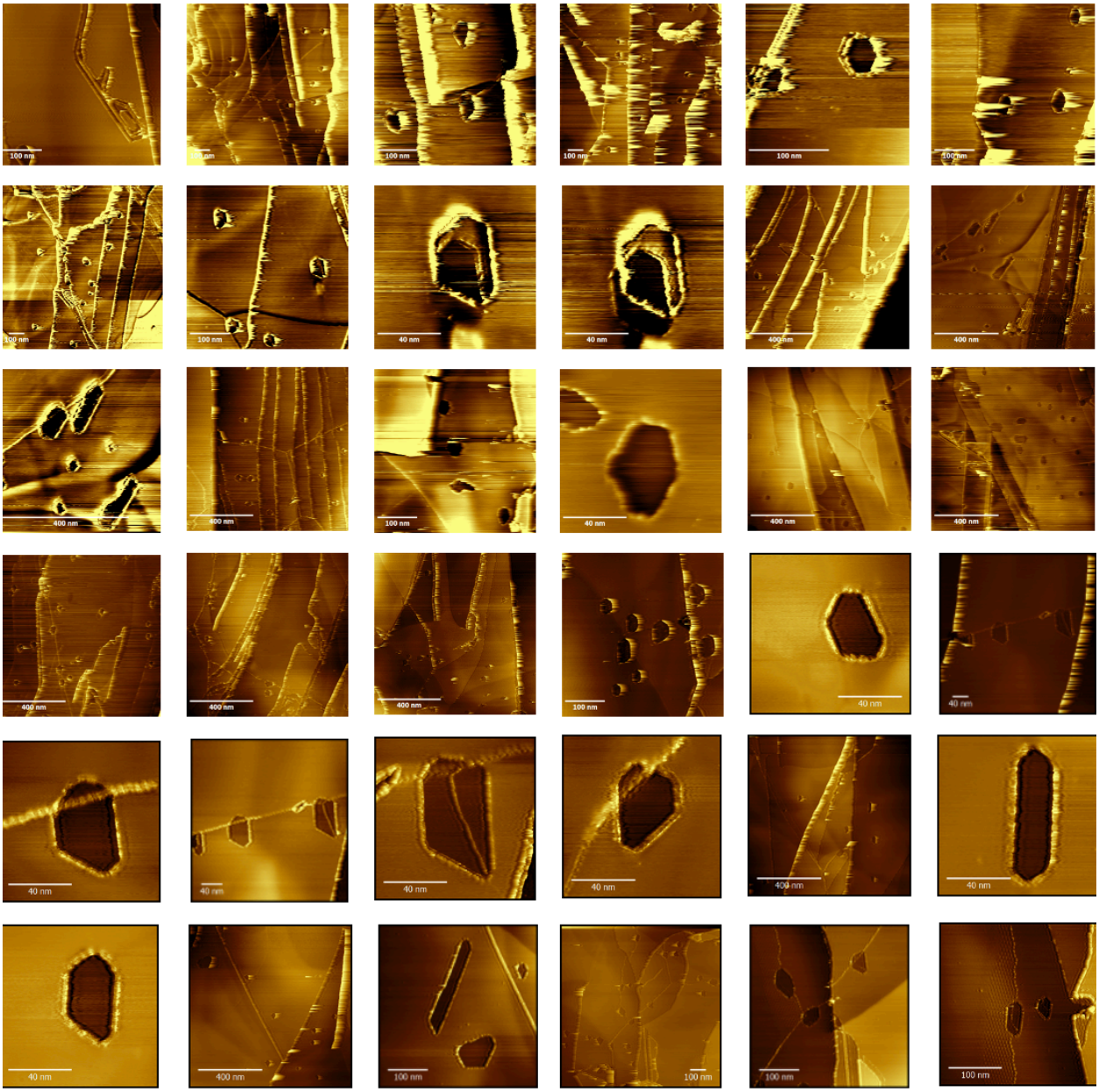


Figure A1.39: Fourth set of 36 images used in the eighth row of Table 3.1.

Filenames for **Figure A1.39** from top left to bottom right:

Directory: Appendix\A1-40\ 45 Degrees, 1100C, 0.7eV Beam, Grade 2, 31hr
121217_0011, 121217_0012, 121217_0013, 121317_0001, 121317_0002, 121317_0003, 121317_0004, 121317_0005, 121317_0007, 121317_0008, 121317_0009, 121317_0010, 121317_0011, 121317_0012, 121417_0002, 121417_0003, 121417_0007, 121417_0008, 121517_0001, 121517_0002, 121517_0003, 121517_0004, 121917_0001, 121917_0002, 121917_0003, 121917_0004, 121917_0005, 121917_0006, 122017_0001, 122017_0002, 122017_0003, 122017_0004, 122017_0005, 122017_0006, 122017_0007, 122017_0008

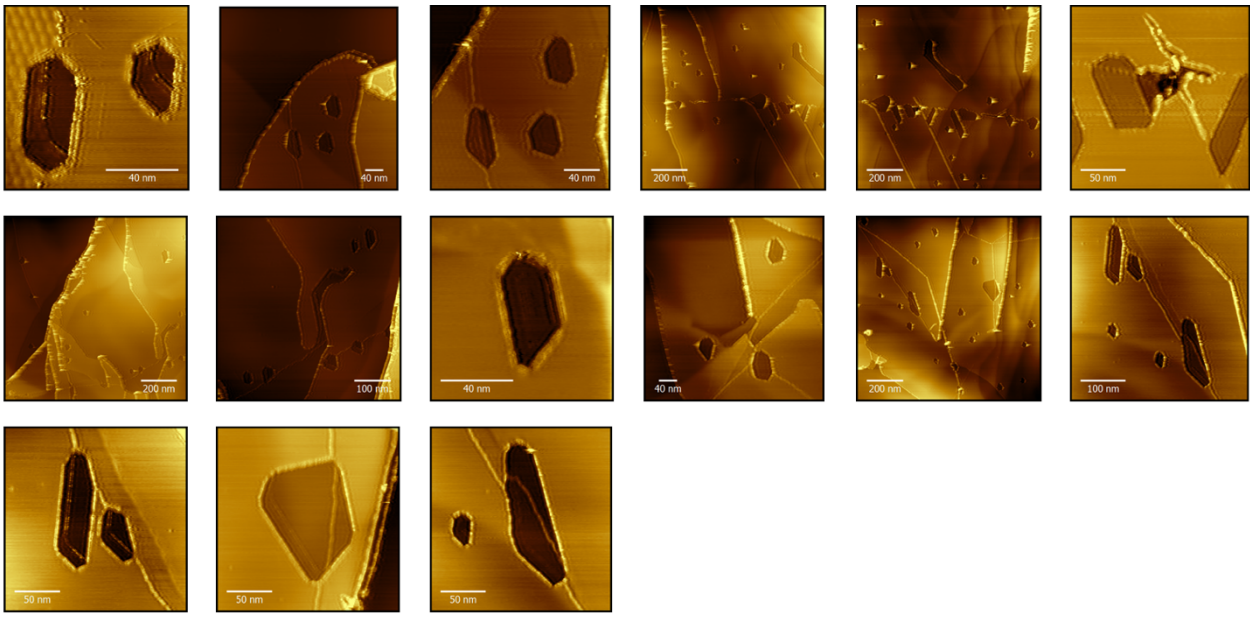


Figure A1.40: Last set of 15 images used in the eighth row of Table 3.1.

Filenames for **Figure A1.40** from top left to bottom right:

Directory: Appendix\A1-41\ 45 Degrees, 1100C, 0.7eV Beam, Grade 2, 31hr
122017_0009, 122017_0010, 122017_0011, 122017_0012, 122017_0013, 122017_0014, 122117_0001, 122117_0002, 122117_0003, 122117_0004, 122117_0005, 122117_0006, 122117_0007, 122117_0008, 122117_0009

A2: Room Temperature Oxidation of GaAs(110) Using High Translational Kinetic Energy Molecular Beams of O_2 Visualized by STM

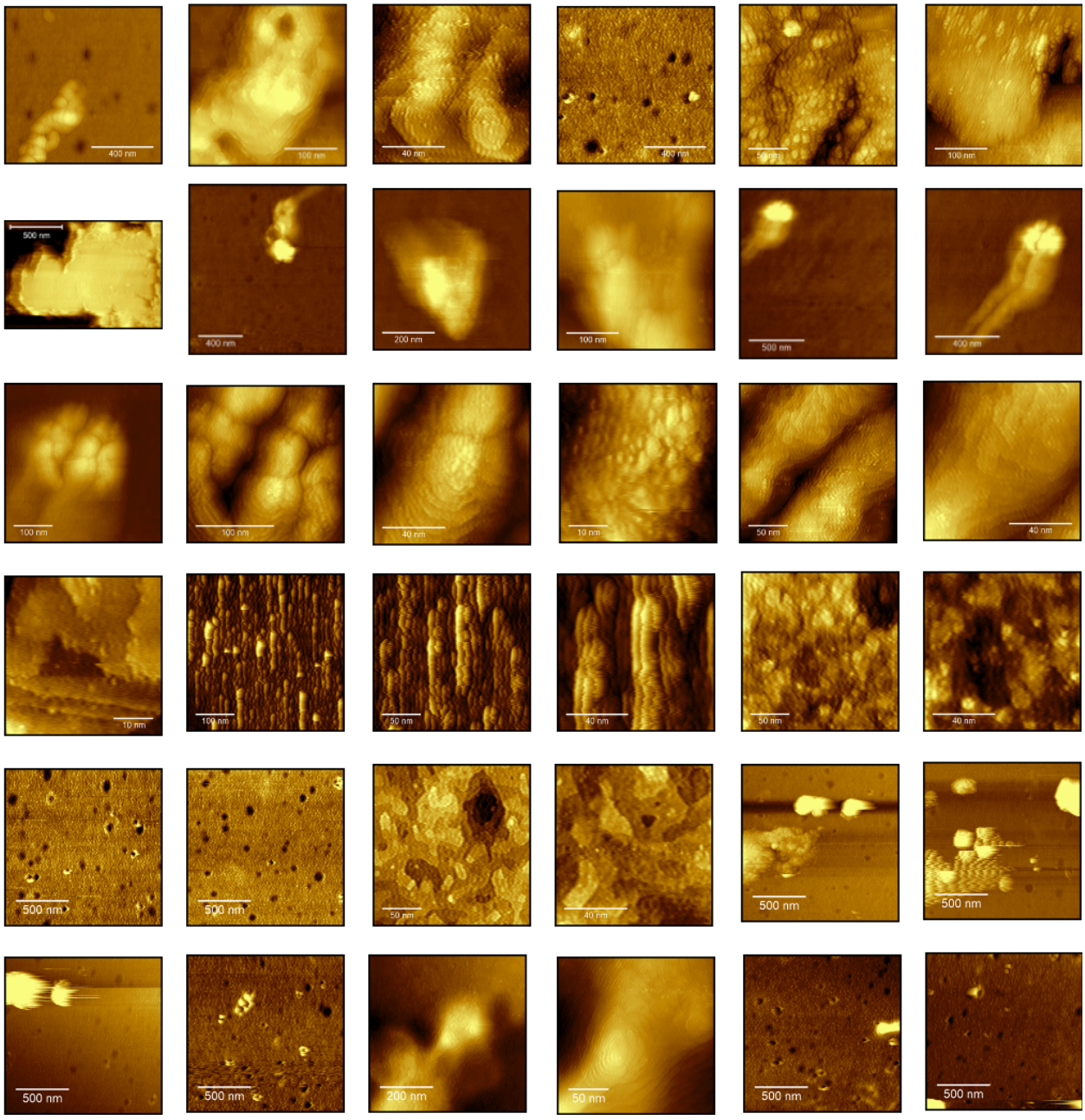


Figure A2.1: First set of 36 images used in Figure 4.2 and the heterogeneous reactivity series in Figure 4.9.

Filenames for **Figure A2.1** from top left to bottom right:

Directory: Appendix\A1-42\ 0.4eV Beam, 16hr
012218_0022, 012218_0024, 012218_0025, 012218_0026, 012218_0028, 012318_0003, 012318_0005_crop, 012318_0008, 012318_0012, 012318_0013, 012318_0016, 012318_0017, 012318_0018, 012318_0019, 012318_0020, 012318_0021, 012318_0022, 012318_0023, 012318_0024, 012318_0031, 012318_0032, 012318_0033, 012318_0034, 012318_0035

Directory: Appendix\A1-42\ 0.7eV Beam, 13hr
020418_0001, 020418_0002, 020418_0003, 020418_0004, 020418_0005, 020418_0008, 020418_0009, 020418_0010, 020418_0011, 020418_0012, 020418_0014, 020418_0015

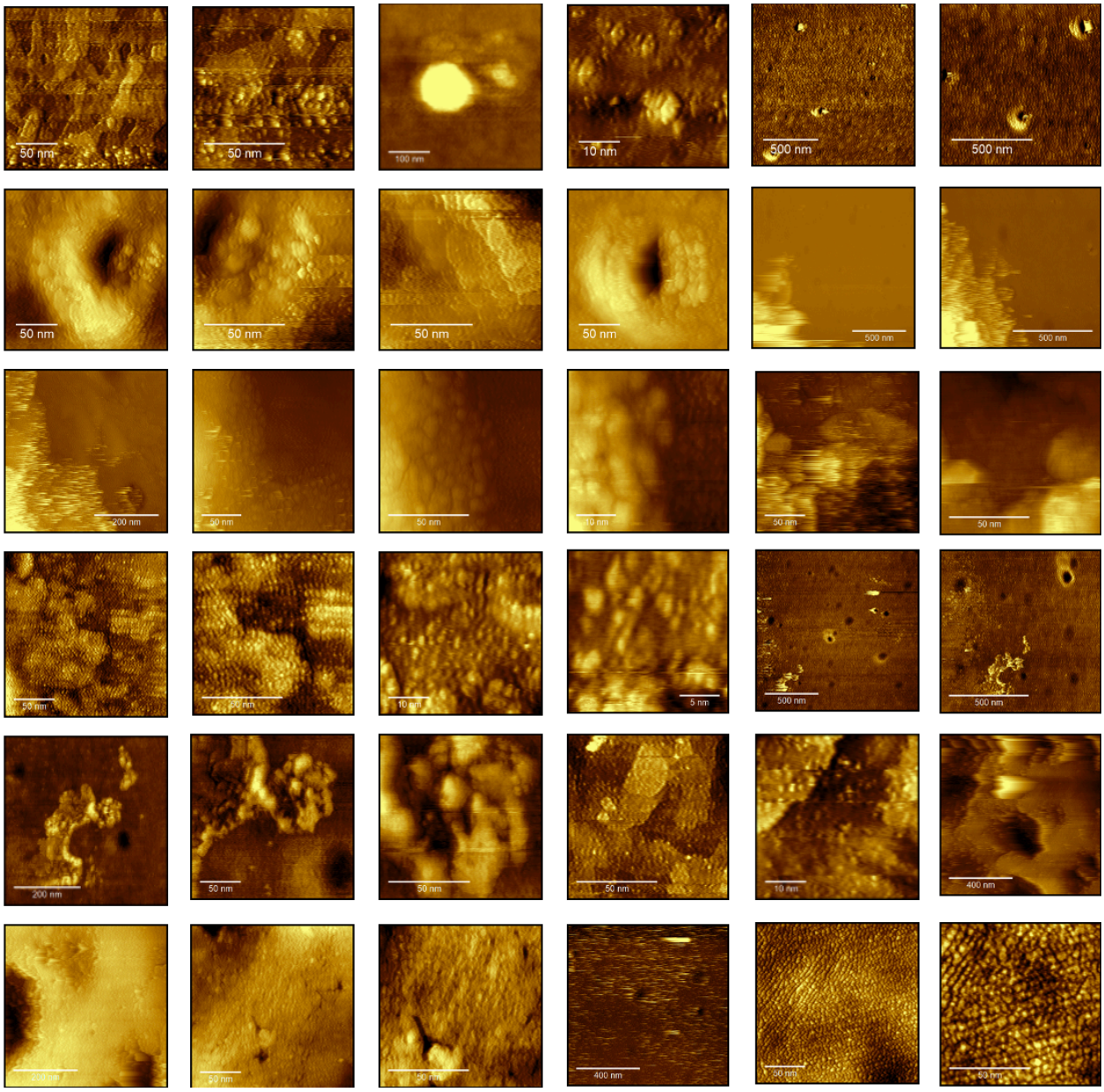


Figure A2.2: Second set of 36 images used in Figure 4.2 and the heterogeneous reactivity series in Figure 4.9.

Filenames for **Figure A2.2** from top left to bottom right:

Directory: Appendix\A1-43\ 0.7eV Beam, 13hr
020418_0016, 020418_0017, 020418_0020, 020418_0025, 020418_0026, 020418_0027, 020418_0028, 020418_0029, 020418_0030, 020418_0031

Directory: Appendix\A1-43\ 1.0eV Beam, 12hr
022219_0001, 022219_0002, 022219_0003, 022219_0004, 022219_0005, 022219_0006, 022219_0007, 022219_0008, 022219_0009, 022219_0010, 022219_0011, 022219_0012, 022219_0013, 022219_0014, 022219_0015, 022219_0016, 022219_0017, 022219_0018, 022219_0019, 022219_0020, 022219_0021, 022219_0022, 022219_0023, 022219_0024, 022219_0025, 022219_0026

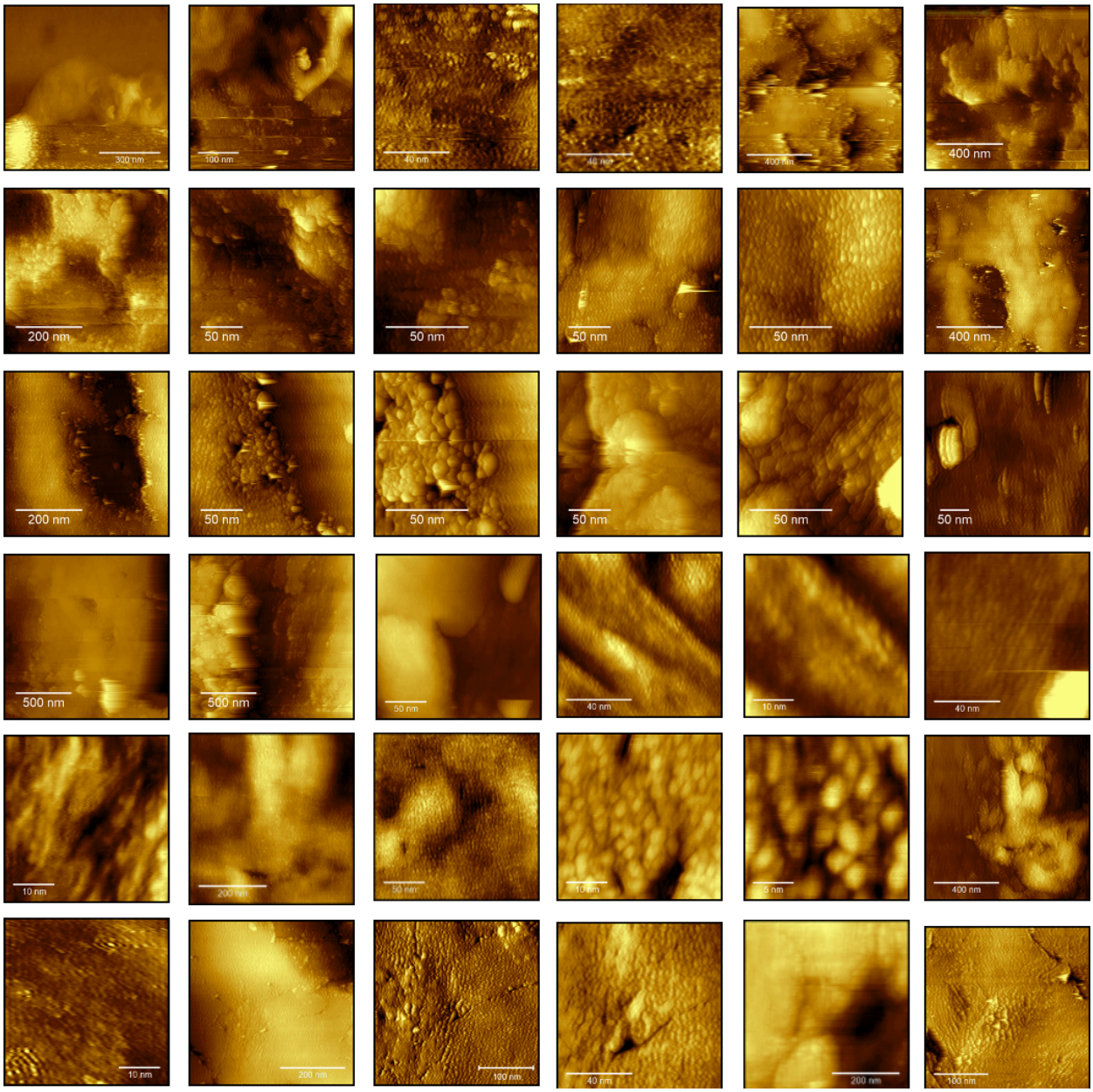


Figure A2.3: Third set of 36 images used in Figure 4.2 and the heterogeneous reactivity series in Figure 4.9.

Filenames for **Figure A2.3** from top left to bottom right:

Directory: Appendix\A1-44\ 1.0eV Beam, 12hr
022419_0002, 022419_0003, 022419_0004, 022419_0005, 022419_0007

Directory: Appendix\A1-44\ 1.1eV Beam, 7.5hr
030719_0026, 030719_0027, 030719_0028, 030719_0029, 030719_0032, 030719_0033, 030719_0034, 030719_0035, 030719_0036, 030719_0037, 030719_0040, 030719_0041, 030719_0042, 030819_0001, 030819_0002

Directory: Appendix\A1-44\ 1.2eV Beam, 75min
011018_0035, 011018_0036, 011018_0037, 011018_0038, 011018_0039, 011018_0040, 011018_0041, 011018_0042, 011018_0043, 011018_0044, 011018_0045, 011018_0048, 011018_0049, 011018_0050, 011018_0052

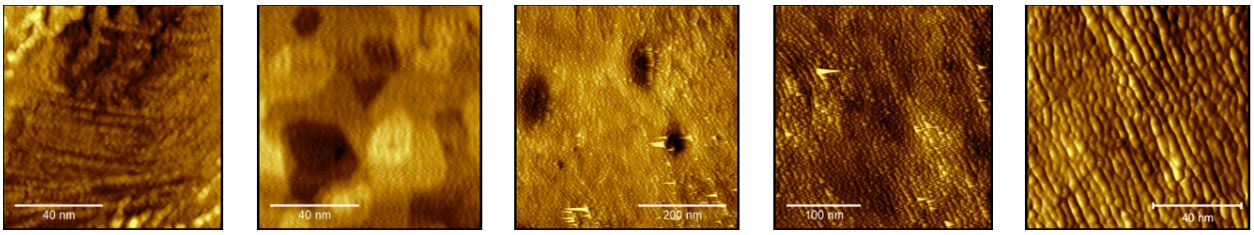


Figure A2.4: Last set of 5 images used in Figure 4.2 and the heterogeneous reactivity series in Figure 4.9.

Filenames for **Figure A2.4** from top left to bottom right:

Directory: Appendix\A1-45\ 1.2eV Beam, 75min
011018_0054, 011018_0056, 011118_0002, 011118_0003, 011118_0004

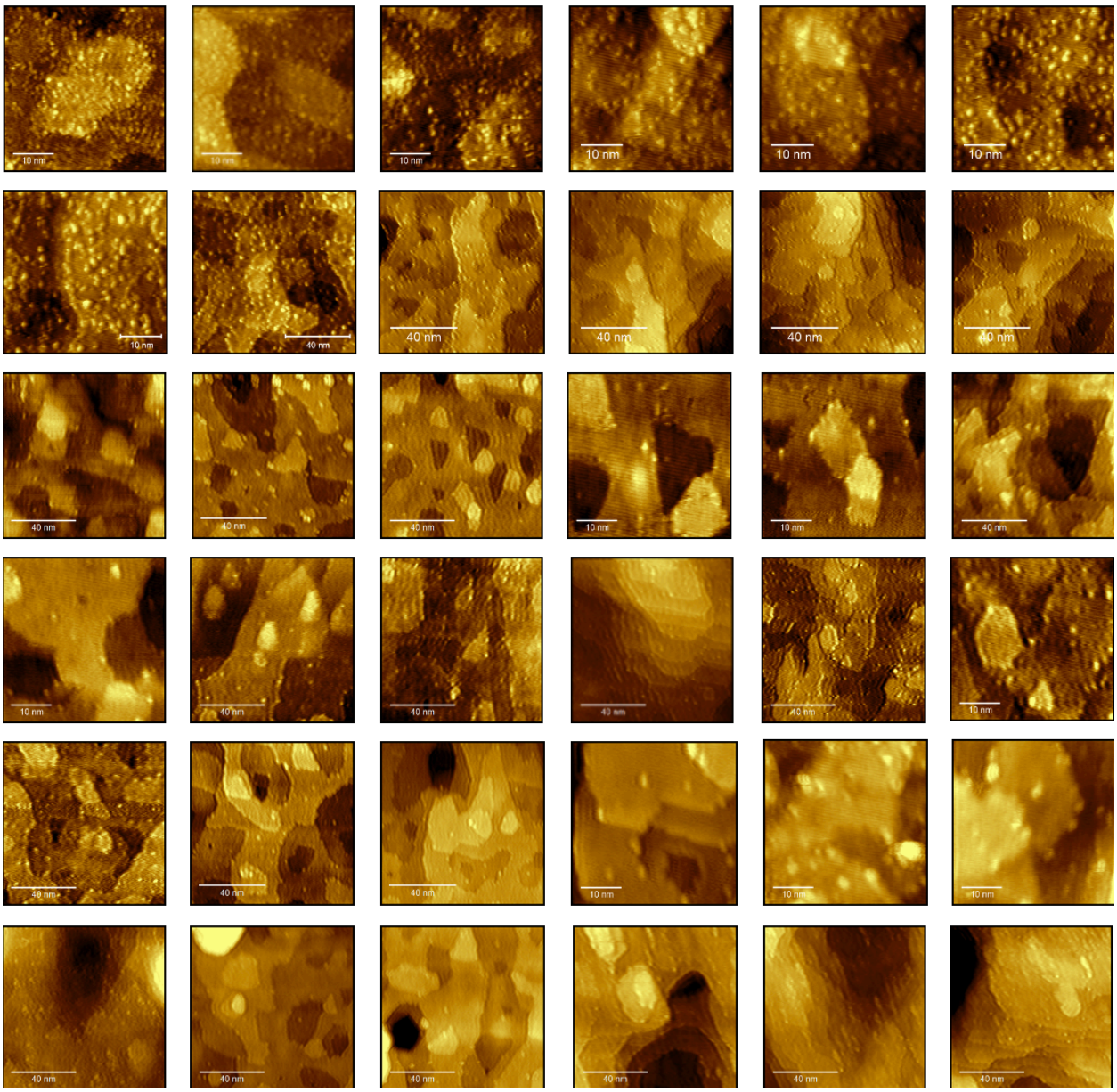


Figure A2.5: First set of 36 images used in Figure 4.8 and the homogeneous reactivity series in Figure 4.9.

Filenames for **Figure A2.5** from top left to bottom right:

Directory: Appendix\A1-46\Bright Sites, Clean
010318_0002, 010318_0005, 011218_0003, 011218_0004, 011218_0005, 011218_0007, 011218_0019, 020518_0002, 020518_0009, 021118_0014, 021118_0016, 021118_0017, 021218_0007, 022818_0007, 022818_0008, 022818_0009, 022818_0016, 022818_0020, 022818_0023, 022818_0026, 022818_0027, 030118_0001, 030118_0002, 030118_0003

Directory: Appendix\A1-46\Bright Sites, 1.0eV, 10hr
022119_0012, 022119_0013, 022119_0019, 022119_0028, 022119_0029, 022119_0030, 022119_0031

Directory: Appendix\A1-46\Bright Sites, 1.1eV, 1.5hr
030118_0025, 030118_0034, 030118_0035, 030118_0036, 030118_0037

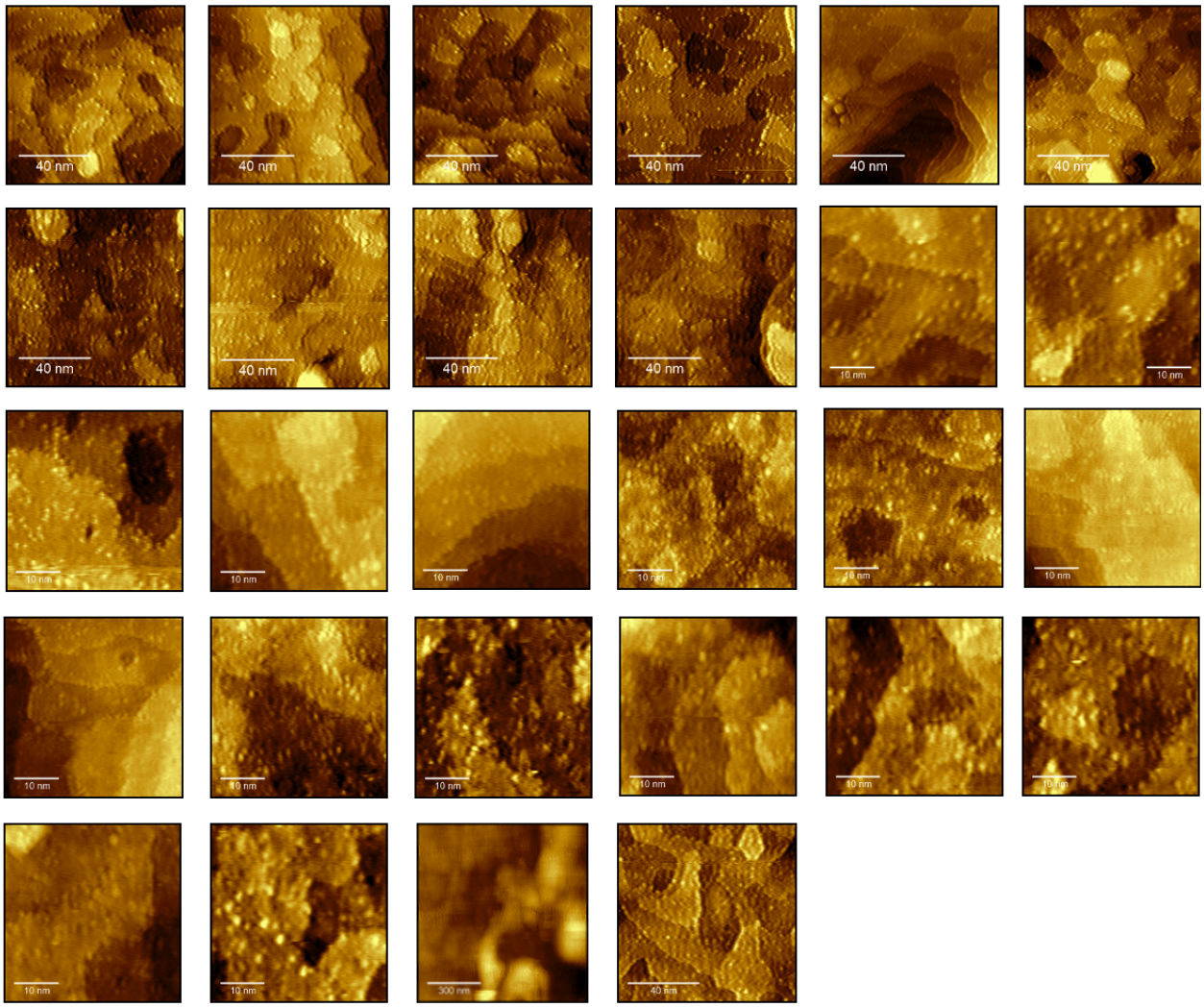


Figure A2.6: Last set of 28 images used in Figure 4.8 and the homogeneous reactivity series in Figure 4.9.

Filenames for **Figure A2.6** from top left to bottom right:

Directory: Appendix\A1-47\Bright Sites, 1.1eV, 1.5hr
030118_0038, 030118_0039, 030118_0040, 030218_0004

Directory: Appendix\A1-47\Bright Sites, 1.1eV, 1.75hr
030219_0011, 030219_0012,030219_0016, 030219_0017, 030219_0018, 030219_0019

Directory: Appendix\A1-47\Bright Sites, 1.1eV, 3.5hr
030419_0023, 030419_0024, 030419_0025, 030419_0026, 030419_0027

Directory: Appendix\A1-47\Bright Sites, 1.1eV, 4hr
030519_0010, 030519_0011, 030519_0012, 030519_0013

Directory: Appendix\A1-47\Bright Sites, 1.1eV, 5.5hr
030719_0006, 030719_0007, 030719_0008, 030719_0009, 030719_0010, 030719_0011, 030719_0012

Directory: Appendix\A1-47\Bright Sites, 1.2eV, 1hr
010918_0046, 011018_0021

A3: STM Visualization of N_2 Dissociative Chemisorption on Ru(0001) at High Impinging Kinetic Energies

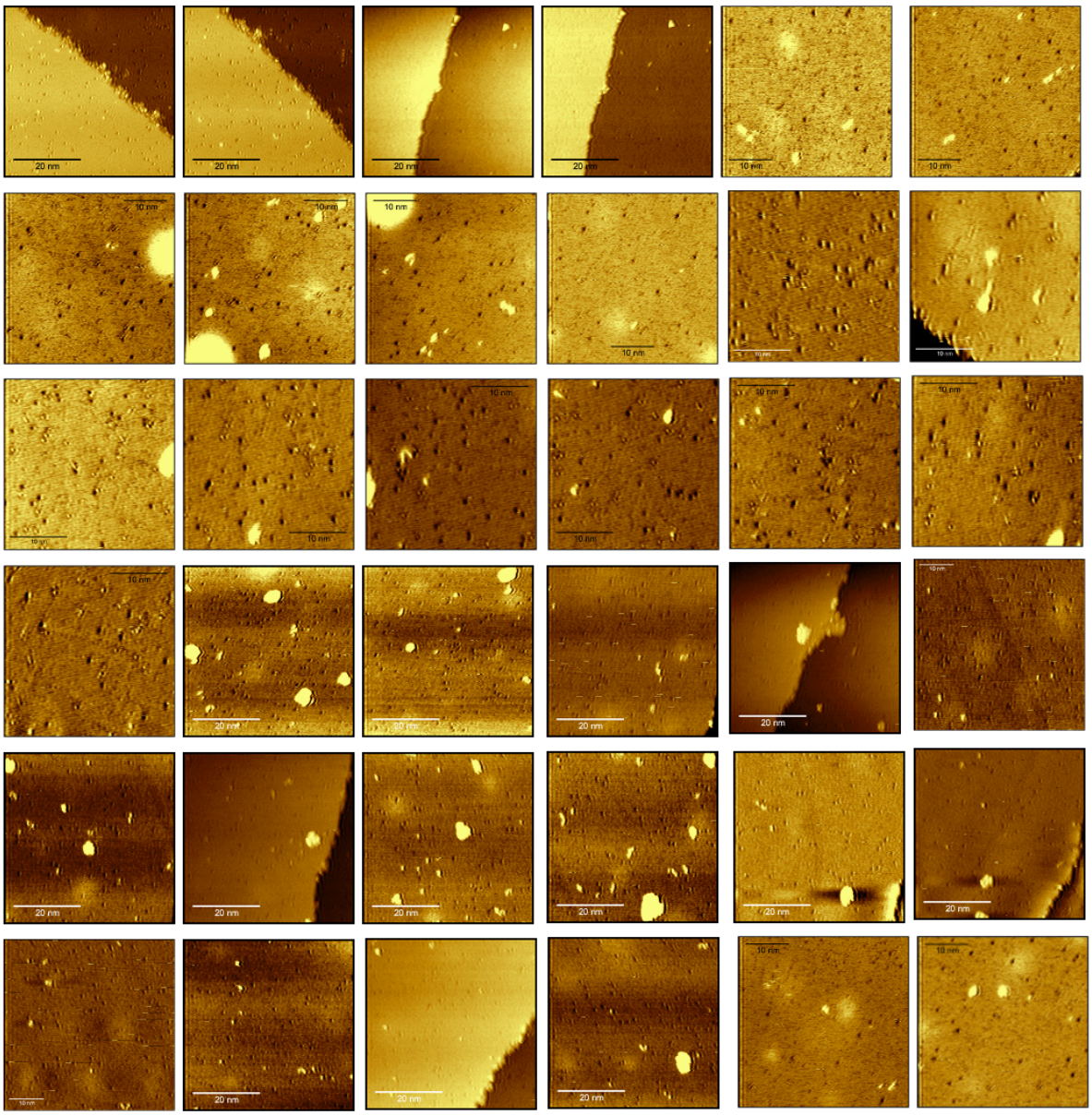


Figure A3.1: First set of 2 images used in Figure 5.4 and first set of 34 images used for Figure 5.6.

Filenames for **Figure A3.1** from top left to bottom right:

Directory: Appendix\A1-48\Diffusion_09-06-20
090620_0043, 090620_0055

Directory: Appendix\A1-48\Diffusion_09-08-20
090720_0026, 090720_0037

Directory: Appendix\A1-48\Statistical_730_Normal_5_min
092920_0018, 092920_0019, 092920_0020, 092920_0022, 092920_0023, 092920_0024, 092920_0025, 092920_0026

Directory: Appendix\A1-48\Statistical_730_Normal_15_min
092020_0029, 092020_0030, 092020_0032, 092020_0033, 092020_0034, 092020_0036, 092020_0038, 092020_0041, 092020_0042

Directory: Appendix\A1-48\Statistical_730_Normal_105_min
091420_0026, 091420_0027, 091420_0028, 091420_0029, 091420_0030, 091420_0031, 091420_0032, 091420_0033, 091420_0034, 091420_0035, 091420_0036, 091420_0037, 091420_0038, 091420_0039, 091420_0040

Directory: Appendix\A1-48\Statistical_730_Normal_5_min
092920_0019, 092920_0026

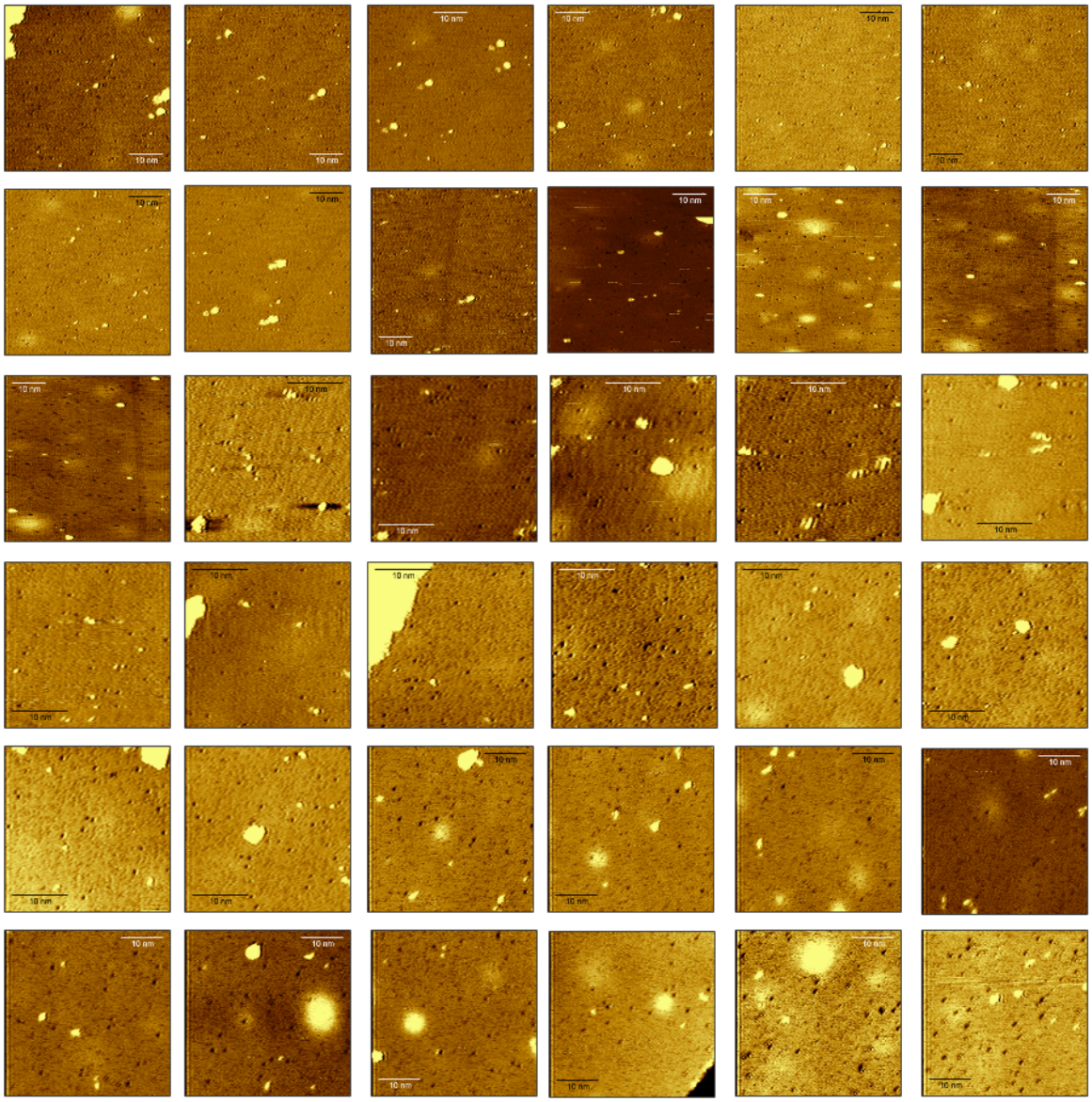


Figure A3.2: Second set of 36 images used in Figure 5.6.

Filenames for **Figure A3.2** from top left to bottom right:

Directory: Appendix\A1-49\Statistical_730_45deg_15_min
092818_0026, 092818_0027, 092818_0028, 092818_0029, 092818_0030, 092818_0031, 092818_0032, 092818_0033, 092818_0034, 092820_0041, 092820_0042, 092820_0043, 092820_0044

Directory: Appendix\A1-49\Statistical_730_45deg_45_min
092120_0021, 092120_0022, 092120_0023, 092120_0024, 092120_0025, 092120_0026, 092120_0027, 092120_0029, 092120_0030, 092120_0031, 092120_0032, 092120_0033, 092120_0034

Directory: Appendix\A1-49\Statistical_730_Normal_5_min
092920_0027, 092920_0028, 092920_0029, 092920_0030, 092920_0031, 092920_0032, 092920_0033, 092920_0034, 092920_0037, 092920_0038

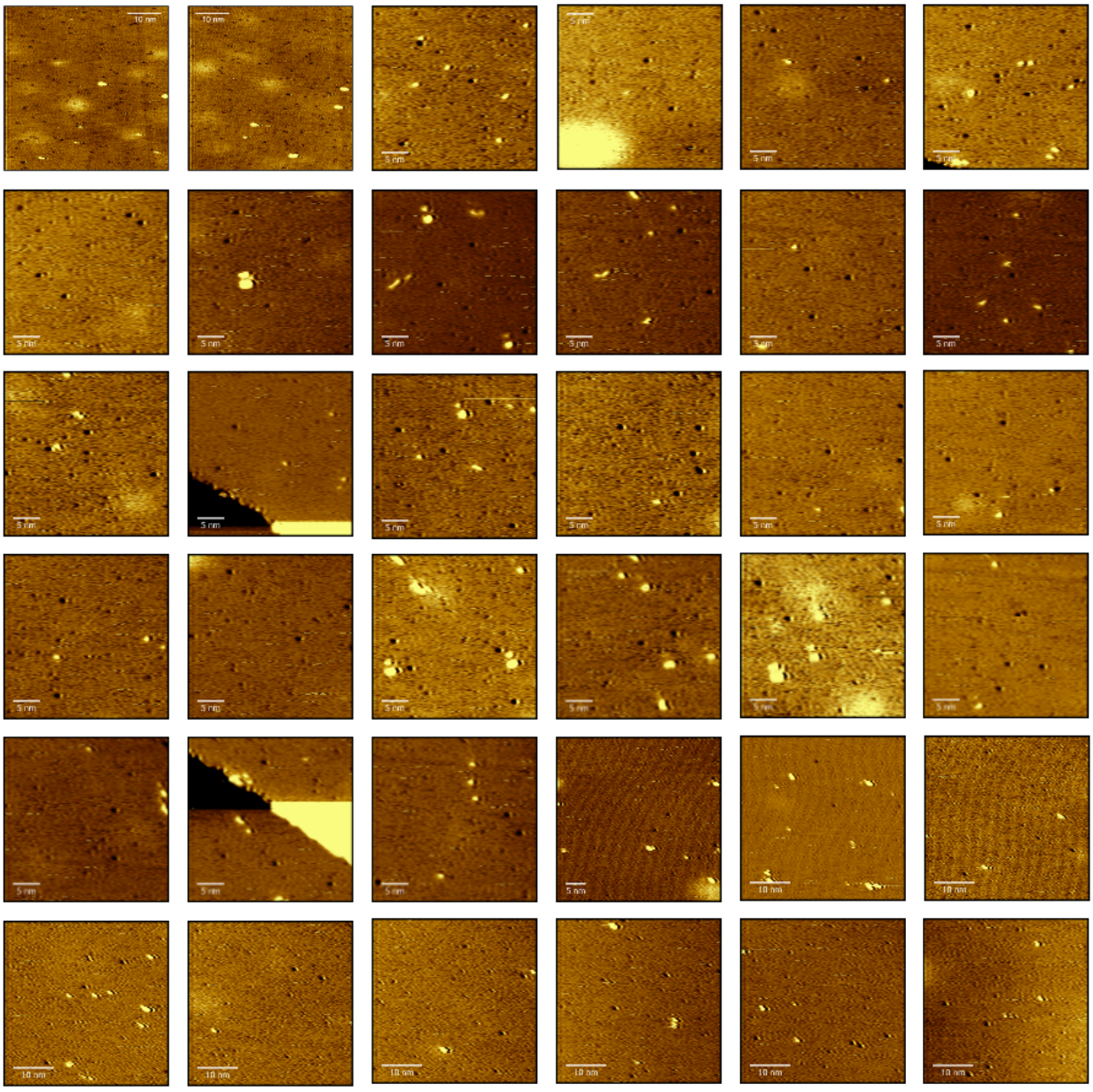


Figure A3.3: Last set of 2 images used in Figure 5.6, first set of 34 images used Figure 5.8.

Filenames for **Figure A3.3** from top left to bottom right:

Directory: Appendix\A1-50\Statistical_730_45deg_15_min
092820_0045, 092820_0046

Directory: Appendix\A1-50\ Statistical_730_Normal_90s
112020_0015, 112020_0016, 112020_0019, 112020_0020, 112020_0024, 112020_0026, 112020_0027, 112020_0029, 112020_0030, 112020_0031, 112020_0032, 112020_0033, 112020_0034, 112020_0035, 112020_0036, 112020_0039, 112020_0040, 112020_0042, 112020_0043, 112020_0045, 112020_0047, 112020_0048, 112020_0050, 112020_0051, 112020_0053

Directory: Appendix\A1-50\Statistical_730_45deg_150s
112320_0017, 112320_0018, 112320_0019, 112320_0022, 112320_0025, 112320_0030, 112320_0031, 112320_0033, 112320_0035

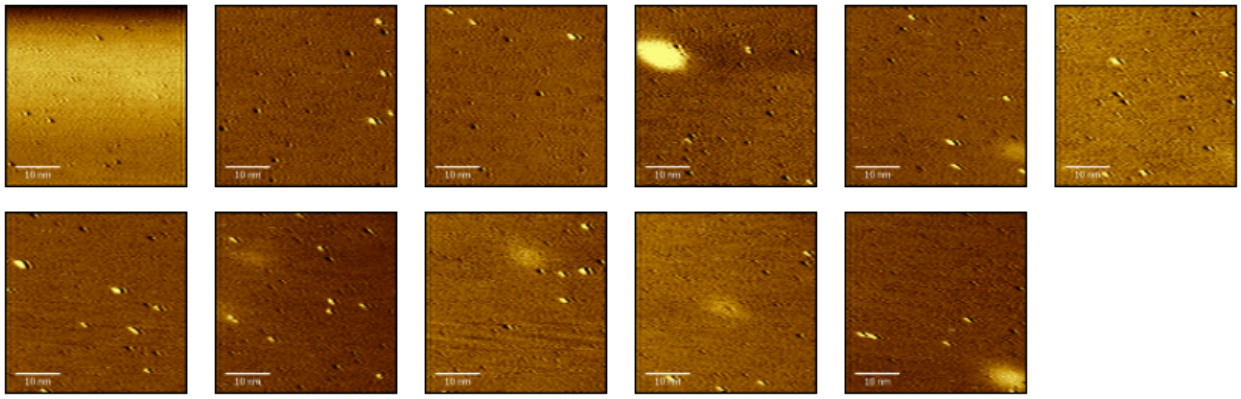


Figure A3.4: Last set of 11 images used in Figure 5.8.

Filenames for **Figure A3.4** from top left to bottom right:

Directory: Appendix\A1-51\Statistical_730_45deg_150s
112320_0039, 112320_0040, 112320_0041, 112320_0044, 112320_0047, 112320_0048, 112320_0052, 112320_0053, 112320_0054, 112320_0055, 112320_0056

A4: Copyright Attribution

Chapter 3 is adapted with permission from Edel, R.; Grabnic, T.; Wiggins, B.; Sibener, S. J. Atomically-Resolved Oxidative Erosion and Ablation of Basal Plane HOPG Graphite Using Supersonic Beams of O_2 with Scanning Tunneling Microscopy Visualization. *The Journal of Physical Chemistry C* **2018**, *122* (26), 14706–14713. Copyright © 2018 American Chemical Society[76] and from Hariharan, S.; Majumder, M.; Edel, R.; Grabnic, T.; Sibener, S. J.; Hase, W. L. Exploratory Direct Dynamics Simulations of 3O2 Reaction with Graphene at High Temperatures. *J. Phys. Chem. C* **2018**, *122* (51), 29368–29379. Copyright © 2018 American Chemical Society.[60]

Chapter 4 is adapted with permission from T. Grabnic, R. Edel, S.J. Sibener, Room temperature oxidation of GaAs(110) using high translational kinetic energy molecular beams of O2 visualized by STM, Surface Science. 692 (2020) 121516. Copyright © 2019 Elsevier B.V.[153]

References

(1) Langmuir, I. Part II.—"Heterogeneous Reactions". Chemical Reactions on Surfaces. *Trans. Faraday Soc.* **1922**, *17* (0), 607–620.

(2) Born, M.; Oppenheimer, R. Zur Quantentheorie Der Molekeln. *Annalen der Physik* **1927**, *389* (20), 457–484.

(3) Binnig, G.; Rohrer, H.; Gerber, Ch.; Weibel, E. Surface Studies by Scanning Tunneling Microscopy. *Physical Review Letters* **1982**, *49* (1), 57–61.

(4) Binnig, G.; Rohrer, H.; Gerber, Ch.; Weibel, E. Tunneling through a Controllable Vacuum Gap. *Applied Physics Letters* **1982**, *40* (2), 178–180.

(5) Binnig, G.; Rohrer, H. Scanning Tunneling Microscopy—from Birth to Adolescence(Nobel Lecture). *Angewandte Chemie International Edition in English* **1987**, *26* (7), 606–614.

(6) Griffiths, D. J.; Schroeter, D. F. *Introduction to Quantum Mechanics*; Cambridge University Press, 2018.

(7) Tersoff, J.; Hamann, D. R. Theory of the Scanning Tunneling Microscope. *Phys. Rev. B* **1985**, *31* (2), 805–813.

(8) Kantrowitz, A.; Grey, J. A High Intensity Source for the Molecular Beam. Part I. Theoretical. *Review of Scientific Instruments* **1951**, *22* (5), 328–332.

(9) Ramsey, N. *Molecular Beams*; OUP Oxford, 1956.

(10) Anderson, J. B.; Fenn, J. B. Velocity Distributions in Molecular Beams from Nozzle Sources. *The Physics of Fluids* **1965**, *8* (5), 780–787.

(11) Morse, M. D. 2 - Supersonic Beam Sources. In *Experimental Methods in the Physical Sciences*; Dunning, F. B., Hulet, R. G., Eds.; Atomic, Molecular, and Optical Physics: Atoms and Molecules; Academic Press, 1996; Vol. 29, pp 21–47.

(12) Anderson, J. B.; Andres, R. P.; Fenn, J. B. Supersonic Nozzle Beams. In *Advances in Chemical Physics*; John Wiley & Sons, Ltd, 2007; pp 275–317.

(13) Scoles, G. Atomic and Molecular Beam Methods; 1988.

(14) Nass, A.; Steffens, E. Direct Simulation of Low-Pressure Supersonic Gas Expansions and Its Experimental Verification. *Nuclear Instruments and Methods in Physics Research Section A: Accelerators, Spectrometers, Detectors and Associated Equipment* **2009**, *598* (3), 653–666.

(15) Ilyin, A. M. Auger Electron Spectroscopy. In *Microscopy Methods in Nanomaterials Characterization*; Elsevier, 2017; pp 363–381.

(16) Meitner, L. Über den Zusammenhang zwischen β- und γ-Strahlen. *Z. Physik* **1922**, *9* (1), 145–152.

(17) AUGER, P. Sur Les Rayons β Secondaires Produits Dans Un Gaz Par Des Rayons X. *CR Acad. Sci. (F)* **1923**, *177*, 169.

(18) Oura, K.; Lifshits, V. G.; Saranin, A.; Zotov, A. V.; Katayama, M. *Surface Science: An Introduction*; Advanced Texts in Physics; Springer-Verlag: Berlin Heidelberg, 2003.

(19) Pan, S. H.; Hudson, E. W.; Davis, J. C. 3He Refrigerator Based Very Low Temperature Scanning Tunneling Microscope. *Review of Scientific Instruments* **1999**, *70* (2), 1459–1463.

(20) Gibson, K. D.; Killelea, D. R.; Yuan, H.; Becker, J. S.; Sibener, S. J. Determination of the Sticking Coefficient and Scattering Dynamics of Water on Ice Using Molecular Beam Techniques. *The Journal of Chemical Physics* **2011**, *134* (3), 034703.

(21) Thompson, R. Adsorption, Diffusion, and Reaction in Condensed Films: Nerve Agent Simulants, Extraterrestrial Ices, and Olefin Oxidation, University of Chicago, Chicago, IL, 2020.

(22) *Foundations of Vacuum Science and Technology*; Lafferty, J. M., Ed.; Wiley: New York, 1998.

(23) Huber, K.; Herzberg, G. *Molecular Spectra and Molecular Structure: IV. Constants of Diatomic Molecules*; Springer US, 1979.

(24) Nečas, D.; Klapetek, P. Gwyddion: An Open-Source Software for SPM Data Analysis. *Open Physics* **2011**, *10* (1), 181–188.

(25) Edel, R. A. Oxidation of Semiconductors and Semimetals by Supersonic Beams of O2 with Scanning Tunneling Microscopy Visualization. Ph.D., The University of Chicago, United States -- Illinois, 2019.

(26) Schneider, C. A.; Rasband, W. S.; Eliceiri, K. W. NIH Image to ImageJ: 25 Years of Image Analysis. *Nature Methods* **2012**, *9* (7), 671–675.

(27) Blyholder, G.; Eyring, H. Kinetics of Graphite Oxidation. *The Journal of Physical Chemistry* **1957**, *61* (5), 682–688.

(28) Strange, J. F.; Walker, P. L. Carbon-Carbon Dioxide Reaction: Langmuir-Hinshelwood Kinetics at Intermediate Pressures. *Carbon* **1976**, *14* (6), 345–350.

(29) Marchon, B.; Carrazza, J.; Heinemann, H.; Somorjai, G. A. TPD and XPS Studies of O_2, CO_2, and H_2O Adsorption on Clean Polycrystalline Graphite. *Carbon* **1988**, *26* (4), 507–514.

(30) Kamioka, I.; Izumi, K.; Kitajima, M.; Kawabe, T.; Ishioka, K.; Nakamura, K. G. Translational Energy Distribution of CO Produced in Infrared-Laser-Assisted Reaction of O_2 with a Graphite Surface. *Japanese journal of applied physics* **1998**, *37* (1A), L74.

(31) Olander, D. R.; Siekhaus, W.; Jones, R.; Schwarz, J. A. Reactions of Modulated Molecular Beams with Pyrolytic Graphite. I. Oxidation of the Basal Plane. *The Journal of Chemical Physics* **1972**, *57* (1), 408–420.

(32) Olander, D. R.; Jones, R. H.; Schwarz, J. A.; Siekhaus, W. J. Reactions of Modulated Molecular Beams with Pyrolytic Graphite. II Oxidation of the Prism Plane. *The Journal of Chemical Physics* **1972**, *57* (1), 421–433.

(33) Acharya, T. R.; Olander, D. R. The Rate of Oxidation of the Basal and Prismatic Surfaces of Pyrolytic Graphite in the Transition Regime between Chemical and Diffusional Control. *Carbon* **1973**, *11* (1), 7–18.

(34) Sun, T.; Yao, X.; Fabris, S. Effects of Thermal Electronic Excitations on the Diffusion of Oxygen Adatoms on Graphene. *J. Phys. Chem. A* **2016**, *120* (17), 2607–2613.

(35) Chang, H.; Bard, A. J. Scanning Tunneling Microscopy Studies of Carbon-Oxygen Reactions on Highly Oriented Pyrolytic Graphite. *Journal of the American Chemical Society* **1991**, *113* (15), 5588–5596.

(36) Chu, X.; Schmidt, L. D. Reactions of NO, O_2, H_2O, and CO_2 with the Basal Plane of Graphite. *Surface Science* **1992**, *268* (1), 325–332.

(37) Stevens, F.; Kolodny, L. A.; Beebe, T. P. Kinetics of Graphite Oxidation: Monolayer and Multilayer Etch Pits in HOPG Studied by STM. *J. Phys. Chem. B* **1998**, *102* (52), 10799–10804.

(38) Hahn, J. R. Kinetic Study of Graphite Oxidation Along Two Lattice Directions. *Carbon* **2005**, *43* (7), 1506–1511.

(39) Xu, S. C.; Chen, H.-L.; Lin, M. C. Quantum Chemical Prediction of Reaction Pathways and Rate Constants for the Reactions of O_x (x = 1 and 2) with Pristine and Defective Graphite (0001) Surfaces. *J. Phys. Chem. C* **2012**, *116* (2), 1841–1849.

(40) Wiggins, B.; Avila-Bront, L. G.; Edel, R.; Sibener, S. J. Temporally and Spatially Resolved Oxidation of Si(111)-(7 × 7) Using Kinetic Energy Controlled Supersonic Beams in Combination with Scanning Tunneling Microscopy. *J. Phys. Chem. C* **2016**, *120* (15), 8191–8197.

(41) Hahn, J. R.; Kang, H. Vacancy and Interstitial Defects at Graphite Surfaces: Scanning Tunneling Microscopic Study of the Structure, Electronic Property, and Yield for Ion-Induced Defect Creation. *Phys. Rev. B* **1999**, *60* (8), 6007–6017.

(42) Lee, S. M.; Lee, Y. H.; Hwang, Y. G.; Hahn, J. R.; Kang, H. Defect-Induced Oxidation of Graphite. *Phys. Rev. Lett.* **1999**, *82* (1), 217–220.

(43) Chu, X.; Schmidt, L. D. Gasification of Graphite Studied by Scanning Tunneling Microscopy. *Carbon* **1991**, *29* (8), 1251–1255.

(44) Atamny, F.; Schlögl, R.; Wirth, W. J.; Stephan, J. Topochemistry of Graphite Oxidation. *Ultramicroscopy* **1992**, *42*, 660–667.

(45) Klusek, Z. Scanning Tunneling Microscopy and Spectroscopy of the Thermally Oxidized (0001) Basal Plane of Highly Oriented Pyrolitic Graphite. *Applied Surface Science* **1998**, *125* (3), 339–350.

(46) Tandon, D.; Hippo, E. J.; Marsh, H.; Sebok, E. Surface Topography of Oxidized HOPG by Scanning Tunneling Microscopy. *Carbon* **1997**, *35* (1), 35–44.

(47) Zhu, Y.-J.; Hansen, T. A.; Ammermann, S.; McBride, J. D.; Beebe, T. P. Nanometer-Size Monolayer and Multilayer Molecule Corrals on HOPG: A Depth-Resolved Mechanistic Study by STM. *J. Phys. Chem. B* **2001**, *105* (32), 7632–7638.

(48) Böttcher, A.; Heil, M.; Stürzl, N.; Jester, S. S.; Malik, S.; Pérez-Willard, F.; Patrice Brenner; Gerthsen, D.; Kappes, M. M. Nanostructuring the Graphite Basal Plane by Focused Ion Beam Patterning and Oxygen Etching. *Nanotechnology* **2006**, *17* (23), 5889.

(49) Paredes, J. I.; Martínez-Alonso, A.; Tascón, J. M. D. Comparative Study of the Air and Oxygen Plasma Oxidation of Highly Oriented Pyrolytic Graphite: A Scanning Tunneling and Atomic Force Microscopy Investigation. *Carbon* **2000**, *38* (8), 1183–1197.

(50) Murray, V. J.; Marshall, B. C.; Woodburn, P. J.; Minton, T. K. Inelastic and Reactive Scattering Dynamics of Hyperthermal O and O_2 on Hot Vitreous Carbon Surfaces. *The Journal of Physical Chemistry C* **2015**, *119* (26), 14780–14796.

(51) Murray, V. J.; Smoll, E. J.; Minton, T. K. Dynamics of Graphite Oxidation at High Temperature. *J. Phys. Chem. C* **2018**.

(52) Liu, G. N.-K. *High Temperature Oxidation of Graphite by a Dissociated Oxygen Beam*; 1973.

(53) Sun, T.; Fabris, S.; Baroni, S. Surface Precursors and Reaction Mechanisms for the Thermal Reduction of Graphene Basal Surfaces Oxidized by Atomic Oxygen. *J. Phys. Chem. C* **2011**, *115* (11), 4730–4737.

(54) Poovathingal, S.; Schwartzentruber, T. E.; Srinivasan, S. G.; van Duin, A. C. T. Large Scale Computational Chemistry Modeling of the Oxidation of Highly Oriented Pyrolytic Graphite. *J. Phys. Chem. A* **2013**, *117* (13), 2692–2703.

(55) Carlsson, J. M.; Hanke, F.; Linic, S.; Scheffler, M. Two-Step Mechanism for Low-Temperature Oxidation of Vacancies in Graphene. *Phys. Rev. Lett.* **2009**, *102* (16), 166104.

(56) Delehouzé, A.; Rebillat, F.; Weisbecker, P.; Leyssale, J.-M.; Epherre, J.-F.; Labrugère, C.; Vignoles, G. L. Temperature Induced Transition from Hexagonal to Circular Pits in Graphite Oxidation by O_2. *Applied Physics Letters* **2011**, *99* (4), 044102.

(57) Stevens, F.; Beebe, T. P. Computer Modeling of Graphite Oxidation: Differences Between Monolayer and Multilayer Etching. *Computers & Chemistry* **1999**, *23* (2), 175–183.

(58) Hahn, J. R.; Kang, H.; Song, S.; Jeon, I. C. Observation of Charge Enhancement Induced by Graphite Atomic Vacancy: A Comparative STM and AFM Study. *Phys. Rev. B* **1996**, *53* (4), R1725–R1728.

(59) Hembacher, S.; Giessibl, F.; Mannhart, J.; F Quate, C. Revealing the Hidden Atom in Graphite by Low-Temperature Atomic Force Microscopy. *Proceedings of the National Academy of Sciences of the United States of America* **2003**, *100*, 12539–12542.

(60) Hariharan, S.; Majumder, M.; Edel, R.; Grabnic, T.; Sibener, S. J.; Hase, W. L. Exploratory Direct Dynamics Simulations of 3O2 Reaction with Graphene at High Temperatures. *J. Phys. Chem. C* **2018**, *122* (51), 29368–29379.

(61) Chu, X.; Schmidt, L. D. Intrinsic Rates of Nitrogen Oxide (NO_x)-Carbon Reactions. *Industrial & engineering chemistry research* **1993**, *32* (7), 1359–1366.

(62) Tracz, A.; Wegner, G.; Rabe, J. P. Kinetics of Surface Roughening via Pit Growth During the Oxidation of the Basal Plane of Graphite. 1. Experiments. *Langmuir* **1993**, *9* (11), 3033–3038.

(63) Rodriguez-reinoso, F.; Thrower, P. A. Microscopic Studies of Oxidized Highly Oriented Pyrolytic Graphites. *Carbon* **1974**, *12* (3), 269–279.

(64) del Alamo, J. A. Nanometre-Scale Electronics with III–V Compound Semiconductors. *Nature* **2011**, *479* (7373), 317–323.

(65) Whitesides, George. M. Materials for Advanced Electronic Devices. In *Biotechnology and Materials Science: Chemistry for the Future*; Good, M., L., Baum, R., Peterson, I., Henderson, N., Eds.; American Chemical Society: Washington, DC, 1988; pp 85–99.

(66) Schmuki, P.; Sproule, G. I.; Bardwell, J. A.; Lu, Z. H.; Graham, M. J. Thin Anodic Oxides Formed on GaAs in Aqueous Solutions. *Journal of Applied Physics* **1996**, *79* (9), 7303–7311.

(67) Wang, H.-H.; Wu, J.-Y.; Wang, Y.-H.; Houng, M.-P. Effects of PH Values on the Kinetics of Liquid-Phase Chemical-Enhanced Oxidation of GaAs. *J. Electrochem. Soc.* **1999**, *146* (6), 2328–2332.

(68) Telford, M. Progress in GaAs Manufacturing Technology. *III-Vs Review* **2001**, *14* (6), 22–26.

(69) Pakes, A.; Skeldon, P.; Thompson, G. E.; Hussey, R. J.; Moisa, S.; Sproule, G. I.; Landheer, D.; Graham, M. J. Composition and Growth of Anodic and Thermal Oxides on InP and GaAs. *Surface and Interface Analysis* **2002**, *34* (1), 481–484.

(70) Lee, H.-Y. Growth of GaAs Oxide Layer Using Photoelectrochemical Method. *Journal of The Electrochemical Society* **2008**, *155* (7), G141.

(71) Lee, H.-Y.; Lin, Y.-F. GaAs Metal-Oxide-Semiconductor Devices with a Complex Gate Oxide Composed of SiO2and GaAs Oxide Grown Using a Photoelectrochemical Oxidation Method. *Semicond. Sci. Technol.* **2009**, *25* (1), 015005.

(72) Gucmann, F.; Kúdela, R.; Kordoš, P.; Dobročka, E.; Gaži, Š.; Dérer, J.; Liday, J.; Vogrinčič, P.; Gregušová, D. III-As Heterostructure Field-Effect Transistors with Recessed Ex-Situ Gate Oxide by O2 Plasma-Oxidized GaAs Cap. *Journal of Vacuum Science & Technology B* **2015**, *33* (1), 01A111.

(73) Sharma, H.; Moumanis, K.; Dubowski, J. J. PH-Dependent Photocorrosion of GaAs/AlGaAs Quantum Well Microstructures. *J. Phys. Chem. C* **2016**, *120* (45), 26129–26137.

(74) Childs, K. D.; Lagally, M. G. Species-Specific Densities of States of Ga and As in the Chemisorption of Oxygen on GaAs(110). *Phys. Rev. B* **1984**, *30* (10), 5742–5752.

(75) Mönch, W. Oxidation of Silicon and III–V Compound Semiconductors. In *Semiconductor Surfaces and Interfaces*; Mönch, W., Ed.; Springer Series in Surface Sciences; Springer Berlin Heidelberg: Berlin, Heidelberg, 2001; pp 353–376.

(76) Edel, R.; Grabnic, T.; Wiggins, B.; Sibener, S. J. Atomically-Resolved Oxidative Erosion and Ablation of Basal Plane HOPG Graphite Using Supersonic Beams of O_2 with Scanning Tunneling Microscopy Visualization. *The Journal of Physical Chemistry C* **2018**, *122* (26), 14706–14713.

(77) Frankel, D. J.; Anderson, J. R.; Lapeyre, G. J. UV Photoemission Study of Low Temperature Oxygen Adsorption on GaAs(110). *Journal of Vacuum Science & Technology B: Microelectronics Processing and Phenomena* **1983**, *1* (3), 763–766.

(78) Bartels, F.; Surkamp, L.; Clemens, H. J.; Mönch, W. Oxygen and Hydrogen Adsorption on GaAs(110). *Journal of Vacuum Science & Technology B: Microelectronics Processing and Phenomena* **1983**, *1* (3), 756–762.

(79) Hughes, G.; Ludeke, R. O 1s Studies of the Oxidation of InP(110) and GaAs(110) Surfaces. *Journal of Vacuum Science & Technology B: Microelectronics Processing and Phenomena* **1986**, *4* (4), 1109–1114.

(80) Mönch, W. On the Oxidation of III–V Compound Semiconductors. *Surface Science* **1986**, *168* (1), 577–593.

(81) Bartels, F.; Mönch, W. On the Growth Mode of Oxide Films on Cleaved GaAs(110) Surfaces at Room Temperature. *Solid State Communications* **1986**, *57* (8), 571–574.

(82) Bartels, F.; Mönch, W. Oxidation Mechanism of III–V Semiconductors. *Vacuum* **1990**, *41* (1), 667–668.

(83) Landgren, G.; Ludeke, R.; Jugnet, Y.; Morar, J. F.; Himpsel, F. J. The Oxidation of GaAs(110): A Reevaluation. *Journal of Vacuum Science & Technology B: Microelectronics Processing and Phenomena* **1984**, *2* (3), 351–358.

(84) Landgren, G.; Ludeke, R.; Morar, J. F.; Jugnet, Y.; Himpsel, F. J. Oxidation of GaAs(110): New Results and Models. *Physical Review B* **1984**, *30* (8), 4839–4841.

(85) Bertness, K. A.; Yeh, J.-J.; Friedman, D. J.; Mahowald, P. H.; Wahi, A. K.; Kendelewicz, T.; Lindau, I.; Spicer, W. E. Growth Structure of Chemisorbed Oxygen on GaAs(110) and InP(110) Surfaces. *Physical Review B* **1988**, *38* (8), 5406–5421.

(86) Cabrera, N.; Mott, N. F. Theory of the Oxidation of Metals. *Rep. Prog. Phys.* **1949**, *12* (1), 163–184.

(87) Pianetta, P.; Lindau, I.; Garner, C. M.; Spicer, W. E. Oxidation Properties of GaAs (110) Surfaces. *Physical Review Letters* **1976**, *37* (17), 1166–1169.

(88) Pianetta, P.; Lindau, I.; Garner, C.; Spicer, W. E. Determination of the Oxygen Binding Site on GaAs(110) Using Soft-X-Ray-Photoemission Spectroscopy. *Physical Review Letters* **1975**, *35* (20), 1356–1359.

(89) Pianetta, P.; Lindau, I.; Garner, C. M.; Spicer, W. E. Chemisorption and Oxidation Studies of the (110) Surfaces of GaAs, GaSb, and InP. *Physical Review B* **1978**, *18* (6), 2792–2806.

(90) Ludeke, R. The Oxidation of the GaAs (110) Surface. *Solid State Communications* **1977**, *21* (8), 815–818.

(91) Ludeke, R. Oxidation Properties of GaAs (110) Surfaces. *Physical Review B* **1977**, *16* (12), 5598–5599.

(92) Brundle, C. R.; Seybold, D. Oxygen Interaction with GaAs Surfaces: An XPS/UPS Study. *Journal of Vacuum Science and Technology* **1979**, *16* (5), 1186–1190.

(93) Tsai, M.-H.; Packard, W. E.; Dow, J. D.; Kasowski, R. V. Oxidation of the GaAs(110) Surface. *Physica B: Condensed Matter* **1993**, *192* (4), 365–370.

(94) Spicer, W. E.; Lindau, I.; Gregory, P. E.; Garner, C. M.; Pianetta, P.; Chye, P. W. Synchrotron Radiation Studies of Electronic Structure and Surface Chemistry of GaAs, GaSb, and InP. *Journal of Vacuum Science and Technology* **1976**, *13* (4), 780–785.

(95) Dorn, R.; Lüth, H.; Russell, G. J. Adsorption of Oxygen on Clean Cleaved (110) Gallium-Arsenide Surfaces. *Physical Review B* **1974**, *10* (12), 5049–5056.

(96) Chye, P. W.; Pianetta, P.; Lindau, I.; Spicer, W. E. Oxygen Sorption and Excitonic Effects on GaAs Surfaces. *Journal of Vacuum Science and Technology* **1977**, *14* (4), 917–919.

(97) Ludeke, R.; Koma, A. Electronic Surface States on Clean and Oxygen-exposed GaAs Surfaces. *Journal of Vacuum Science and Technology* **1976**, *13* (1), 241–247.

(98) Stroscio, J. A.; Feenstra, R. M.; Fein, A. P. Structure of Oxygen Adsorbed on the GaAs(110) Surface Studied Using Scanning Tunneling Microscopy. *Phys. Rev. B* **1987**, *36* (14), 7718–7721.

(99) Kruse, P.; McLean, J. G.; Kummel, A. C. Relative Reactivity of Arsenic and Gallium Dimers and Backbonds during the Adsorption of Molecular Oxygen on GaAs(100)(6×6). *J. Chem. Phys.* **2000**, *113* (20), 9217–9223.

(100) Kruse, P.; McLean, J. G.; Kummel, A. C. Chemically Selective Adsorption of Molecular Oxygen on GaAs(100)c(2×8). *The Journal of Chemical Physics* **2000**, *113* (20), 9224–9232.

(101) Passlack, M.; Hong, M.; Mannaerts, J. P.; Opila, R. L.; Ren, F. Thermodynamic and Photochemical Stability of Low Interface State Density Ga2O3–GaAs Structures Fabricated by in Situ Molecular Beam Epitaxy. *Appl. Phys. Lett.* **1996**, *69* (3), 302–304.

(102) Feenstra, R. M.; Stroscio, J. A.; Tersoff, J.; Fein, A. P. Atom-Selective Imaging of the GaAs(110) Surface. *Physical Review Letters* **1987**, *58* (12), 1192–1195.

(103) Stroscio, J. A.; Feenstra, R. M.; Fein, A. P. Local State Density and Long-Range Screening of Adsorbed Oxygen Atoms on the GaAs(110) Surface. *Physical Review Letters* **1987**, *58* (16), 1668–1671.

(104) Moriarty, P.; Hughes, G. An Investigation of the Early Stages of Native Oxide Growth on Chemically Etched and Sulfur-Treated GaAs(100) and InP(100) Surfaces by Scanning Tunnelling Microscopy. *Ultramicroscopy* **1992**, *42–44*, 956–961.

(105) Nevo, I.; Aloni, S.; Cohen, S. R.; Hasse, G. The Effect of Adsorbed Oxygen on the Surface Potential of N-GaAs(110). *The Journal of Chemical Physics* **2005**, *123* (6), 064705.

(106) Hollinger, G.; Hughes, G.; Himpsel, F. J.; Jordan, J. L.; Morar, J. F.; Houzay, F. Early Stages in the Formation of the Oxide-InP(110) Interface. *Surface Science* **1986**, *168* (1), 617–625.

(107) King, D. A.; Wells, M. G. Molecular Beam Investigation of Adsorption Kinetics on Bulk Metal Targets: Nitrogen on Tungsten. *Surface Science* **1972**, *29* (2), 454–482.

(108) Piercy, P.; Castonguay, A. M.-J. Diffusion-Limited Kinetics of Terrace Growth on GaAs(110). *Physical Review B* **2005**, *72* (11).

(109) Pechman, R. J.; Wang, X.-S.; Weaver, J. H. Vacancy Kinetics and Sputtering of GaAs(110). *Physical Review B* **1995**, *51* (16), 10929–10936.

(110) Wang, X.-S.; Pechman, R. J.; Weaver, J. H. Trends in Surface Roughening: Analysis of Ion-Sputtered GaAs(110). *Surface Science* **1996**, *364* (1), L511–L518.

(111) Barrett, N. T.; Greaves, G. N.; Pizzini, S.; Roberts, K. J. The Local Atomic Structure of the Oxide Coating on Polished GaAs(100). *Surface Science* **1990**, *227* (3), 337–346.

(112) Proietti, M. G.; Garcia, J.; Chaboy, J.; Morier-Genoud, F.; Martin, D. Structural Properties of GaAs Oxide Layers Grown on Polished (100) Surfaces. *J. Phys.: Condens. Matter* **1993**, *5* (9), 1229–1238.

(113) Thurmond, C. D.; Schwartz, G. P.; Kammlott, G. W.; Schwartz, B. GaAs Oxidation and the Ga-As-O Equilibrium Phase Diagram. *J. Electrochem. Soc.* **1980**, *127* (6), 1366.

(114) Donnelly, K. Simulation to Determine the Variance and Edge-Effect of Total Nearest Neighbour Distance. *Simulation methods in archeology* **1978**.

(115) Herron, J. A.; Tonelli, S.; Mavrikakis, M. Atomic and Molecular Adsorption on Ru(0001). *Surface Science* **2013**, *614*, 64–74.

(116) Jacobi, K. Nitrogen on Ruthenium Single-Crystal Surfaces. *physica status solidi (a)* **2000**, *177* (1), 37–51.

(117) Ertl, G. Primary Steps in Catalytic Synthesis of Ammonia. *Journal of Vacuum Science & Technology A* **1983**, *1* (2), 1247–1253.

(118) Nielsen, A. *Ammonia: Catalysis and Manufacture*; Springer Science & Business Media, 2012.

(119) Rosowski, F.; Hornung, A.; Hinrichsen, O.; Herein, D.; Muhler, M.; Ertl, G. Ruthenium Catalysts for Ammonia Synthesis at High Pressures: Preparation, Characterization, and Power-Law Kinetics. *Applied Catalysis A: General* **1997**, *151* (2), 443–460.

(120) Logadóttir, Á.; Nørskov, J. K. Ammonia Synthesis over a Ru(0001) Surface Studied by Density Functional Calculations. *Journal of Catalysis* **2003**, *220* (2), 273–279.

(121) Honkala, K.; Hellman, A.; Remediakis, I. N.; Logadottir, A.; Carlsson, A.; Dahl, S.; Christensen, C. H.; Nørskov, J. K. Ammonia Synthesis from First-Principles Calculations. *Science* **2005**, *307* (5709), 555–558.

(122) Yang, X.-L.; Zhang, W.-Q.; Xia, C.-G.; Xiong, X.-M.; Mu, X.-Y.; Hu, B. Low Temperature Ruthenium Catalyst for Ammonia Synthesis Supported on BaCeO3 Nanocrystals. *Catalysis Communications* **2010**, *11* (10), 867–870.

(123) Fajardo, J.; Peters, J. C. Catalytic Nitrogen-to-Ammonia Conversion by Osmium and Ruthenium Complexes. *J. Am. Chem. Soc.* **2017**, *139* (45), 16105–16108.

(124) Foster, S. L.; Bakovic, S. I. P.; Duda, R. D.; Maheshwari, S.; Milton, R. D.; Minteer, S. D.; Janik, M. J.; Renner, J. N.; Greenlee, L. F. Catalysts for Nitrogen Reduction to Ammonia. *Nature Catalysis* **2018**, *1* (7), 490–500.

(125) Ertl, G. Reactions at Surfaces: From Atoms to Complexity (Nobel Lecture). *Angewandte Chemie International Edition* **2008**, *47* (19), 3524–3535.

(126) Michelsen, H. A.; Auerbach, D. J. A Critical Examination of Data on the Dissociative Adsorption and Associative Desorption of Hydrogen at Copper Surfaces. *J. Chem. Phys.* **1991**, *94* (11), 7502–7520.

(127) Kroes, G.-J. Six-Dimensional Quantum Dynamics of Dissociative Chemisorption of H2 on Metal Surfaces. *Progress in Surface Science* **1999**, *60* (1), 1–85.

(128) Mortensen, H.; Diekhöner, L.; Baurichter, A.; Luntz, A. C. CH4 Dissociation on Ru(0001): A View from Both Sides of the Barrier. *J. Chem. Phys.* **2002**, *116* (13), 5781–5794.

(129) Luntz, A. C.; Harris, J. CH4 Dissociation on Metals: A Quantum Dynamics Model. *Surface Science* **1991**, *258* (1), 397–426.

(130) Romm, L.; Katz, G.; Kosloff, R.; Asscher, M. Dissociative Chemisorption of N2 on Ru(001) Enhanced by Vibrational and Kinetic Energy: Molecular Beam Experiments and Quantum Mechanical Calculations. *The Journal of Physical Chemistry B* **1997**, *101* (12), 2213–2217.

(131) C. Egeberg, R.; H. Larsen, J.; Chorkendorff, I. Molecular Beam Study of N 2 Dissociation on Ru(0001). *Physical Chemistry Chemical Physics* **2001**, *3* (11), 2007–2011.

(132) Diekhöner, L.; Mortensen, H.; Baurichter, A.; Jensen, E.; Petrunin, V. V.; Luntz, A. C. N2 Dissociative Adsorption on Ru(0001): The Role of Energy Loss. *J. Chem. Phys.* **2001**, *115* (19), 9028–9035.

(133) Katz, G.; Kosloff, R. Temperature Dependence of Nitrogen Dissociation on Metal Surfaces. *J. Chem. Phys.* **1995**, *103* (21), 9475–9481.

(134) Diekhöner, L.; Hornekær, L.; Mortensen, H.; Jensen, E.; Baurichter, A.; Petrunin, V. V.; Luntz, A. C. Indirect Evidence for Strong Nonadiabatic Coupling in N2 Associative Desorption from and Dissociative Adsorption on Ru(0001). *J. Chem. Phys.* **2002**, *117* (10), 5018–5030.

(135) Romm, L.; Citri, O.; Kosloff, R.; Asscher, M. A Remarkable Heavy Atom Isotope Effect in the Dissociative Chemisorption of Nitrogen on Ru(001). *J. Chem. Phys.* **2000**, *112* (19), 8221–8224.

(136) Mortensen, H.; Jensen, E.; Diekhöner, L.; Baurichter, A.; Luntz, A. C.; Petrunin, V. V. State Resolved Inelastic Scattering of N2 from Ru(0001). *J. Chem. Phys.* **2003**, *118* (24), 11200–11209.

(137) Spiering, P.; Shakouri, K.; Behler, J.; Kroes, G.-J.; Meyer, J. Orbital-Dependent Electronic Friction Significantly Affects the Description of Reactive Scattering of N2 from Ru(0001). *J. Phys. Chem. Lett.* **2019**, *10* (11), 2957–2962.

(138) Dou, W.; Subotnik, J. E. Nonadiabatic Molecular Dynamics at Metal Surfaces. *J. Phys. Chem. A* **2020**, *124* (5), 757–771.

(139) Shakouri, K.; Behler, J.; Meyer, J.; Kroes, G.-J. Accurate Neural Network Description of Surface Phonons in Reactive Gas–Surface Dynamics: N2 + Ru(0001). *J. Phys. Chem. Lett.* **2017**, *8* (10), 2131–2136.

(140) Shakouri, K.; Behler, J.; Meyer, J.; Kroes, G.-J. Analysis of Energy Dissipation Channels in a Benchmark System of Activated Dissociation: N2 on Ru(0001). *J. Phys. Chem. C* **2018**, *122* (41), 23470–23480.

(141) van Harrevelt, R.; Honkala, K.; Nørskov, J. K.; Manthe, U. The Reaction Rate for Dissociative Adsorption of N2 on Stepped Ru(0001): Six-Dimensional Quantum Calculations. *J. Chem. Phys.* **2005**, *122* (23), 234702.

(142) Díaz, C.; Vincent, J. K.; Krishnamohan, G. P.; Olsen, R. A.; Kroes, G. J.; Honkala, K.; Nørskov, J. K. Reactive and Nonreactive Scattering of N2 from Ru(0001): A Six-Dimensional Adiabatic Study. *J. Chem. Phys.* **2006**, *125* (11), 114706.

(143) Díaz, C.; Vincent, J. K.; Krishnamohan, G. P.; Olsen, R. A.; Kroes, G. J.; Honkala, K.; Nørskov, J. K. Multidimensional Effects on Dissociation of N2 on Ru(0001). *Phys. Rev. Lett.* **2006**, *96* (9), 096102.

(144) Danielson, L. R.; Dresser, M. J.; Donaldson, E. E.; Dickinson, J. T. Adsorption and Desorption of Ammonia, Hydrogen, and Nitrogen on Ruthenium (0001). *Surface Science* **1978**, *71* (3), 599–614.

(145) Shi, H.; Jacobi, K.; Ertl, G. Dissociative Chemisorption of Nitrogen on Ru(0001). *J. Chem. Phys.* **1993**, *99* (11), 9248–9254.

(146) Dietrich, H.; Geng, P.; Jacobi, K.; Ertl, G. Sticking Coefficient for Dissociative Adsorption of N2 on Ru Single-crystal Surfaces. *J. Chem. Phys.* **1996**, *104* (1), 375–381.

(147) Hammer, B. Coverage Dependence of ${\mathrm{N}}_{2}$ Dissociation at an N, O, or H Precovered Ru(0001) Surface Investigated with Density Functional Theory. *Phys. Rev. B* **2001**, *63* (20), 205423.

(148) Dahl, S.; Logadottir, A.; Egeberg, R. C.; Larsen, J. H.; Chorkendorff, I.; Törnqvist, E.; Nørskov, J. K. Role of Steps in N 2 Activation on Ru(0001). *Physical Review Letters* **1999**, *83* (9), 1814–1817.

(149) Dahl, S.; Törnqvist, E.; Chorkendorff, I. Dissociative Adsorption of N2 on Ru(0001): A Surface Reaction Totally Dominated by Steps. *Journal of Catalysis* **2000**, *192* (2), 381–390.

(150) Papageorgopoulos, D. C.; Berenbak, B.; Verwoest, M.; Riedmüller, B.; Stolte, S.; Kleyn, A. W. A Molecular Beam Study of the Scattering and Chemisorption Dynamics of N2 on Ru(0001). *Chemical Physics Letters* **1999**, *305* (5), 401–407.

(151) Trost, J.; Zambelli, T.; Wintterlin, J.; Ertl, G. Adsorbate-Adsorbate Interactions from Statistical Analysis of STM Images: N/Ru(0001). *Physical Review B* **1996**, *54* (24), 17850–17857.

(152) Zambelli, T.; Trost, J.; Wintterlin, J.; Ertl, G. Diffusion and Atomic Hopping of N Atoms on Ru(0001) Studied by Scanning Tunneling Microscopy. *Phys. Rev. Lett.* **1996**, *76* (5), 795–798.

(153) Grabnic, T.; Edel, R.; Sibener, S. J. Room Temperature Oxidation of GaAs(110) Using High Translational Kinetic Energy Molecular Beams of O2 Visualized by STM. *Surface Science* **2020**, *692*, 121516.

(154) Grant, J. T.; Haas, T. W. A Study of Ru(0001) and Rh(111) Surfaces Using LEED and Auger Electron Spectroscopy. *Surface Science* **1970**, *21* (1), 76–85.

(155) Madey, T. E.; Albert Engelhardt, H.; Menzel, D. Adsorption of Oxygen and Oxidation of CO on the Ruthenium (001) Surface. *Surface Science* **1975**, *48* (2), 304–328.

(156) Xu, W.-Y.; Huang, L.; Que, Y.-D.; Li, E.; Zhang, H.-G.; Lin, X.; Wang, Y.-L.; Du, S.-X.; Gao, H.-J. High Quality Sub-Monolayer, Monolayer, and Bilayer Graphene on Ru(0001). *Chinese Physics B* **2014**, *23* (9), 098101.

(157) Schwegmann, S.; Seitsonen, A. P.; Dietrich, H.; Bludau, H.; Over, H.; Jacobi, K.; Ertl, G. The Adsorption of Atomic Nitrogen on Ru(0001): Geometry and Energetics. *Chemical Physics Letters* **1997**, *264* (6), 680–686.

(158) Hammer, B. Adsorption, Diffusion, and Dissociation of NO, N and O on Flat and Stepped Ru(0001). *Surface Science* **2000**, *459* (3), 323–348.